SETTIMANA ITALIA • CINA
della Scienza, della Tecnologia e dell'Innovazione
中意创新合作周

Results from the Moon Mapping project

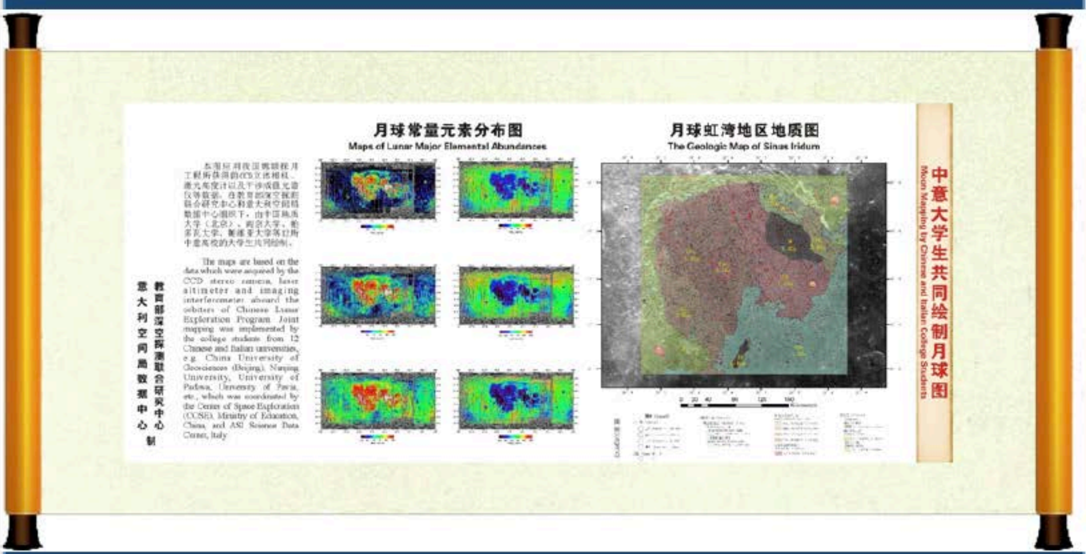

中意月球测图项目成果

Risultati del progetto Moon Mapping

The Moon Mapping project

The Moon Mapping project brings together students and researchers from Italy and China to jointly work on the analysis of data from the Chinese lunar missions Chang'e-1 and Chang'e-2.

The project combines complementary expertise from several universities and research institutions in both Countries, such as automatic crater recognition and characterization from remote sensing data and advanced 3D visualizations. Six workshops and several meetings have been organized in different cities in Italy and China.

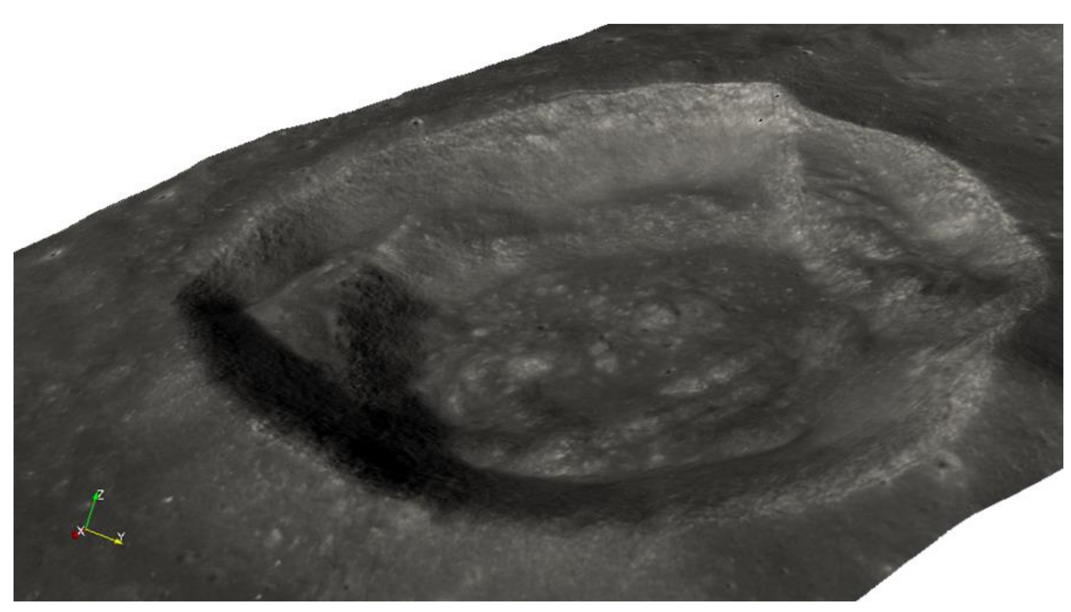

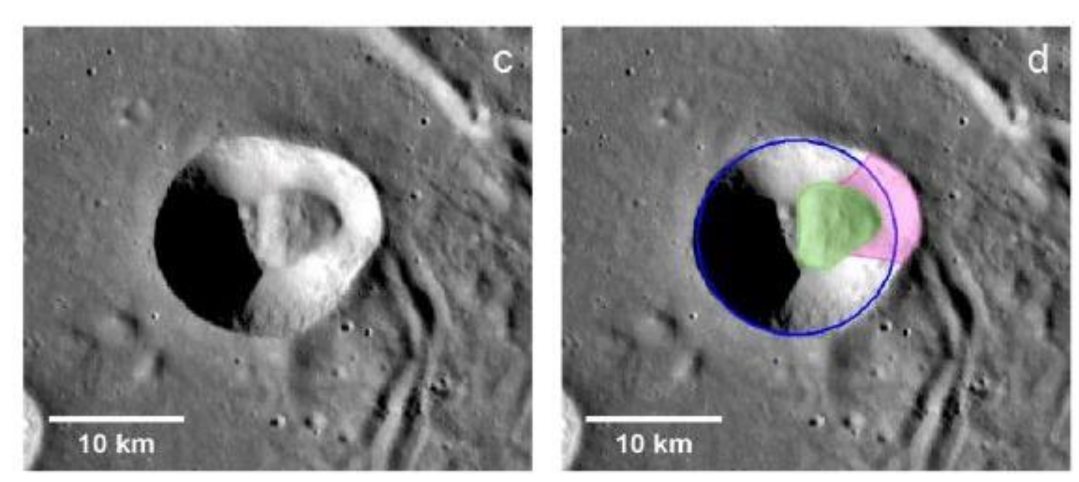

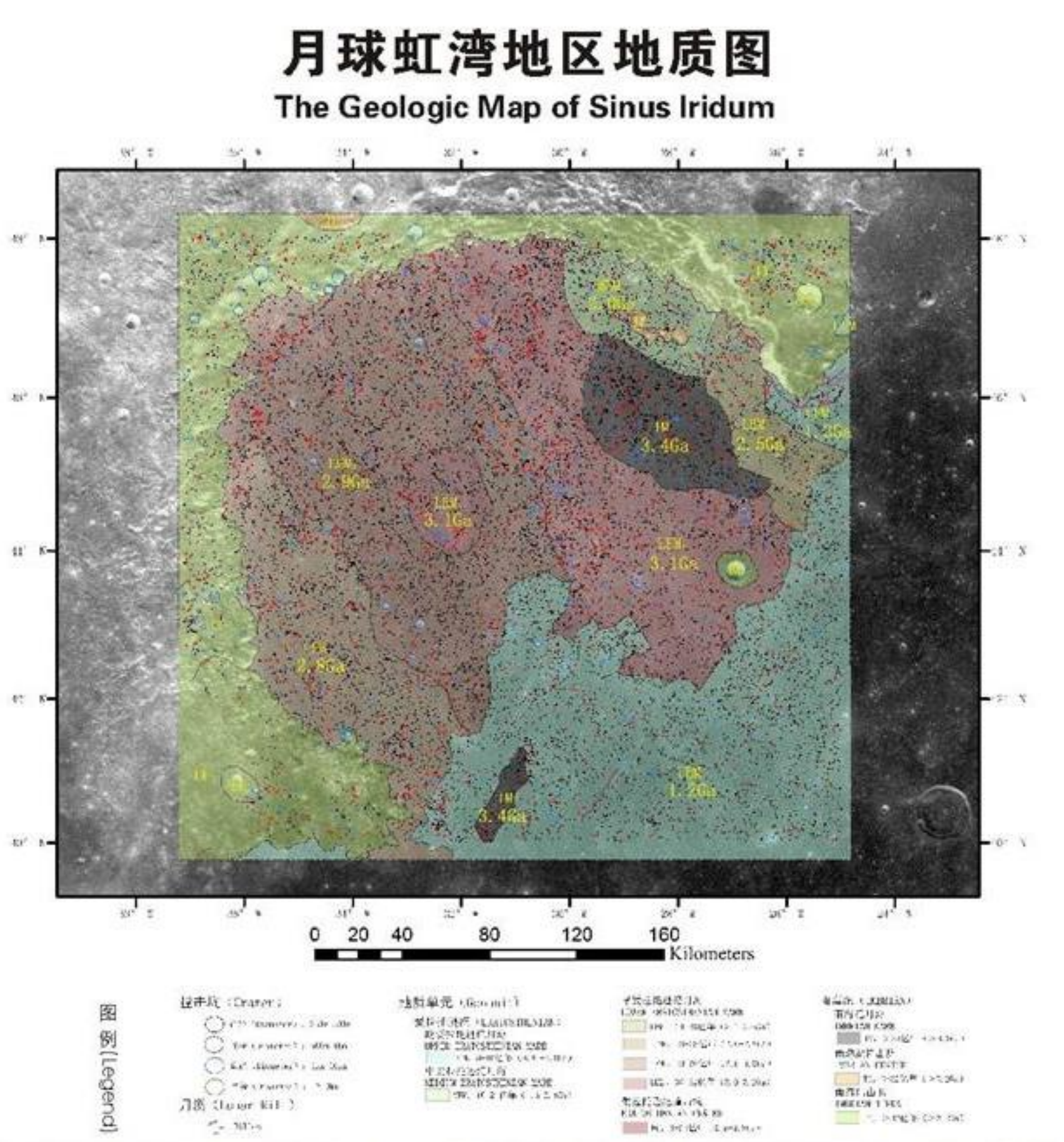

One of the important outcomes of the project is a geological map of the Sinus Iridum region on the Moon. This map was presented to the Chinese and Italian ministers during the «China-Italy Science, Technology & Innovation Week» held in Beijing in November 2017

月球常量元素分布图

Maps of Lunar Major Elemental Abundances

本图应用我国嫦娥探月工程所获得的CCD立体相机、激光高度计以及干涉成像光谱仪等数据，在教育部深空探测联合研究中心和意大利空间局数据中心组织下，由中国地质大学（北京）、南京大学、帕多瓦大学、帕维亚大学等12所中意高校的大学生共同绘制。

The maps are based on the data which were acquired by the CCD stereo camera, laser altimeter and imaging interferometer aboard the orbiters of Chinese Lunar Exploration Program. Joint mapping was implemented by the college students from 12 Chinese and Italian universities, e.g. China University of Geosciences (Beijing), Nanjing University, University of Padova, University of Pavia, etc., which was coordinated by the Center of Space Exploration (COSE), Ministry of Education, China, and ASI Science Data Center, Italy.

教育部深空探测联合研究中心
意大利空间局数据中心 制

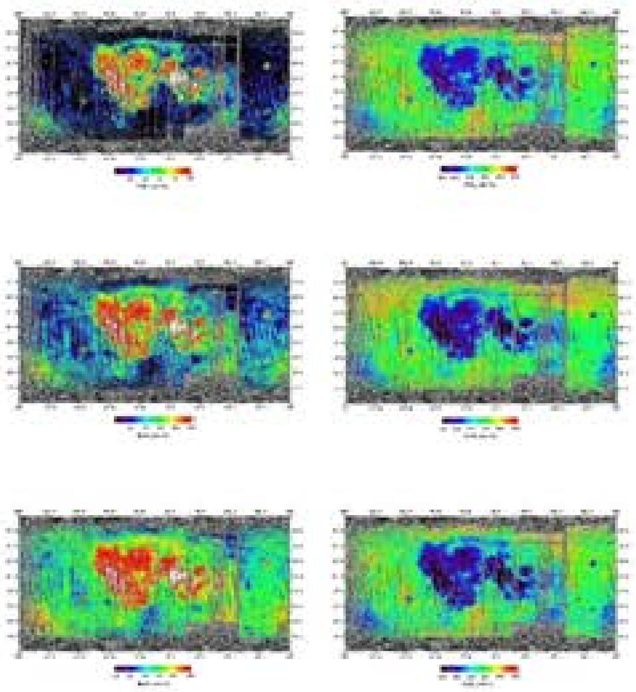

月球虹湾地区地质图

The Geologic Map of Sinus Iridum

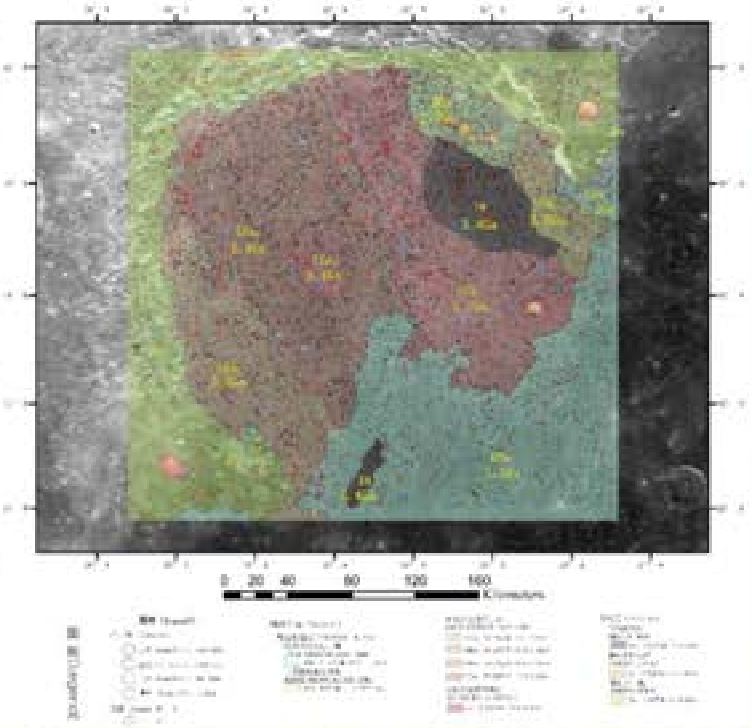


意携手·创新共赢
届中意创新合作周
17.11.14
主办单位 Hosts:
中华人民共和国科学技术部
承办单位 Organizers:
北京市科学技术委员会(中意技术转移中心)
Beijing Municipal Science & Technology Commission
月球常量元素分布图
月球虹湾地区地质图

Moon Mapping

Participating Universities and Research Institutions

- Chongqing University – COSE
- Tsinghua University, Beijing
- Peking University
- China University of Geosciences, Beijing
- China University of Geosciences, Wuhan
- East China Normal University, Shanghai
- Nanjing University

- Italian Space Agency – Roma
- Politecnico di Milano
- Università di Pavia
- INAF-OAPD e Università di Padova
- CNR-IRPI, Perugia
- INAF-IASP, Roma
- Università di Pescara-Chieti
- Università di Cagliari

THE 'MOON MAPPING' PROJECT TO PROMOTE COOPERATION BETWEEN STUDENTS OF ITALY AND CHINA

M. Scaioni [a,*1], P. Giommi [b], M.T. Brunetti [c], C. Carli [d], P. Cerroni [d], G. Cremonese [e], G. Forlani [f], P. Gamba [g], M. Lavagna [h], M.T. Melis [i], M. Massironi [j], G. Ori [k], F. Salese [k], A. Zinzi [b,l], G. Xie [m], Z. Kang [n], R. Shi [o], Y. Sun [p], Y. Wu [q]

[a] Dept. of Architecture, Built environment and Construction engineering (ABC), Politecnico di Milano
via Ponzio 31, 20133 Milano, Italy – marco.scaioni@polimi.it
[b] ASI Science Data Center, Italian Space Agency (ASI-ASDC), Roma, Italy – {paolo.giommi,zinzi}@asdc.asi.it
[c] Research Institute for Geo-Hydrological Protection – Italian National Research Council (IRPI-CNR)
via Madonna Alta, 126, 06128 Perugia, Italy – mariateresa.brunetti@irpi.cnr.it
[d] National Institute for Astrophysics, Institute for Space Astrophysics and Planetology (INAF-IAPS)
via fosso del cavaliere, 00133 Roma, Italy – {cristian.carli,priscilla.cerroni}@iaps.inaf.it
[e] National Institute for Astrophysics, Astronomical Observatory of Padua (INAF-OAPD), Padova, Italy
gabriele.cremonese@oapd.inaf.it
[f] Dept. of Civil, Environmental, Land Management Engineering and Architecture (DICATeA), University of Parma
Parco Area delle Scienze 181/A, 43124 Parma, Italy – gianfranco.forlani@unipr.it
[g] Dept. of Electrical, Computer and Biomedical Engineering, University of Pavia, via Ferrata 5, 27100 Pavia, Italy
paolo.gamba@unipv.it
[h] Dept. of Aerospace Science & Technology, Politecnico di Milano, via La Masa 34, 20156 Milano, Italy
michelle.lavagna@polimi.it
[i] Dept. of Chemical and Geological Sciences, University of Cagliari, via Trentino 51, 09127 Cagliari, Italy
titimelis@unica.it
[j] Dept. of Geosciences, University of Padua, via G. Gradenigo 6, 35131 Padova, Italy – matteo.massironi@unipd.it
[k] IRSPS - Dept. of Engineering and Geology, Università d'Annunzio,
65127 Pescara, Italy{ggori,francesco}@irsps.unich.it
[l] National Institute for Astrophysics, Astronomical Observatory of Rome (INAF-OAR), Roma, Italy
[m] Center of Space Exploration, China Ministry of Education, Chongqing University, Chongqing, China
[n] Dept. of Remote Sensing and Geo-Information Engineering, School of Land Science and Technology
China University of Geosciences, Xueyuan Road 29, Haidian District, 100083 Beijing, China – zzkang@cugb.edu.cn
[o] School of Geographic Sciences, East China Normal University, Shanghai, China
[p] Department of Computer Science and Technology, Tsinghua University, Beijing, China – syk@tsinghua.edu.cn
[q] School of Geographic and Oceanographic Sciences, Nanjing University
Xianlin Boulevard 163, Qixia District, Nanjing 210023, China – wu@nju.edu.cn

Commission VI, WG VI/3

KEY WORDS: Planetary mapping, Moon, Chang'E 1/2, Student Exchange, International Cooperation

ABSTRACT:

The research project 'Moon Mapping' has been established in 2014 between the Italian and Chinese Governments to promote cooperation and exchange between undergraduate students from both countries. The operational phase of the project started in early 2015, and will end in 2017, for a total length of three years. The main aim is to train new scholars to be able to work on different kinds of remotely-sensed data collected over the Moon surface by the Chinese space missions Chang'E-1/2. The project coordination has been assigned to the Italian Space Agency for the Italian side and to the Center of Space Exploration, China Ministry of Education, for the Chinese side. Several Chinese universities and Italian national research institutes and universities have been officially involved in this project. Six main research topics have been identified: (1) map of the solar wind ion; (2) geomorphological map of the Moon; (3) data preprocessing of Chang'E-1 mission; (4) map of element distribution; (5) establishment of 3D digital visualization system; and (6) compilation and publication of a tutorial on joint lunar mapping.

(*) corresponding author

1. GENESIS OF THE PROJECT

On the basis of the great experience that Italy and China have achieved in space exploration over the last decades, the governments of both countries agreed to foster scientific and technological cooperation in this field. In addition, both countries would like to promote the exploitation of existing large archives of data sets, in particular the ones collected during the recent Chinese missions (Chang'E series) on the Moon (see Sect. 3). In this context, the education and the exchange of new generation scholars to be enrolled in space exploration and planetary sciences are seen as a crucial points in both countries.

According to these preliminary considerations, in 2012 the 'Joint Lunar Map Drawing Project by Chinese and Italian College Students,' also know as 'Moon Mapping Project' (MMP), was organized. The definitive signature was held in Rome on 23 January 2015 by the Italian Space Agency (ASI) Science Data Center (ASDC) director Paolo Giommi and the vice-president of the Chinese Center for Space Exploration (COSE) Gengxin Xie. The focus of this project is improve cooperation in space applications, to train new Italian and Chinese university undergraduate students to work on different kinds of remotely-sensed data collected over the Moon surface by the Chinese space missions Chang'E-1/2, to make easier student exchange between both countries, and to create scientific opportunities.

The operational phase started on Jan 2015 and is expected to complete at the end of 2017, for a total length of three-year activities. The project coordination has been assigned to the Italian Space Agency (ASI) for the Italian side and to COSE for the Chinese side. Several universities and national-level research institutes have been officially involved in the MMP on both countries, as presented in Table 1.

Six main research topics have been focused, as it is summarized in Table 2 (see Sect. 3). Each topic is coordinated by two institutions, one per each country. Students have been assigned to each topic to cooperate under the guide of supervisors. A schedule of mutual visits and workshops has been defined to help and promote exchanges along the three years of the project. With the exception of the first round meetings to set up the organization of the project and to prepare a common research plan, students are involved in project meetings so that they may consolidate the cooperation among them, especially between students from both countries. Further discussion on the student involvement, which may be considered as a key-point of the MMP, are given in next subsection 1.2.

The expected follow-up will consist on one side on the preparation of a new generation of young scholars to contribute to planetary science and space exploration. On the other, the MMP is expected to output scientific publications, a tutorial aimed at introducing people to work on planetary data, and a 3D Atlas of the Moon to display the results of the analysis obtained during the research activities.

Further information, documents and news can be found at the website http://solarsystem.asdc.asi.it/change.

Project Topics		**Topic Coordinators**	
		Italy	**China**
1	Map of the solar wind ion	ASDC	Tsingua University
2	Geomorphologicl map of the Moon	Politecnico Milan	China Univ. Geosciences
3	Data preprocessing of Chang'E 1 mission	INAF-IAPS	East China Normal Uni
4	Map of element distribution	Univ. of Cagliari	Nanjing University
5	3D visualization system	ASDC	China Univ. Geosciences
6	Tutorial and Atlas on joint lunar mapping	Chongqing University	University d'Annunzio

Table 2. – Topics of 'Moon Mapping Project' and institutions leading research activities in Italy and China.

Institution	**Department**	**Location, Country**
Italian Space Agency (ASI)	ASI Science Data Centre (ASDC)	Rome, Italy
National Inst. of Astrophysics (INAF)	Astronomical Observatory of Rome (OAR)	Rome, Italy
	Institute for Space Astrophysics and Planetology (IAPS)	
	Astronomical Observatory of Padua (OAPD)	Padua, Italy
National Research Council (CNR)	Research Inst. for Geo-Hydrological Protection (IRPI)	Perugia, Italy
Politecnico di Milano (Technical University of Milan)	Dept. of Aerospace Science and Technology	Milan, Italy
	Dept. Architecture, Built environment and Construction Engineering (ABC)	
University of Cagliari	Dept. of Chemical and Geological Sciences	Cagliari, Italy
University d'Annunzio	IRSPS – Dept. of Engineering and Geology	Pescara, Italy
University of Padua	Dept. of Geosciences	Padua, Italy
University of Parma	Dept. of Civil, Environmental, Land Management Engineering and Architecture (DICATeA)	Parma, Italy
University of Pavia	Dept. of Electrical, Computer and Biomedical Engineering	Pavia, Italy
China Ministry of Education	Center of Space Exploration (COSE), Chongqing University	Chongqing, China
China University of Geosciences	Dept. of Remote Sensing and Geo-Information Engineering, School of Land Science and Technology	Beijing, China
East China Normal University	School of Geographic Sciences	Shanghai, China
Nanjing University	School of Geographic and Oceanographic Sciences	Nanjing, China
Tsinghua University	Dept. of Computer Science and Technology	Beijing, China

Table 1. - Members of 'Moon Mapping Project' between Italy and China.

1.2 Involvement of students

The core of 'Moon Mapping' project is represented by the central role of undergraduate students who are expected carry out the research activity under supervision of senior researches from universities and other institutions.
Students are assigned to specific Topics and Sub-Topics of the project. Since there is a parallel structure involving both Italian and Chinese project members, also students have a direct counterpart working on a related topic. This strict cooperation would like to give the chance to compare different approaches to the research work, and to improve the capability to accomplish scientific investigations thanks to the exchange of ideas.On the other hand, students have the chance to work together with expert scholars in the field of Moon exploration and planetary research, and can benefit from the experience of the international network related to the MMP.
Besides students who directly attend to the research activity, some dissemination actions are planned during the last year of the project. In particular, the organization of an international summer school on the processing techniques remote sensing data on the Moon is scheduled. This important activity will spread out the knowledge achieved during the MMP to a larger scenario of young scholars not only limited to Italy and China, but with the chance to involve students from other countries as well.

2. DATA SETS FROM CHANG'E 1/2 MISSIONS

The Chinese Lunar Exploration Program (CLEP), also known as the Chang'E (the Chinese Moon goddess), is an series of missions organized by the China National Space Administration (CNSA). The program incorporates lunar orbiters, landers, rovers and sample return spacecraft, launched using Long March rockets.
The first spacecraft of CLEP/Chang'E program, the Chang'E 1 (CE-1 - see Subsect. 2.1) lunar orbiter, was launched on 2007. A second orbiter, Chang'E 2 (CE-2), was launched on 2010 (see Subsect. 2.2). Chang'E 3 (CE-3), which includes a lander and a rover, was launched on 1 December 2013 and successfully soft-landed on Mare Ibridum on 14 December 2013. The 'Yutu' rover travelled 114 m. CE-3 will be followed by a sample return mission, Chang'e 5 scheduled for 2017.
The 'Moon Mapping' project was initially focused to exploit data from CE-1 mission, but subsequently the availability of some data sets from CE-2 became possible. A part of the data sets from CE-1/CE-2 missions can be downloaded from the webpage http://moon.bao.ac.cn/ceweb/datasrv/dmsce1 .jsp.

2.1 Chang'E 1

On October 24, 2007, CE-1 was successfully launched from the Xichang Satellite Launch Center. Up until 1st July 2008, CE-1 has accomplished lunar global data acquisition. CE-1 carries 8 instruments (CCD stereo camera, laser altimeter, Gamma Spectrometers, X-Ray Spectrometers, ow-Energy Ion Detector, High-Energy Solar Particle Detector, Microwave Detector, Interferometer Spectrometer Imager) which have obtained about 1370G of data. These data have been published online at present, available for international planet researchers (see above).
CE-1 mission had four major goals:

1. Obtaining 3D reconstructions of the landforms and geological structures of the lunar surface, so as to provide a reference for planned future soft landings. The orbit of CE-1 around the Moon was designed to provide complete coverage, including areas near the north and south poles not covered by previous missions;
2. Analysing and mapping the abundance and distribution of various chemical elements on the lunar surface as part of an evaluation of potentially useful resources on the Moon. China hopes to extend the number of elements studied to 14 (K, Th, U, O, Si, Mg, Al, Ca, Te, Ti, Na, Mn, Cr, La) compared to the 10 elements (K, U, Th, Fe, Ti, O, Si, Al, Mg, Ca) previously probed by NASA's Lunar Prospector;
3. Probing the features of the lunar soil and assessing its depth, as well as the amount of helium-3 (^3He) present; and
4. Probing the space environment between 40,000 km - 400,000 km from the Earth, recording data on the solar wind and studying the impact of solar activity on the Earth and the Moon.

In addition, the lunar probe engineering system, composed of five major systems – the satellite system, the launch vehicle system, the launch site system, the monitoring and control system and the ground application system – accomplished five goals:

- Researching, developing and launching China's first lunar probe;
- Mastering the basic technology of placing satellites in lunar orbit;
- Conducting China's first scientific exploration of the Moon;
- Initially forming a lunar probe space engineering system; and
- Accumulating experience for the successive phases of China's lunar exploration program.

2.2 Chang'E 2

CE-2 is a Chinese unmanned lunar probe that was launched on 1 October 2010. It was a follow-up to the CE-1 lunar probe, which was launched in 2007. CE-2 was part of the first phase of the Chinese Lunar Exploration Program, and conducted research from a 100-kilometer-high lunar orbit in preparation for the December 2013 soft landing by the CE-3 lander and rover. CE-2 was similar in design to CE-1, although it featured some technical improvements, including a more advanced onboard camera. After completing its primary objective, the probe left lunar orbit for the Earth–Sun L2 Lagrangian point, to test the Chinese tracking and control network, making the China National Space Administration the third space agency after NASA and ESA to have visited this point. It entered orbit around L2 on 25 August 2011, and began transmitting data from its new position in September 2011. In April 2012, CE-2 departed L2 to begin an extended mission to the asteroid 4179 Toutatis, which it successfully flew by in December 2012. This success made China's CNSA the fourth space agency to directly explore asteroids, after NASA, Europe's ESA and Japan's JAXA. As of 2014, CE-2 has travelled over 100 million kilometres from Earth, and is conducting a long-term mission to verify China's deep-space tracking and control systems.

3. PLANNED RESEARCH ACTIVITIES

In this section the research content to be developed in each project Topic is briefly outline. The purpose here is not to draw a state-of-the-art on the use of CE-1/2 data for mapping different characteristics on the Moon, but just to focus on the activities that are strictly related to MMP. Some projects members have already developed their own studies that are not mentioned here, since they have been carried out independently from MMP.

3.1 Topic 1

The aim of Topic 1 is to produce a map of the solar wind ions on the basis of CE-1 data. Based on the lunar probe data and existing research results, the distribution of solar wind ion at critical moments will be drawn, by which to provide an interactive visualization approach for drawing low-energy solar ion flow distribution at arbitrary time, giving a real-time display of solar wind ion flow and its direction.
The workplan of this Topic is as follows. In a first stage, a sample of data from CE-1 Solar Wind Ion Detector are delivered (664 files collected from 26 Nov 2007 to 31 Dec 2007). Data are organized in a database hosted on a server at ASDC. File format are transformed to be ready to use. The following two data post-processing/analysis steps have been started:

1. Spacecraft velocity evaluation;
2. Sun Incidence angle evaluation.

Next steps in data post-processing will be:

1. Merging of SWIDA and SWIDB (time synchronization);
2. Evaluation of solar wind parameters by SWIDA/B data fit;
3. Production of Multidimensional solar wind maps;
4. Evaluation of Earth/Sun magnetic fields; and
5. Correction of the magnetic field effects.

3.2 Topic 2

This Topic is focused on the analysis of Moon geomorphology and the production of geomorphological maps representing different aspects. It is organized in three Sub-topics.

a. *Sub-topics 2.1*: is devoted to the extraction of geometrical features for characterization of the impact structures and proximal ejecta, development of crater morphology and degradation;
b. *Sub-topic 2.2*: focuses to the extraction and characterization of landslides on the Moon surface, in particular into the impact craters. Analysis of landslide triggering process and impact-related effects will be investigated as well; and
c. *Sub-topic 2.3*: has the aim of doing research and characterization of lava-tubes below the Moon surface and their relations with sinuous rilles.

Impact craters are one of the most important geological processes in the understanding of the formation and evolution of our Solar System. They have been observed on planets and small bodies' surfaces, and therefore they kept the record of the cumulative effects of subsequent impacts, volcanic emplacements, tectonics, and so on. The MMP team has developed a valuable expertise on studying the impact craters starting from the DTM generation using stereo images and proceeding with the morphometric analysis. The morphometric characterization of the craters allows estimating the slope, the openness, the profile and plan curvature, and calculating the different geometrical planes. Furthermore the analysis of the impact process by means of the so-called shock physics codes has been started. In particular, the iSale hydrocode is adopted that relies on elasto-plastic constitutive models, fragmentation models, a number of EoS, multiple materials and a porosity compaction model.
In line with the consolidated cooperation with China University of Geosciences on geometrical feature extraction from Moon images (Kang et al., 2015), the team at University of Pavia is currently working on the extraction of hints to craters and ridges using both 2D and 3D information from the stereo cameras of CE-1 and CE-2. The research work includes the definition of advanced techniques for the extraction of circular and linear geometrical features and the combination via feature level fusion of multiple hints for the detection of objects of interest, according to the procedure graphically described in Figure 3.

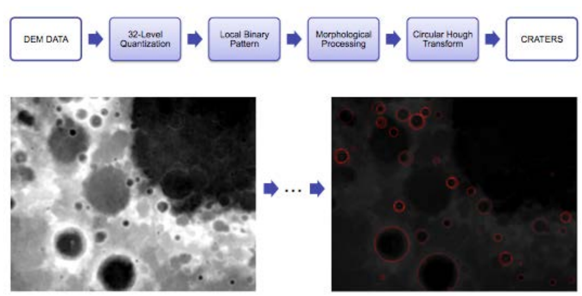

Figure 3. - Crater extraction procedure scheme developed by University of Pavia.

Results, although preliminary, show potential in the approach, that will be further optimized to deal with large images, with the aim to be useful for finer resolution data on wide portions of the lunar surface.

A working group (Politecnico di Milano-ABC, CNR-IRPI, University of Cagliari, INAF-OAR and INAF-OAPD) has been established to study large rock slides inside impact craters and to prepare a landslide inventory to be included in the Atlas (see Subsect. 3.6). So far, image from WAC (Wide Angle Camera) and DEM from LROC (NASA) at 100 m/px have been used to visually recognize 60 landslides in impact craters (Brunetti et al., 2015).

On the other hand, the need for a more objective automatic method is required in order to make the recognition process independent from the subjective interpretation and to carry out an exhaustive search (see Guzzetti et al., 2012; Scaioni et al. 2014). In Mahanti et al. (2014) the Chebyshev polynomials have been applied to interpolate crater cross-sectional profiles in order to obtain a parametric characterization useful for classification into different morphological shapes. Indeed, besides some important mathematical properties (e.g., orthogonality) that distinguish Chebyshev polynomials from other approximating functions, the lower order coefficients are correlated to some geomorphological characteristic of the crater and its surroundings. As an example, the zero order coefficient represents the average ground surface elevation, the 1st order is related with the local topographic slope and 2nd with the crater depth. The purpose of the interpolation with the Chebyshev polynomials is to model each crater with a theoretical shape. An example of interpolation is shown in Figure 4. The use of such polynomial approximations for detecting post-impact degradation processes in lunar craters has been already proposed in Mahanti et al. (2015). Here the analysis of odd coefficients of Chebyshev polynomials has been applied to detect asymmetries in the crater profile. The concept that is pursued in this subtopic is to recognize landslides by analyzing the discrepancy between the actual crater cross-sectional profiles and the theoretical ones (Yordanov et al., 2016). Four cross-sections are considered per each crater. Deviations from the theoretical shape can be detected through the analysis of the Chebyshev coefficients so that the landslide is automatically identified. Whilst the LROC-DEM has been used for the initial set up of the methodology, data from CE-2 will be also considered in a successive stage, due to similar spatial resolution. Indeed, the acquired stereo images from the equipped charge-coupled-device (CCD) camera can reach a resolution of 7 m from CE-2 circular orbit (reaching a minimum distance from ground of approx. 100 km), and 1.5 m around the perilune (minimum distance from ground of approx. 15 km), see Zhao et al. (2011).

Further studies will include: the measurement of the landslide volume; the analysis of relationships between landslides and characteristics of the hosting craters as well as the surrounding terrain; the lithological and mineralogical characterization of surfaces using multispectral data acquired by the IIM data from CE-1.

Another working group (CNR-IRPI, University of Cagliari) will focus on the research and characterization of lava-tubes below the Moon surface. Recent planetary missions have made available large amounts of remote sensing data. Among the many interesting results obtained from the analysis of high-resolution images is the detection of lava tubes on Mars and on the Moon (Haruyama et al., 2009). These caves, also present on Earth, originate from cooling and the subsequent consolidation of the outermost part of very fluid lava flows. In the harsh lunar environment, lava tubes can provide a natural shelter. Detection and characterization of lava tubes and their relations with sinuous rilles will use data available from the multispectral sensor IIM and the CCD.

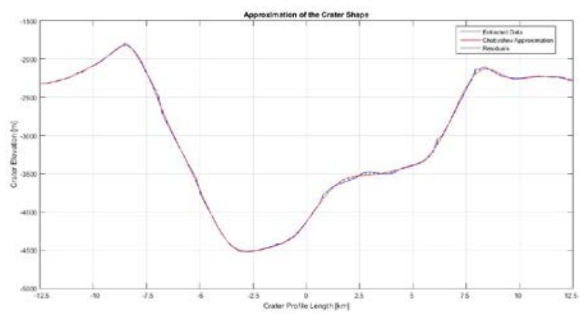

Figure 4. - Example of interpolation of a lunar crater cross-sectional profile using Chebyshev polynomials.

3.3 Topic 3

Topic 3 has the aim of investigating calibration and preprocessing procedures for the sensors in the CE-1 payload. Prior to data analysis and application, pre-processing on the remotely sensed raw data is necessary for correcting distortion due to the characteristics of imaging systems and imaging conditions. It normally precedes further manipulation and analysis of the image data to extract specific information. The pre-processing of data is a crucial step in the remote sensing analytical workflow, and is often the most time consuming and costly.

Since the CE-1 ended about seven years ago, several research groups have already started working on data preprocessing. Hu et al. (2013) have coped with the calibration of laser altimetry data, obtaining significant improvement on the quality of the final DEM. Wu et al. (2013) have dealt with the photometric correction and in-flight calibration of Interference Imaging Spectrometer (IIM) data onboard CE-1. In the literature, several experiences about calibration of other sensors during space missions are reported. For example, Haruyama et al. (2008) have worked on the radiometric calibration of digital camera adopted during SELENE mission.

Whilst other Topics of MMP are focused to output specific products, Topic 3 has a more general purpose and it's expected to contribute to those aspects of sensor data processing that may be required in other Topics of the project. In Figure 5, the pre-processing workflow of IIM data implemented during MMP is shown.

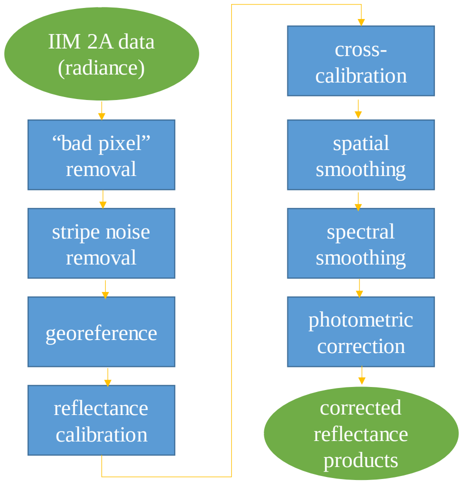

Figure 5. - IIM pre-processing workflow.

3.4 Topic 4

The aim of Topic 4 is to output a map of element distribution on the Moon surface on the basis of data acquired by the Interference Imaging Spectrometer (IIM) onboard CE-1 (Wu et al., 2010). IIM sensor covers a spectral range (0.48-0.96 µm) that can be used to retrieve information about the differences of lunar surface composition. Indeed, reflectance spectra may offer important information on mineralogy and lithology. Starting from the experiences of Wu et al. (2010; 2013), the calibrated data acquired by IIM sensor will be used for the spectral characterization of the surfaces in terms of elements distribution, mineralogical composition and lithologic characterization. Both the indirect approach based on spectral parameters (see, e.g., Lucey et al., 2000), and the direct indication retrievable from the 0.9 µm (Fe^{2+} bearing silicates) absorption can be applied (even if IIM spectral range cannot investigate completely this absorption with respect to longer wavelength sensors). Moreover, by correlating spectral analysis of IIM data with other hyperspectral images covering a larger wavelength range (i.e., M3 data from sensor on onboard Indian satellite Chandrayaan-1 – see, e.g., Pieters et al., 2011), it will be possible to extrapolate more mineralogical indication from IIM data set. Laboratory spectral analysis on terrestrial analogues (e.g., Serventi et al., 2014), as well as lunar meteorites or lunar samples, can be useful to define these spectral relationships (e.g. Lucey et al., 2000).
At this first phase the IIM data are obtainable through the MATISSE web-tool (see Subsect. 3.5). The data are georeferenced and the full set of 26 bands, ranging from 522.37-918,109 nm, is available.
As described in subsection 2.2, the IIM data will be also used for a specific lithological analysis of the landslides in the larger craters. In Figure 6, a preliminary processing result of these data is shown: the surface of this crater (diameter 7.5 km) presents specific spectral anomalies.
The results of the research activities in Topic 4 will be integrated with photo-interpretation and classification of the main elements as volcanic morphologies and craters to support the evolution and dynamics of these morphologies. It is also planned to compare the processed data with existing spectral imagery as Clementine UVVIS camera bands and M3 products.

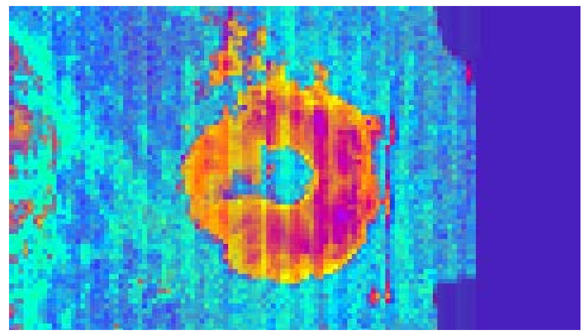

Figure 6. - The visualization of a lunar crater generated with a decorrelated stretching of a color composite using CE-1 IIM.

3.5 Topic 5

This Topic, devoted to the establishment of a 3D visualization system, would likely interact with the majority of the other Topics as, thanks to advanced visualization procedures, data analysis would boost with a great impact on scientific return.
At the present time the Italian side of the Moon Mapping project is focused in adding to the MATISSE web-tool (http://tools.asdc.asi.it/matisse.jsp - Zinzi et al., 2016) the data acquired by the Chinese missions to the Moon.
Very recently, all the CE-1 observations acquired with the visible CCD camera and the VIS/IR IIM spectrometer have been made available to the MMP users using MATISSE.
Furthermore, higher-order products of both CE-1 and CE-2 are already present in the MATISSE database, including DEM and orthoimages.
Using MATISSE it is possible to retrieve spatial data on the basis of a geographical query and to select one or more observations in order to either display a single observation or compute high-order products (i.e., mosaics, ratios, differences, RGB images) on the basis of available observations. The corresponding outputs can be managed by means of popular GIS desktop software packages (with GeoTIFF and ENVI format outputs) or using the advanced 3D tools provided by Paraview files (Fig. 7).
In the next future the number of observations available would likely rise, including also Solar Wind Ion Detector (SWID) and CE-2 data set, thus allowing the full exploitation of the available archives.

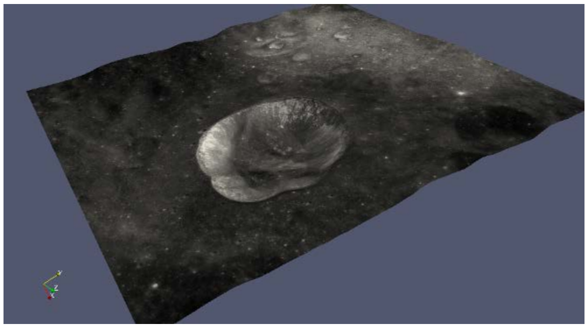

Figure 7. - The 3D visualization of a lunar crater generated using CE-2 high resolution ortophoto and NASA DEM (details in Zinzi et al., 2016).

3.6 Topic 6

IRSPS will edit a Moon Atlas dealing with the geological characterization of a number of sites in proximity of the maximum illumination areas of the lunar poles. The Atlas dataset will be based on CE-1 and CE-2 images and data. The Atlas will use as starting point the work by Mazarico et al. (2011) and will concentrate on both lunar poles. These areas bear strong scientific interest such as the history of volatile (Chin et al., 2007), but, also, they are interesting for the human exploration.
Data from these areas are critical for the planning and operations of future surface mission since:

- these sunlit areas could be prime locations for the establishment of solar photovoltaic arrays, and, consequently, they are rather efficient in power generation;
- sunlit area are thermally benign, the surface temperatures at the lunar equator and mid-latitudes depend almost entirely upon incident solar illumination, whereas the surface temperature of the permanent or quasi-permanent lit areas is nearly constant (Mazarico et al., 2011) facilitating the thermal design of surface habitats and equipment;
- lunar regions from about 80° to the pole are of particular interest due to the possible presence of volatiles (Watson et al., 1961; Paige et al., 2010), especially in the permanent shadow regions (PSRs) seen as potential cold traps of volatiles (Nozette et al., 1996; Feldman et al., 2000; Bussey et al., 2003; Mitrofanov et al., 2010a,b).

4. CONCLUSIONS AND PROSPECTS

This paper has outlined the 'Moon Mapping Project' between university and research institutes of Italy and China. The project has seen its kick-off on 2015 and is going to develop up to the scheduled end on 2017. The focus of the project is to promote cooperation between both countries in space applications and science. The main feature that characterize 'Moon Mapping Project' is the strong student-oriented character. The research activity are promoted to actively involve undergraduate students and to make easier exchanges between both countries. Using the data of China's lunar exploration, undergraduates from both countries work together to map the moon in three dimension, and share the cooperation achievements globally.
The cooperation between Italy and China is expected to deepen cooperation in the field of science and education. The main anticipated achievement of the cooperation is the joint publication of a textbook on lunar remote-sensing image processing. The textbook will be published in English and will be used either in relevant university classes and also as a guide-book in museums.

Acknowledgements

The main acknowledgements go to the Italian Space Agency and the Center of Space Exploration of China Ministry of Education which have promoted, funded and supported this project. Acknowledgements also go to all administrations of Italian and Chinese universities and research centres involved in 'Moon Mapping Project,' since they are actively contributing to its positive development. The authors would like to sincerely thank the Embassy of Italy in Beijing and especially the Science & Technology Councellor (Prof. Plinio Innocenzi) who promoted this project and gave a great support during the preparation stage. The authors would also thank all colleagues that have been supporting in some way the research or the organizational activities (travels, workshops, etc.). Eventually, many thanks go to students, who are playing a primary role in this project.

REFERENCES

References from journals:

Brunetti, M.T., Xiao, Z., Komatsu, G., Peruccacci, S., Guzzetti, F., 2015. Large rockslides in impact craters on the Moon and Mercury. *Icarus*, 260: 289-300.

Bussey, D.B.J., Lucey, P.G., Steutel, D., Robinson, M.S., Spudis, P.D., Edwards, K.D., 2003. Permanent shadow in simple craters near the lunar poles. *Geophysical Research Letters*, Vol. 30, paper No. 1278.

Chin, G., and other 16, 2007. Lunar Reconnaissance Orbiter overview: The instrument suite and mission. *Space Science Review*, Vol. 129, 29 pages.

Feldman, W., Lawrence, D., Elphic, R., Barraclough, B., Maurice, S., Genetay, I., Binder, A., 2000. Polar hydrogen deposits on the Moon. *Journal of Geophysical Research*, Vol. 105: 4175-4195.

Guzzetti, F., Mondini, A.C., Cardinali, M., Fiorucci, F., Santangelo, M., Chang, K.T., 2012. Landslide inventory maps: new tools for and old problem. *Earth Science Review*, Vol. 112(1-2): 42-66.

Haruyama, J., and 11 others, 2008. Planned radiometrically calibrated and geometrically corrected products of lunar high-resolution Terrain Camera on SELENE. *Advances in Space Research*, Vol. 42: 310-316.

Haruyama, J., and 13 others, 2009. Possible lunar lava tube skylight observed by SELENE cameras. *Geophysical Research Letters*, Vol. 36(21), paper no. L21206.

Hu, W., Di, K., Liu, Z., Ping, J., 2013. A new lunar global DEM derived from Chang'E-1 Laser Altimeter data based on crossover adjustment with local topographic constraint. *Planetary and Space Science*, Vol. 87: 173-182.

Jin, S., Arivazhagan, S., Araki, H., 2013. New results and questions of lunar exploration from SELENE, Chang'E-1, Chandrayaan-1 and LRO/LCROSS. *Advances in Space Research*, Vol. 52: 285-305.

Kang, Z., Luo, Z., Hu, T., Gamba, P., 2015. Automatic extraction and identify-cation of lunar impact craters based on optical data and DEMs acquired by the Chang'E satellites. *IEEE Journal of Selected Topics in Applied Earth Observation and Remote Sensing*, Vol. 8(10): 4751-4761.

Lucey, P.G., Blewett, D.T., Jolliff, B.L., 2000. Lunar iron and titanium abundance algorithms based on final processing of Clementine ultraviolet-visible images. *Journal of Geophysical Research*, Vol. 105(E8): 20,297–20,305.

Mahanti, P., Robinson, M.S., Humm, D.C., Stopar, J.D., 2014. A standardized approach for quantitative characterization of impact crater topography. *Icarus*, Vol. 241: 114-129.

Mazarico, E., Neumann, G.A., Smith, D.E., Zuber, M.T., Torrence, M.H., 2011. Illumination conditions of the lunar polar regions using LOLA topography. *Icarus*, Vol. 211: 1066-1081.

Mitrofanov, I.G., and other 28, 2010a. Testing for hydrogen in permanently shadowed regions at the lunar south pole with the lunar exploration neutron detector on board LRO. *Science*, Vol. 330: 483-486.

Mitrofanov, I.G., and other 35, 2010b. Lunar exploration neutron detector for the NASA Lunar Reconnaissance Orbiter. *Space Science Review*, Vol. 150: 183-207.

Nozette, S., Lichtenberg, C.L., Spudis, P., Bonner, R., Ort, W., Malaret, E., Robinson, M., Shoemaker, E.M., 1996. The Clementine bistatic radar experiment. *Science*, Vol. 274: 1495-1498.

Paige, D.A. and other 26, 2010. Diviner lunar radiometer observations of cold traps in the Moon's south polar region. *Science*, Vol. 330: 479-482.

Pieters, and other 26, 2011. Mg-spinel lithology: A new rock type on the lunar farside. *Journal of Geophysical Research*, Vol. 116., paper No. E00G08.

Scaioni, M., Longoni, L., Melillo, V., Papini, M., 2014. Remote Sensing for Landslide Investigations: An Overview of Recent Achievements and Perspectives. *Remote Sensing*, Vol. 6(10): 9600-9652.

Sun, H., Dai, S., Yang, J., Wu, J., Jiang, J., 2005. Scientific objectives and payloads of Chang'E-1 lunar satellite. *Journal of Earth System Science*, Vol. 114(6): 789-794.

Watson, K., Murray, B.C., Brown, H., 1961. The behavior of volatiles on the lunar surface. *Journal of Geophysical Research*, Vol. 66: 3033-3045.

Wu, Y., and other 9, 2010. A preliminary experience in the use of Chang'E-1 IIM data. *Planetary and Space Science*, Vol. 58(14-15): 1922-1933.

Wu, Y., Besse, S., Li, J.-Y., Combe, J.-P., Wang, Z., Zhou, X., Wang, C., 2013. Photometric correction and in-flight calibration of Chang' E-1 Interference Imaging Spectrometer (IIM) data. *Icarus*, Vol. 222: 283-295.

Zhao, B., Yang, J., Wen, D., Gao, W., Chang, L., Song, Z., Xue, B., Zhao, W., 2011. Overall scheme and on-orbit images of Chang'E-2 lunar satellite CCD stereo camera. *Science China - Technological Sciences*, Vol 54: 2237-2242.

Zinzi, A., Capria, M.T., Palomba, E., Giommi, P., Antonelli, L.A., 2016. MATISSE: A novel tool to access, visualize and analyse data from planetary exploration missions. *Astronomy and Computing*, Vol. 15: 16-28.

References from books:

Serventi, G., Carli, C., Sgavetti, M., 2014. *Laboratory Analysis (Reflectance Spectroscopy) of Terrestrial Analogues. Encyclopedia of Lunar Science*. Springer International Publishing Switzerland, pp. 1-9.

References from Other Literature:

Mahanti, P., Robinson, M.S., Thompson, T.J., 2015. Characterization of lunar crater wall slumping from Chebyshev approximation of lunar crater shapes. In: Proc. "Annual Meeting of the Lunar Exploration Analysis Group (LEAG)," 20-22 Oct. 2015, Columbia, Maryland, U.S., paper No. 2081.

Yordanov, V., Scaioni, M., Brunetti, M.T., Melis, M.T., Zinzi, A., Giommi, P., 2016. Mapping Landslides in Lunar Impact Craters Using Chebyshev Polynomials and DEM's. *Int. Arch. Photogramm. Remote Sens. Spatial Inf. Sci.*, Vol. XLI-VI Prague, Czech Republic, 8 pages.

An Approach for Recognising Large Landslides Inside Lunar Impact Craters

V. Yordanov[1], M.T. Brunetti[2], M.T. Melis[3], A. Zinzi[4], M. Scaioni[1]

1. Introduction

The Moon is the closest celestial body to the Earth and as such it is also the only natural satellite orbiting around our planet. Consequently, it has been also the object for numerous studies. Among them, geological studies have investigated slope failures [Bart, 2007; Brunetti et al., 2015; Buczkowski et al., 2016; De Blasio et al., 2011; Krohn et al., 2014; Massironi et al., 2012; Mazzantiet al., 2016; Quantin et al., 2004; Waltham et al., 2008; Williams et al., 2013]. First Pike (1971) performed studies about mass movements on the Moon using images obtained during the Apollo 10 mission. More recently, Xiao et al. (2013) studied lunar landslides and classified them into different morphologic groups, based on the criterion obtained for landslide classification on Earth (Cruden & Varnes, 1996). In Brunetti et al. (2015) a visual analysis is applied to detect large landslide features on the Moon, Mars and Mercury.

The mass wasting processes could be considered as one of the most important factors for surface degradation in planetary science. Indeed, due to the variety and extent of this phenomenon, the number of methods for recognition and mapping different types of landslides also broadly varies. Geological slope failures on the Moon's surface have already been observed, but a detailed and exhaustive lunar landslide inventory has not been produced yet. The following proposed approach has the goal to imply all the distinctive features of the problem with identification of lunar landslides in impact craters and to resolve them, with a low-level of uncertainty, resulting in a more objective and less time-consuming methodology. In particular, the approach is focused into the recognition of large slope failures (slumps) inside the cavities of simple impact craters.

1.1 Simple impact craters

In terrestrial planets one of the most frequent and common, surface changing process is the impact cratering, that not only influences the surface, but also it may affect the planetary evolution in any aspect.

Although the impact craters can be labelled in general as circular rimmed depressions, they may largely differ from one another and can by classified according to size, substrate material, weathering and age. The fundamental shape of an impact crater is a bowl-shaped depression with elevated rims. The size of the craters widely varies in diameter (measured from rim to rim) from millimetre level to more than 2,500 km diameter. With increasing the diameter, the impact crates become proportionally shallower and more complex in shape, including terraced walls and central

---

[1] Department of Architecture, Built environment and Construction engineering, Politecnico di Milano, Milano, Italy
[2] Research Institute for Geo-Hydrological Protection – Italian research Council, Perugia, Italy
[3] Department of Chemical and Geological Sciences, University of Cagliary, Cagliary, Italy
[4] Space Science Data Center – ASI, INAF-OAR, Rome, Italy

peaks. Studies show that on all terrestrial planets and moons, such morphologic changes are notable (Pike, 1980). Furthermore, craters' types are classified in the literature according to the morphologic features into simple, complex and multi-ring basins (Melosh, 2011).

Simple impact craters' shape can be conveniently described as a simple bowl-shaped. In addition, they have small, rounded or in some cases flat floors, with smooth walls, see Fig. 1. Craters from this class have a rim-to-rim diameter up to 15 km on the Moon and 3 to 6 km on Earth. The sharp-crested rim stands about 4% of the crater diameter above the surrounding plain, which is a blanket with a mixture of ejecta and debris scoured from the pre-existing surface. The depth-to-diameter ratio of 1/5 is relatively high (Melosh, 2011). The floor of simple impact craters is covered by a

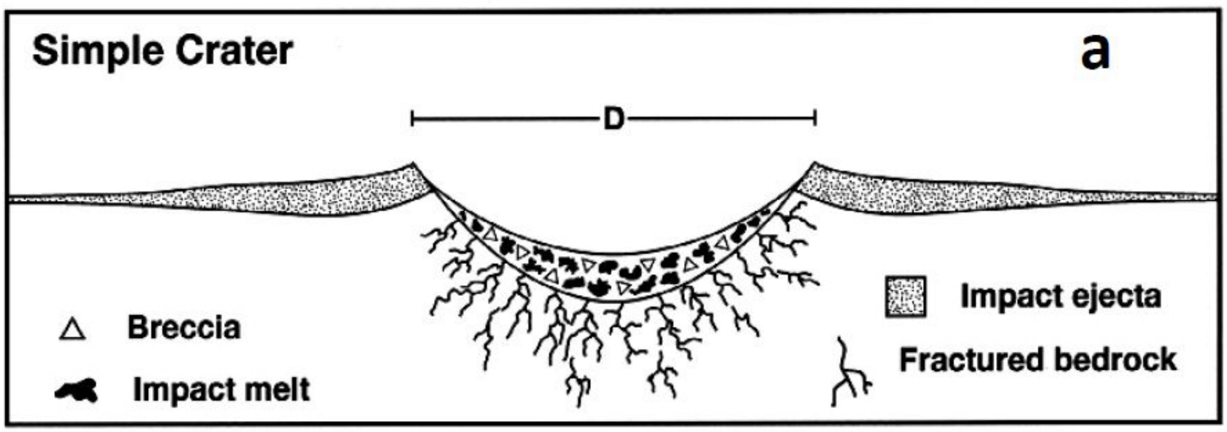

Fig. 1. General structure of a simple impact crater (Credits: NASA)

lens of broken rock ("breccia") which slumped down immediately after the impact. The thickness of this lens is around ½ to ⅓ of the crater rim-to-floor depth.

1.2 Slumps

The Moon's surface is rich of surface features. Thus mass wasting processes can be identified on various lunar terrains, such as impact craters, volcanic domes, tectonics scarps, rilles, wrinkle ridges, etc. (Xiao et al., 2013). Despite of, the variety of multiple surface forms, the dominant features are impact craters and most of the lunar slope failures occur on their walls. Since the Apollo missions, some studies were performed, to study landslide's morphological and distribution characteristics, as well as predisposing factors and triggering mechanisms (Pike, 1970; Xiao et al., 2013; Kumar et al., 2013; Brunetti et al., 2015). Regardless the absence of water, different authors classified lunar landslides in the same type used on Earth. As a result, Moon's mass wasting features can be grouped as falls, slides, slumps, flows and creeps on the basis of their morphology, possible models of emplacement, and sizes of emplaced material (Xiao et al., 2013).

The focus of this work is detecting large scale landslides and more precise – slumps. They can be defined as sudden mass movements of large amounts of rocks and/or fine material travelling for short distances (Ritter et al., 2006). Lunar slumps usually occur soon after the formation of the impact crater, when impact melt and debris are unstable on the crater walls. The mass movement usually is sliding along a concave-upward shape or planar surface.

Geological slope failures are usually related to instabilities in slopes and driven by gravity. There is delicate but important difference between predisposing factors and triggering ones. Typically, it is possible to determine one or more causes for landslide but only factor that triggers mass movement. Predisposing causes can be considered as the factors leading the slope to become unstable, hence to failure. On Earth, geological, morphological, physical factors and even human activity can lead to the instability of the surface features. So a combination of causes and a single triggering event can finally have initiated the mass movement.

On the Moon the lack of water, the volcanic and tectonic activities lead to different triggering factors, compared to the Earth. The large number of meteorite impacts in a variety of sizes is considered as triggering factor for mass movements, directly and indirectly. Firstly, impact may induce shock waves that may directly disturb materials on slopes forming mass wasting landforms (Lindsay, 1976), followed by crushed subsurface bedrock and formation of fractured zones that sometimes extend several radii beneath the crater floor (Melosh, 1989).

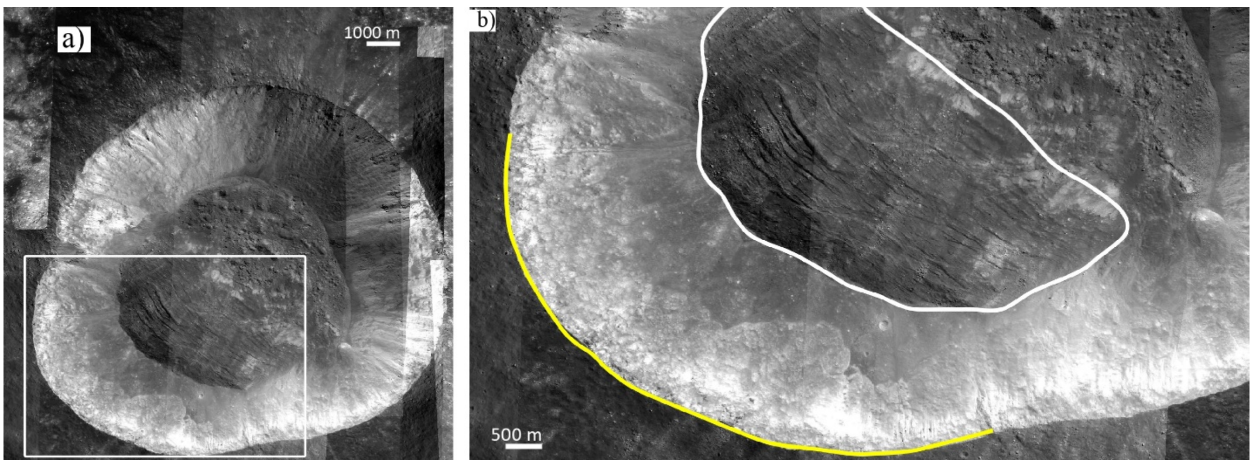

Fig. 2. Example of a slumped crater wall

2. Suitable data for the analysis

In the recent years, several space agencies have operating missions orbiting around the Moon, carrying on-board measuring instruments helping the scientists to explore Lunar's surface. Some of those missions are: the Lunar Reconnaissance Orbiter (LRO) by National Aeronautics and Space Administrations (NASA, United States) and Chang'E missions by the Chinese Nationals Space Administration (CNSA, P.R. China). Each of these missions is revised in the following sections.

2.1. Lunar Reconnaissance Orbiter – (NASA)

LRO has six individual instruments on-board, with the purpose to produce accurate maps and to obtain high-resolution images. Among other purposes, these images will be used to assess potential future landing sites, to locate lunar resources, and to characterize the radiation environment (Chin et al., 2007). The suitable instrument for the desired is the Lunar Reconnaissance Orbiter Camera (LROC). The LROC is a combination of two narrow-angle cameras (NAC's) and a wide-angle camera (WAC). NAC's may capture images at ground sample resolution (GSD) of 0.5 m over a 5 km swath, while the images from WAC may reach, a GSD of 100 m over a 60 km swath. As a result, the NAC's images have been used to produce regional high resolution DTMs, while WAC stereo-images to obtain a near-global digital terrain model (DTM) at resolution 100 m x 100 m was produced (Global Lunar DTM at 100 m - GLD100). This DTM covers 98.2% of the entire lunar surface (Scholten et al., 2012), with average accuracy of elevation better than ±20 m. The already mentioned products were also used for the study of landslide features on the lunar surface, through the QuickMap™ web interface (http://target.lroc.asu.edu/q3/) and from the LROC's data dissemination web-portal (http://wms.lroc.asu.edu/lroc/rdr_product_select)

2.2. Chang'E – CNSA

Chang'E is a series of robotic missions by the CNSA with the objective of lunar surface topography mapping and geological survey, as well as the analysis of surface material composition of the Moon. In the spirit of the Chinese-Italian collaborative project "Moon Mapping", data recorded by the CCD camera on-board of the orbiter Chang'E 1/2 was used (Scaioni et al., 2016). The camera may provide images with GSD between 1.5 and 7 m. Data from Chang'E missions are available from Multi-purpose Advanced Tool for Instruments for the Solar System Exploration (MATISSE) platform developed by the Italian Space Agency ASI (http://tools.asdc.asi.it/matisse.jsp). MATISSE allows to operate with geographic/geometric queries for both public and proprietary data (Zinzi et al., 2016).

3. Chebyshev polynomials for large landslides recognition

3.1. Introduction

In general, most of the landslides in impact craters, and in particular slumps, are occurring shortly after the formation of the crater's cavity. Mostly, the predisposing factors are related with soil instability, whilst the triggering factor might be moonquakes or new impacts from meteorites in the nearby area. Pommerol et al., (2012) proposed a method for detecting lunar landslides in impact craters, which is based on the extraction of some crater measurable features (diameter and depth at different locations, circularity, slope, etc.) and qualitative characteristics (central peaks, surface texture, asymmetries, etc.). This method relies on the assumption of a theoretical model that should be applied to compare groups of similar craters and they cannot provide a detailed description of the crater's shape to be analysed for the detection of the surface degradation processes (Mahanti et al., 2015).

In Mahanti et al. (2014) the Chebyshev polynomials are used (Mason & Handscomb, 2010) for approximating craters' cross-sectional profiles. The proposed method can be assumed as data-driven, due to the lack of a priori model to be assumed. Chebyshev polynomials, in fact are a series of orthogonal polynomials, where each of them has a unique and uncorrelated shape with respect to any other members of the series. Further, in Mahanti (et al., 2015) the method was proposed to be suitable for landslide recognition. Further, in Yordanov et al. (2016) and Scaioni et al. (2018) the use of Chebyshev polynomials was proven to be effective with the task of recognition slumps in craters' cavities.

3.2. Mathematical background

Since an in-depth description of the Chebyshev polynomials has already been provided in the recent literature (see Mahanti et al., 2014; Yordanov et al., 2016; Scaioni et al., 2018), only a general overview is presented in the following.

Due to the simplicity of the Chebyshev coefficients, Mahanti et al. (2014) suggests the use of Type I Chebyshev polynomials. The formulation of polynomials' basis functions is based on a recursive series, where the domain is defined between -1 and +1:

$$T_{n+1}(x) = 2xT_n(x) - T_{n-1}(x); \qquad |x| \leq 1 \tag{1}$$

where Tn (x) is the polynomial piece of order n. The pieces of order 0 and 1 are $T_0(x) = 1$ and $T_1(x) = x$, respectively. In order to approximate a function f(x), a linear combination p(x) of the basis functions is adopted:

$$f(x) \cong p_M(x) + o(x_M) = \sum_{n=0}^{M} C_n\, T_n(x) + o(x_M) \tag{2}$$

where M is the degree of the Chebyshev polynomial and Cn are the coefficients that modulate the amplitude of each basis component. Coefficients Cn are estimated on a Least-squares basis in order to fit with real profile data. The residual approximation error (x_M) is equal to the sum of the missing terms after degree M that are not considered in the approximation.

As it results from Eq.'s (1) and (2), in the Chebyshev polynomial series even (symmetric w.r.t. vertical axis) and odd (anti-symmetric) basis functions alternatively appear. Consequently, the size of odd coefficients may express the degree of asymmetry of the approximated crater profile.

4. Application of Chebyshev polynomials

In general, Chebyshev polynomials are efficient for approximating crater cross-sectional profiles, due to their relevant properties that have been already discussed. Therefore, the property used as the main assumption for the purpose of landslide recognition is recalled here.

Due to the orthogonality of the polynomials and the fact that some combinations of different coefficients can represent various morphological features inside a crater (such as the presence of central peak, terraced walls etc.), one can understand the role of single coefficients in the crater's cross-section approximation process. Therefore, it should be noted that the odd Chebyshev polynomials are responsible for the asymmetry in the approximating functions. As well, due to the assumed general bowl-shape profile of a crater, one can consider a single cross-section as symmetrical w.r.t. its centre. Thus, an analysis of the odd polynomials should detect any asymmetry (if present) in the crater cross-sectional profile, which could indicate a presence of a large landslide.

The estimation of the Chebyshev polynomial coefficients is usually carried out on the basis of Least-squares (LS) method (Teunissen, 2009). Taking advantage of the above mentioned property, Mahanti et al. (2014) demonstrated that lunar crater cross-sectional profiles could be approximated by using the first 17 coefficients (M=16) and also that it is possible to describe in a compact standard format the profile for classification and inventory purpose. Furthermore, it has been verified by Mahanti et al. (2015) that four transversal crater cross-sections are sufficient for detecting large landslides in lunar craters. As already mentioned, the main assumption is that a strong asymmetrical component in the polynomials can be considered as a signature of a mass movement process, needing an independent analysis per each cross-section.

In this manner, four crater cross-sectional profiles have been extracted from a DEM and interpolated using bilinear interpolation. As it can be seen in Fig. 3, all these profiles pass through the geographic centre of the crater (according to the lunar ellipsoid) and are aligned along directions: West-East (W-E), South-North (S-N), South West-North East (SW-NE), North West-South East (NW-SE). The length of each section has been extended beyond both rims of up to an extent that is approximately 30% of the rim-to-rim distance. Because of the properties of Chebyshev polynomials, the distance should be normalized in the range of -1 and +1. Since the analysis is focused on the asymmetrical components of the approximation, it should be ensured that there is no influence from side features, such as the general slope of the terrain or even the slope of crater’s floor. Knowing which are the Chebyshev coefficients related to possible interfering features, their effect can be removed by simply posing those coefficients equal to zero. Furthermore, for a case where no slumps are affecting the crater, Scaioni et al. (2018) stated that Chebyshev approximation should mainly consist of non-zero even coefficients, while the odd coefficients should be close to zero. On the contrary, in the case a slump is present, the odd

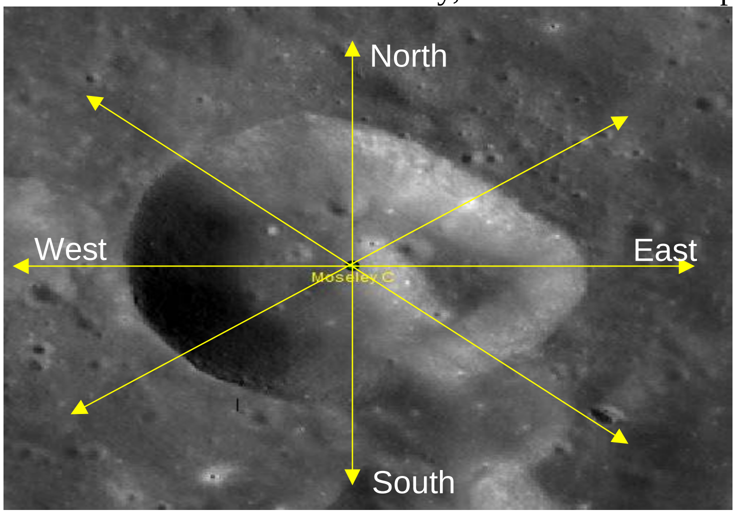

Fig. 3. Profile directions of craters' cross-sections adopted for landslide detection on the basis of Chebyshev polynomials

coefficients should be significantly different from zero. The general workflow of the analysis is shown in Fig. 4.

4.1. Landslide detection

In theory, the statistical significance or even testing the size of the odd Chebyshev coefficients should provide a straightforward mean for detection an asymmetry in a cross-section, which could lead to slump recognition. Actually, after some experiments reported in Yordanov et al. (2016) the results obtained from the approach were not satisfying. This outcome could due to some interferences of noise or local effects Therefore another approach was adopted by Scaioni et. (2018) based on the analysis of the absolute size of Chebyshev coefficients. Firstly, the contribution of odd Chebyshev coefficients to the interpolated elevation profiles is computed per each points. Then, the Root Mean Square Error (RMSE) of the profile is obtained. The final assumption adopted is that in a symmetrical cross-section the RMSE should be small, tending to zero, while it should be increasing in the case of an asymmetric profile.

In this manner, the RMSE values should be compared to a threshold. Two threshold types were proposed and already discussed in Scaioni et al., (2018): Empirical Absolute Threshold (EAT) and Statistical Adaptive Threshold (SAT). The difference between both is that EAT applies the same criterion to all craters' cross-section under analysis, which is also relevant for the craters under consideration. On the contrary, SAT defines a unique threshold per each impact crater. This adaptive approach relies on the statistical analysis of all extracted profiles from the same crater. Both thresholding criteria obtained very satisfactory results, and in particular when using EAT (100 m), a success rate of correct identification of cross-sections with landslides equals 87.7%, was achieved. When using SAT (with a threshold equals to k=0.8 times the RMSE of the crater's profile), an accuracy of 83.1% is obtained. It is worth mentioning the fact that both thresholding criteria exhibited a "trade-off" effect, meaning that a low threshold value can recognize a section as one affected by a landslide (in reality it is true). On the other hand, it can recognize asymmetry in a section where no landslide is present. Moreover, a high threshold value may omit an asymmetry in a cross-section, which will lead to wrong classification as "no landslide".

4.2. Application of the approach using elevation data from different DEMs

In the previous paper, the proposed approach for landslide recognition was applied to 51 craters using elevation data from NASA's WAC GLD100 with spatial resolution of 100 m x 100 m. Here, two additional craters have been analysed, with the difference that elevation data related to them has been obtained from different DEM products, namely a DEM derived from CNSA's Chang'E 1 (500 m x 500 m) data, NASA's WAC GLD100, and regional products derived from NASA's NAC with spatial resolution of 2 m x 2 m.

The two target craters have been chosen in a manner that they share common features as other simple craters (Scaioni et al., 2018), meaning a diameter between 7 km and 29 km, the maximum

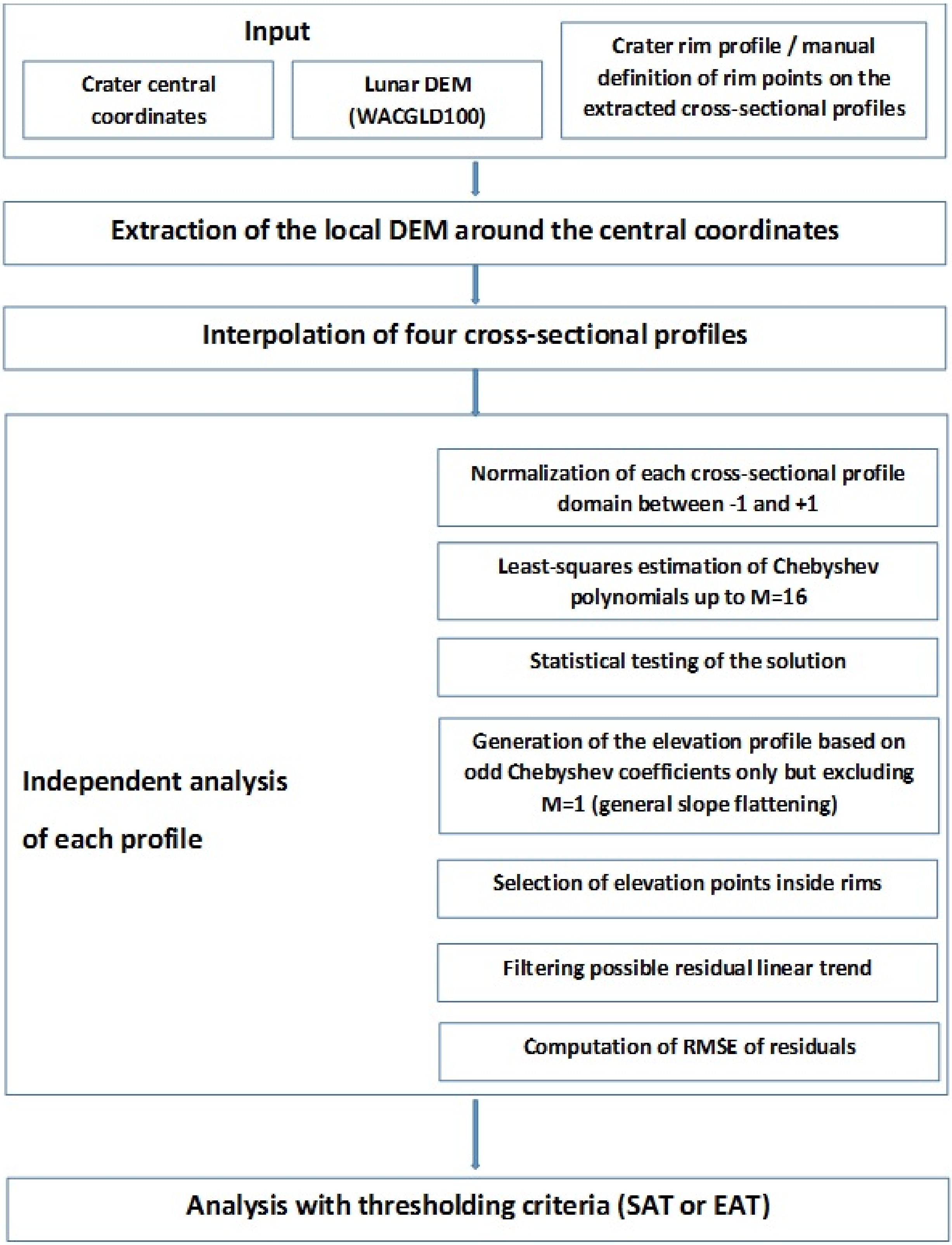

Fig. 4. Workflow of the algorithm adopted to detect the presence of a slump in a cross-sectional profile of a lunar crater

slope inside the crater to be less than 35°. Therefore, for this research Hahn A and Herodotus A craters have been chose. Both are part of families, a group of more impact craters. During the selection process, Hahn A has been classified as a crater with landslides while Herodotus A as one without landslide. They have been preliminary classified using the visual analysis procedure proposed by Brunetti et al. (2015). More in particular, Hahn A has a diameter of 18300 m and depth around 3000 m, while Herodotus A is much smaller in diameter (9970 m), yet with depth of 3000 m. On Figs. 5 and 6, orthophotos of both craters obtained from processing CNSA satellite Chang'E 2 data (with spatial resolution of 7 m x 7 m) are reported.

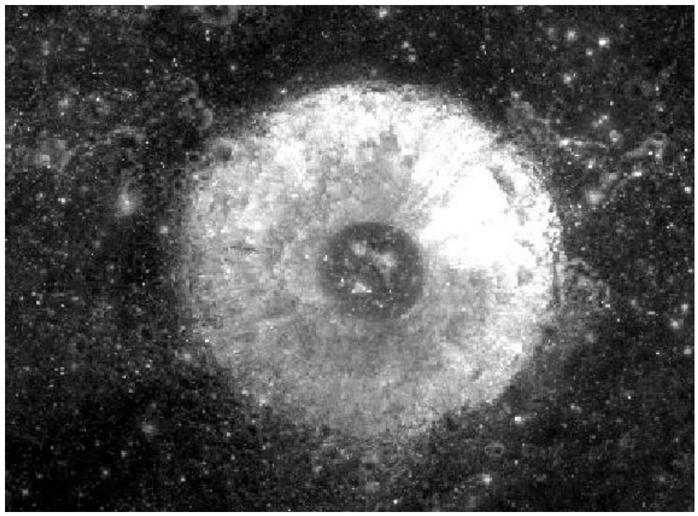

Fig. 5. Crater Herodotus A - orthophoto from Chang'E 2 data, downloaded from MATISSE

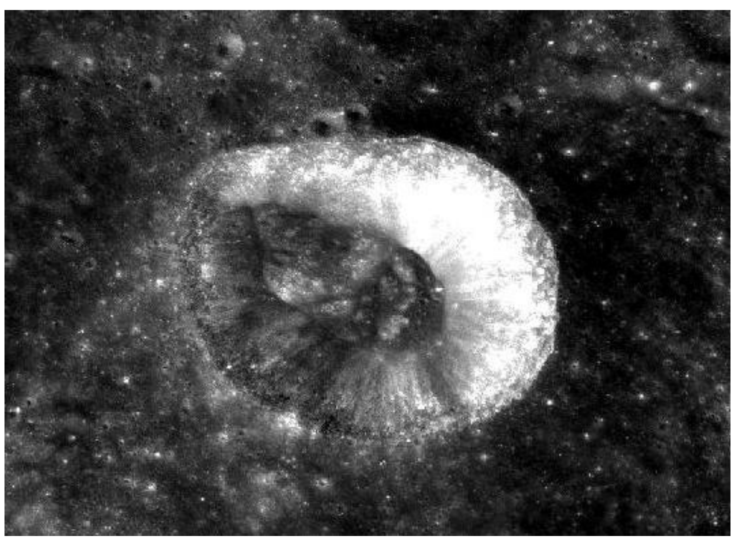

Fig. 6. Crater Hahn A - orthophoto from Chang'E 2 data, downloaded from MATISSE

4.3 Chebyshev approximation

As mentioned before a total number of 17 coefficients (M=16) is enough for approximating a crater's cross-section. On Figs. 7a and 7b is reported the approximated profile of crater Hahn A W-E direction using data from Chang'E 1 and WAC DEMs. After obtaining the Chebyshev approximation it is important to exclude the general terrain slope, the external parts of the crater (meaning the effect of the rims), and the effect of crater's floor. When all possible interfering features are excluded, one should construct the asymmetrical profile, meaning that all even coefficients should be set to zero. The final step is the computation of the residuals between the real cross-section profile and the interpolated crater. The graphical results of the approximation process are displayed in Figs. 7c and 7d.

4.4 Applying the thresholding criteria

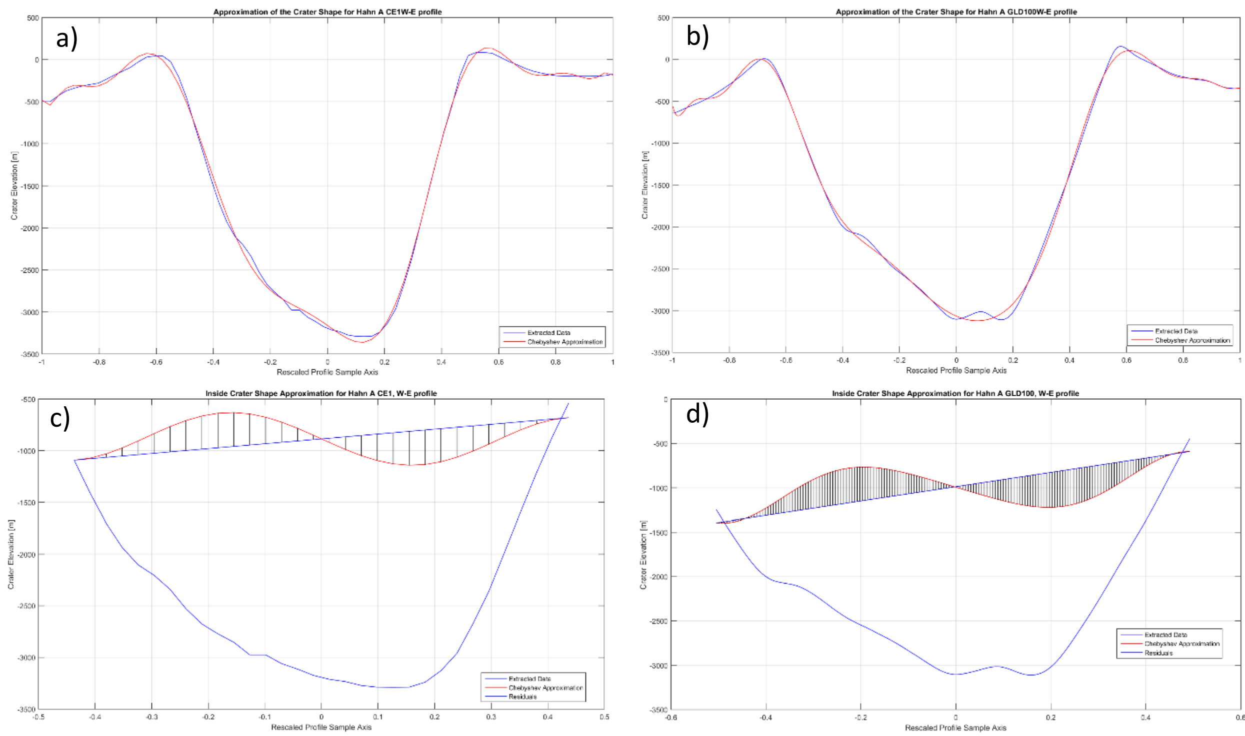

Fig. 7. Application of the algorithm along crater Hahn A's cross-section in West-East direction. Fig.s a) and c) are obtained with data from Chang'E 1's DEM; Figs. b) and d) using data from WAC GLD100. Figs. a) and b) represents a crater's profile approximated with Chebyshev polynomials using 17 coefficients (M=16). Figs. c) and d) show the asymmetrical profiles reconstructed with only odd Chebyshev coefficients; with computed residuals from horizontal line are also displayed, Standard deviation have results c) σ=214.89 m and σ=253.51 m for the case d)

In this work, for both craters Hahn A and Herodotus A, the already mentioned thresholding criteria (EAT and SAT) have been adopted with their best performance values: 100 m for EAT and k*RMS, where k=0.8 for SAT. In Fig. 8 the obtained results are shown.

In the case of crater Hahn A, both of the thresholding methods correctly classified all of the craters' cross-sections. The criteria EAT is distinctively below from the obtained values of profiles W-S and SW-NE, and at the same high enough above N-S and NW-SE. Therefore, W-S and SW-NE are recognised as cross-sections with landslide and the other two (N-S and NW-SE) as ones without any asymmetry. The later fact could be also noted on the elevation profiles in Fig. 9 where the profiles in SW-NE and NW-SE directions are compared.

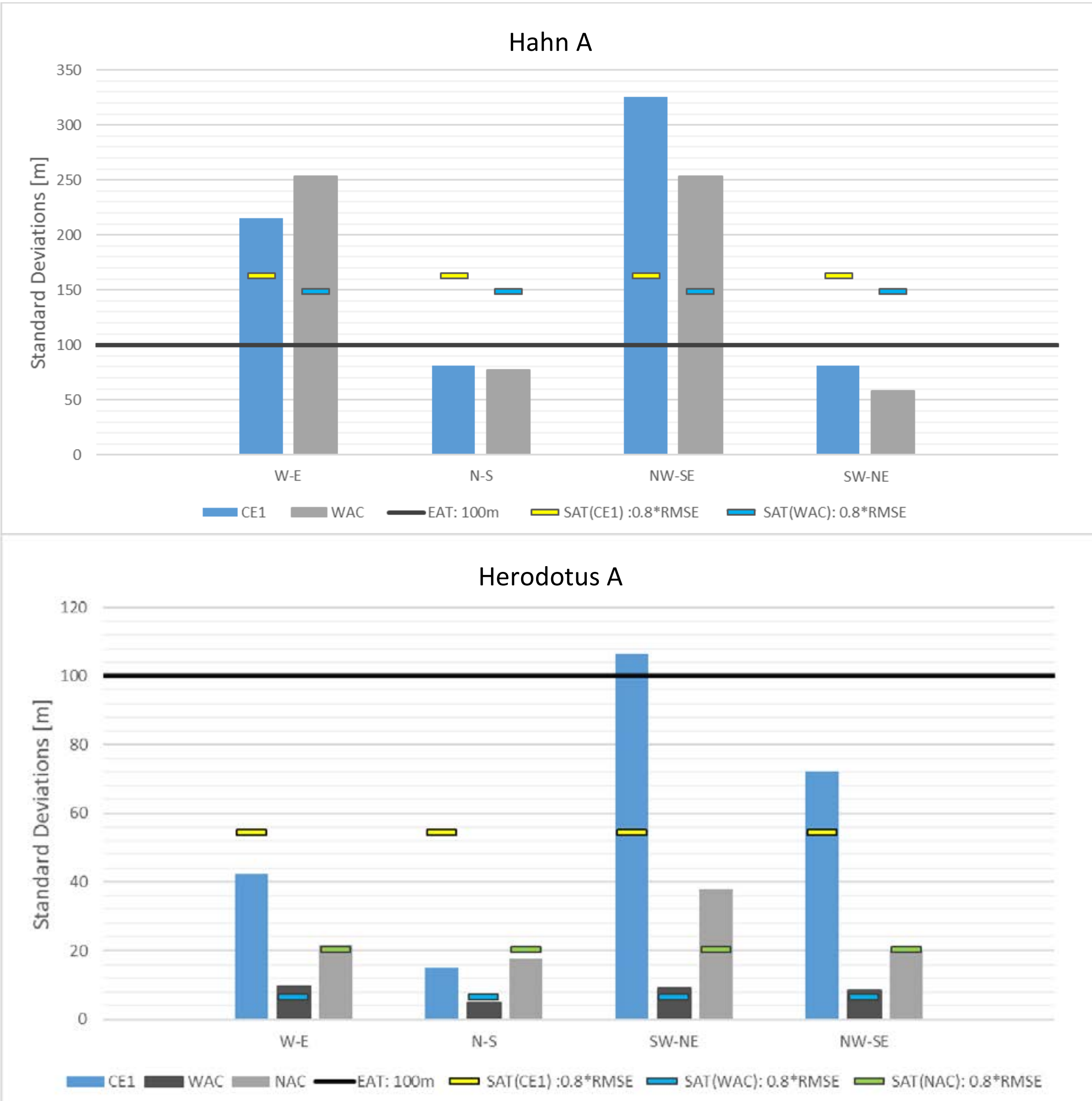

Fig. 8. Application of the thresholding methods (EAT and SAT) to cross-sections of craters Hahn A and Herodotus A, in order to determine the presence of landslides

On the other hand, when looking at the results from the analysis of crater Herodotus A, one can notice the difference in the recognition outcome from EAT and SAT, as previously reported in Scaioni et al. (2018). In the application of EAT with threshold 100 m, just one profile's (SW-NE with Chang'E 1 DEM) standard deviation is higher than the threshold value. In total the success rate of EAT is 91.67%, while the SAT with 0.8*RMS drops to 41.67% overall, correct recognition. Meaning that only five of the cross-sections have been correctly recognised as 'without landslide'.

Looking at the overall standard deviation values from all DEM's, it can be noticed that they are relatively lower than, for example, the ones obtained for Hahn A. This result could be explained

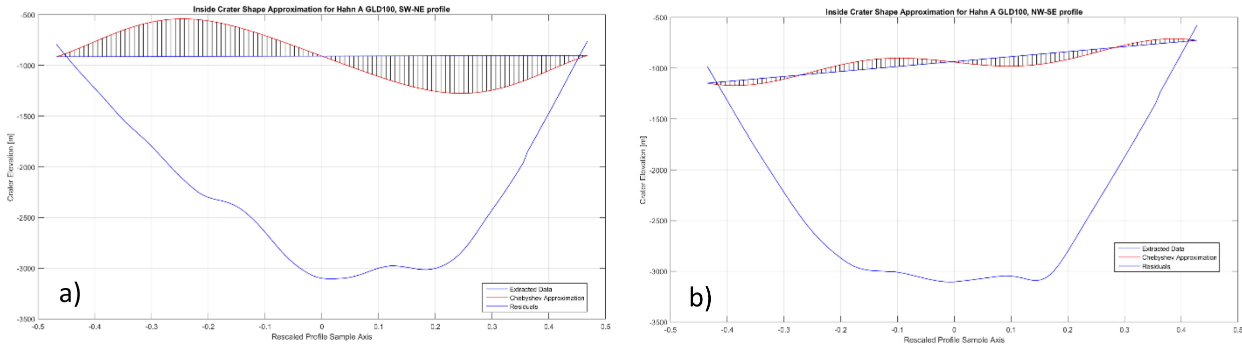

Fig. 9. Approximation plots with only asymmetrical components and computed residuals to the horizontal lines for crater Hahn A: a) SW-NE direction and b) NW-SE direction

by the fact that Herodotus A has been already visually recognised as crater ‘without landslides’, therefore the values of residuals for each profile should tend to zero. The values of residuals from Chang’E 1’s DEM are relatively higher than the other data sets. This could be due to a complex reason combining crater’s diameter (D=9970 m) and the linear sampling distance of 500m. Therefore, one may conclude that the spatial resolution of that particular DEM is too sparse for a crater of this size. Nevertheless, the analysis of WAC GLD100 exhibits values remarkably lower than Chang’E 1’s, also from the regional NAC product. The latter is an odd result even when comparing different products’ accuracies. For Chang’E 1’s DEM it has been estimated to have horizontal accuracy of 192m and vertical accuracy of 120m (Li et al., 2015), while WACGLD100 has horizontal accuracy 18m and 2m vertical accuracy, respectively (Scholten et al., 2012). NAC local DEM’s obtain even higher horizontally and vertical accuracy (Henriksen et al., 2016), which are equal to <10m and 1, respectively.

5. Discussion and conclusion

In this work the approach applied for landslide recognition has the purpose to automate a straightforward procedure to differentiate craters affected by landslides from the ones that were not. It is less time-consuming and more objective than other procedures proposed in the literature. The basic advantages of the method have already been discussed in previous publications (Yordanov et al., 2016; Scaioni et al., 2018), where the obtained results were very satisfying using both thresholding methods (EAT and SAT). Where applying the EAT thresholding criterion 92.8% of the cross-sections, affected from slumps, were correctly recognised. Nevertheless, there are options for improvement. Here, a preliminary check whether analyses using data sets from different DEMs could yield more satisfactory results, have been carried out. It has been observed that high-resolution data sets could produce high deviations from the approximations, of course less that will the low resolution Chang’E 1’s DEM.

REFERENCES:

Bart Comparison of small lunar landslides and Martian gullies,2007, Icarus, 187, 417–421. doi:10.1016/j.icarus.2006.11.004

Brunetti, Xiao, Komatsu, Peruccacci & Guzzetti, Large rockslides in impact craters on the Moon and Mercury, 2015, Icarus, 260, 289–300. doi:10.1016/j.icarus.2015.07.014

Buczkowski, Schmidt, Williams, Mest, Scully, Ermakov & Russell, The geomorphology of Ceres, 2016, Science, 353(6303), aaf4332. doi:10.1126/science.aaf4332

Chin, Lunar Reconnaissance Orbiter overview: The intrument suite and mission, 2007, Space Science Review, Issue 129, pp. 391-419.

Cruden & Varnes, Landslide types and processes, 1996, Transportation Research Board, National Academy of Sciences, 247, 36–75.

De Blasio, Landslides in Valles Marineris (Mars): A possible role of basal lubrication by sub-surface ice, 2011, Planetary Space Science, 59, 1384–1392. doi:10.1016/j.pss.2011.04.015

Henriksen, Manheim, Speyerer, Boyd & Robinson, LROC NAC Digital Terrain Model (DTM) Production, 2016, In Lunar and Planetary Science Conference (Vol. 47, p. 1266).

Krohn, Jaumann, Otto, Hoogenboom, Wagner, Buczkowski & Raymond, Mass movement on Vesta at steep scarps and crater rims, 2014, Icarus, 244(2014), 120–132. doi:10.1016/j.icarus.2014.03.013

Li, Liu, Mu, Ren & Zuo, The Chang'E-1 Topographic Atlas of the Moon, 2015, Springer.

Lindsay, Energy at the lunar surfaces, 1976, In: Kopal, Z., Cameron, A.G.W.(Eds.), Lunar Stratigraphy and Sedimentology. In: Developments in Solar System and Space Science, vol.3.Elsevier,pp.45–55..

Mahanti, Robinson & Thompson, Characterization of lunar crater wall slumping from Chebyshev approximation of lunar crater shapes, 2015. s.l., In Proc. Of "Annual Meeting of the Lunar Exploration Analysis Group (LEAG)" 20-22 Oct. 2015, Columbia, Maryland, U.S., paper No.2081.

Mahanti, Robinson, Humm& Stopar, A standardized approach for quantitative characterization of impact crater topography, 2014, Icarus, Volume 241, pp. 114-129.

Mason& Handscomb, Chebyshev Polynomials, 2010, s.l.:CRC Press.

Massironi, Marchi, Pajola, Snodgrass, Thomas, Tubiana & Koschny, Geological map and stratigraphy of asteroid 21 Lutetia, 2012, Planetary and Space Science, 66, 125–136. doi:10.1016/j.pss.2011.12.024

Mazzanti, De Blasio, Di Bastiano & Bozzano, Inferring the high velocity of landslides in Valles Marineris on Mars from morphological analysis, 2016, Earth, Planets and Space, 68(1). doi:10.1186/s40623-015-0369-x

Melosh, Impact cratering: A geologic process, 1989, New York: Oxford University Press.

Melosh, Planetary surface processes, 2011, New York: Cambridge University.

Pike, Formation of complex impact structures, 1980, Icarus, Issue 43, pp. 1-19.

Pike, Some preliminary interpretations of lunar mass-wasting processes from Apollo 10 photography. Analysis of Apollo 10 photography and visual observations, 1971, Vols. NASA-SP-232, pp. 14–20). Washington, D. C: NASA Spec. Publ.

Pommerol, Chakraborty & Thomas, Comparative study of the surface roughness on the Moon, Mars, Mercury, 2012, Planetary Space Science, 73(1), pp. 287-293.

Quantin, Allemand & Delacourt, Morphology and geometry of valles marineris landslides. Planetary Space Science, 2004, 52(11), 1011–1022. doi:10.1016/j.pss.2004.07.016

Ritter, Kochel & Miller, Process Geomorphology, 2006, Waveland Press, LongGrove, Issue 4th edition, pp. 79-133.

Scaioni, Yordanov, Brunetti, Melis, Zinzi, Kang & Giommi, Recognition of landslides in lunar impact craters, 2018, European Journal of Remote Sensing, 51:1, 47-61, DOI: 10.1080/22797254.2017.1401908

Scaioni et al., The 'Moon Mapping' Project To Promote Cooperation Between Students Of Italy And China, 2016, s.l., Int. Arch. Photogramm. Remote Sens. Spatial Inf. Sci., XLI-B6, 71-78, doi:10.5194/isprs-archives-XLI-B6-71-2016.

Scholten et al., GLD100: The near-global lunar 100m raster DTM from LROC WAC stereo image camera, 2012, Journal of Geophysical Research, Volume 117, E00H17.

Teunissen, Adjusment theory. An introduction, 2009, VSSD Delft, The Netherlands: Series on Mathematical Geodesy and Positioning.

Waltham, Pickering & Bray, Particulate gravity currents on Venus, 2008, Journal of Geophysical Research, Planets, 113, E2. doi:10.1029/2007JE002913

Williams, O'Brien, Schenk, Denevi, Carsenty, Marchi & Davison, Lobate and flow-like features on asteroid Vesta, 2013, Planetary Space Science. doi:10.1016/j.pss.2013.06.017

Xiao, Zeng, Ding& Molaro, Mass wasting features on the Moon–How active is the lunar surface?, 2013, Earth and Planetary Science Letters, 376, 1–11.doi:10.1016/j.epsl.2013.06.015

Yordanov, Scaioni, Brunetti, Melis, Zinzi & Giommi, Mapping landslides in lunar impact craters using Chebyshev polynomials and Dem's, 2016, International Archives of the Photogrammetry, Remote Sensing and Spatial Information Sciences, XLI-B6, 17–24. doi:10.5194/isprs-archives-XLI-B6-17-2016

Zinzi, Capria, Palomba, Giommi & Antonelli, MATISSE: A novel tool to access, visualize and analyse data from planetary exploration missions, 2016, Astronomy and Computing, 15, 16–28. doi:10.1016/j.ascom.2016.02.006

MINERAL ABUNDANCES ON THE MOON USING CHANG'E PROBE DATA

David Marzi, Andrea Marinoni, Paolo Gamba

Telecommunications and Remote Sensing Lab., Dept. of Electrical, Computer and Biomedical Engineering, University of Pavia, Pavia, Italy.

ABSTRACT

The data acquired by the Inference Imaging Spectrometer (IIM) sensor on board of the Chinese Chang'E-1 mission can be used to infer important information on the Moon surface composition. In this work, the multi-path and multi-reflection phenomena occurring on its rugged surface recorded at the IIM rather coarse resolution (200m) are described by means of nonlinear spectral analysis based on the p-linear mixture model (pLMM) and the p-harmonic mixture model (pHMM). The analysis by pLMM and pHMM provides details on the materials and elements on the Moon surface, and their abundance distribution and fractional cover can be properly estimated without any a priori information on its chemical composition. Mineral map extractions using pLMM and pHMM have been considered and compared with those obtained by means of the modified partial least squares regression (PLSR) methodology, assessing the reliability and accuracy of the pLMM- and pHMM-based approach.

INTRODUCTION

Recent advancements in remote sensing technology have allowed important improvements in Earth and planetary surface observations [1]. High spectral resolution in the records acquired by probes and sensors has allowed to better understand the mineralogical structure of the considered targets. As the effort required to obtain surface data and samples from extraterrestrial bodies is huge, planetary research and exploration can take particularly advantage of remote hyperspectral sensing [2,3]. As a matter of fact, the surface characterization can be enhanced by an accurate map of the surface composition extracted from remotely data acquired by spectrometers, without the need to reach the surface [3,4].

Among extraterrestrial bodies, the Moon is a very important element for many different reasons, especially in terms of geophysical characteristics. In fact, such as the Earth, Moon is a differentiated planet, and the deposit and evolution of magmatic lithologies, which include mafic minerals (i.e., minerals enriched in iron and magnesium, such as olivine, orthopyroxene and clinopyroxene), form the majority of its crust [5-7]. The knowledge of the specific mineral assemblages and their major element chemistry can be used to estimate the geological mechanisms that formed the materials at the surface and near-surface through various mantle processes and crystallization conditions. Furthermore, the exploration of the surface composition and mineralogy can describe the Moon geologic history, delivering important details on its planetary thermal and chemical evolution [8].

The study of the Moon surface by means of hyperspectral data sets has been typically carried out searching for modal and chemical signatures of peculiar surface rocks. In that sense, deconvolution methods (e.g., modified Gaussian model (MGM) and partial least squares regression (PLSR)) are used to retrieve a reliable estimate of the abundances of each mineral in a given region [7, 9, 10]. The accuracy of these techniques is very high: however, they suffer from a large computational complexity, particularly relevant in case large-scale datasets are considered.

Another option is the use of spectral unmixing techniques, that are significantly less demanding from the computation point of view [1, 11-13]. Spectral unmixing aims at separating the target pixel spectrum into a set of constituent spectral signatures (endmembers) combined by means of a set of fractional abundances. Nonlinear spectral unmixing have been proved to be able to achieve accurate characterization of any surface, since these algorithms are able to effectively describe spectrally and geometrically complex scenarios [1, 11-14].

In this paper, we want to report that higher order nonlinear spectral unmixing methods provide accurate characterization of the mineralogical composition of the Moon surface. Indeed, a reliable distribution of the minerals' abundances can be efficiently obtained by higher order mixture modeling. Specifically, the outcomes of spectral unmixing are used to estimate the minerals in four test areas. A comparison of these values with the outcome of the well established PLSR method is used to validate the experimental results. The outcomes of the proposed investigation show that nonlinear spectral unmixing is able to provide significant information about the Moon surface composition.

METHODS

A precise characterization of the elements in the local instantaneous field-of-view can be retrieved by means of unmixing techniques, since their outcomes can describe the interactions among the basic materials in the area [11-14]. Indeed, spectral unmixing methods are not sensitive on statistical distribution parameters: in fact, the endmembers spectra are typically the only input for the inversion process carried out over the mixture models. Moreover, it is very well known that absorption characteristics vary nonlinearly according to the abundance distribution. Hence, it is no surprise that relevant information on the physical-chemical composition of the materials on the Moon surface can be obtained by nonlinear spectral unmixing methods.

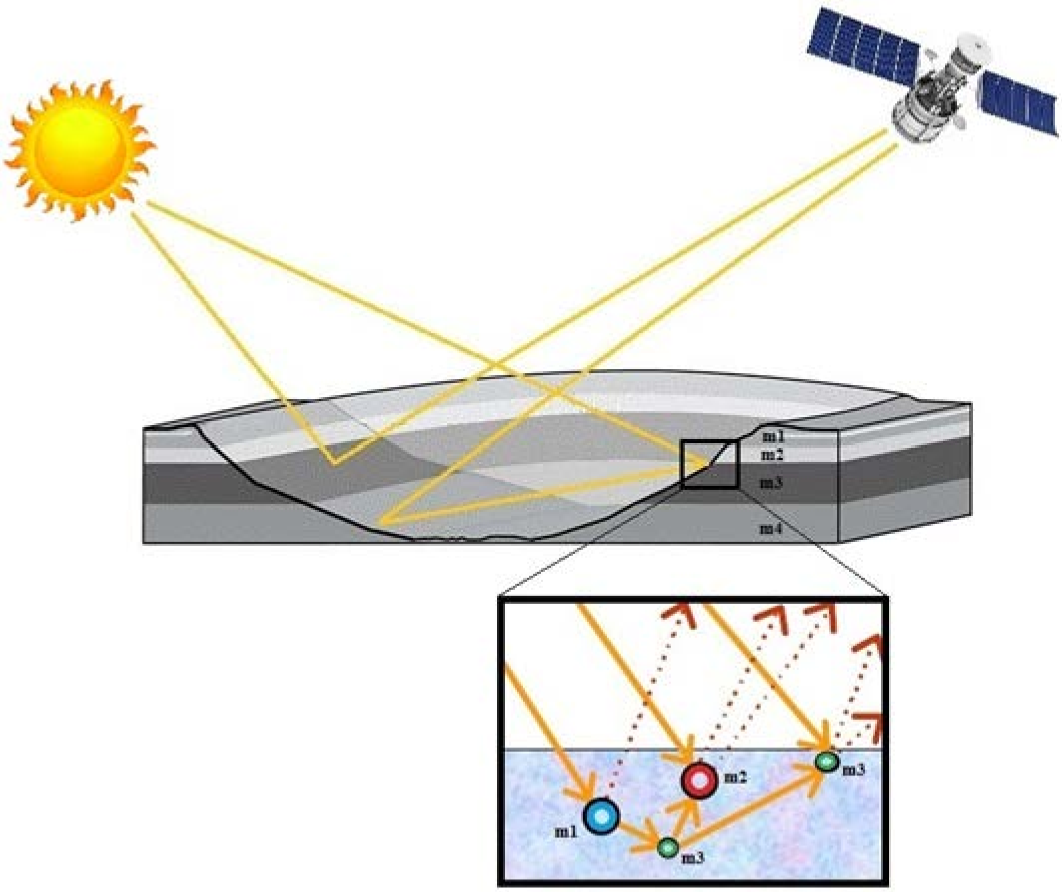

Figure 1. *Simplified representation of the acquisition of mixed spectra on extraterrestrial surfaces*

Furthermore, extraterrestrial surfaces (which are typically characterized by intimate mixtures – see **FIGURE 1**) can be properly described by higher order nonlinear mixture models, able to consider and address several features without a priori information such as grain size and illumination angles [1,3,5,7,12]. The general expression of these models can be written as follows:

$$\underline{y}_l = \sum_{k=1}^{p}\sum_{r=1}^{R} \omega_{rkl}\psi_k(\underline{m}_r) \qquad (1)$$

where $\underline{y}_l = \lfloor y_{l_n} \rfloor_{=1,\dots,N}$, $y_{l_n} \in \Re$ is the N-band spectral signature of the l-th pixel, R is the number of endmembers, and $\underline{m}_r = \lfloor m_{r_n} \rfloor_{=1,\dots,N}$ is the the N-band spectral signature of the r-th endmember, being $r \in \{1,\dots,R\}$. Further, $\psi_k(0)$ represents a k-th order nonlinear function of the given endmember spectrum. Hence, when $\psi_k(\underline{m}_r) = \underline{m}_r^k$ (where $\underline{m}_r^k = \lfloor m_{r_n}^k \rfloor_{=1,\dots,N}$), the aforesaid equation identifies the p-linear mixture model (pLMM) [11]. Moreover, when $\psi_k(\underline{m}_r) = \sin \underline{m}_r{}^k + \cos \underline{m}_r{}^k$ (where $\underline{m}_r^k = \lfloor m_{r_n}^k \rfloor_{=1,\dots,N}$), (1) identifies the p-harmonic mixture model (pHMM) [12]. Finally, it is worth to note that, if p=1, (1) identifies the classic linear mixture model (LMM), whilst p=2 leads to the general expression of the bilinear mixture model [1].

In order to understand the nature of the endmember combination that delivers the given target observation spectral signature, each ω term must be computed. Indeed, a linear system involving the original hyperspectral data and the endmembers' spectra delivered by an endmember extraction algorithm (EEA) can be used to estimate the coefficients driving the nonlinear combination in (1), if the polytope decomposition (POD) of the signatures is employed [11,12]. Further, a more accurate estimation of the endmember abundances can be obtained by properly combining the linear and nonlinear coefficients that have been retrieved. In fact, a global metric based on the polytope representation can be used to this scope [11]. Specifically, the spectral representation of the reconstructed pixel $\underline{\hat{y}}_l$ can be written as a function of the ω_l as extracted according to the overdetermined linear programming optimization, as follows:

$$\underline{\hat{y}}_{l_n} = \sum_{r=1}^{R} \varphi_{rl_n}\psi_1(m_{r_n}) = \sum_{k=1}^{p}\sum_{r=1}^{R} \omega_{krl}\psi_k(m_{r_n}) \qquad (2)$$

where φ_{rl_n} is the overall contribution of the r-th endmember to the reconstruction of the l-th pixel over the n-th band. Hence, it is possible to think to φ_{rl_n} as the compression/expansion factor of the r-th endmember over the n-th direction in the N-dimensional space. In fact, as the relevance of the r-th endmember in contributing to the reconstruction of the l-th pixel increases, the amplitude of $\underline{\varphi}_{rl} = \lfloor \varphi_{rl_n} \rfloor_{n=1,\dots,N}$ gets larger as well. The polytope that is induced by the vertices identified by $\underline{\varphi}_{rl}$ (which by definition is a simplex [3]) can provide information on the contribution of each endmember to the reconstruction of the l-th pixel. In fact, its volume is defined as $V_{\underline{\varphi}_{rl}} = \frac{1}{N!}\det\left[\Delta(\underline{\varphi}_{rl})\right] = \frac{1}{N!}\prod_{n=1}^{N}\varphi_{rl_n}$, where $\Delta(\underline{\varphi}_{rl}) = \lfloor \delta_{ij}(\underline{\varphi}_{rl}) \rfloor_{(i,j)\in\{1,\dots,N\}^2}$ is the diagonal matrix induced by the $\underline{\varphi}_{rl}$ spectral signature [11-14]. Thus, $V_{\underline{\varphi}_{rl}}$ involves all the spectral interactions provided by the aforesaid endmember, so it can provide a valid and reliable characterization of r-th endmember aggregate abundance.

Thus, the r-th endmember abundance $\hat{a}_{rl}$ can be defined as:

$$\hat{a}_{rl} = \frac{V_{\underline{\varphi}_{rl}}}{\sum_{i=1}^{R} V_{\underline{\varphi}_{rl}}} \qquad (3)$$

which fulfills the sum-to-one and the non-negativity constraint [1]. Furthermore, it is a more stable and reliable metric in order to get an evaluation of the presence of each endmember in the scene [11-14]. Specifically, $\hat{a}_{rl}$ represents an aggregate metric to estimate the abundance of the *r*-th endmember in a pixel.

As previously mentioned, signals that are remotely sensed by spectrometers can be affected by geomorphological and geophysical properties of the considered scenarios. Thus, it leads to a cumbersome acquisition of univocal and well defined spectral signatures of minerals over extraterrestrial bodies' surface. Therefore, several spectra identifying minerals with different geophysical features are used as endmembers' library, so that a thorough overview of the actual occurrence of each element in the considered scene can be achieved. Indeed, the overall endmember library $\underline{\underline{M}} = \{\underline{m}_r\}_{r=1,\dots,R}$ can be written as $\underline{\underline{M}} = \bigcup_{s=1}^{S} \underline{\underline{M}}_s$, where $\underline{\underline{M}}_s$ identifies the set of spectral signatures which can be associated with the *s*-th specific mineral compound. Then, it is possible to retrieve a thorough estimate of the actual abundance of the *s*-th mineral over the *l*-th pixel (namely $\hat{\alpha}_{sl}$) as follows:

$$\hat{\alpha}_{sl} = \sum_{j:\underline{m}_j \in \underline{\underline{M}}_s} \frac{\hat{a}_{jl}}{\sum_{r=1}^{R} \hat{a}_{rl}} \qquad (4)$$

These metrics are used to analyze the datasets described in the following Section.

DATASETS AND RESULTS

The datasets that have been considered are provided by the IIM sensor on Chang'E-1 satellite. The IIM is a Sagnac-based spatially modulated Fourier transform imaging spectrometer on-board the first lunar satellite of China, Chang'E-1 [9,10,15]. It mapped the lunar surface with a swath of 25.6 km and spatial resolution of 200 m from a polar orbit of 200 km altitude. Within the wavelength range of IIM, i.e., 480.9–946.8 nm, this sensor has 32 continuous channels with a theoretical spectral resolution of 330 cm^{-1} (variable from the finest case of 7.5 nm at 480 nm to the widest value of 29 nm at 946 nm) according to Sparrow's criterion. The spectral resolution and wavelength position in the laboratory test with the gas laser and semiconductor laser shows that the actual resolution is about 355 cm^{-1}, and maximal shift of 2.48 nm at 831.2 nm for the wavelength position. The signal–to-noise (SNR) of the in-flight data, was evaluated with a simple mean/standard deviation method. Then, only 26 bands are kept to proceed with investigation [9].

Figure 2. *Moon surface portion considered in this work. The blue, yellow, red, and green boxes respectively identify the location of the crater, corrugated, flat, and mixed areas that are shown in Figure 3.*

We focused our attention on a wide region of Moon surface explored by means of IIM records (**FIGURE 2**). The selected area is located around Laplace A and Helicon craters in Sinus Iridum and Mare Imbrium. This portion of Moon surface is especially interesting because it identifies a general flat terrain, which can be eventually used as landing site for future missions. Specifically, we analyzed four zones in this scenario that are characterized by different geomorphic properties, including a crater, a corrugated area, a flat plain, and a “mixed” area (i.e., where mountains and plains are mixed). These scenes are shown in **FIGURE 3**.

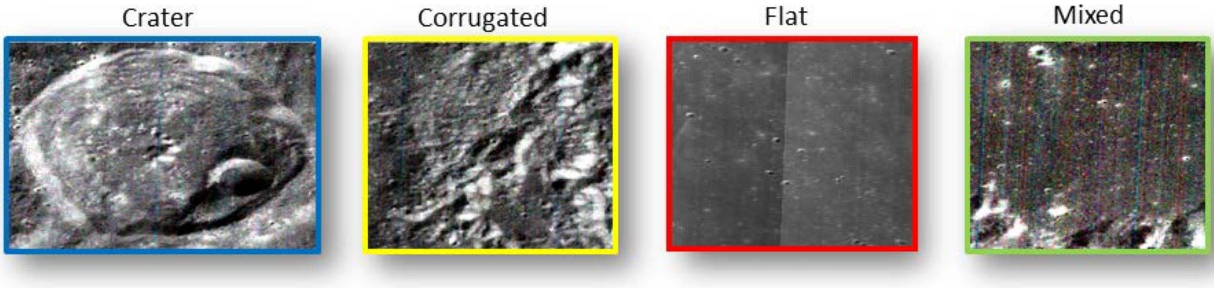

Figure 3. *Four areas with different geomorphic properties that have been analyzed: “crater”, “corrugated”, “flat”, and “mixed”. Their location on the Moon surface is reported respectively by the blue, yellow, red, and green boxes in Figure 2.*

Higher order nonlinear spectral unmixing models based on pLMM and pHMM were considered. Moreover, we provided in input to the spectral unmixing schemes the spectral signatures identifying six major elements on Moon surface, i.e., FeO, TiO2, MgO, Al2O3, CaO and SiO2. In order to evaluate the actual ability of this approach to detect and quantify the abundance distribution of these elements, we compared the retrieved abundance maps with those obtained by considering the PLSR framework in [9]. As an aggregated identifier of the mapping quality, the root mean square error (RMSE) of the abundances estimated by PLSR in [9] and the corresponding quantities calculated according to the outcomes of the spectral unmixing techniques was considered.

FIGURES 4 and 5 show the RMSE distribution obtained over the four areas for each element when pLMM- and pHMM-based unmixing is employed respectively, where p spanned from 1 to 12. Please consider that p=1 identifies the results achieved by classic LMM-based spectral unmixing. Experimental results report that the use of higher order nonlinear mixture models provides higher accuracy in estimating the abundance of all the six major elements than linear or bilinear models. This result is somehow expected, given the capabilities of higher order nonlinear models to track sophisticated mixtures in spectrally and geometrically complex scenes. Specifically, the 8-LMM and 9-HMM models are able to obtain the best abundance estimates, and the blurriness produced by linear and low order nonlinear mixture models is dramatically reduced.

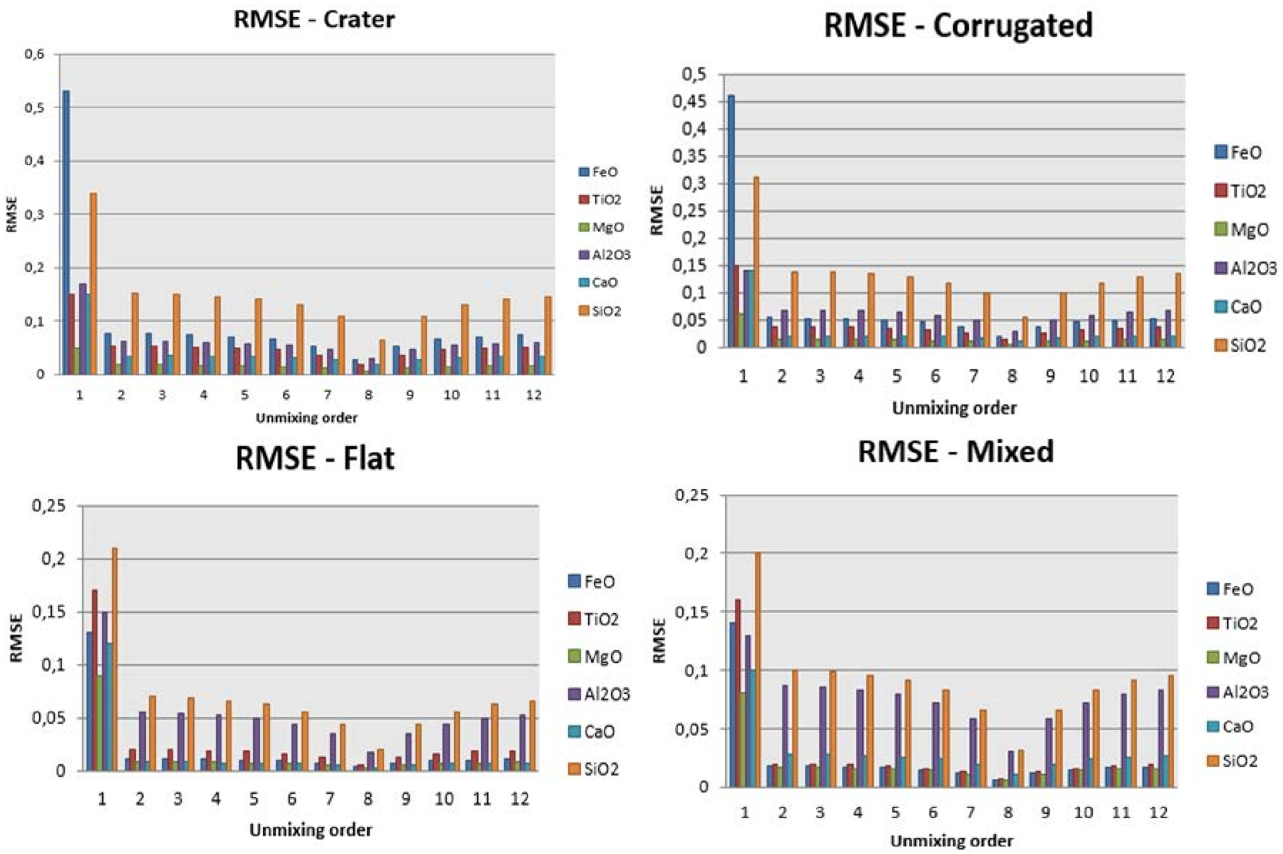

Figure 4. *Root mean square error (RMSE) distribution obtained over the four areas for each element when pLMM-based unmixing is employed, with p spanning from 1 to 12.*

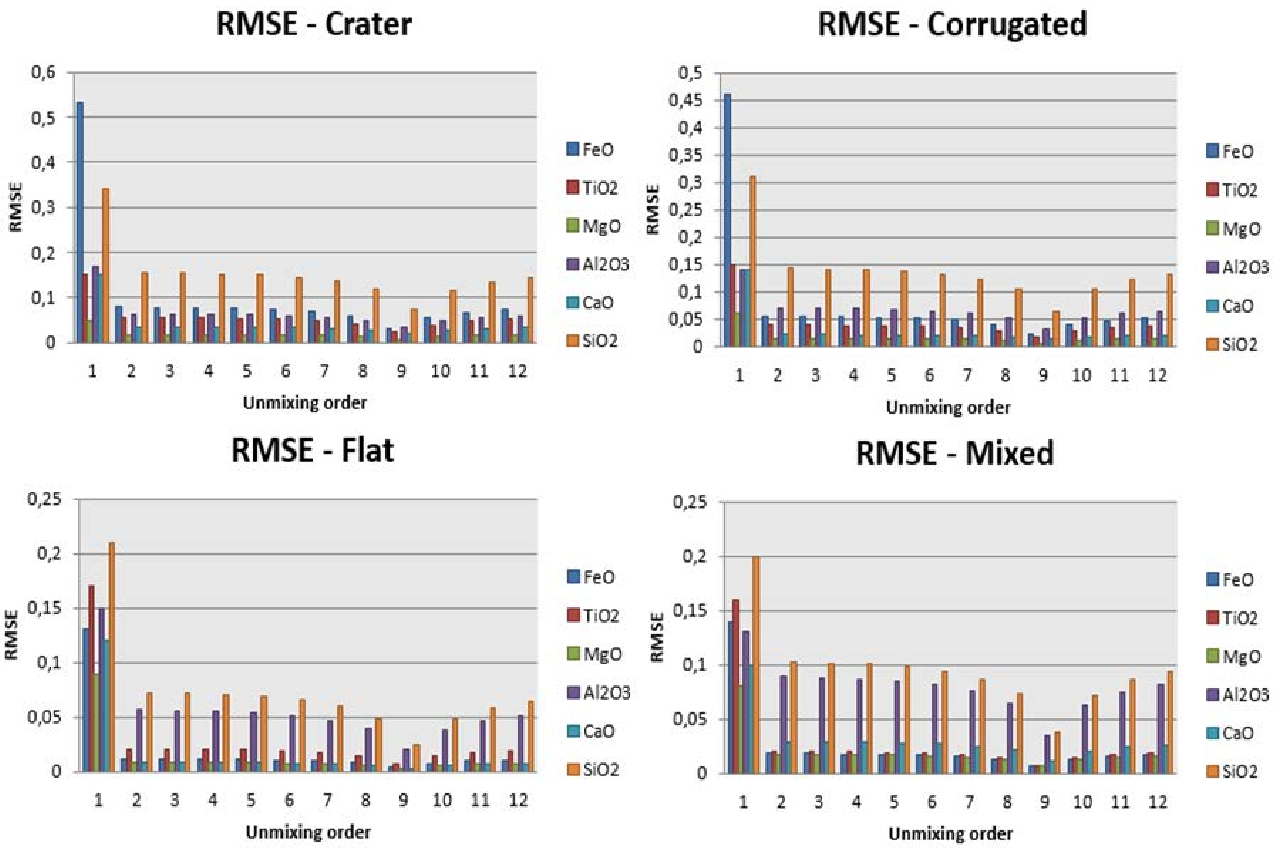

Figure 5. *Root mean square error (RMSE) distribution obtained over the four areas for each element when pHMM-based unmixing is employed, with p spanning from 1 to 12.*

FIGURES 6 and 7 show the results obtained using 8-LMM and 9-HMM, respectively. The approach based on non-linear spectral unmixing is able to accurately track the elements' distribution, since the produced maps do not differ significantly from the PLSR outcomes, as previously discussed for **FIGURES 4 and 5**. Specifically, it is apparent that the error obtained for most of the considered endmembers is less than 10%, which represents a robust result from a statistical point of view. However, the average abundance error for SiO2 is greater than 30%. This effect can be explained taking into account the chemical properties of SiO2 itself. Specifically, SiO2 shows a non-orthorombic crystalline structure, which implies a very fine grain size of the SiO2 minerals on the surface. These properties cause strong nonlinear interaction on the reflectance contribution for the SiO2 minerals at a macroscopic scale. Thus, PLSR estimates might not be very accurate, since that framework definitely relies on the linearity of the minerals' reflectance [9].

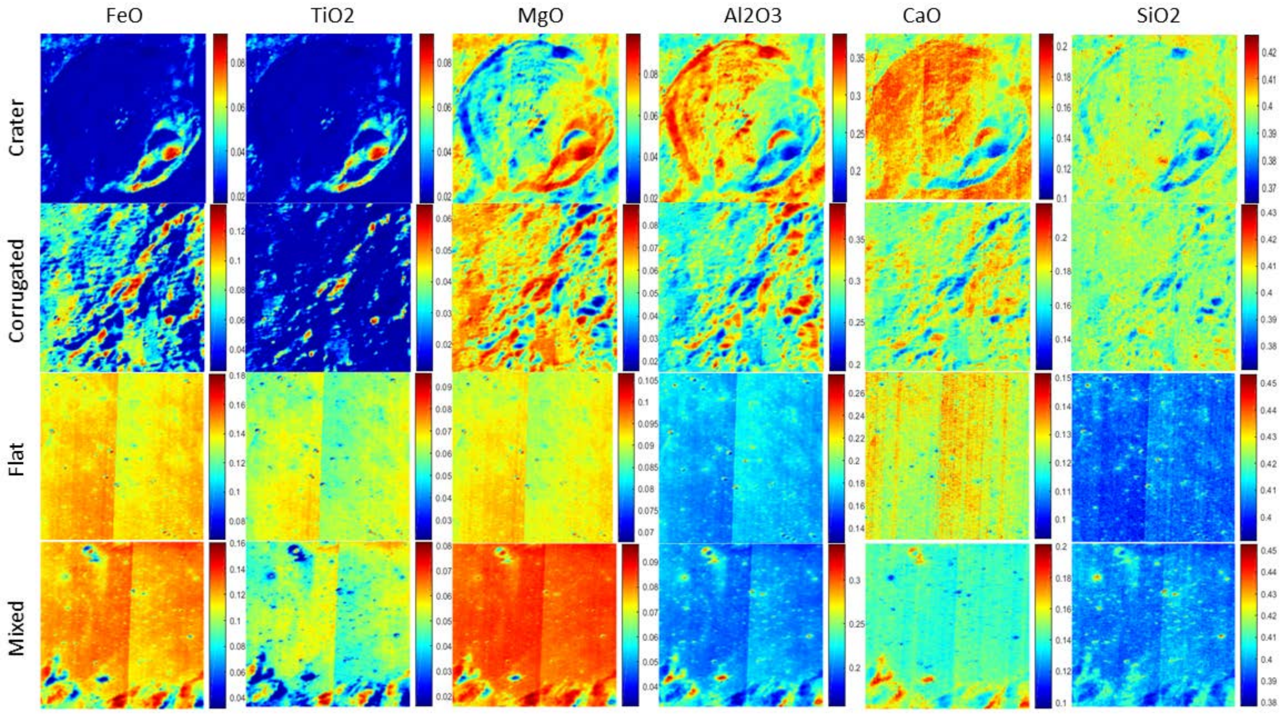

Figure 6. *Abundance distribution obtained over the four areas for each element when 8LMM-based unmixing is employed.*

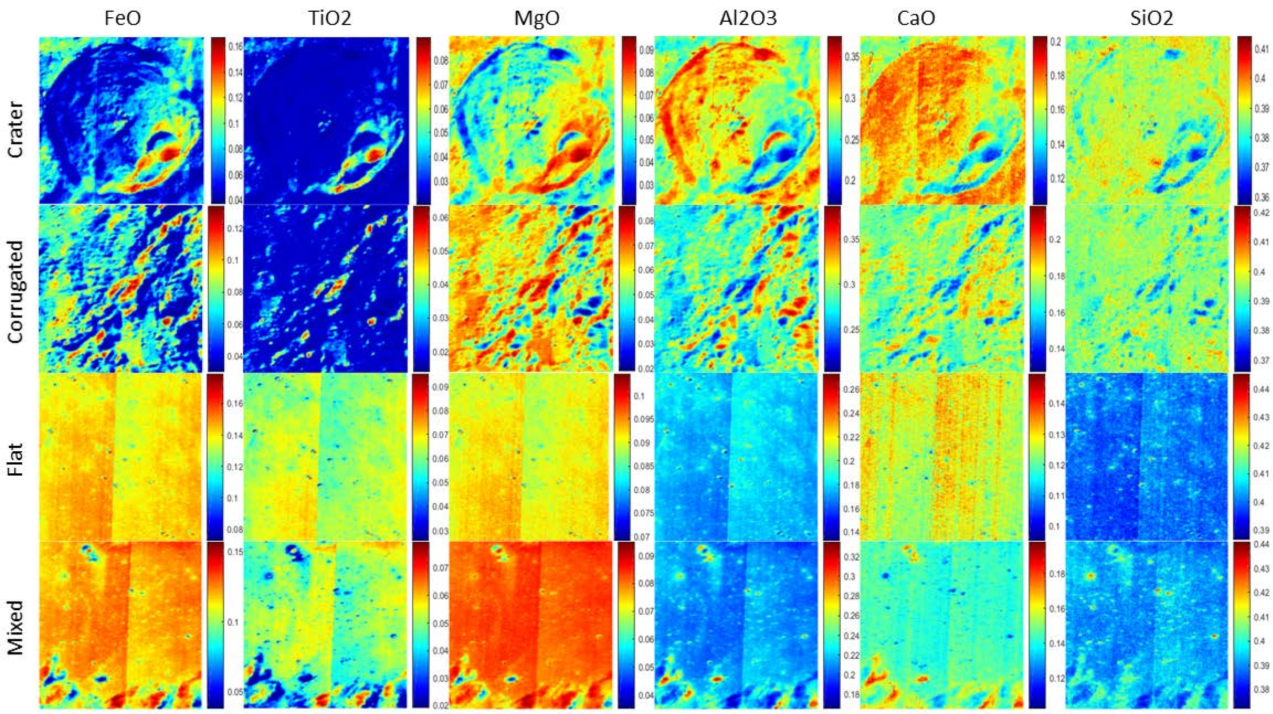

Figure 7. *Abundance distribution obtained over the four areas for each element when 9HMM-based unmixing is employed.*

CONCLUSIONS

In this chapter, a novel approach to extracting mineralogical composition of extraterrestrial planets by means of higher order nonlinear spectral unmixing has been considered and discussed. The proposed scheme is able to provide accurate estimations of mineral abundance distributions on the Moon surface. Furthermore, it provides detailed information on the surface geophysical composition. Experimental results show that the proposed approach is actually able to extract element maps highly correlated to reference mineral distributions. Future works will focus on exploiting the results obtained from the proposed method to achieve higher-resolution high-accuracy quantification of the elements. Moreover, relevant information on the origins on the elements distribution on Moon can be retrieved by fusing the outcomes of the architectures introduced in this chapter and other data on the geomorphic conditions of the surface, such as the digital elevation models (DEMs) of Moon that have been produced by means of the other sensors carried by Chang'E-1 satellite. **FIGURE 8** reports an example of the visualization of the element abundance distribution estimated by using 8LMM-based spectral unmixing on the DEM of the crater region. Hence, the proposed study can play a key role in understanding and quantifying the actual impact and relevance of the physical phenomena occurring on Moon surface.

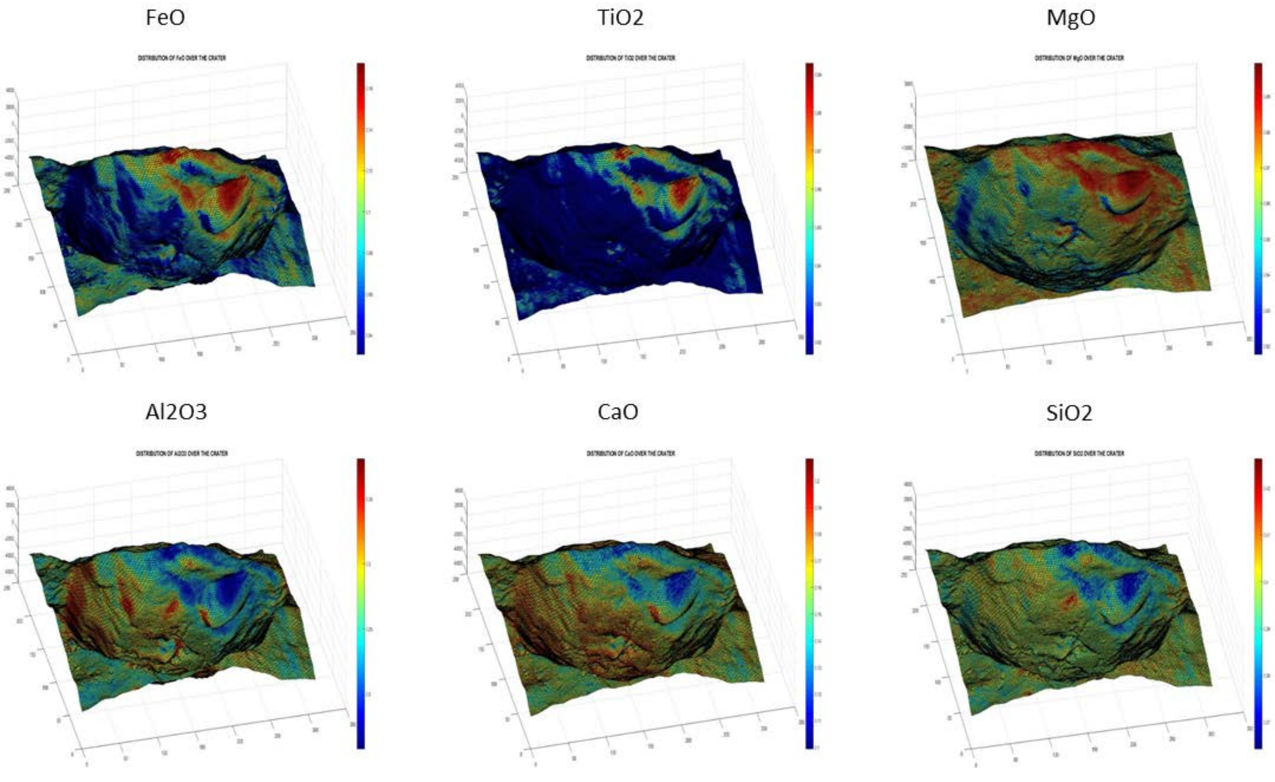

Figure 8. *Visualization of the element abundance distribution obtained over the crater area when 8LMM-based unmixing is employed according to the digital elevation model (DEM) of the region.*

ACKOWLEDGEMENTS

This work has been developed within the MoonMapping project, sponsored by Agenzia Spaziale Italiana (ASI) and Chinese Center Of Space Exploration (COSE).

REFERENCES

[1] R. Heylen, M. Parente and P. Gader, "A review of nonlinear hyperspectral unmixing methods," *IEEE Journal of Selected Topics in Applied Earth Observations and Remote Sensing,* pp. 1844-1868, 2014.

[2] J. B. Adams, "Visible and near IR diffuse reflectance spectra of pyroxenes as applied to remote sensing of solid objects in the solar system," *Journal of Geophysical Research,* vol. 79, no. 32, p. 4829–4836, 1974.

[3] R. L. Klima, C. M. Pieters and M. D. Dyar, "Spectroscopy of synthetic Mg-Fe pyroxenes I: Spin-allowed and spin-forbidden crystal field bands in the visible and near-infrared," *Meteoritics and Planetary Science,* vol. 42, no. 2, pp. 235-253, 2007.

[4] J. M. Sunshine, C. M. Pieters and S. F. Pratt, "Deconvolution of mineral absorption bands: an improved approach," *Journal of Geophysical Research,* vol. 93, p. 6955–6966, 1990.

[5] R. G. Burns, Mineralogical applications of crystal field theory, 2nd edition, Cambridge: Cambridge university Press, 1993.

[6] R. G. Burns, "Crystal field spectra and evidence of cation ordering in olivine minerals," *American Mineralogist,* vol. 55, pp. 1608-1632, 1970.

[7] H. Clénet et al., "A systematic mapping procedure based on the modified gaussian model to characterize magmatic units from olivine/pyroxenes mixtures: Application to the syrtis major volcanic shield on mars," *Journal of Geophysical Research: Planets,* vol. 118, p. 1632–1655, 2013.

[8] G. R. Hunt and J. W. Salisbury, "Visible and near infrared spectra of minerals and rocks, I, Silicate minerals," *Modern Geology,* vol. 1, pp. 283-300, 1970.

[9] Y. Wu, "Major elements and mg] of the moon: Results from chang'e-1 interference imaging spectrometer (iim) data," *Geochimica et Cosmochimica Acta,* vol. 93, pp. 214-234, 2012.

[10] Y. Wu et al., "Global estimates of lunar iron and titanium contents from the chang'e-1 iim data," *J. Geophys. Res.,* vol. 117, no. E2, pp. 1-23, 2012.

[11] A. Marinoni and P. Gamba, "A novel approach for efficient p-linear hyperspectral unmixing," *IEEE Journal of Selected Topics on Signal Processing,* vol. 9, no. 6, pp. 1156-1168, 2015.

[12] A. Marinoni, A. Plaza and P. Gamba, "Harmonic mixture modeling for efficient nonlinear hyperspectral unmixing," *IEEE J. Sel. Top. App. Earth Obs. Rem. Sens.,* 2016.

[13] A. Marinoni, J. Plaza, A. Plaza and P. Gamba, "Nonlinear hyperspectral unmixing using nonlinearity order estimation and polytope decomposition," *IEEE Journal of Selected Topics in Applied Earth Observations and Remote Sensing,* vol. 8, no. 6, p. 2644–2654, 2015.

[14] A. Marinoni and P. Gamba, "Accurate Detection of Anthropogenic Settlements in Hyperspectral Images by Higher Order Nonlinear Unmixing," *IEEE Journal of Selected Topics in Applied Earth Observations and Remote Sensing,* vol. 9, no. 5, pp. 1792 - 1801, 2016.

[15] Z. Ling et al., "Correlated compositional and mineralogical investigations at the chang'e-3 landing site," *Nature Communications,* vol. 6, no. 8880, pp. 1-9, 2015.

[16] M. Parente, J. L. Bishop and J. F. Bell, "Spectral unmixing for mineral identification in pancam images of soils in Gusev crater, Mars," *Icarus,* vol. 203, pp. 421-436, 2009.

First geologic interpretation of Krieger crater

C. Collu[1], S. Podda[1], V. Demurtas[1], F. Perseu[1], M.T. Melis[1]

1. Study area

The crater Krieger is a complex crater located in the Oceanus Procellarum, the most wide mare in the near side of the Moon. The geological and morphological characteristics of this crater were studied and summarized in a geomorphologic map of the area of interest, in scale 1:200 000.

The study area (fig. 1) is located in the Aristarchus region, a complex volcanic district in the eastern margin of the Oceanus Procellarum which includes a great amount of different geomorphological features like basaltic flows, pyroclastic deposits, volcanic constructs, domes and sinuous rilles (Zisk, et al., 1977).

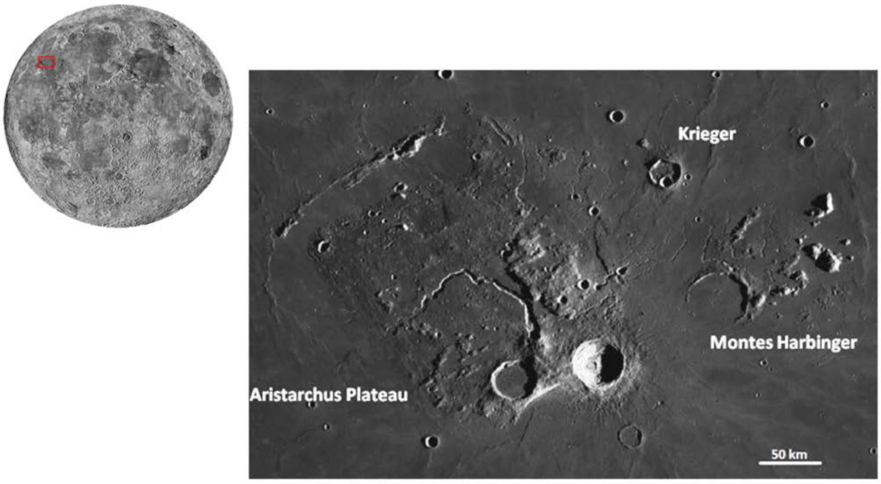

Figure 1. WAC (LRO) image of the Aristarchus region (NASA, QuickMap LROC, 2018). The main features are the Aristarcus Plateau and the Montes Harbinger district. The Krieger crater is located in the NE part of the region.

2. Geological setting

The geology of the Oceanus Procellarum was studied by several authors, mainly on the basis of crater-count techniques and multispectral analysis, identifying numerous basaltic units of different ages. One of these studies (Zhang, Zou, Zheng, Fu, & Zhu, 2014) mapped the mare materials by the spectral analysis of lunar soil maturity variations, TiO_2 and FeO contents (fig. 2). In this work the study area is divided into two different basaltic units, the PL7 (in the southern) and L4 unit (in the northern). Both of them are low in titanium and have the same iron content, but they show a different amount of olivine and/or soil maturity. In fact, the L4

[1] Dipartimento di Scienze chimiche e geologiche, Università di Cagliari, Italy

unit is formed by a olivine-rich basalts and more recent soil materials in comparison with the PL7 unit. It suggest a most recent origin for the L4 unit compared to the other one.

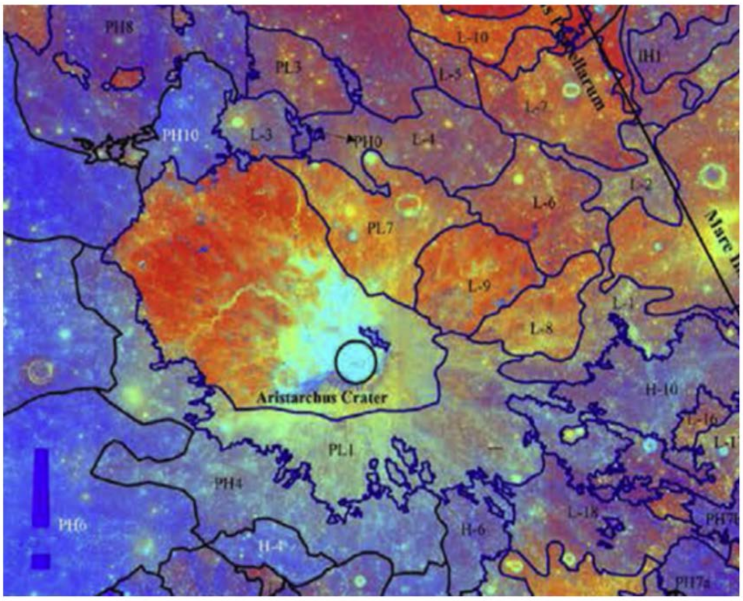

Figure 2. An extract of the Zhang et al.'s Map of the Oceanus Procellarum spectral characterization. Basaltic units' boundaries are drawn with blue and black lines (Zhang, Zou, Zheng, Fu, & Zhu, 2014).

2. Data and Methodology

In this work the geomorphologic study on the area of interest was based on:

• the photo-interpretation of a mosaic made by 20 NAC images (Narrow Angle Camera) from the LRO mission, with a resolution of 1.5 m/pixel;

• the analysis of the SLDEM2015 digital elevation model, created by the combination of Lunar Orbiter Laser Altimeter (LOLA) and SELENE (Kaguya) data with a spatial resolution of 60 m/pixel and a vertical accuracy of 3-4 meters; these data were used to create a topographic map and several topographic profiles;

• the analysis of multispectral data taken by the Moon Mineralogy Mapper (Chandrayaan), that have a spatial resolution of 140 m/pixel and a spectral resolution of 20-40 nm; the spectral characteristics of the lunar surface were pointed out by a RGB composite map of three parameters (1 µm and 2 µm absorption bands and the reflectance value at 1.58 µm) and a SAM classification map, made by collecting end-member spectra identified in the study area.

3 Results

The Krieger crater has a diameter of 24 km and shows on the southern wall a simple crater called Van Biersbroeck, of 11 km in diameter. A sinous rille, Rima Krieger, rises from the western wall. Two smaller craters occur in the eastern corner of the study area, Rocco and Ruth (fig. 3).

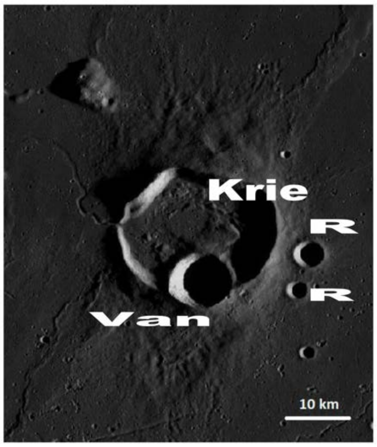

Figure 3. WAC image of the study area (NASA, QuickMap LROC, 2018).

Analyzing the Krieger from the morphologic point of view, it shows a complex structure with asymmetrical walls, in particular between the western and the eastern one (fig. 4).

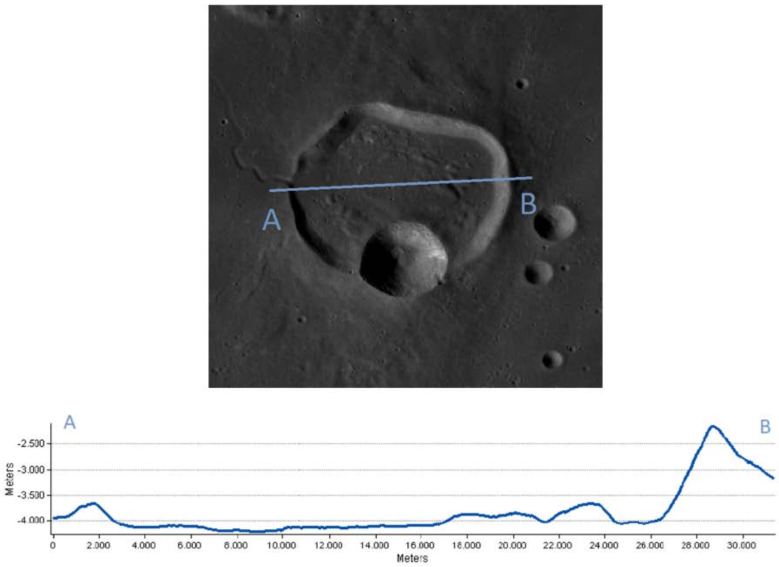

Figure 4. West-East topographic profile of the Krieger crater. The western wall appears lower than 1000 meters amount in comparison with the eastern one (Basemap: WAC image, LROC data; DEM: SLDEM2015, LOLA-SELENE data) .

The maps produced by the spectral characterization of the study area (fig. 5) shows a compositional differentiation in the considered part of lunar surface.

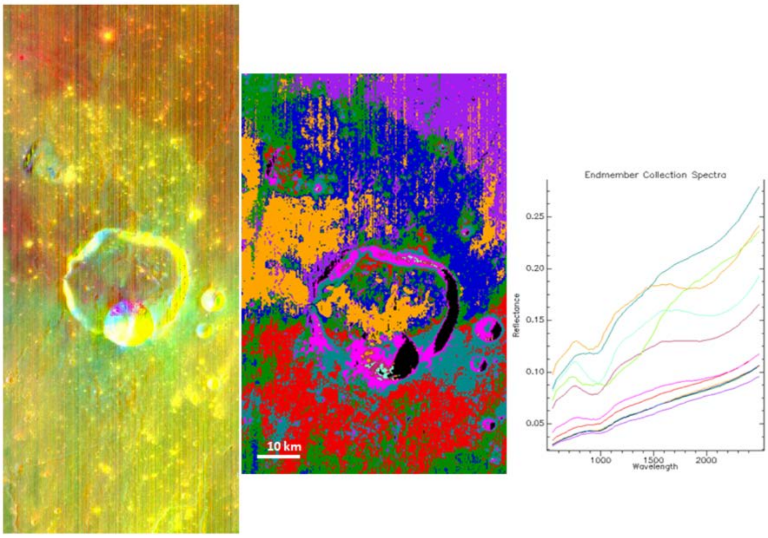

Figure 5. RGB composite map of the three parameters (1 μm and 2 μm absorption bands, red and green channels respectively, and the reflectance value at 1.58 μm in the blue channel) on the left, and a SAM classification map (in the centre), made by collecting end-member spectra of the area (shown on the right).

A clear differentiation can be notice between the northern part of the area and the southern one, which is identfied by a basaltic material with a lower olivine content. It may suggest that the two areas were interested by two different volcanic events. Generally olivine-rich basalts have also a high-titanium content and are younger in respect of the other ones (Staid, et al., 2011). So it's reasonable to think that the southern basalts are older than the northern ones, also according to other works (Boyce & Jonnson, 1978; Whitford-Stark & Head, 1980).

The results of these analysis showed different types of materials and morphological variations that have been interpreted and mapped on the geomorphologic map of the study area.
The identified geomorphologic units were referred to three lunar eras: Pre-Imbrian, Imbrian and Eratosthenian. Most of the study area was composed by Imbrian materials, whereas the simple crater-deposits were attributed to Eratosthenian. An extract of the legend and a sketch map of the geomorphologic map of the Krieger crater are reported in fig. 6.

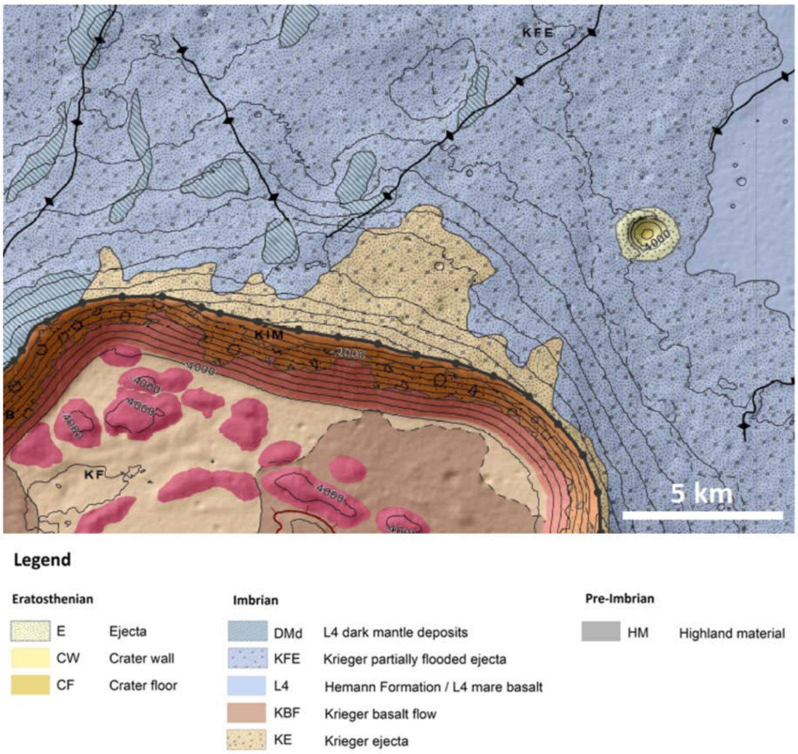

Figure 6. Sketch map and an extract of the legend of the geomorphologic map of Krieger crater.

The pre-Imbrian units are characterized by high values of reflectance, so they had been interpreted as highland-materials, older than Imbrian basaltic volcanism.
Imbrian period was interested by basaltic flows and the impact-cratering process that created the Krieger (Wilhelms, Mccauley, & Trask, 1987). The basaltic flows identified are three:

- the substrate over which Krieger crater formed, consisting of basalt with low olivine and titanium content (PL7 unit in Zhang et al's work);
- olivine-rich basalts, that cover part of the Krieger floor and the western area of the mare; the source of this volcanic event could be the impact-fracture system on the Krieger floor;
- olivine and titanium-rich basalts (L4 unit in Zhang et al's work), which extend in the nothern part of the study area and interest also the surrounding Krieger ejecta.

Other imbrian deposits are associated with the impact-cratering process of the Krieger (ejecta, dikes, etc.).

The basaltic volcanism ceased in the Eratosthenian, therefore the only materials associated with this period are the crater deposits of Van Biesbroeck, Rocco, Ruth and other smaller craters.

The complex morphologic features of the Krieger are probably caused by several types of degradation processes, like the later volcanism occurred in the proximity of the crater and the Eratosthenian impacts, especially Van Biesbroeck's collision.

In conclusion, further studies are necessary to better define the lithologies and the geomorphologic processes, in particular quantitative analysis of muntispectral data, to identify mineralogic mixtures that cause the morphologic features of the reflectance spectra.

Bibliography

Boyce, J.M., Jonnson, D.A., (1978) Ages of flow units in the far eastern maria and implications for basin-filling history. Proc. Lunar Planet. Sci. Conf. 9, 3275–3283.

NASA. (2018). QuickMap LROC. Tratto da QuickMap: https://quickmap.lroc.asu.edu.

Staid, M. I., Pieters, C. M., Besse, S., Boardman, J., Dhingra, D., Green, R., et al. (2011). The mineralogy of late stage lunar volcanism as observed by the Moon Mineralogy Mapper on Chandrayaan-1. Journal of Geophysical Research , 116, 1-15.

Whitford-Stark, J., & Head, J. (1980). Stratigraphy of Oceanus Procellarum basalts: Sources and styles of emplacement. J. Geophys. Res. , 85, 6579-6609.

Wilhelms, D. E., Mccauley, J. F., & Trask, N. J. (1987). The geologic history of the Moon. US Government Printing Office.

Zhang, F., Zou, Y., Zheng, Y., Fu, X., & Zhu, Y. (2014). Lunar mare basalts in the Aristarchus region: Implications for the stratigraphic sequence from Clementine UVVIS data. Icarus , 227, 132-151.

Zisk, S. H., Hodges, C. A., Moore, H. J., Shorthill, R. W., Thompson, T. W., Whitaker, E. A., et al. (1977).

Detection, classification and mapping of lunar rilles

S. Fiorucci[1], M. T. Brunetti[2]

1. Introduction

Lunar rilles are any of the long, narrow depressions on the surface of the Moon that resemble channels. These structures have different characteristics, which are related to their origin. In the following a classification of the lunar rilles in different groups with similar morphometric features and likely the same formation mechanisms is proposed.

2. Study area

The detection, classification and mapping of lunar rilles has been achieved in the Sinus Iridium study area, which is located in the 270°W 360°E – 0°N 60°N Moon quadrant (**Figure 1**). The area measures 10^5 km^2. **Figure 2** shows the mosaic of the Sinus Iridium study area obtained with Chang'e2 raster images.

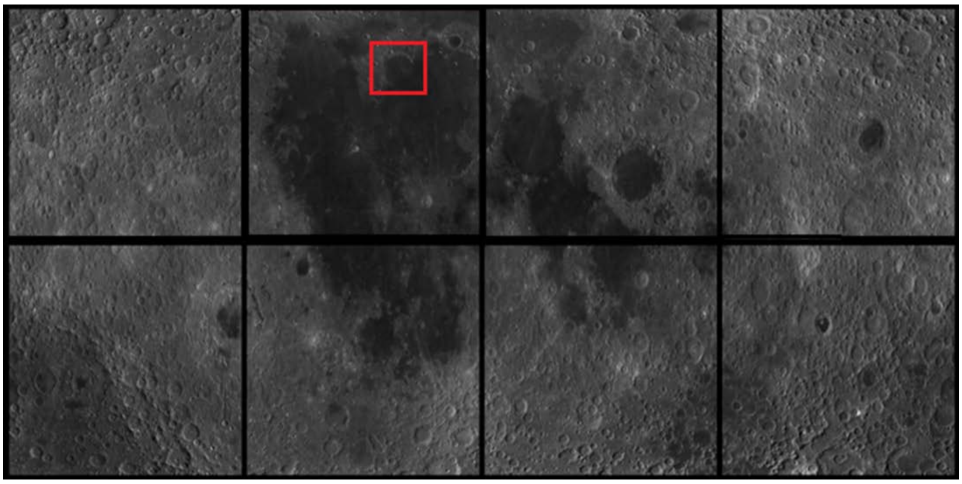

Figure 1. Stereographic view of the Moon's surface (LROC); the red square indicates the area we have focused on (credit: NASA/Goddard Space Flight Center/Arizona State University).

[1] Dipartimento di Fisica e Geologia, Università di Perugia, Italy
[2] Consiglio Nazionale delle Ricerche, Istituto di Ricerca per la Protezione Idrogeologica, Perugia, Italy

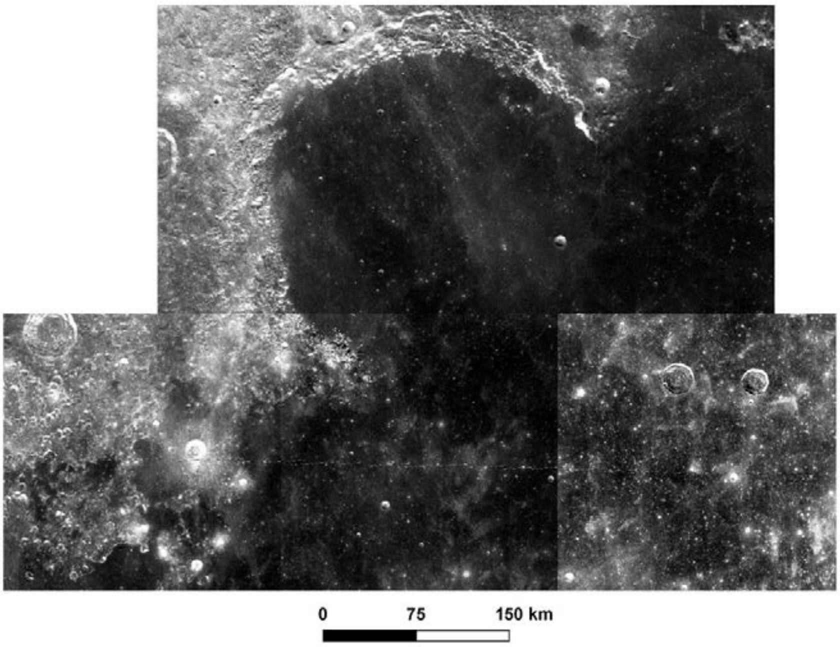

Figure 2. Mosaic of the Sinus Iridium study area (Chang'e2).

3. Methods

A DEM (Digital Elevation Model) from Lunar Orbiter Laser Altimeter (LOLA, Smith et al., 2010) with a resolution of 6 m/pixel (**Figure 3a**), monochrome images taken by the Wide Angle Camera (WAC, Robinson et al., 2010) of the Lunar Reconnaissance Orbiter Camera (LROC, Chin et al., 2007) (http://www.lroc.asu.edu/) with a resolution of 100 m/pixel (**Figure 3b**) and raster images from Chang'e2 with a resolution of 7 m/pixel have been used to identify and map the rilles.

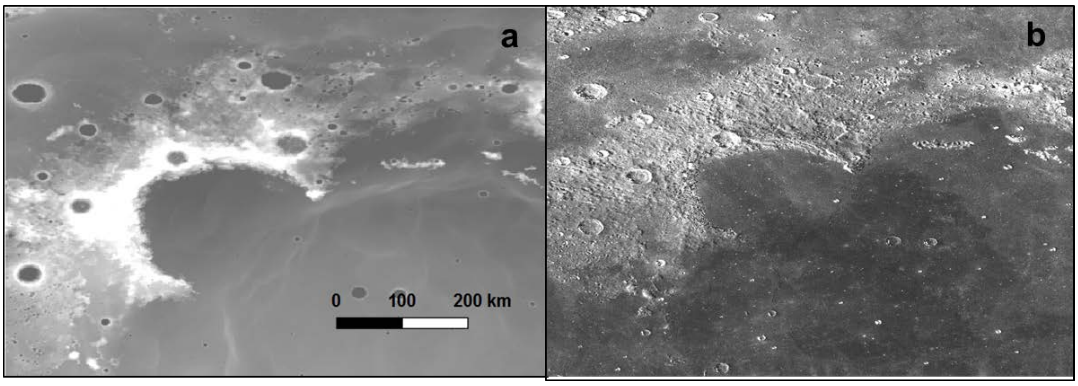

Figure 3. (a) A cut out of the DEM used. (b) LROC raster image of the same area (credit: NASA/Goddard Space Flight Center/Arizona State University).

Lunar rilles include generic sinuous rilles and additional structures that were classified and mapped to highlight the main differences with the sinuous rilles and to provide a comparison to distinguish one from the other. The mapped structures are grouped and classified in:

1. Generic sinuous rilles (SR)
2. Cracks on lava deposits (CL)
3. Surface lava flows (LF)
4. Subsurface lava tubes or catena (crater chains, CC)
5. Tectonic structures (TS)

Generic sinuous rilles (SR)

Generic sinuos rilles (**Figure 4a** and **4b**) exhibit varying degrees of sinuosity with parallel, laterally continuous walls. Generally, SRs avoid topographic obstacles. These SRs can be better defined and associated to a specific origin after a detailed morphometric analysis and a regional interpretation (Hurwitz et al., 2013).

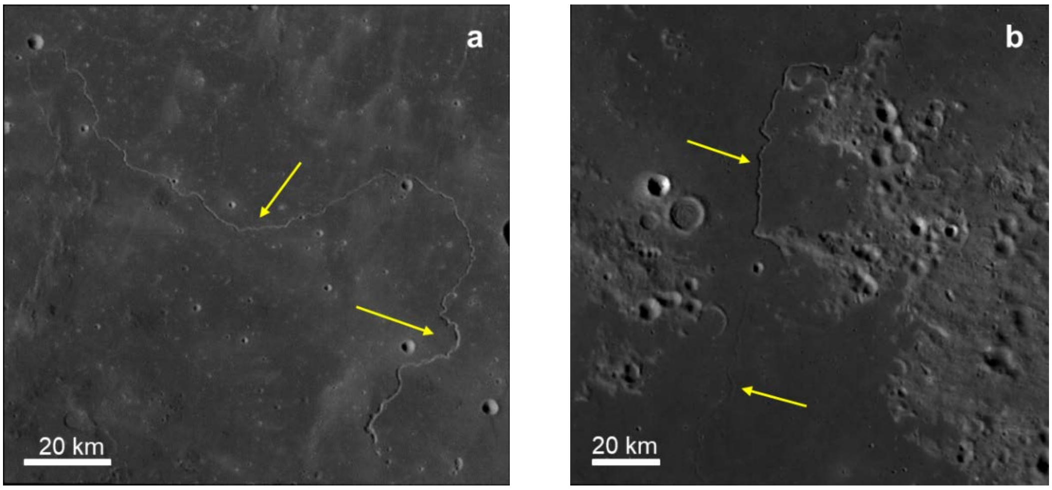

Figure 4. The yellow arrows in (a) and (b) indicate examples of SR (credit: NASA/Goddard Space Flight Center/Arizona State University).

Cracks on lava deposits (CL)

Cracks on lava deposits (**Figure 5a** and **5b**) are branched linear or arcuate patterns with a low degree of sinuosity and a clear angular and sub-angular pattern.

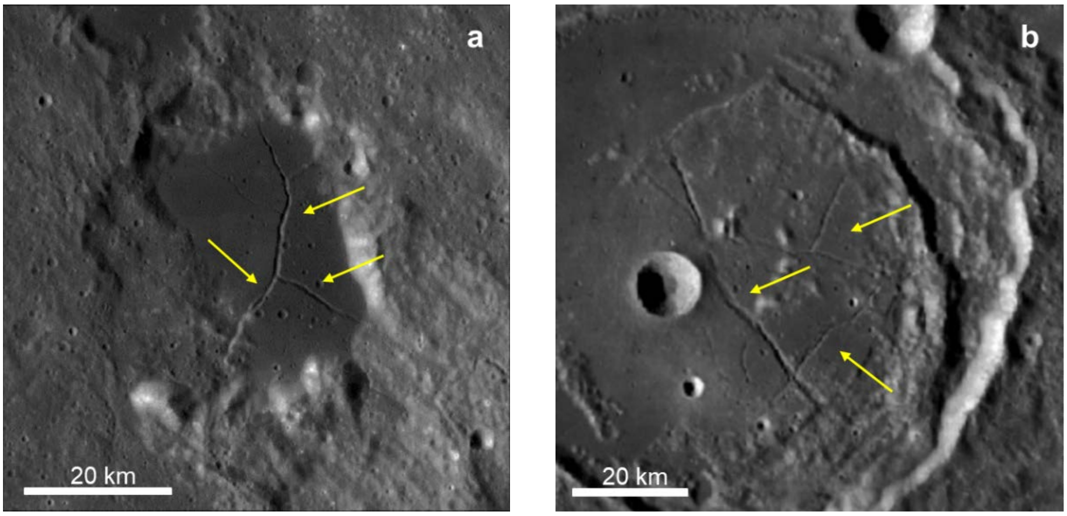

Figure 5. The yellow arrows in (a) and (b) indicate examples of CL (credit: NASA/Goddard Space Flight Center/Arizona State University).

Surface Lava Flow (LF)

Surface Lava Flows (**Figure 6a** and **6b**) are shallow leveed channels exhibiting varying degrees of sinuosity. These features are often associated to potential source vents. The width of the channel decreases with the distance from the source vent.

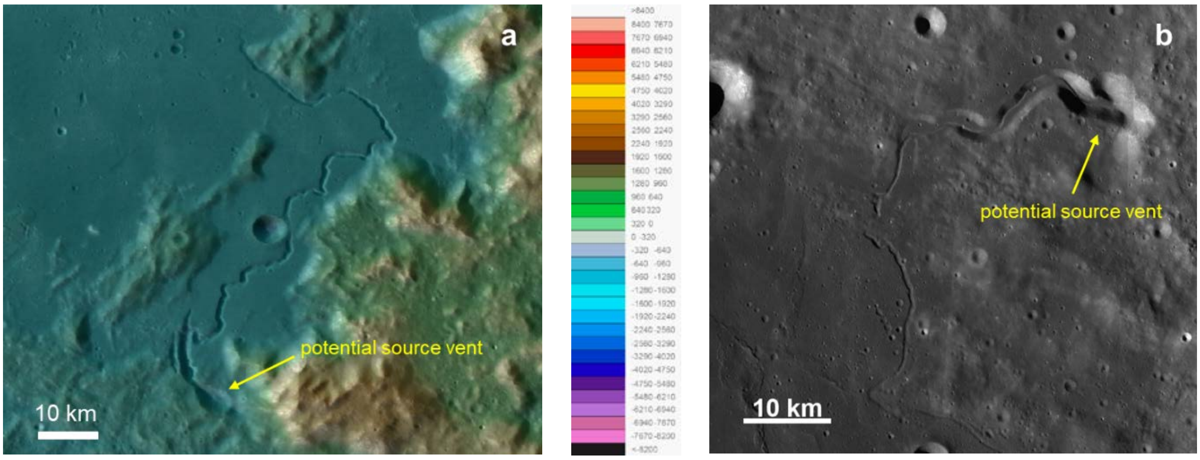

Figure 6. The yellow arrows in (a) and (b) indicate the potential source vents of the two LF (credit: NASA/Goddard Space Flight Center/Arizona State University).

Subsurface lava tubes or catena (crater chains, CC)

Subsurface lava tubes (**Figure 7a** and **7b**) are chains of craters (catena) due to multiple collapses along a subsurface lava tube.

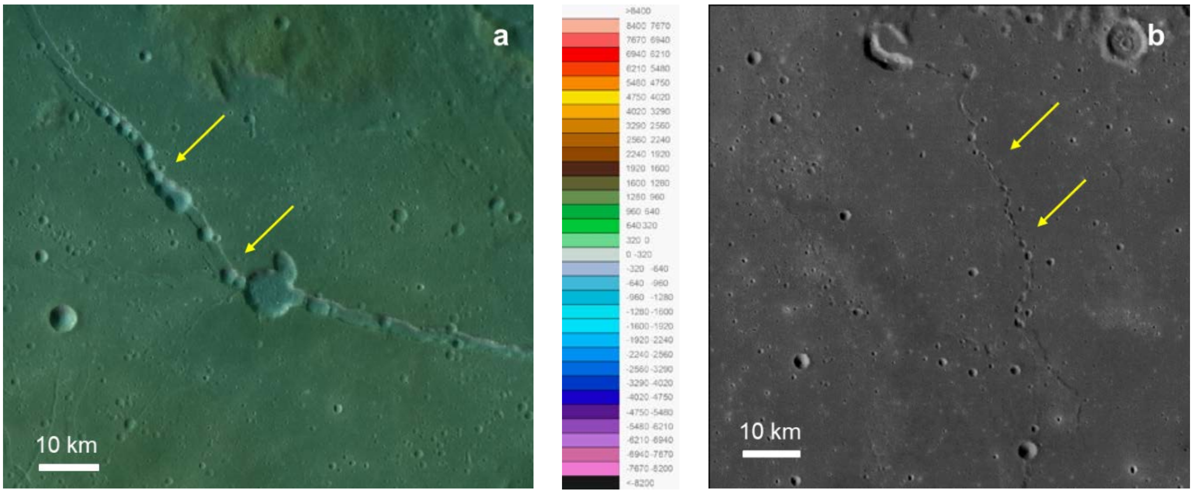

Figure 7. The yellow arrows in (a) and (b) indicate examples of CC (credit: NASA/Goddard Space Flight Center/Arizona State University).

Tectonic structures (TS)

Tectonic structures (**Figure 8a** and **8b**) have straight or gently arcuate parallel walls. Generally, they are not continuous but composed by cut strokes. The depression can be partially covered by the lava erupted and flowed back (drain back process). they have a linear trend. Generally, a main tectonic structure is associated to a family composed by lineaments/discontinuities as steps on the surface (thrust faults). In other cases, they can be graben and they can be straight or arcuate parallel walls bounded by steep, inward-dipping normal faults. Generally, they cut across topographic obstacles.

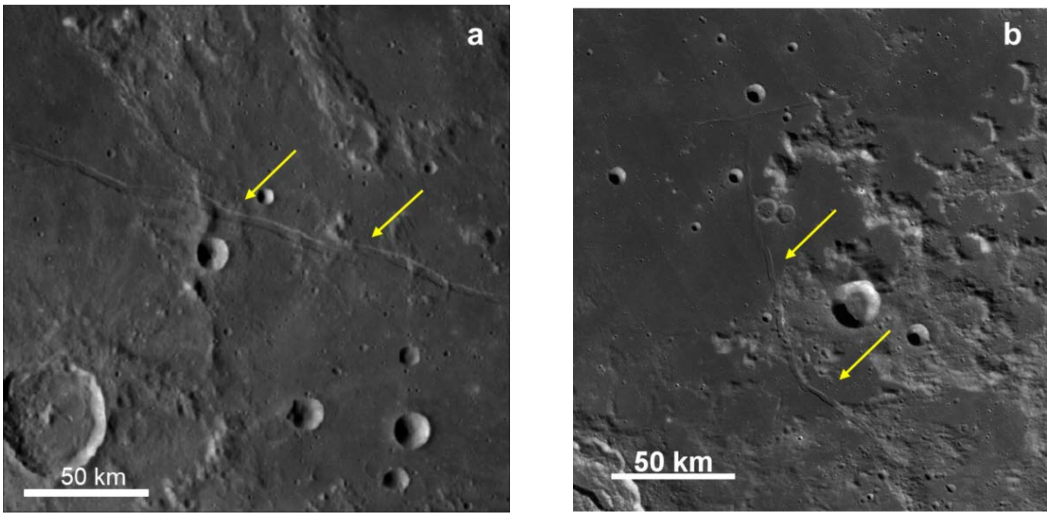

Figure 8. The yellow arrows in (a) and (b) indicate examples of TS (credit: NASA/Goddard Space Flight Center/Arizona State University).

4. Results

Using high-resolution images of Chang 'e2 we 74 polygons and 112 curves have been classified and mapped in the Sinus Iridium area (Figure 9). For the mapped structures, a chart with the most relevant morphometric parameters is available.

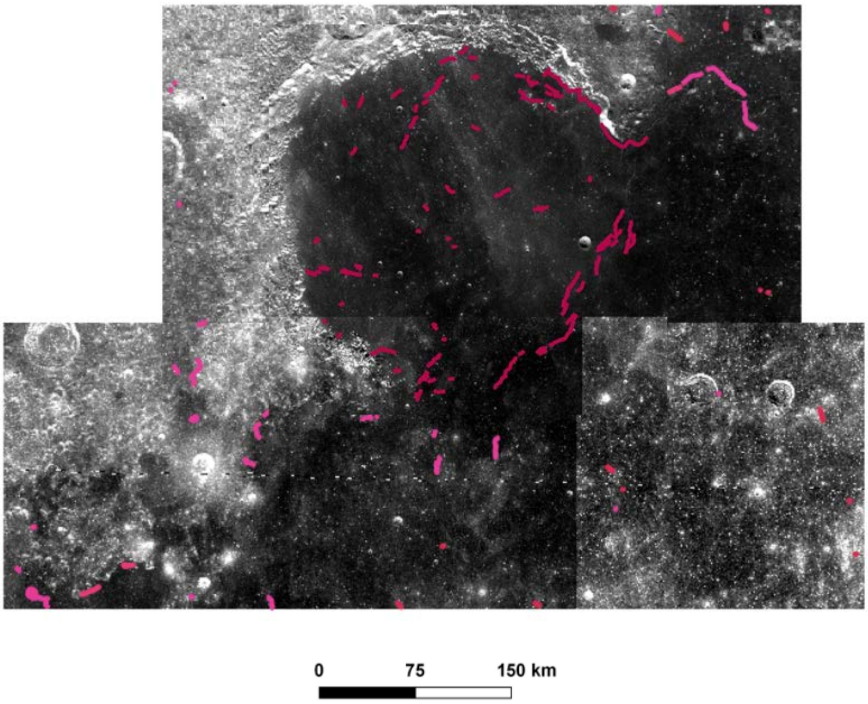

Figure 9: Lunar rilles mapped in the Sinus Iridium study area.

Bibliography

Chin, G., et al. (2007), Lunar Reconnaissance Orbiter overview: The instrument suite and mission, *Space Sci. Rev.*, **129**, 391–419, doi:10.1007/s11214-007-9153-y.

Robinson, M.S. et al., 2010. Lunar Reconnaissance Orbiter Camera (LROC) instrument overview. Space Sci. Rev. **150** (1–4), 81–124. http://dx.doi.org/10.1007/s11214-010-9634-2.

Smith, D. E., et al. (2010), The Lunar Orbiter Laser Altimeter investigation on the Lunar Reconnaissance Orbiter mission, *Space Sci. Rev.*, **150**, 209–241, doi:10.1007/s11214-009-9512-y.

Morphometric analysis of sinuous rilles on the lunar near side

S. Podda[1], C. Collu[1], V. Demurtas[1], F. Perseu[1], M.T. Melis[1]

1. Introduction

Lunar sinuous rilles are enigmatic features that would represent the remnants of shallow lava channels or subsurface lava tubes collapsed.
These channels are characterized by highly varying depths and widths with parallel, laterally continuous walls, that exhibit varying degrees of sinuosity (Figure 1). The exact mode of sinuous rilles formation is still debated, particularly in regards to whether these channels originated by constructive or erosive processes. In this chapter a morphometric analysis of sinuous rilles is proposed because it can facilitate a better understanding of how these features formed (Hurwitz et al. 2013).

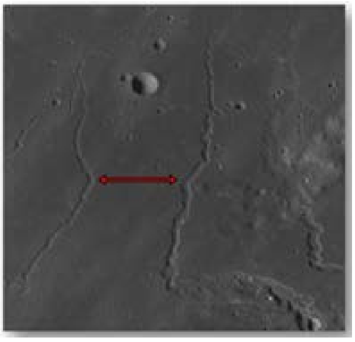

Figure 1. The image shows some examples of lunar sinuous rilles indicated by the red arrow.

2. Study area

The study area is located on the lunar near side in the 0°E 90°E - 0°N 60°N Moon quadrant. It is characterized by numerous maria that represent the main areas of sinuous rilles formation (Figure 2).

[1] Dipartimento di Scienze chimiche e geologiche, Università di Cagliari, Italy.

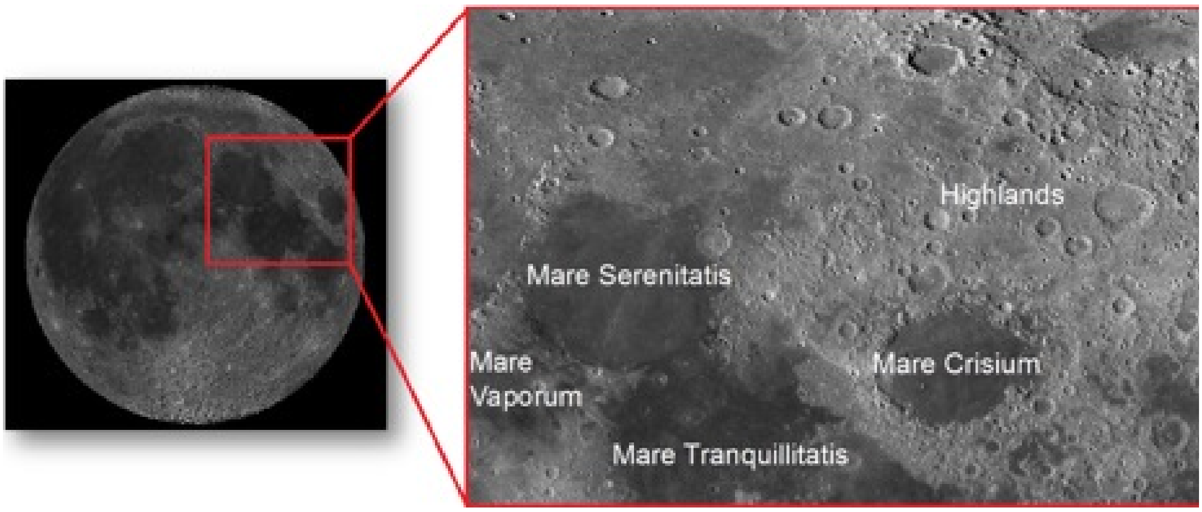

Figure 2. The image on the left shows the orthographic projection of the lunar near side (QuickMap - LROC- ASU), the red square indicates the study area visible on the right (WAC Global Morphologic Map).

2. Methodology and results

Sinuous rilles of varied morphologies have been identified on the area, using the WAC Global Morphologic Map and the SLDEM 2015 (Figure 3). The WAC Global Morphologic Map represents the mosaic of the images taken by the Wide Angle Camera (Lunar Reconnaissance Orbiter Camera) with a resolution of 100 m/pixel (Robinson et al. 2010). The SLDEM2015 is a global lunar DEM deriving from the combination of Lunar Orbiter Laser Altimeter data and Selenological and Engineering Explorer (SELENE or Kaguya, operated by the Japan Aerospace exploration Agency) data. The SLDEM2015 has a resolution of ~ 60 m/pixel and a vertical accuracy of ~ 3 - 4 m (Barker et al. 2015).

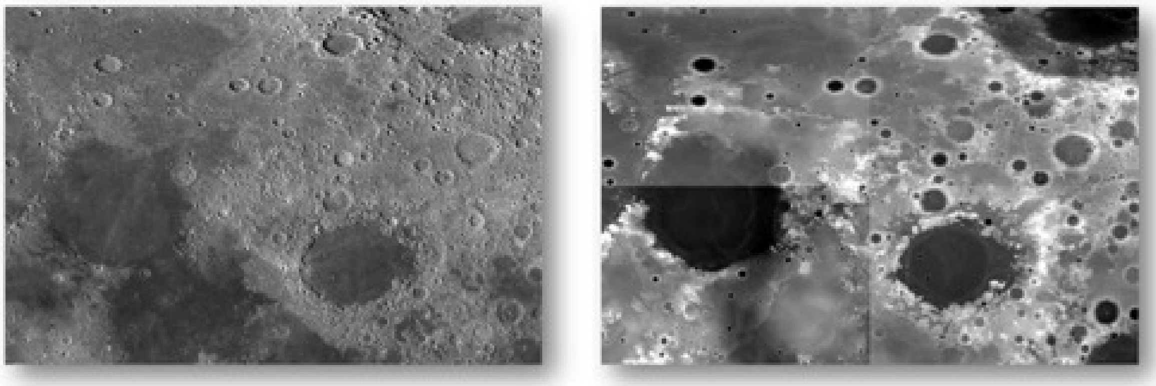

Figure 3. The images represent the study area, on the left there is the quadrant of the WAC Global Morphologic Map, on the right the quadrant of the SLDEM2015 is visible.

A photo interpretation work and mapping (Figure 4) of sinuous rilles have been made with these data, considering that the channels tend to avoid topographic obstructions.

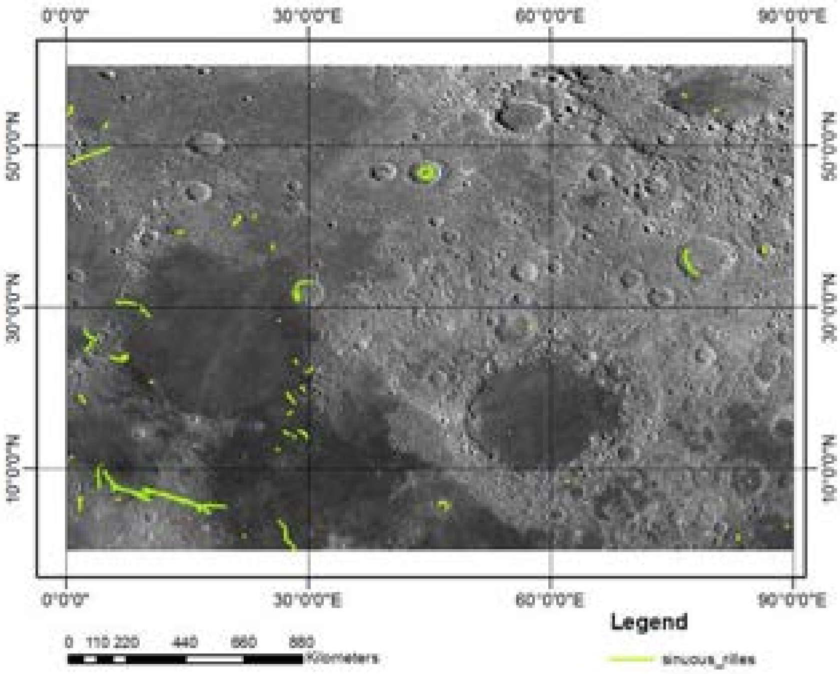

Figure 4. Lunar sinuous rilles mapped in the study area.

Subsequently measurements of morphological parameters (width, depth, length, sinuosity index and regional slope) have been collected for each sinuous rilles to characterize the range of channels dimensions and to identify morphological potential trends.

Width

Sinuous rille width represents the distance between the top of the two parallel walls of each channel measured perpendicularly to the propagation direction of the lava flow (Figure 5). Width measurement has been acquired at several points of each sinuous rille, and then all the values have been averaged to get a characteristic width of each sinuous rille.

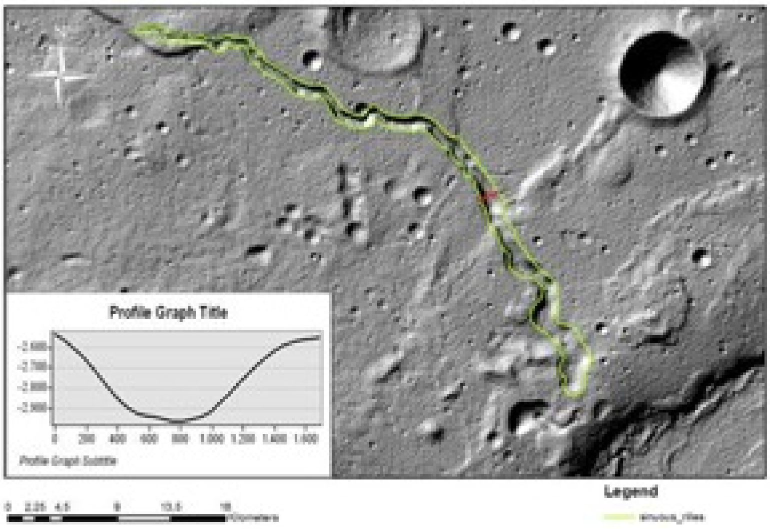

Figure 5. The image shows how the width measurements have been acquired; the red line indicates one of the several measurement points.

Depth

Sinuous rille depth is defined as the difference of altitude between the terrain surrounding the channel and the bottom of the channel. Depth value has been measured at several points along the length of each sinuous rille, and then the measurements have been averaged to get a characteristic depth of each sinuous rille.

Length

Sinuous rille length is defined as the average length of the two walls. Each wall has been mapped individually (Figure 6) and the calculated lengths for each one have been averaged.

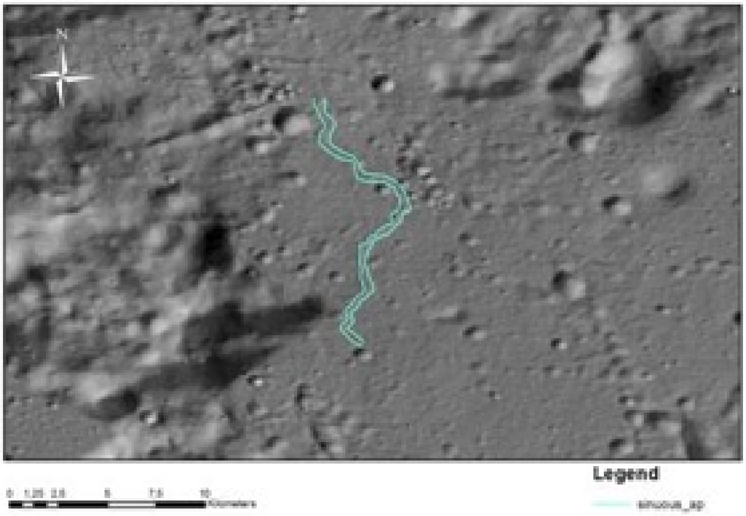

Figure 6. The image represents an example of length measurement. The walls of each sinuous rille have been mapped individually to calculate their length.

Sinuosity index

Sinuosity index is a dimensionless quantity derived by the ratio of the channel length and the distance (straight line) between the end points of the channel. Sinuosity values for terrestrial channels typically range from 1 to 5.

Regional slope

The regional slope represents the slope (degrees) of the terrain on which sinuous rilles formed (Hurwitz et al. 2013). This value has been calculated as the ratio of the difference in elevation between the source area and the terminus area of each sinuous rille and the distance (straight line) between the two areas.

Other information about the sinuous rilles like latitude, longitude, azimuth and the rilles location have been collected. In Figure 7, in a table (Figure 7) in addition to the morphological measurements.

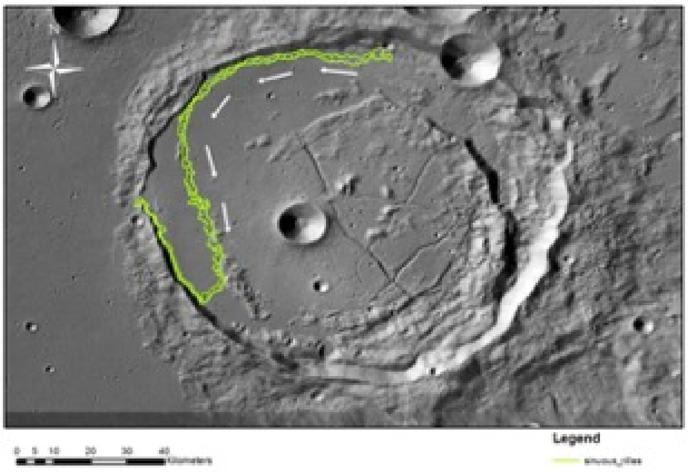

Rille Number	Lat (center)	Long (center)	Azimuth	Width (m)	Depth (m)	Length (m)	Length (m)	Length (m)	Length (m)	Sinuosity	Slope surface (degrees)	Rille Location
				mean	mean	Wall A	Wall B	mean	Rilles (straight line)			
50	32,3108	28,9262	36,50	1146,67	176,15	221115	191794	206454,5	85144,5349	2,42	-0,05	Crater Posidonius

Figura 7. The image shows one of the several sinuous rilles mapped in the study area; below the image there is the table with all data measured on this sinuous rille.

A morphometric analysis (like the one just described) of several sinuous rilles with a regional interpretation are necessary to define the origin and the characteristics of the sinuous rilles.

Bibliography

Barker M. K., Mazarico E., Neumann G. A., Zuber M. T., Haruyama J., Smith D. E., (2015), “A new lunar digital elevation model from the Lunar Orbiter Laser Altimeter and SELENE Terrain Camera”, Icarus, pp 1-10;

Hurwitz D. M., Head J. W., Hiesinger H., (2013), “Lunar sinuous rilles: Distribution, characteristics, and implications for their origin”, Planetary and Space Science, pp 1-38;

Robinson M.S., Brylow S.M., Tschimmel M., Humm D.,. Lawrence S.J, Thomas P.C., Denevi B.W., Bowman-Cisneros E., Zerr J., Ravine M.A., Caplinger M.A., Ghaemi F.T., Schaffner J.A., Malin M.C., Mahanti P., Bartels A., Anderson J., Tran T.N., Eliason E.M., McEwen A.S., Turtle E., Jolliff B.L., Hiesinger H., (2010), “Lunar Reconnaissance Orbiter Camera (LROC) Instrument Overview”, Springer, pp 81-124;

Introduction to 3D visualization of the map atlas

Angelo Zinzi
(Space Science Data Center – ASI)

Abstract

The possibility of exploiting the data acquired by different instruments with a 3D visualization is recently becoming a mandatory requirement for a great part of space missions (e.g., Zinzi et al., 2018). In this context, we adapted MATISSE (Multi-purpose Advanced Tool for the Instrument for the Solar System Exploration – Zinzi et al., 2016) to the needs of the Moon Mapping project, by adding to its database observations and high-order outputs coming from Chang'e 1 and Chang'e 2 (in the following CE1 and CE2, respectively) Chinese missions to the Moon. This task also required the development of *ad hoc* software to read and project the data, mostly formatted compliant to the PDS (Planetary Data System) standard.
The possibility of analyzing the data with an effective three-dimensional perspective added value to their scientific content, thus emphasizing some key aspects, but also gave an easy and "smart" access to the data to non-professional users, one of the main target of this project.

1. Introduction

MATISSE is the web-tool developed by the Space Science Data Center of the Italian Space Agency (SSDC-ASI) in order to access, visualize and analyze data from planetary exploration missions (Fig. 1). Thanks to its modular structure, it can be easily adapted to different types of observations and upgraded with new data. Therefore, it came straightforward to use it inside the Moon Mapping project as the ideal tool for searching, analyze and display data from the CE1 and CE2 instruments.
For the Moon Mapping project, the tool has been mostly used by people pertaining to Topics 2 and 3 of the project, both related to the surface characteristics of the Moon studied by means of visible cameras and infrared spectrometers.
Furthermore, the possibility of obtaining captivating and easy to understand visualizations of lunar surface, perfectly suited for people non directly involved in scientific research (e.g., students), made the MATISSE tool one of the fundamental pieces of the Moon Mapping project.
Its main usage has been related to search observations inside the database by using geographical metadata (i.e., latitudes and longitudes) and then projecting and visualizing them.

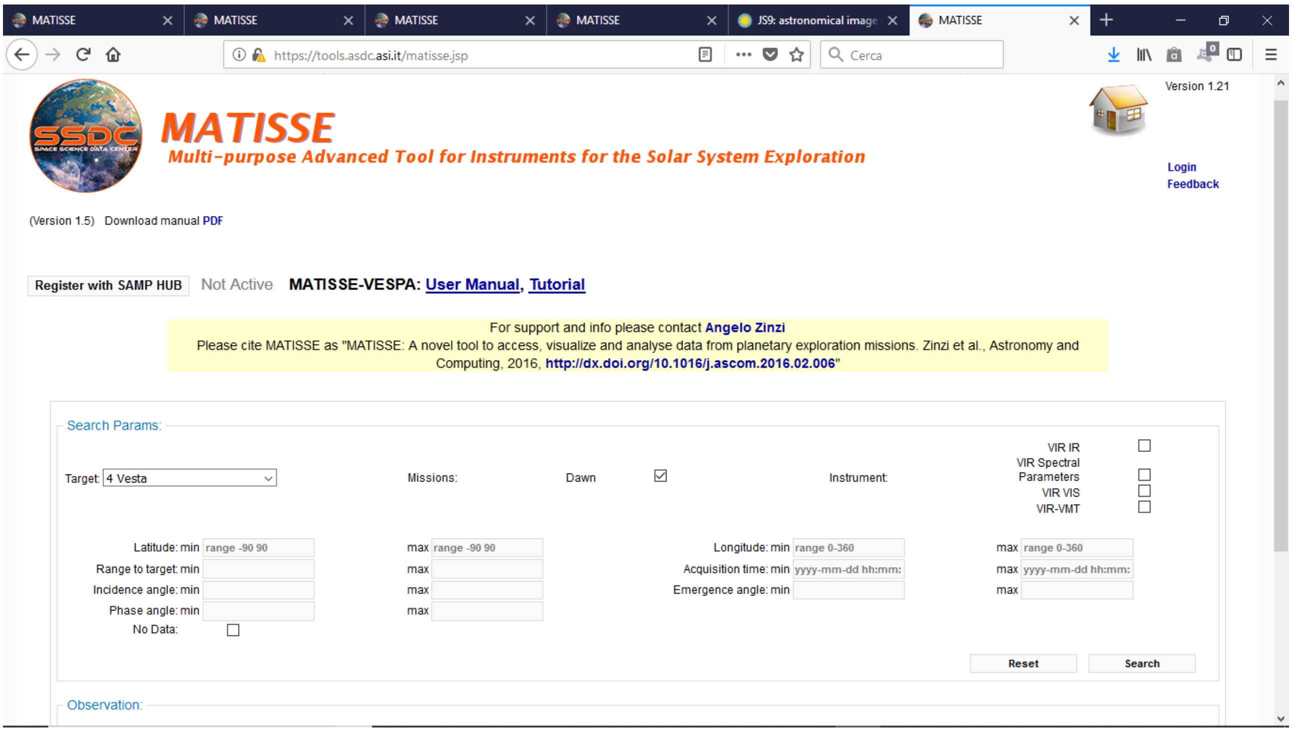

Fig. 1: The MATISSE homepage (https://tools.ssdc.asi.it/matisse.jsp)

2. Ingestion of Chinese data in MATISSE

MATISSE ingests five different kinds of data from the Chang'e missions:

- visible cameras (CCD) from both CE1 and CE2;
- infrared imaging spectrometer (IIM) from CE1;
- Digital Elevation Model (DEM) computed on the basis of CE1 data;
- Ortophoto (DOM) from CE1 and CE2;
- Global Elemental Abundance Maps (EAM) from CE1.

All these data, together with their observational geometries, were provided in PDS format, but, since a single, pre-designed, software cannot read this standard, the first task to be completed was the development of software capable of correctly opening the files and, subsequently, their addition to the MATISSE pipeline.

Single observations (i.e., CCD and IIM) were originally produced exactly as they were acquired, therefore, without a standard projection; on the contrary, high-order products and maps have been delivered to MATISSE already projected by the Chinese data processors.

The output of the reading procedure is passed to the MATISSE pipeline and then the process is exactly as accurately described by Zinzi et al. (2016) and Zinzi et al. (2018), ending with both 2D (ENVI, GeoTIFF, FITS) and 3D (Paraview) outputs.

Three-dimensional outputs are generated by means of VTK libraries so that they can be opened with Paraview free software: this is a powerful and easy solution suited for both scientific and outreach aims. The possibility of further process the data with both predefined and Python scripting filters makes it a perfect tool for science analysis. On the other hand, its straightforward 3D visualization and usability make it easy to use for non-professional people (Fig. 2).

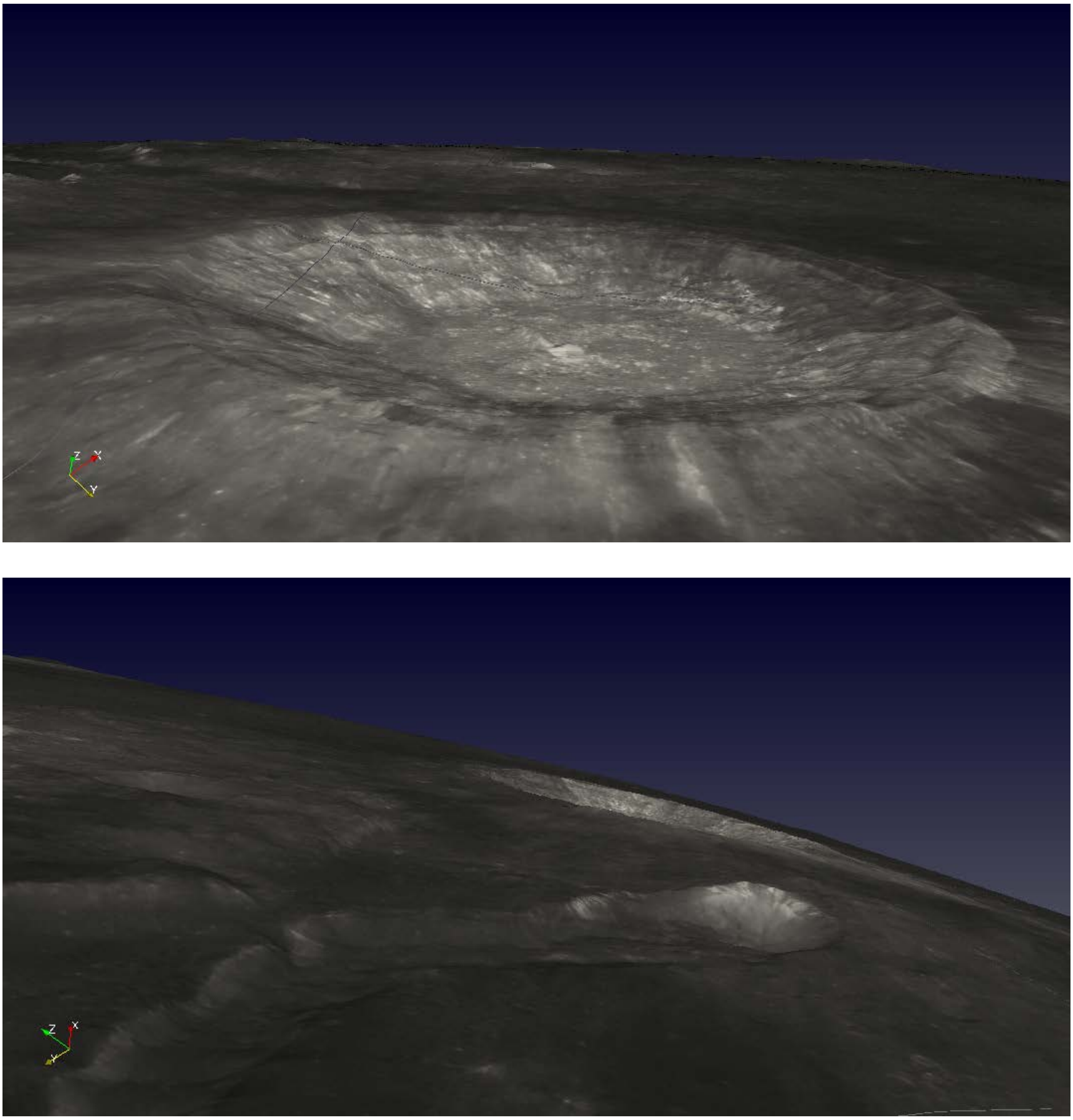

Fig. 2: Examples of 3D visualization of the Moon with MATISSE

3. Examples of 3D visualization uses in educational programs

Apart from its utility as a research tool, MATISSE can be fruitfully become part of educational projects.

Its user-friendly interface and its captivating final products are, indeed, extremely fascinating for non professional users looking for real solar system exploration data.

This approach has been already used in a series of projects, both in Italy and in the United States, clearly demonstrating that also lightly-trained high-school students can use MATISSE to replicate real scientific studies.

In particular Italian students involved in a ministerial educational program used MATISSE after a no more than 2 hours of training during their visit at the Italian Space Agency HQ in Rome. Their goal was to discriminate the composition of dark region of the asteroid Vesta using the data from the VIR

infrared imaging spectrometer onboard the NASA Dawn mission (Fig. 3), as already done by Palomba et al. (2014).
The same activity is now officially part the curriculum of the "Introduction to Modern Astro-Plasma Physics" course of the East Windsor Regional School District in Hightstown, NJ (USA).

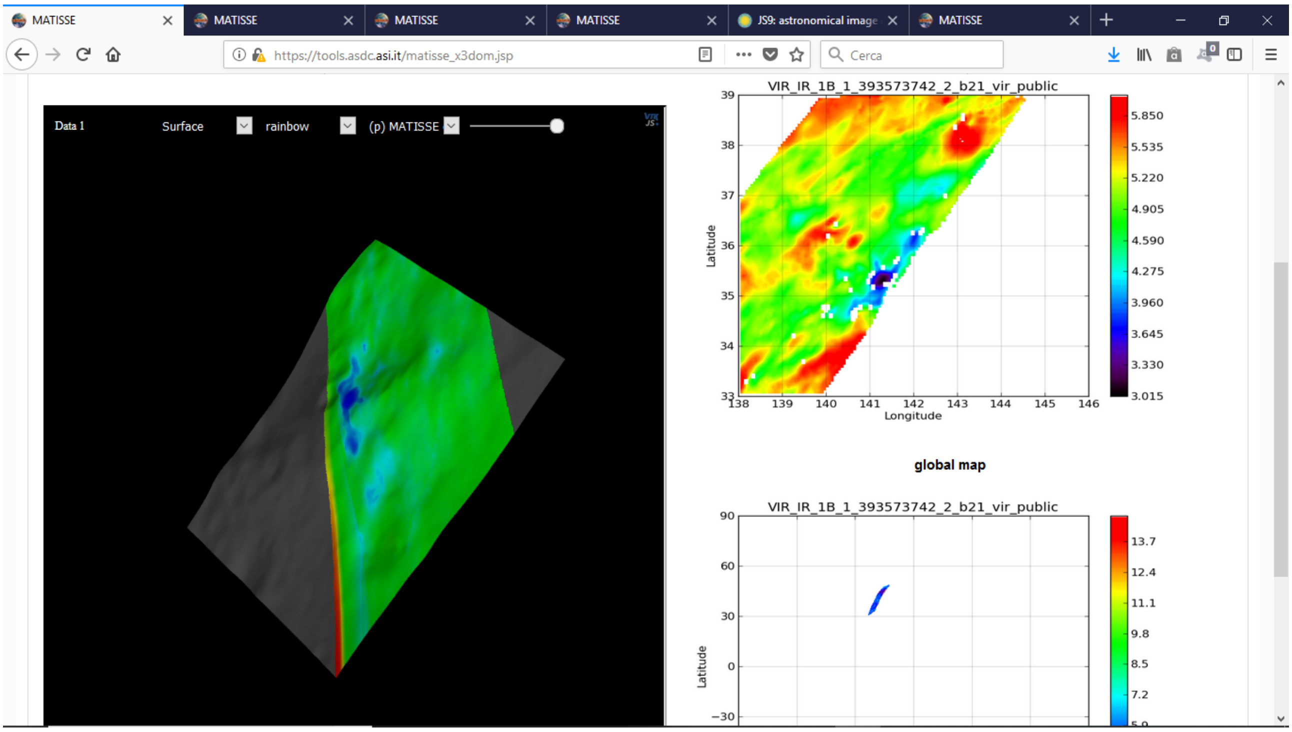

Fig. 3: MATISSE output page for the educational projects involving VIR-Dawn data of asteroid Vesta

4. Using MATISSE for the Moon Mapping interactive atlas

Thanks to these features, MATISSE could certainly play a key role as part of the interactive atlas of the Moon originally thought to be part of the project output.
The software architecture is ready to ingest such a task and the project will become operative as soon as Chang'e data part of the Moon Mapping project will become of public domain.
In this way people from around the world would use MATISSE to look for Chang'e data of the Moon and some selected examples could be rapidly visualized in order to demonstrate the advances allowed by the Chinese-Italian collaboration during the Moon Mapping project.

References

Palomba E. et al., 2014, Icarus, 240, 58
Zinzi A. et al., 2016, Astronomy and Computing, 15, 16
Zinzi A. et al., 2018, Advances in Space Research, 62, 8

Analysis of Solar Wind Ion detectors.

F. Nozzoli[a,b]

[a] *INFN-TIFPA, I38123-Trento, Italy*
[b] *ASI Space Science Data Center (SSDC), I00133-Roma, Italy*

Abstract

Solar Wind Ion flux measured by Chang'E-1 Moon-orbiting spacecraft has been analyzed for the Moon Mapping Sino-Italian project. The electrostatic spectrometer alignment and the data quality selections are described. As a result, the first image of the Sun using charged particles is shown. The Chang'E-1 ion flux collected in the periods December/2007-February/2008 and May/2008-July/2008 showed large variations that seem to be in correlation with the solar activity.

Keywords: Solar Wind; Solar Flares; multi-messenger astronomy.

1. Introduction

The nature of solar wind has always been an important object of study throughout the history of outer space exploration and in recent decades there have been a lot of space projects which probed it, e.g., SOHO [1] and WIND [2] which are near the SunEarth L1 Lagrange point, STEREO [3] and Ulysses [4] which are in heliocentric orbits, and FAST [5] and CHAMP [6] which orbit about the Earth. In recent years, the exploration and investigation of the Moon and cislunar space have once again become a hot topic. Japan launched her second lunar orbiter spacecraft, SELENE (SELenological and ENgineering Explorer), better known in Japan by its nickname Kaguya [7] on September 14, 2007. India launched Chandrayaan-1 [8], her first unmanned lunar probe in October 2008. During this period, China also constructed and launched her

Email address: `francesco.nozzoli@unitn.it` (F. Nozzoli)

November 28, 2018

first unmanned lunar-orbiting spacecraft ChangE-1 (abbreviation CE-1) in October 2007, which carried several kinds of scientific instruments, among which was Solar Wind Ion Detector (SWID). As its name implies, it was designed to detect the solar wind ion differential number flux. These lunar exploration programs together with others sent back to Earth a large and varied volume of data which are essential for furthering our understanding of the Moon and cislunar space environment. Much research has been carried out to investigate the nature of the solar wind, based on the data collected by numerous spacecrafts launched in many decades, analyzing the composition of the solar wind, or to improve our understanding of the Sun. This allows to probe the structure of solar wind and to construct a model of the cislunar space environment in which solar wind plays an important role. The solar wind is composed of ions, chiefly consisting of electrons and protons together with smaller numbers of nuclei of heavier elements such as He++ and C6+ , N7+, and O6+. These particles are accelerated by the difference in pressure between the corona and the interplanetary space, to velocities large enough to allow them to escape from the Suns gravitational field. The solar wind is a key factor in the formation of the Earths magnetosphere, due to its interaction with the Earths magnetic field.

2. The SWID detectors

The equipment carried by CE-1 is called the Solar Wind Ion Detector (SWID), described by [9]. The SWID has a field of view (FOV) of approximately $6.7^0 \times 180^o$, and can therefore be considered to lie in a plane. The instrument detects ion differential number flux arriving from half (180^o) of that plane, with a Micro channel plate detector anode divided into 12 equal readouts, each with an angular view of 15^o (see Fig. 1.Left). The instrument is able to detect ion differential number flux distributed in 48 energy levels on a logarithmic scale ranging from 0.05 to 20 keV. Finally, two identical SWIDs were installed on CE-1, namely SWIDA and SWIDB, fixed such that they were mutually perpendicular in order to supplement each others limited FOV, as illustrated in Fig. 1.Right [10].

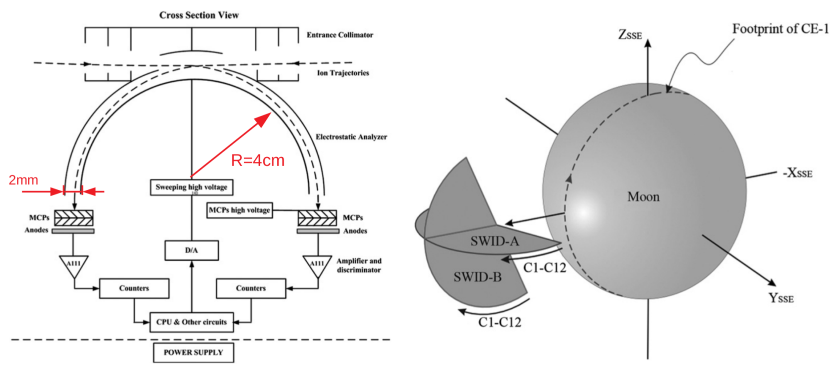

Figure 1: Left: Basic principle diagram of SWID. Right: Installation geometry of two SWIDs instruments in the selenocentric solar ecliptic (SSE) coordinate system. Two vertical fans show the field-of-views of SWIDs. The dashed line indicates the footprint of the spacecraft.

3. Data sample

SWID data are stored in the standard Planetary Data System (PDS) format, where each record consists of a time, a 48-by-12 matrix storing ion differential number flux data across the 48 energy levels and 12 directions as described above, along with GSE coordinates and MCC coordinates of CE-1 (the definitions of both coordinate systems are given in Section 3), Quality state, and Instrument Sun Incidence Angle. A sample record of a data file from SWIDA is provided in Table 1. For more information on the data of SWID, please refer to [11] and references therein. Interpreting the SWID data files is not immediately intuitive; extracting the directional data (i.e., the direction a particular differential number flux is coming from) is particularly difficult, because the direction is a function of the relative positions of the Sun, Earth, and Moon, in addition to the position of the spacecraft and orientation of the SWID. There is also a large volume of data to handle: the measurement intervals of both SWIDA and SWIDB were around 3s, stored as separate files for each 2-h orbit around the Moon, with each file therefore typically holding over 2000 records. SWIDA and SWIDB amassed about 5000 files during their lifetimes, amounting to over 57 GB of data.

Data item	Unit	Sample
Time	Timestamp	2007-11-26T21:10:40.893Z
Flux	[keV cm^2 s sr]$^{-1}$	a [48x12] matrix
GSE coo	Earth radii	-48.5635,-30.1448,4.4484
MCC coo	km	-172.1049,-21.0871,1945.3538
Sun angle	Deg.	84.2097, 158.3941, 110.7401
Quality stat.	Bit-coded	0 x 0000FF

Table 1: A sample record of a SWIDA data file.

A specially developed 3D visualization method to handle a single CE-1 SWIDs data record is described in [11].

In the following a global analysis of CE-1 SWIDs data is considered.

3.1. Channels alignment validation

The nominal alignment of Solar Wind Ion detector Channels with respect to Chang'E-1 attitude are described in ref. [10]. Here a data driven validation procedure, is briefly addressed.

As shown in fig. 2, when the Sun is passing in the Field of View (FoV) of each channel there is a large enhancement of flux measurement due to unshielded direct measurement of the Solar Wind; this allows to extract the alignment of each channel by fit procedure (continuous line) that can be compared with nominal alignment (dashed line).

Due to the alignment of the Chang'E-1 orbital plane with SWIDB plane (Fig. 1.Right) when the Sun lies in the FoV of one of the SWIDB channel it will be in the acceptance of all the other SWIDB channels within the same orbit (i.e. in the same Sun activity level). This allow the validation the nominal alignment of SWIDB channels within 7.5^o (half channel) of global angular rotation in SWIDB plane. On the other hand, due to perpendicularity SWIDA plane with respect to SWIDB plane and due to the limited period of data taking (December/2007-February/2008 and May/2008-July/2008) the Sun was passing in the FoV only

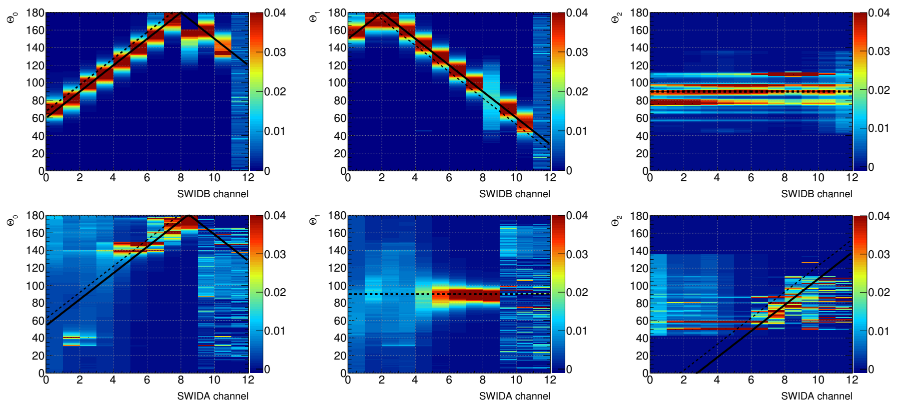

Figure 2: Solar wind ion flux distribution normalized for each SWID channel. Vertical axis is the component of the Sun angle as stored in the data files. Continuous lines are the channel alignment direction obtained by fit, dashed lines are the nominal channel alignment as described in ref. [10]. For the period of the data sample, the Sun was passing in the FoV acceptance for all SWIDB channels and only for the SWIDA channels #6 to #9.

for the SWIDA channels #6 to #9. Moreover the very different Sun activity level in different data taking periods poses additional difficulties with the comparison of the flux measured with different Sun angles with respect to SWIDA channels. This allow the validation the nominal alignment of SWIDA channels within $\sim 15^o$ (one channel) of global angular rotation in SWIDA plane. As a result of the channel alignment validation, the director cosines for each SWID channel can be described as (k=[1,12]):

$$\begin{aligned}
SWIDA[k]_x &= 0 \\
SWIDA[k]_y &= -cos\left[\pi(231-15k)/180\right] \\
SWIDA[k]_z &= cos\left[\pi(39+15k)/180\right] \\
SWIDB[k]_x &= cos\left[\pi(217.5-15k)/180\right] \\
SWIDB[k]_y &= 0 \\
SWIDB[k]_z &= cos\left[\pi(52.5+15k)/180\right] \qquad (1)
\end{aligned}$$

Finally from fig. 2 it is also confirmed that SWIDB channel #12 and SWIDA channel #11 and #12 are blocked by the satellite body and that response of SWIDB channel #9 is degraded, as stated in ref. [10].

On the other hand in this analysis also SWIDA channel #10 seems to be not usable, with features similar to channels #11 and #12 of SWIDA. A summary of SWIDA and SWIDB channel geometrical configurations and blocked/broken channels is given in fig. 3.

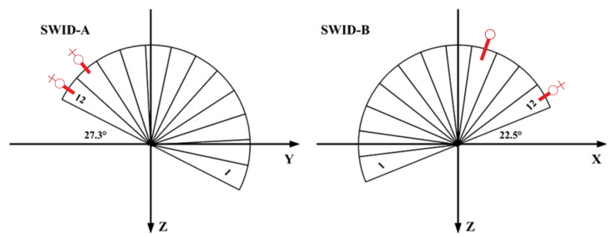

Figure 3: Summary of geometrical positions of SWIDA and SWIDB channels. Markers are shown on blocked/broken channels.

3.2. Data quality selections

In left plot of figure 4 an example of Solar wind ion flux measured by channel # 8 of SWID-B detector as a function of the cosine of the Sun angle it is shown. The vertical axis is the energy bin number. Unfiltered CE-1 SWIDs data shows specific noisy energy channels (horizontal rows) and noisy periods (vertical rows). The noisy energy channels are removed requiring these quality criteria on the spectral shape of SWID measurement, removing un-natural peaking spectra: i) that more than a single energy channel must be nonzero. ii) more than two energy channels should contain more than half of the average energy flux. iii) a shape indicator with number of filled (nonzero) energy channels is used to remove measurement where most of the energy channels are empty. On the other hand, to remove the noisy periods the average flux measured by blocked channels SWIDA #10,#11,#12 and SWIDB #12 was considered as a classifier. A cut on this quantity remove a population of noisy periods, due, as an example, to known solar flares.

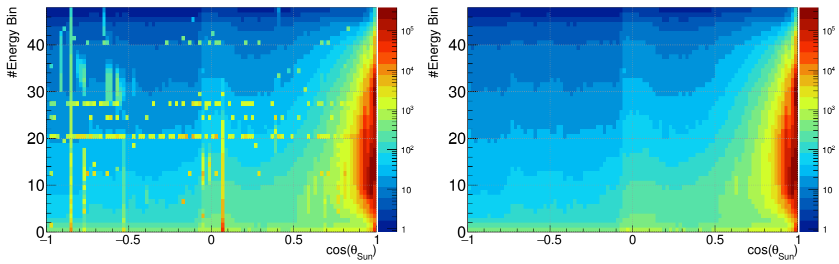

Figure 4: Example of Solar wind ion flux measured by channel # 8 of SWID-B detector as a function of the cosine of the Sun angle with respect to the channel. Vertical axis is the energy bin number. Left plot shows the raw flux data, right plot shows the same data sample after the data quality sections described in the text.

The result of these data quality selections is shown in Fig.4.Right.

4. Solar wind distribution map

As shown also in Fig.4, the solar wind flux measured by a specific SWID channel is maximum when the Sun lies in the FoV of that channel (cos θ_{sun}=1). Considering the $6.5^o \times 15^o$ FWHM distributions of each channel (Fig. 1) the angular resolution of SWID channels is expected to be of the order of few degree. Such a modest resolution is not enough to detect the details of the Sun surface structure, but, thanks to the absence of a strong lunar magnetosphere, an image of the Sun in the sky as a source of the solar wind ions can be produced by stacking all the SWIDA/B measurements.

This is shown in Fig.5 where the charged particle image of our star obtained by CE-1 is compared with the other existing multimessenger images of the Sun, namely: gamma rays from Fermi-LAT [12] and neutrinos from Super-Kamiokande [13].

As described in the following, the effect of the large time variability on the solar wind flux, due to variation of Sun activity, affects with systematics the

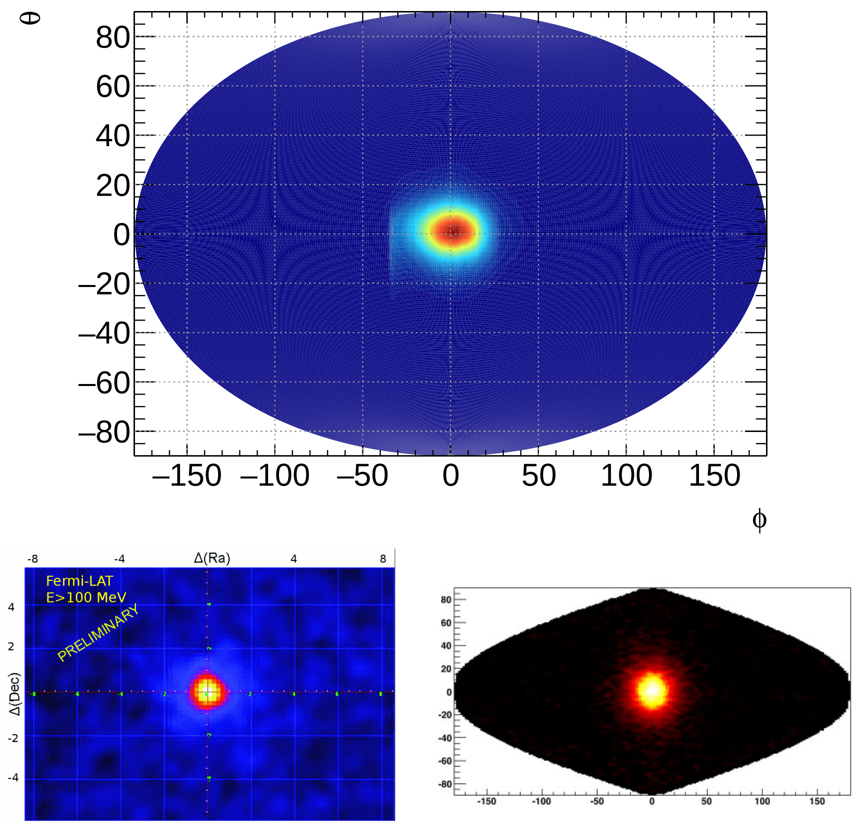

Figure 5: Top figure: Sun centered solar wind flux map as measured by Chang'E-1. The apparent angular size of the Sun in this map is compatible with the 15^oFWHM angular aperture of the Chang'E-1 SWID channels. As a comparison, in the bottom figures the Sun as observed with different particle/messengers: Sun centered flux map for E>100 MeV gamma rays as measured by Fermi-LAT [12] (bottom left) and for neutrinos as measured in 12 years by Super-Kamiokande [13] (bottom right).

"pointing" capability of SWIDs channels that cannot span a large fraction of the sky at the same time.

5. Sun activity

During the Chang'E-1 SWIDs data taking: December/2007-February/2008 and May/2008-July/2008 the Sun was exactly passing the Solar minimum activity, at the end of the cycle 23. Despite the minimum of Solar activity, large time variations in the sunspots number [14] and in the magnitude of solar flares [15, 16] has been observed.

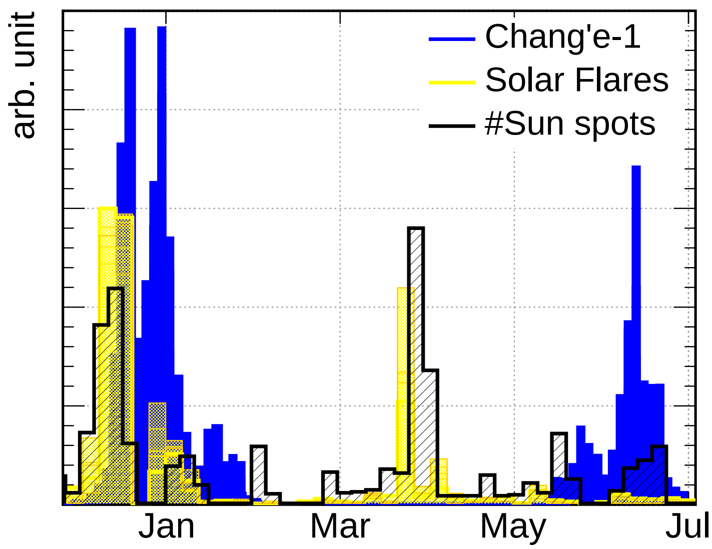

Figure 6: Sun activity as measured by Chang'E-1 in the periods December/2007-February/2008 and May/2008-July/2008 (blue) as compared with number of sunspots [14] (black/hatched) and with the magnitude of solar flares as measured by Hinode [15] and RHESSI [16] satellites (yellow).

In Fig.6 these known observables related to solar activity are compared with the variations of Solar wind flux as measured by Chang'E-1 SWID detectors. The existence of some correlations is very interesting, considering that the three quantities are based on very different effects related to the same variability source. In particular the solar wind measured by CE-1 needs approximately a couple of day to cover the 1AU of distance of the Moon from the Sun, on the contrary of the fast photon signal measured by the other observables.

6. Conclusions

SWIDs, as two scientific instruments of ChangE-1, were able to measure the solar wind and the plasma environment near the Moon. Besides the normal in-flight observations, SWIDs was able to provide an interesting image of the Sun based on charged particles, enriching the collection of multimessenger pictures of our star. The correlation of the flux variability as measured by CE-1 with respect to the other existing flare indicators can be of large interest from the point of view of space weather studies and applications.

References

[1] V. Domingo et al., Sol. Phys. **162** (1995) 1.

[2] K.W. Ogilvie et al., Sp. Sci. Rev. **71** (1995) 55.

[3] M.L. Kaiser, Adv. in Sp. Res. **36** (2005) 1483.

[4] K.P. Wenzel et al., Adv. in Sp. Res. **9** (1989) 25.

[5] C.W. Carlson et al., Geophys. Res. Lett. **25** (1998) 2013.

[6] C. Reigber et al., Adv. in Sp. Res. **30** (2002) 129.

[7] M. Kato et al., Sp. Sci. Rev. **154** (2010) 3.

[8] J.N. Goswami, Proc. 41st Lunar and Planetary Science Conference. The Woodlands. Texas. USA. LPI Contribution No. 1533, p. 1591.

[9] S. Huixian et al., J. of Earth Syst. Sci. **114** (2005) 789.

[10] L.G. Kong et al. Plan. Sp. Sci. **62** (2012) 23.

[11] T. Zhang et al. Comp. & Geosci. **37** (2011) 171.

[12] S. Raino et al. (Fermi-LAT coll.), Nucl. Part. Phys. Proc. **291293** (2017) 3639. arXiV:0912.3775.

[13] Super-Kamiokande Official Website: http://www-sk.icrr.u-tokyo.ac.jp/sk/sk/solar-e.html

[14] J.H. King and N.E. Papitashvili, J. Geophys. Res. **110** (2005) A02209. OMNI data were obtained from the GSFC/SPDF OMNIWeb interface at https://omniweb.gsfc.nasa.gov

[15] Watanabe, K., S. Masuda, and T. Segawa, Hinode Flare Catalogue, Solar Physics, **279** (2012) 317-322.

[16] Rhessi catalogue hosted by the Goddard Space Flight Center: https://hesperia.gsfc.nasa.gov/rhessi3/

EUROPEAN JOURNAL OF REMOTE SENSING, 2017
VOL. 51, NO. 1, 47–61
https://doi.org/10.1080/22797254.2017.1401908

Taylor & Francis
Taylor & Francis Group

REVIEW ARTICLE

OPEN ACCESS Check for updates

Recognition of landslides in lunar impact craters

Marco Scaioni [a], Vasil Yordanov[a], Maria Teresa Brunetti[b], Maria Teresa Melis [c], Angelo Zinzi [d], Zhizhong Kang [e] and Paolo Giommi [f]

[a]Department of Architecture, Built environment and Construction engineering, Politecnico di Milano, Milano, Italy; [b]Research Institute for Geo-Hydrological Protection–Italian National Research Council, Perugia, Italy; [c]Department of Chemical and Geological Sciences, University of Cagliari, Cagliari, Italy; [d]ASI Science Data Center, INAF-OAR, Rome, Italy; [e]China University of Geosciences, Beijing, P.R. China; [f]Italian Space Agency, ASI, Roma, Italy

ABSTRACT
Landslides have been observed on several planets and minor bodies of the solar System, including the Moon. Notwithstanding different types of slope failures have been studied on the Moon, a detailed lunar landslide inventory is still pending. Undoubtedly, such will be in a benefit for future geological and morphological studies, as well in hazard, risk and susceptibility assessments. A preliminary survey of lunar landslides in impact craters has been done using visual inspection on images and digital elevation model (DEM) (Brunetti et al. 2015) but this method suffers from subjective interpretation. A new methodology based on polynomial interpolation of crater cross-sections extracted from global lunar DEMs is presented in this paper. Because of their properties, Chebyshev polynomials were already exploited for parametric classification of different crater morphologies (Mahanti et al., 2014). Here, their use has been extended to the discrimination of slumps in simple impact craters. Two criteria for recognition have provided the best results: one based on fixing an empirical absolute thresholding and a second based on statistical adaptive thresholding. The application of both criteria to a data set made up of 204 lunar craters' cross-sections has demonstrated that the former criterion provides the best recognition.

ARTICLE HISTORY
Received 8 February 2017
Revised 31 October 2017
Accepted 3 November 2017

KEYWORDS
Moon; landslides; craters; Chebyshev polynomials; digital elevation model (DEM); morphological analysis

Introduction

Different types of mass wasting processes have been observed on several planetary and minor bodies of the solar System, as reported in the abundant literature on this topic (Bart, 2007; Brunetti, Xiao, Komatsu, Peruccacci, & Guzzetti, 2015; Buczkowski et al., 2016; De Blasio et al. 2011; Krohn et al., 2014; Massironi et al., 2012; Mazzanti, De Blasio, Di Bastiano, & Bozzano, 2016; Quantin, Allemand, & Delacourt, 2004; Waltham, Pickering, & Bray, 2008; Williams et al., 2013; Xiao & Komatsu, 2013)). On the Moon, first studies about mass movements were published by Pike (1971) using images from the Apollo 10 Mission. He managed to recognize and classify landslides as creeps, crater wall slumps, debris flow and rock falls. However, before 2009 only few studies have been concentrated on landslides on the Moon. Recently, Xiao, Zeng, Ding, and Molaro (2013) studied lunar landslides and classified them into different morphologic groups on the basis of criteria similar to those applied by Cruden and Varnes (1996), which is usually assumed as consolidated international reference for classifying crater inner wall landslides on the Earth. Xiao et al. (2013) selected more than 300 examples of slope failures on the Moon that were identified as falls, flows, slides, slumps and creeps. In the large majority of cases, lunar slope failures are found in craters sizing up to a few tens of kilometres. The high energy released during the impact may have left some unstable areas inside the crater, which came to collapse afterwards. Sentil Kumar, Keerthi, Sentil Kumar, and Mustard (2013) investigated debris flow-type mass movements and suggested that these features were originated by a more recent activity than the impact cratering itself, probably due to moonquakes produced by other meteorite impacts in the nearby. Recently, Brunetti et al. (2014, 2015) used a visual analysis for detecting and classifying landslides on Mars, the Moon and Mercury.

In this research, the recognition process of lunar landslides has been applied to detect slumps in simple impact craters, i.e. those cavities typically bowl-shaped and not affected by terraced rims (Melosh, 1989), secondary impacts or heavily degraded. Figure 1 shows some examples of slumps in lunar impact craters.

Geological, morphological, physical factors and even human activity on the Earth (e.g. road cuts) may lead to the instability of the surface features,

CONTACT Maria Teresa Melis titimelis@unica.it Department of Chemical and Geological Sciences, University of Cagliari, via Trentino 51, Cagliari 09127, Italy

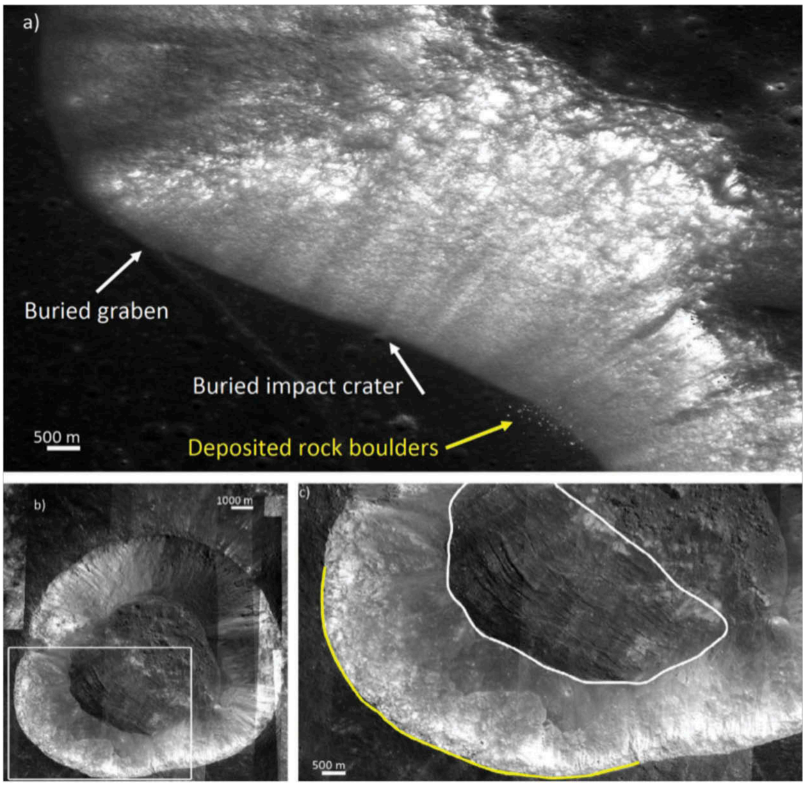

Figure 1. Some examples of lunar slumps: (a) a slump along the promontorium Laplace where the deposit has buried a small crater and part of graben (white arrows); the traces of a few fallen boulders due to a subsequent rock fall can be noted as well (yellow arrows); (b) a slumped wall on the Crater Tharp; (c) a close up of the slump of Crater Tharp, in yellow is highlighted the crown and in white the deposit. Images obtained via QuickMap™ tool.

and may be considered as predisposing factors for landslides. While multiple combined factors may concur to the instability of a slope, usually only a single triggering factor is responsible for the landslide occurrence. The triggering factors for lunar landslides are distinctively different from the ones on the Earth. The large number of various size meteorite impacts are considered as the main direct triggering factor for mass movements on the Moon. These may also act as predisposing factors. Indeed, impacts may induce shock waves that directly disturb materials on slopes forming mass wasting landforms (Lindsay, 1976). This process may result in crushed subsurface bedrock and formation of fractured zones that sometimes extend for several times the crater radius beneath the crater floor (Melosh, 1989). In such a weakened region, a landslide may be triggered in a second stage by another impact in the nearby or by a moonquake.

After reviewing of recent missions to the Moon and the available data sets in Section "Recent missions to the moon and data applied in the work,", it turns out that a consolidated methodology for the automatic or semi-automatic recognition of landslides in lunar impact craters has not been defined yet (see Section "Visual detection of landslides within simple impact craters"). Consequently, a new method based on the approximation of crater cross-sectional profiles with Chebyshev polynomials is described in Section "Landslide recognition based on the Chebyshev polynomials ." Thanks to the analysis of the asymmetry of such profiles, the presence of landslide features in lunar impact craters is recognized. Experimental results are reported in Section "Application 1 along with GLD100," while Section "Conclusions and future developments" hosts discussions and some final considerations.

Recent missions to the moon and data applied in the work

For centuries, mankind has been interested in studying the Moon, but it was only in the middle of the 20th century that the first space missions and probes started approaching the Earth's satellite. In the last decade, with the help of the major space agencies and their exploration missions, scientists started to have access to huge data sets holding the potential for unprecedented scientific discoveries (Zinzi et al., 2016) . At present, three ongoing lunar missions must be mentioned: the Lunar Reconnaissance Orbiter (LRO) by National Aeronautics and Space Administrations (NASA, United States), the SELenological and ENgineering Explorer (SELENE-KAGUYA) by the Japan Aerospace Exploration

Agency (JAXA, Japan), and Chang'E missions by the Chinese Nationals Space Administration (CNSA, P.R. China). LRO (Chin et al., 2007; Robinson et al., 2010) and SELENE-KAGUYA (Araki et al., 2007) are orbiters with on-board measuring instruments. Chang'E is an ambitious program composed of several missions dedicated to the exploration of the Moon. The first missions in the series (Chang'E-1 and Chang'E-2) had the main aims of providing a digital elevation model (DEM) of the lunar surface and mapping the abundance and distribution of various chemical elements [Sun et al., 2005]. Chang'E-3 (Li, Liu, et al., 2015) is an unmanned exploration mission incorporating a robotic lander and a rover (Yutu), that has already travelled 114 m on the lunar surface.

LRO has six individual instruments on-board, with the purpose of producing accurate maps and obtain high-resolution images, to assess potential future landing sites and lunar resources, and to characterize the radiation environment (Chin et al., 2007). The instrumental payload on-board LRO also includes the Lunar Reconnaissance Orbiter Camera (LROC), consisting of two Narrow-Angle Cameras (NAC's) and a Wide-Angle Camera (WAC). NAC's ground sampling distance (GSD) may reach 0.5 m pixel size over a 5 km swath, while WAC provides images at average GSD of 100 m over a 60 km swath in seven spectral bands. As a result from the WAC stereo images a nearly global DEM with a resolution 100 m x 100 m was produced using photogrammetric image matching (GLD100), see (Scholten et al., 2012). This DEM covers 98.2% of the entire lunar surface, with an average elevation accuracy in the order of ±20 m, which may be even better than ±10 m in the maria. The GLD100 as well as WAC and NAC images were used for the study of landslide features on the lunar surface. Such data sets could be accessed through the QuickMap™ web interface (http://target.lroc.asu.edu/q3/) and the open source Java Mission-planning and Analysis for Remote Sensing (JMARS) software. This is a WEB-GIS platform developed by the Arizona State University (http://jmars.asu.edu/) that allows handling planetary remote-sensing data sets.

Visual detection of landslides within simple impact craters

While the automatic identification of lunar impact craters has been successfully achieved (Kang, Luo, Hu, & Gamba, 2015; Vijayan, Vani, & Sanjeevi, 2013; Li, Ling, et al., 2015), to date the detection and mapping of lunar landslides has been obtained only through visual inspection of images (e.g. Brunetti et al., 2015; Xiao et al., 2013). The recognition and mapping of landslides on the Moon surface adopted the same visual interpretation criteria used by geomorphologists to detect and map terrestrial landslides (Antonini et al., 2002; Rib & Liang, 1978; Speight, 1977; Van Zuidam, 1985). For the visual detection and mapping of landslides in impact craters, Brunetti et al. (2015) started with a recognition of the general landscape (e.g. local slopes, terrain steepness) in the areas of the selected crater using available images and DEM's. Then, they extracted several topographic profiles from the DEM, thus allowing the morphology analysis of the crater and of the landslide, and more specifically, the detection of the landslide boundaries. Thereafter, they drew a circle that approximated the crater circumference, to detect the deformation of the crater rim induced by the landslide. The size of the circle was set according to the curvature of the non-collapsed crater rim. Finally, the landslide scarp and deposit were mapped (see examples from Brunetti et al. (2015) in Figure 2).

Brunetti et al. (2015) estimated a 20% uncertainty in the geometric measurement of the landslide area. This uncertainty is ascribed to the complex morphology of the lunar terrain, and to the resolution of images used to detect and map slope failures. In addition, the frequent presence of elongated shadows or overexposed areas prevents the correct identification of landslide boundaries.

Landslide recognition based on the Chebyshev polynomials

Since the presence of an enormous amount of impact craters on the Moon where slumps might have occurred, the definition of a methodology that automatically provides at least a preliminary recognition of such mass wasting processes is still called for. In the previous section, the visual analysis of optical images has proven to be efficient for slump recognition. In the experience of the authors, the visual analysis of optical images works well in the case of interpretation by an expert geologist, but it is highly error prone when some pattern recognition algorithms are applied. Crater geometry could potentially provide more robust information when implemented in an automatic recognition process rather than using images. Any significant deviation of the crater geometry from the original shape of the simple bowl-shaped crater may be interpreted as the presence of a landslide. As it can be seen in Figure 3, the morphology of impact craters might also be quite complex with terraced margins and central peaks (Melosh H.J., 1989) and in such a case the recognition of slumps is more difficult. Also, the impact angle of the meteorite, the sloped terrain, and the degradation processes in the crater may have led to situations where the presence of a slump may be masked, or where morphologies similar to the ones due to slumps

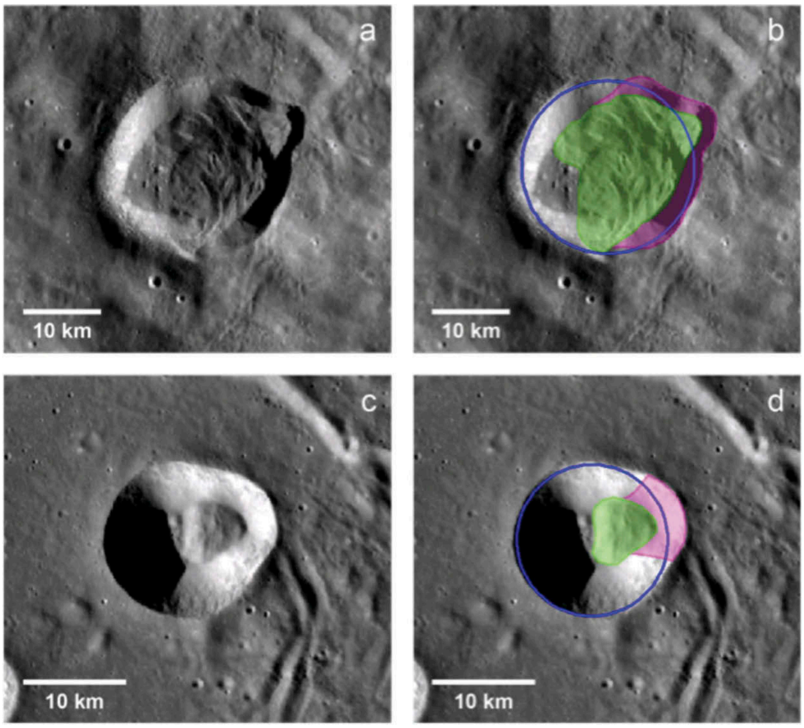

Figure 2. Examples of landslides mapped in two lunar craters. Figures (a) and (b) portray Gerasimovich D; (c) and (d) Cassini A craters. The blue circle approximates the crater rim; purple and green shaded areas are the landslide scarp and deposit, respectively. Credits: (Brunetti et al., 2015) and NASA/Goddard Space Flight Center/ASU.

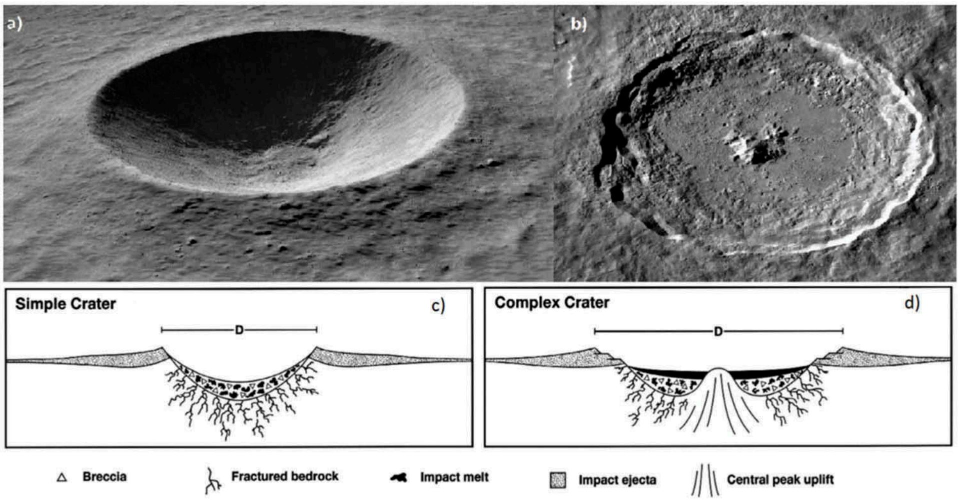

Figure 3. Example of different types of lunar craters, from the simplest one consisting in a single bowl-shape (at the upper left side crater Linné) up to complex craters (at the upper right side crater Tycho). General structure of (c) simple crater and (d) complex crater. Credits: NASA/Goddard/Arizona State University.

may be found. Such cases would easily result in omission and errors during classification. For this reason, the algorithm presented in the following is supposed to work for simple craters having approximately circular shape. These might have resulted from the impact of meteorites whose trajectory is not lower than 10° with respect to the horizontal plane, as stated in Melosh (2011).

Polynomial approximation has been used in Mahanti, Robinson, Humm, and Stopar (2014) to find a characterization of crater cross-sectional profiles. This method can be classified as data-driven, since it does not need any a priori model to be assumed. Since the approximation of more complex shapes of the profiles can be done by simply increasing the order of the approximating polynomial, this solution is potentially efficient also in the case of craters affected by soil degradation processes. The approximation level depends on the degree of the adopted polynomials: the terms that are omitted give rise to the so called truncation error, whose magnitude is related to the specific implemented polynomials. In Mahanti et al. (2014) the Chebyshev polynomials (Mason & Handscomb, 2010) have been used for approximating craters' cross-sectional profiles. Since the presence of a slump in a crater may alter the symmetry of the profiles intersecting the slump's body, the analysis of symmetry might be used for recognition, as in Mahanti, Robinson, and Thompson (2015). The development of the idea, that was briefly introduced in Mahanti et al. (2015), is presented here, after providing a short review on Chebyshev polynomials' mathematical background and their basic properties.

Background on Chebyshev polynomials

The Chebyshev polynomials are a series of orthogonal polynomials, each of them featuring a unique and uncorrelated shape with respect to any other members of the series. Following (Mahanti et al., 2014), the so called Type I Chebyshev polynomials have been adopted for approximating crater cross-sectional profiles. This is motivated by the great simplicity of the coefficients related to this representation. The formulation of polynomials' basis functions is based on a recursive series defined in the domain between −1 and +1:

$$T_{n+1}(x) = 2xT_n(x) - T_{n-1}(x); \; |x| \leq 1, \qquad (1)$$

where $T_n(x)$ is the polynomial basis function of order n. The basis functions of order $n = 0$ and $n = 1$ are $T_0(x) = 1$ and $T_1(x) = x$, respectively. In Figure 4, the graphical plot of the six basis functions of Chebyshev polynomials are shown.

In order to approximate a real function $f(x)$, a linear combination $pM(x)$ of the first $M + 1$ basis functions of Chebyshev polynomials is adopted:

$$f(x) \cong pM(x) + o(x_M) = \sum_{n=0}^{M} C_n T_n(x) + o(x_M), \qquad (2)$$

where M is the degree of the Chebyshev polynomial and C_n are the coefficients that modulate the amplitude of each basis component. Coefficients C_n are estimated on a least-squares basis to fit with real profile data, as discussed in subsection 'Landslide recognition using Chebyshev polynomials'. The residual approximation error $o(x_M)$ is equal to the sum of missing terms after degree M that are not considered in the approximation (i.e. truncation error).

As it results from Equations (1) and (2), in the Chebyshev polynomial series even (symmetric w.r.t. vertical axis) and odd (anti-symmetric) basis functions alternatively appear. Consequently, the size of odd coefficients may express the degree of asymmetry of the approximated function $f(x)$.

Several properties make the Chebyshev polynomials particularly efficient for approximating crater cross-sectional profiles. These could be summarized in five main points:

(i) The basis functions are mutually orthogonal and the estimated coefficients are uncorrelated. This property results in the consequence that, even though the total number of adopted coefficients may be different, the estimated values of the lower order coefficients it is always the same. This property is important because it makes the estimated coefficients independent from the specific estimation process, hence they can be compared in a meaningful way among several cross-sectional profiles. Indeed, lower numbered coefficients C_n have a larger impact in the approximation of the crater profile geometry.

(ii) Chebyshev polynomials may well fit to the interpolated function $f(x)$, i.e. the crater

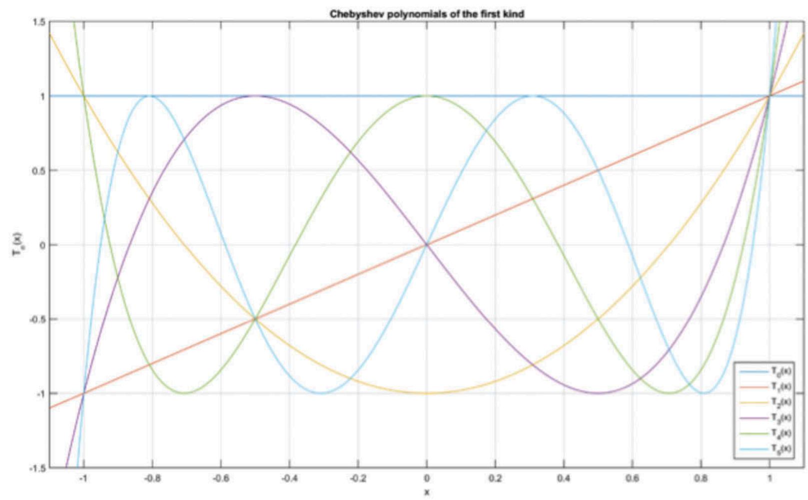

Figure 4. Graphical plots of the first six basis functions of Chebyshev polynomials (in different colours).

cross-sectional profile (Gautschi, 2004; Mason & Handscomb, 2010), if a proper number of basis functions/coefficients is selected; consequently, residuals may also be very small, depending on the number of adopted coefficients. Taking advantage of this property, Mahanti et al. (2014) demonstrated that lunar crater cross-sectional profiles could be approximated by using the first 17 coefficients (M = 16) of Chebyshev polynomials.

(iii) Extreme values of Chebyshev polynomials always occur at some specific positions on the reference axis (x = −1, 0, +1). This property makes easier to link the estimated polynomials' coefficients with the geometry of the crater.

(iv) Correlation among the lower order coefficients as well as some combinations of coefficients with some important morphological properties of the crater and its surrounding terrain exist (average crater profile elevation, local topographic gradient, crater depth, etc.), see (Mahanti et al., 2014). This does not mean that morphological features can be directly obtained from Chebyshev coefficients, but that a set of numerical shape indicators can be related to some morphological properties, through a repeatable almost automatic process.

(v) Detection of asymmetry in the crater cross-sectional profile is possible on the basis of the analysis of odd polynomials' coefficients.

Landslide recognition using Chebyshev polynomials

In this subsection, the description of the algorithm conceived for slump landslide recognition is presented, while next section on "Application 1 along with GLD100" will demonstrate its application. The general workflow that is followed is shown in Figure 5, while in Figure 6 different steps of the analysis of a lunar crater are reported.

The approximation of each profile is accomplished by considering a cross-section extending outside the crater rims to include a small portion of outer terrain. The distance between both extremes of the profile is then normalized in the interval −1 and +1, being this the domain of Chebyshev polynomials, see Equation (1). In the case under consideration, the function to approximate is the discrete crater profile $f(x_i)$, being x the sample direction. Points along the cross-sectional profile must be regularly spaced at the same sampling resolution. Each profile can be extracted from a DEM, in this case the GLD100.

The input is given by the central geographic coordinates (latitude φ_{cc}, longitude λ_{cc}) of the crater with respect to the lunar ellipsoid (Edwards et al., 1996) and the crater cross-sectional profile. Both can be obtained from existing databases (e.g. Losiak et al., 2009), from previous studies (e.g. Brunetti et al., 2015), or simply by manual selection on a digital georeferenced map.

Using this input information, the digital surface model of the whole crater is extracted from a lunar DEM, including an outer region since the profile to extract may comprehend also a portion of external terrain. A window equal to approximately 50% of the profile outside both rims has been adopted here to extract the crater DEM from the global DEM (GLD100). This intermediate step is motivated by the fact the global DEM may also be online, thus first a portion of DEM comprehending the crater is downloaded, then four cross-sectional profiles are manually extracted at 45° relative orientation steps starting from North–South direction, see Figure 7. It has been proven that four profiles are enough for detecting a large mass wasting feature, i. e. slump, while for the purpose of more detailed analyses (e.g. determining the landslide boundaries or the volume of the deposit) higher number of cross-sectional profiles could be considered as useful. Since the slope of lunar DEM is in general quite smooth and flat, a bilinear interpolation of the four closest points is used to derive the elevation h_i of point ith in each cross-sectional profile. Along each profile, points are interpolated at regular spacing δ. The total length of the profile depends on the rim-to-rim distance and maybe uneven for different cross-sections related to the same crater. Indeed, the shape of a crater may be elongated along one direction because of the presence of a slumped wall. An extension of the profile length approximately equal to 30% of the rim-to-rim distance is adopted here. In order to tailor the extraction of cross-sectional profiles, a precise model for the crater rim shape should be applied at this stage. As an alternative, the position of the crater's rims on each profile may be manually picked up.

The Chebyshev polynomial coefficients are estimated here using a standard Least-squares approach. Following the results discussed in Mahanti et al. (2014), coefficients up to order M = 16 are enough for the characterization of the crater morphology. Details about this stage can be found in Yordanov et al. (2016), as well as reports about statistical testing to assess the quality of the interpolation.

Since the coefficient with M = 0 gives the average normalized elevation of the cross-sectional profile and the coefficient with M = 1 gives the general slope, both can be used to shift the elevation around zero mean and to flatten the profile shape. This task helps the application of the criteria for the analysis of the asymmetric component that will be introduced in the following. Indeed, the sum of polynomial members corresponding to odd coefficients represents the asymmetric component of the profile, which is supposed to be due to the presence of a slump. Indeed, in the case

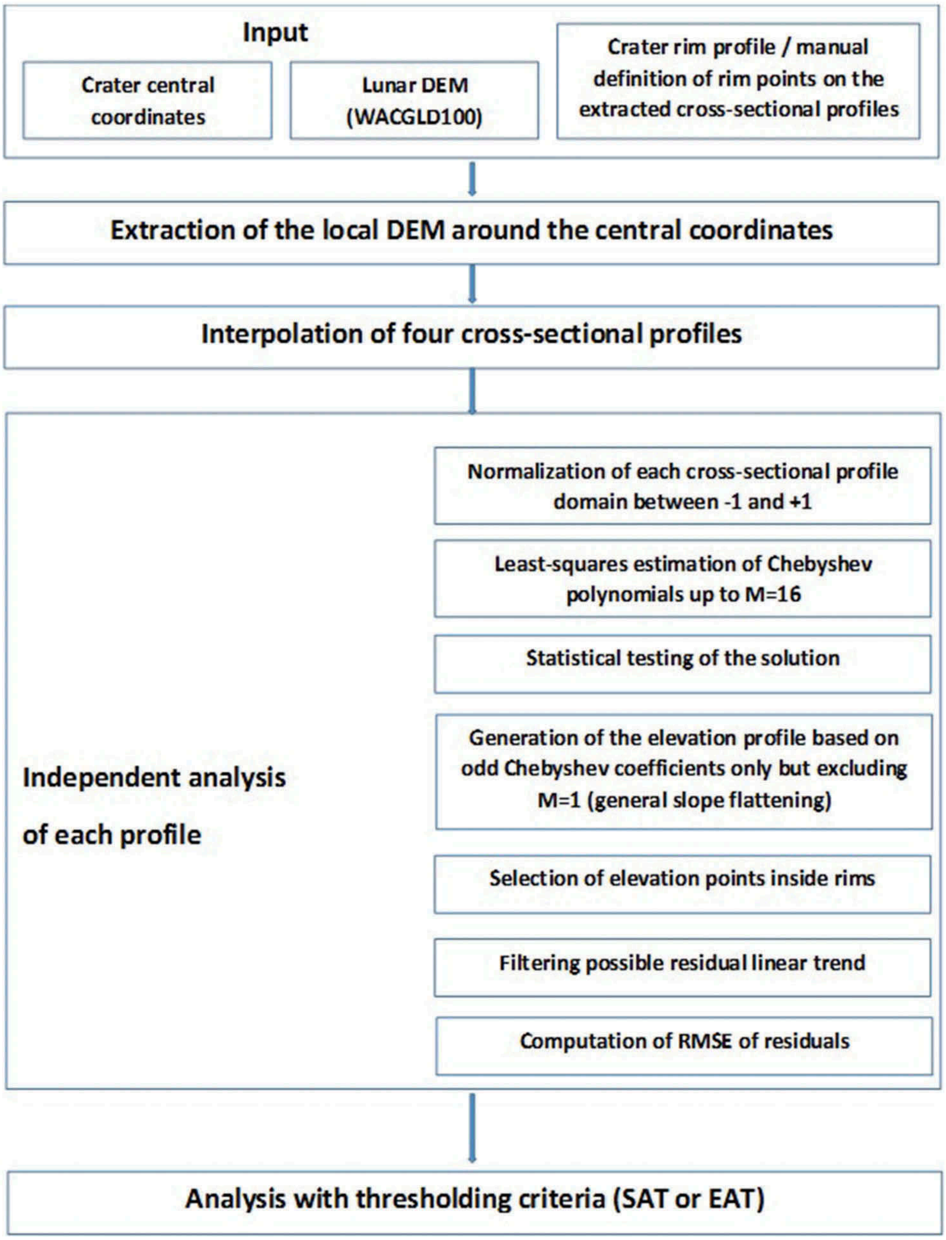

Figure 5. Workflow of the algorithm adopted to detect the presence of a slump in a cross-sectional profile of a lunar crater.

no slump has developed inside the crater, the Chebyshev approximation should mainly consist of non-zero even coefficients, while the odd coefficients should be close to zero. On the contrary, in the case a slump is present, the odd coefficients should be significantly different from zero. Testing the size or the statistical significance of the odd coefficients should theoretically be a direct way to detect symmetry. After a few experiments already reported in Yordanov et al. (2016), the analysis of odd coefficients did not provide satisfying results. This was due to the presence of noise and other local effects in the inner crater topography, which may have caused the odd coefficients to be significantly different from zero even in the case a slump was not present. As an alternative, the analysis of the odd Chebyshev coefficients' absolute size demonstrated to be a more effective way to detect the presence of a significant asymmetric component, then the possible existence of a slump. To carry out such an analysis for a given cross-sectional profile, the contribution of the odd coefficients to the interpolated elevation is computed for any points at position x_i located inside the crater ($x_{\min} < x_i < x_{\max}$, being $x_{\min}$ and $x_{\max}$ the positions of the rim edges in the profile):

$$h_i' = \sum_{M}^{n=3} C_n T_n(x)\, n = \{3, 5, 7, \ldots, M\}. \qquad (3)$$

Here the basis function corresponding to $M = 1$ is omitted since this describes the general slope to be flattened. On the other hand, successive basis functions may describe asymmetries inside the crater and thus are considered in the analysis.

Secondly, the Root Mean Square Error (RMSE) of all elevations h_i is computed for the cross-sectional profile sec:

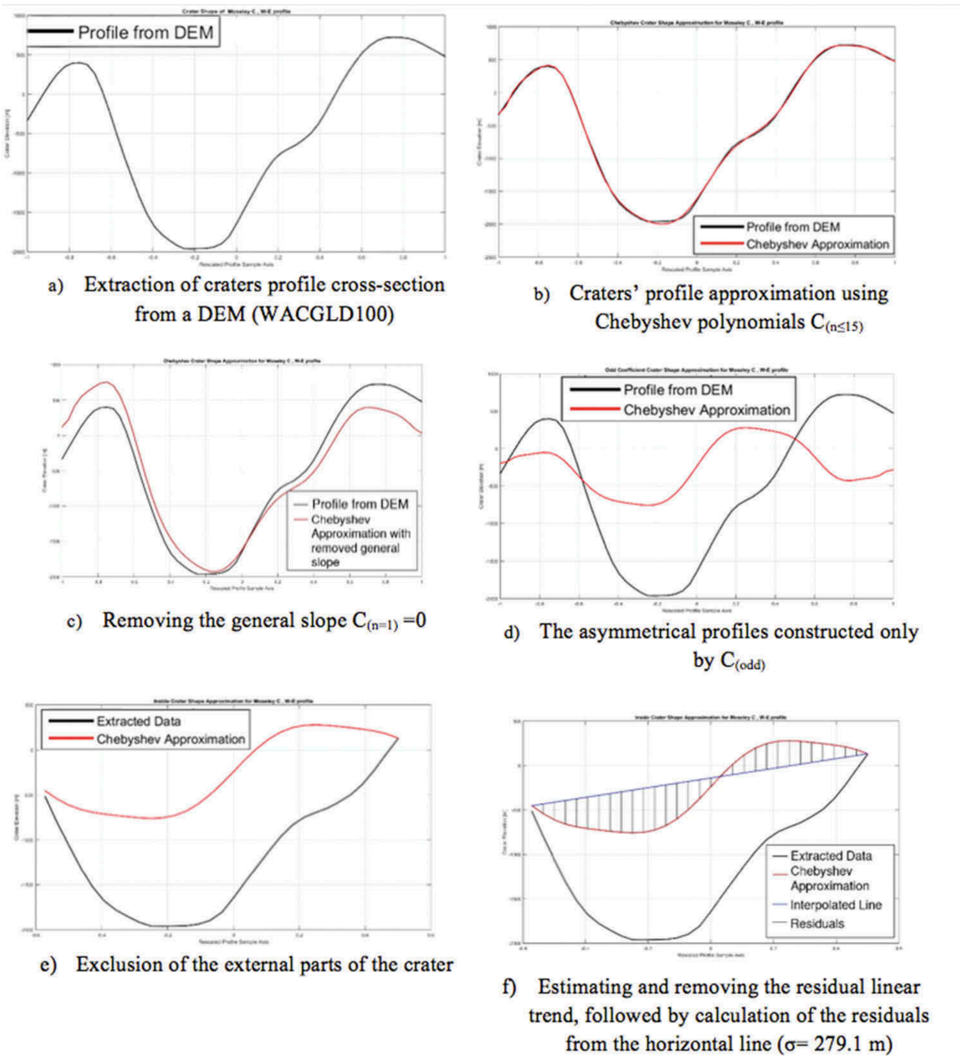

Figure 6. Application of the algorithm described in the workflow in Figure 5 to analyse a cross-sectional profile of crater Moseley C, West–East direction.

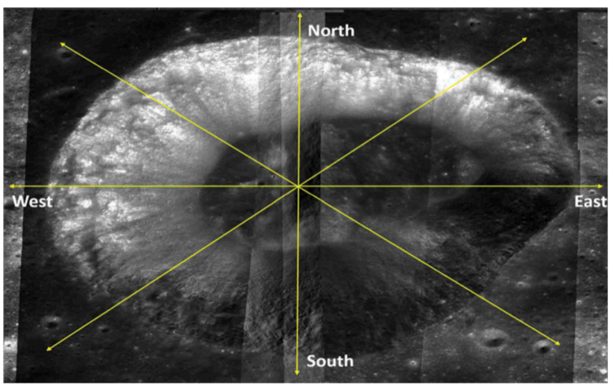

Figure 7. Example of extraction of four cross-sectional profiles to be analysed in the case of Moseley C crater (background image mosaicked from NAC LROC images).

$$\mathrm{RMSE_{sec}} = \frac{\sum_{i=1}^{n_{inn}} (\mathrm{h'}_i - \mathrm{h}_i)^2}{n_{inn}}, \quad (4)$$

where n_{inn} is the number of points located inside the rim-to-rim sector.

Since the $\mathrm{RMSE_{sec}}$ should be small in the case of the absence of a slump (see Figure 8) and large in the presence of a slump (see the last subfigure in Figure 6), the $\mathrm{RMSE_{sec}}$ is tested against a threshold established to operate the landslide recognition. Thresholds can be defined on a statistical basis or on an empirical basis, coming from the observation of cross-sectional profiles that are really affected by slumps. The selection of the threshold type is directly connected to the adopted data set. For this reason, this discussion is done in the experimental Section 'Application 1 along with GLD100'.

Since the bottom of a crater may contain a low-frequency component due to the accumulation of sediment rather than to large sudden slope failures, the presence of a regular linear trend may be detected and removed before the analysis of odd elevation h_i.

Application along with GLD100

During this study a total amount of 51 lunar impact craters (Figure 9) have been analysed to detect the presence of slumps. Among these, 31 had been already classified as affected by landslides (Brunetti

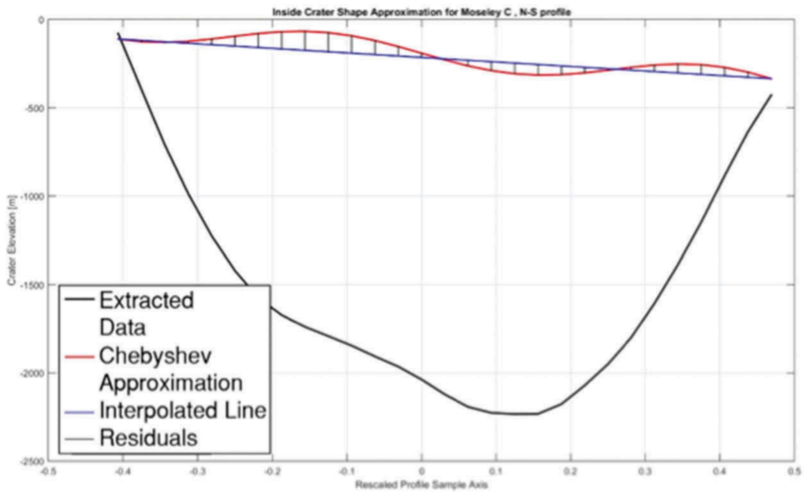

Figure 8. Residuals of the cross-sectional profile estimated on the basis of odd Chebyshev polynomials coefficients with respect to the original profile in the case of crater Moseley C, North–South direction, which does not include a slump.

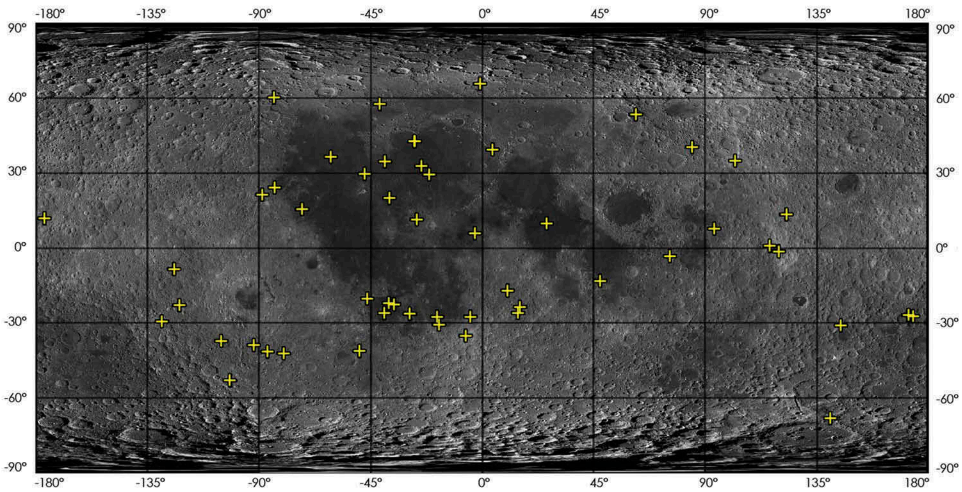

Figure 9. Location of the lunar impact craters selected to be part of the analysis for detecting inner slumps.

et al., 2015), while 20 additional craters without slumps have been investigated for the purpose of having a more consistent data set including either profiles "with landslides" and "without landslides." These last craters have been chosen on a visual-interpretation basis, and with diameter in the range between 7 and 16 km. The diameters of the 51 craters have the following dimensions: 10 craters have diameter between 7 and 10 km, 11 between 10 and 15 km, 12 between 15 and 20 km, 10 between 20 and 25 km, 5 between 25–30 km and 3 craters between 30 and 37 km. Even though, in the literature (Melosh 2011) a simple crater on the Moon is in the range up to 20 km of diameter, in this work larger craters were considered as well due to the fact they did not show those features typical of a complex crater such as central peaks or terraced walls. Nevertheless, we acknowledge that landslides mapped in larger craters could be incomplete terracing due to complex crater formation during the modification stage (Brunetti et al., 2015). The total number of extracted cross-sectional profiles including all four directions has been 204. Each cross-section has been made up of points at linear sampling distance of 200 m, given an original spatial resolution of the adopted DEM 100 m × 100 m. The reduction of resolution was decided to smoothen each section in order to mitigate local noise, and to consider that a cross-section direction may also be non-parallel with respect to the DEM grid axes.

The selection of the impact craters to analyse has been done to have a data set sharing common features:

- Simple bowl-shape crater type;
- Size of the maximum crater diameter ranging from 7 km up to 20 km, with some exception up to a diameter of 37 km but with simple bowled shape;
- Maximum slope inside the crater below 35°; and
- Almost circular shape of the crater.

Through visual recognition each cross-sectional profile has been classified as "with landslide" or "without landslide." In total, 65 cross-sections have been classified as "with landslide" and 139 "without," respectively. Using such a data set made up of both types of cross-sectional profiles, the efficiency of the algorithm to detect slumps against omission and commission errors can be evaluated.

As previously mentioned, two threshold criteria have been proposed to scrutinize the presence of slumps. Indeed, one of the aims of the test within the case study presented above has been to find which threshold would perform better. Both thresholds are designed to analyse the obtained residuals after interpolation and filtering process. In particular, the $RMSE_{sec}$ of residuals, which is expected to be close to zero in the case there is not a landslide in the crater, is analysed. The problem is to decide which is the threshold on the $RMSE_{sec}$ in each individual cross-section. A desired result was to define on one side an unique threshold value, whether adaptive or fixed, in order to be able to analyse different craters under the same conditions. On the other, to establish a numerical procedure for detecting slumps, omitting the human factor throughout the process of analysis. Of course, the presence of noise and the local topographic anomalies make this analysis more complex.

Statistical adaptive thresholding method

The statistical adaptive thresholding (SAT) criterion defines an adaptive threshold depending on each separate impact crater. Thresholding is based on the statistical analysis of all four cross-sectional profiles extracted from the same crater. The basic hypothesis is that the presence of a slump should not affect all cross-sections. Consequently, by comparing the $RMSE_{all}$ computed on all profiles with the ones computed on a single profiles ($RMSE_{sec}$), it should be possible to point out the presence of a slump. A scaling factor k has been introduced, where k ranges from 0.8 and 1.35. The condition for recognizing a landslide in an individual cross-sectional profile is that:

$$RMSE_{sec} > k \times RMSE_{all}. \tag{5}$$

Empirical absolute thresholding method

The empirical absolute thresholding (EAT) criterion defines a fix threshold disregarding, which is the impact crater under analysis. In addition, all four cross-sectional profiles are checked against the same threshold. The adopted values applied to the case study range from 100 to 170 m at 10 m steps. The proposed values range was obtained after testing a much wider spectrum (from 50 to 300 m) and due to not satisfactory results was narrowed down to one described previously.

While in the future development of this research a way to link the empirical threshold to some observable physical properties should be investigated, so far these thresholds have been simply guessed by looking at the size of residuals in the odd coefficient profiles.

Results and discussion

The process for interpolation of crater cross-sectional profiles based on Chebyshev polynomials and the successive computation of RMSE of residuals has been applied to all 51 craters belonging to the case study. The analysis of RMSE has been repeated with both types of thresholding methods and different threshold values. In this manner, all possible combinations were obtained and the achieved results were not influenced by any outer factors. Results are summarized in Table 1.

Disregarding the type of criterion applied, the selection of a higher threshold value has two opposite effects on the true detection of cross-sectional profiles "with landslide" and "without landslide". These

Table 1. Overview of the results obtained in the classification of cross-sectional profiles as "with landslide" and "without landslide," according to diverse thresholding methods and values.

		Landslides				No landslides			
		True		False		True		False	
Threshold method		Num	(%)	Num	(%)	Num	(%)	Num	(%)
SAT-adaptive	0.8 RMS	54	83.1	11	16.9	67	48.2	72	51.8
	1 RMS	52	80.0	13	20.0	83	59.7	56	40.3
	1.1 RMS	50	76.9	15	23.1	90	64.8	49	35.3
	1.15 RMS	47	72.3	18	27.7	97	69.8	42	30.2
	1.2 RMS	46	70.8	19	29.2	105	75.5	34	24.5
	1.25 RMS	43	66.2	22	33.9	106	76.3	33	23.7
	1.3 RMS	40	61.5	25	38.5	111	79.9	28	20.1
	1.35 RMS	38	58.5	27	41.5	116	83.5	23	16.6
EAT-absolute value	100	57	87.7	8	12.3	110	79.1	29	20.9
	110	55	84.6	10	15.4	116	83.5	23	16.6
	120	54	83.1	11	16.9	120	86.3	19	13.7
	130	52	80.0	13	20.0	122	87.8	17	12.2
	140	48	73.9	17	26.2	122	87.8	17	12.2
	150	46	70.8	19	29.2	127	91.4	12	8.6
	170	41	63.1	24	36.9	129	92.8	10	7.2

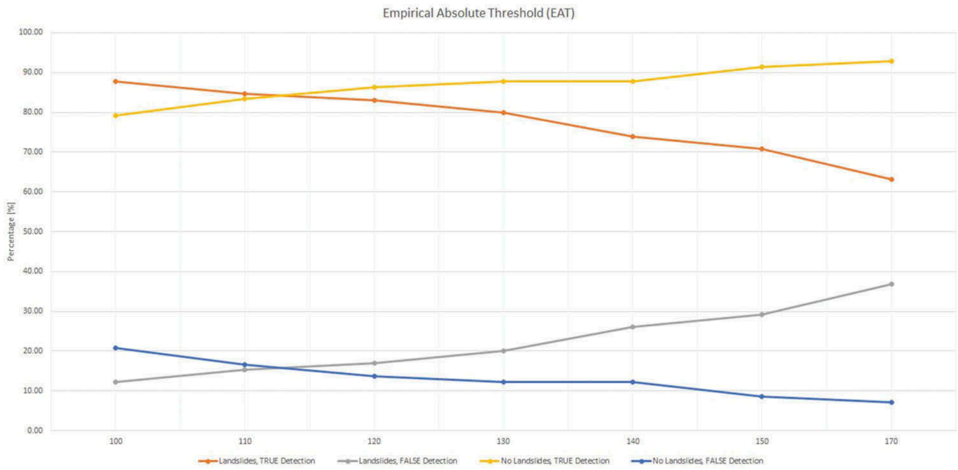

Figure 10. Plots of results in terms of true/false successful classification (%) for both cases “with landslide” and “without landslide” when the empirical absolute thresholding (EAT) is used.

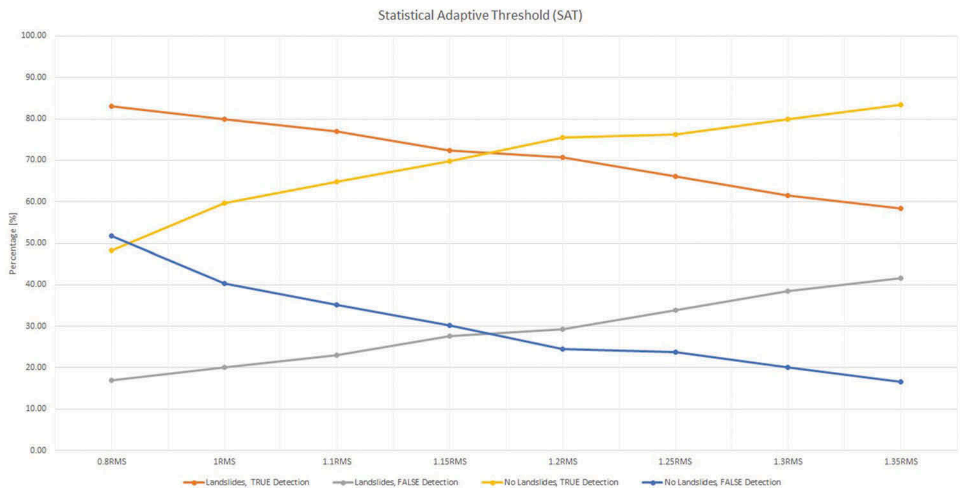

Figure 11. Plots of results in terms of true/false successful classification (%) for both cases “with landslide” and “without landslide” when the statistical adaptive thresholding (SAT) is used.

effects can be clearly seen in Figures 10 and 11. In the former case, the higher the threshold value, the lower the fraction of true classifications. In the latter case, the higher the threshold value, the higher the number of correct classifications. This result is quite logical, since the rising up of the threshold may lead to exclude from the classification as “with landslide” those cross-sectional profiles affected by smaller size slumps. The opposite effect is obtained when considering the classification of cross-sectional profiles “without landslide.” As this is what has happened about the omission errors according to the threshold values, complementary results can be observed in Figures 10 and 11 about commission errors. For instance, as far as the threshold value grows, the fraction of cross-sectional profiles “with landslide” that are not correctly classified increases. This finding means that appropriate thresholds should be applied when the objective is to seek for cross-sections affected by landslides or for profiles which are not affected.

The empirical absolute threshold criterion has offered the best performance in the classification of cross-sectional profiles “without landslide.” Here a result of 92.8% (129 over 139 profiles) has been reached when using an EAT of 170 m, while SAT has provided the best result of 83.5% (116 over 139 profiles) when using a threshold value of $k = 1.35 \cdot \mathrm{RMSE}_{\mathrm{all}}$. When seeking for cross-sections “with landslide”, the EAT has rated 87.7% (57 over 65 profiles) of true classifications when using a threshold equal to 100 m, while SAT has provided 83.1% (54 over 65 profiles) of correct classifications in correspondence of a threshold $k = 0.8$. Omission errors are of course complementary to 100% of correct classifications. In addition, by looking at plots in Figures 10 and 11, a trade-off threshold value optimizing the number of correct classifications in the case of cross-sections “with” and “without landslide” may be set up at the intersection of lines describing the behavior of true classifications (i.e., red and yellow lines, respectively). For EAT, a threshold value of

113 m would give approximately 84% of correct classifications for both cases. For SAT, a threshold value $k = 1.16$ would give approximately 72% of correct classifications.

It should be noted that these results are preliminary and further analyses and expansion of the proposed method are necessary, in order to improve them. This is also to the fact that the variety of cases is huge and some features are wrongly detected, i.e. profiles “with” landslides are recognized as ones “without” and the opposite. But investigating these cases could improve future algorithms. In Figure 12 is represented the W-E profile of the crater Drebbel, with its $RMSE_{sec}$ = 79.07 m, it was recognized as a profile “without” landslides (applied threshold EAT = 100 m). But one can clearly notice the fact that the profile is not clearly symmetric and a feature is interfering the expected bowl-shape. Addition visual analysis at the GLD100 confirmed the feature is a deposit of a collapsed western wall. But the deposit itself was not big enough to be detected by the method. On the other hand, Figure 13 represents the NW-SE profile of crater Schrodinger B, where the $RMSE_{sec}$ = 133.08 m with again EAT = 100 m is recognized as profile “with” landslide. The feature appearing at the bottom of the crater could not be related to a landslide deposit. The high RMSE value could be related to the short-length dunes (red circles) previously detected as well in other craters (e.g. Yordanov et al. (2016)). An increasing of the number of craters’ profiles extracted from the DEM could improve the results and eliminate errors similar to the above discussed. As well, it can contribute for more precise determination whether the deposit is

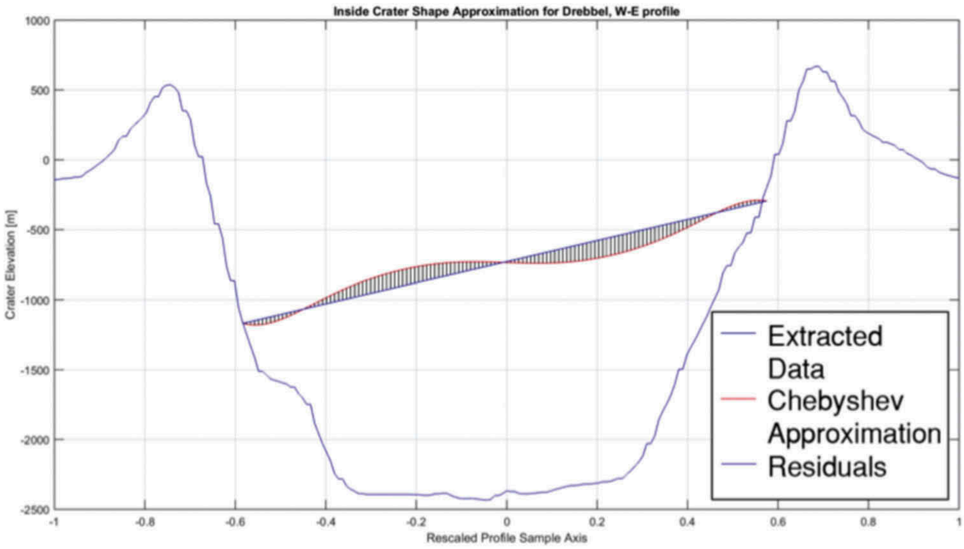

Figure 12. W-E profile of the crater Drebbel, with RMSEsec = 79.07 m and recognized by EAT = 100 m as profile “without” landslides.

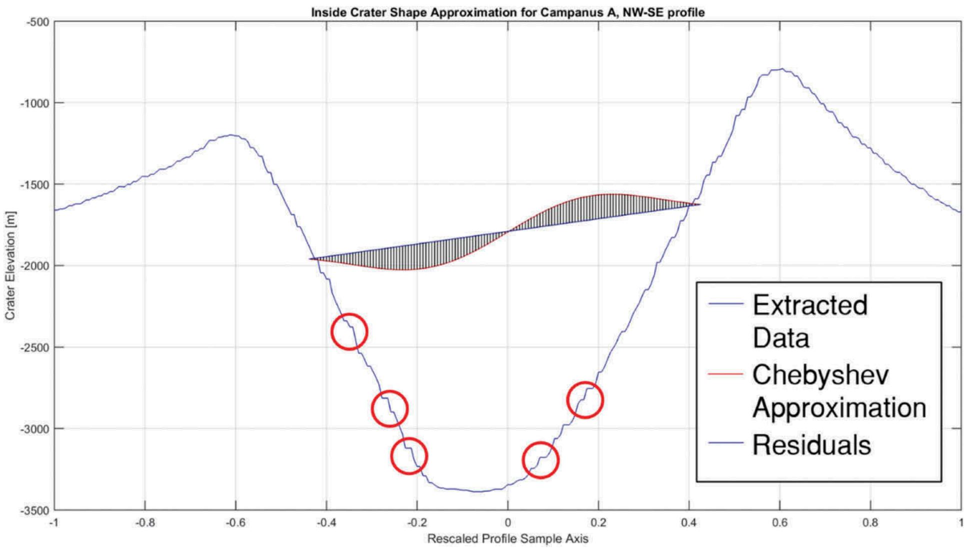

Figure 13. NW-SE profile of the crater Campanus A, with RMSEsec = 103.06m and recognized by EAT = 100 m as profile “with” landslides. The red circles are highlighting the short-length dunes.

from one or more events, to delineate the boundaries of it and even to compute the displaced mass.

Although both criteria have not output largely different results, in general the use of fixed thresholding (EAT) has demonstrated a slightly better performance. It should be also noticed that the selected impact craters share some homogenous properties (as described at the beginning of this section) and are evenly widespread on the entire surface of the Moon (see Figure 9). This leads to the conclusion that the choice of an EAT having a general validity among groups of similar craters is not a difficult task. On the other hand, the selection of a threshold value has been confirmed by using a set of pre-classified cross-sectional profiles for validation. In the development of this research it would be relevant, on one side to link the threshold values to some physical properties of cross-sectional profiles. On the other side, it would be important to extend the analysis to a wider sample of craters, in order to use a subset of pre-classified profiles to define proper thresholds to be extensively applied to non-pre-classified profiles as well. Anyway, the thresholds obtained from this study have been sufficiently proved to have a general validity, so that they will be suitable to be used in future research applications.

Conclusions and future developments

A methodology for the automatic recognition of landslides inside the impact craters on the Moon has been presented and discussed. In particular, the proposed technique works on the basis of Chebyshev polynomial approximations and it is designed for detection of slumps occurred after the meteorite impact that originated the crater. Such phenomenon generally leaves a significant modification of the crater topography, which in the most cases gives an asymmetric shape to the crater itself. The analysis of the odd components of the Chebyshev polynomials is exploited to detect the possible presence of a slump. This procedure is applied to approximate topographic cross sections extracted from four cross-sectional profiles from a global lunar DEM (GLD100).

The best performance in term of successful slump recognition has been obtained when using an empirical absolute threshold (EAT) for discriminating those cross-sectional profiles affected by landslides from others. During the analysis of a case study, 92.8% of cross-sections containing a slump have been correctly classified in almost automatic way, barring the preparation of input data and the definition of crater rims, which is still currently a manual task. Even though non-exhaustive results have been obtained, the analysis could be used as preliminary processing step to be refined afterwards. This option may be relevant to the production of a complete map of slumps in impact craters on the entire Moon or other planetary bodies.

On the other hand, in order to mitigate the number of wrong classification errors, two different actions should be undertaken. On one side, a better definition of the threshold for discriminating those cross-sectional profiles comprehending a slump should be operated. In particular, linking the EAT to some physical properties of the crater morphology and to data quality is expected to give a positive contribution. On the other side, other analyses based on complementary data sources would help make the recognition process more robust. For instance, the use of multispectral data from Chinese Chang'E-1 mission has offered some initial interesting results for the detection of spectral anomalies along the slopes of craters, which can be linked to lithological and morphological different features (Scaioni et al., 2016).

Also some improvements to rise up the level of automation of the whole procedure are needed. One of them consists in the integration of some techniques for extracting craters' rims and other geomorphological features that help the landslide recognition algorithm.

Acknowledgements

The main acknowledgements go to the Italian Space Agency and the Center of Space Exploration of China Ministry of Education which have promoted, funded and supported this project. Acknowledgements also go to all administrations of Italian and Chinese universities and research centres involved in 'Moon Mapping Project.' The authors would like to sincerely thank the Embassy of Italy in Beijing and especially the Science & Technology Counsellor (Professor Plinio Innocenzi). The authors would also thank all those colleagues who have been supporting in some way the research or the organizational activities. Finally, many thanks go to students who effectively contributed to this project.

Disclosure statement

No potential conflict of interest was reported by the authors.

Funding

This work was supported by the Italy-China Cooperation project "Moon Mapping" (Italian Space Agency – ASI), 2014-2017.

ORCID

Marco Scaioni http://orcid.org/0000-0003-4058-6176
Maria Teresa Melis http://orcid.org/0000-0003-0970-1244
Angelo Zinzi http://orcid.org/0000-0001-5263-5348
Zhizhong Kang http://orcid.org/0000-0002-9728-4702
Paolo Giommi http://orcid.org/0000-0002-2265-5003

References

Antonini, G., Ardizzone, F., Cardinali, M., Galli, M., Guzzetti, F., & Reichenbach, P. (2002). Surface deposits and landslide inventory map of the area affected by the 1997 Umbria–Marche earthquakes. *Bollettino Società Geologica Italiana*, *121*(2), 843–853.

Araki, H., Tazawa, S., Noda, H., Tsubokawa, T., Kawano, N., & Sasaki, S. (2008). Observation of the lunar topography by the laser altimeter LALT on board Japanese lunar explorer SELENE. *Advances in Space Research*, *42*, 317. doi:10.1016/j.asr.2007.05.042

Bart, G.D. (2007). Comparison of small lunar landslides and Martian gullies. *Icarus*, *187*, 417–421. doi:10.1016/j.icarus.2006.11.004

Brunetti, M.T., Guzzetti, F., Cardinali, M., Fiorucci, F., Santangelo, M., Mancinelli, P., & Borselli, L. (2014). Analysis of a new geomorphological inventory of landslides in Valles Marineris, Mars. *Earth and Planetary Science Letters*, *405*, 156–168. doi:10.1016/j.epsl.2014.08.025

Brunetti, M.T., Xiao, Z., Komatsu, G., Peruccacci, S., & Guzzetti, F. (2015). Large rockslides in impact craters on the Moon and Mercury. *Icarus*, *260*, 289–300. doi:10.1016/j.icarus.2015.07.014

Buczkowski, D.L., Schmidt, B.E., Williams, D.A., Mest, S. C., Scully, J.E.C., Ermakov, A.I., … Russell, C.T. (2016). The geomorphology of Ceres. *Science*, *353*(6303), aaf4332. doi:10.1126/science.aaf4332

Chin, G., Brylow, S., Foote, M., Garvin, J., Kasper, J., Keller, J., … Zuber, M. (2007). Lunar reconnaissance orbiter overview: The intrument suite and mission. *Space Science Review*, *129*, 391–419. doi:10.1007/s11214-007-9153-y

Cruden, D.M., & Varnes, D.J. (1996). Landslide types and processes. *Transportation Research Board, National Academy of Sciences*, *247*, 36–75.

De Blasio, F.V. (2011). Landslides in Valles Marineris (Mars): A possible role of basal lubrication by sub-surface ice. *Planetary Space Science*, *59*, 1384–1392. doi:10.1016/j.pss.2011.04.015

Edwards, K.E., Colvin, T.R., Becker, T.L., Cook, D., Davies, M.E., Duxbury, T.C., … Sorensen, T. (1996). Global digital mapping of the Moon. *27th Lunar and Planetary Science Conference (1996),* Abstract #1168.

Gautschi, W. (2004). *Orthogonal polynomials: Computation and approximation*. USA: Oxford University Press.

Jay, M.H. (2011). *Planetary surface processes* (Vol. 13). Cambridge, Cambridge University Press.

Kang, Z., Luo, Z., Hu, T., & Gamba, P. (2015, October). Automatic extraction and identification of lunar impact craters based on optical data and DEMs acquired by the Chang'E satellites. *IEEE Journal of Selected Topics in Applied Earth Observations and Remote Sensing*, *8*(10), doi:10.1109/JSTARS.2015.2481407

Krohn, K., Jaumann, R., Otto, K., Hoogenboom, T., Wagner, R., Buczkowski, D.L., … Raymond, C.A. (2014). Mass movement on Vesta at steep scarps and crater rims. *Icarus*, *244*(2014), 120–132. doi:10.1016/j.icarus.2014.03.013

Li, B., Ling, Z.C., Zhang, J., & Wu, Z.C. (2015). Automatic detection and boundary extraction of lunar craters based on LOLA DEM data. *Earth Moon and Planets*, *115*, 59–69. doi:10.1007/s11038-015-9467-9

Li, C., Liu, J., Ren, X., Zuo, W., Tan, X., Wen, W., … Ouyang, Z. (2015). The Chang'e 3 mission overview. *Space Science Reviews*, *190*, 85–101. doi:10.1007/s11214-014-0134-7

Lindsay, J. (1976). Energy at the lunar surfaces. In Z. Kopal & A.G.W. Cameron (Eds.), *Lunar stratigraphy and sedimentology*. In: Developments in Solar System and Space Science, vol.3. Amsterdam Marco: Elsevier, pp.45–55.

Losiak, A., Wilhelms, D.E., Byrne, C.J., Thaisen, K., Weider, S.Z., Kohout, T., … Kring, D.A. (2009). A new lunar impact crater database. Lunar Planet. Sci., 40, no. 1532.

Mahanti, P., Robinson, M., Humm, D., & Stopar, J. (2014). A standardized approach for quantitative characterization of impact crater topography. *Icarus*, *241*, 114–129. doi:10.1016/j.icarus.2014.06.023

Mahanti, P., Robinson, M., & Thompson, T. (2015). Characterization of lunar crater wall slumping from Chebyshev approximation of lunar crater shapes. In *Annual meeting of the Lunar Exploration Analysis Group (LEAG),* Abstract 2081. LPI Contribution No. 1863, Lunar and Planetary Institute, Houston.

Mason, J., & Handscomb, D. (2010). *Chebyshev polynomials*. FL: CRC Press Company.

Massironi, M., Marchi, S., Pajola, M., Snodgrass, C., Thomas, N., Tubiana, C., … Koschny, D. (2012). Geological map and stratigraphy of asteroid 21 Lutetia. *Planetary and Space Science*, *66*, 125–136. doi:10.1016/j.pss.2011.12.024

Mazzanti, P., De Blasio, F.V., Di Bastiano, C., & Bozzano, F. (2016). Inferring the high velocity of landslides in Valles Marineris on Mars from morphological analysis. *Earth, Planets and Space*, *68*(1). doi:10.1186/s40623-015-0369-x

Melosh, H. (1989). *Impact cratering: A geologic process.* New York: Oxford University Press.

Oberst, S.F., Matz, J., Roatsch, K.-D., Wählisch, T., Speyerer, E.J., & Robinson, M.S. (2012). GLD100: The near-global lunar 100m raster DEM from LROC WAC stereo image camera. *Journal of Geophysical Research*, (117), E00H17. doi:10.1029/2011JE003926

Pike, R.J. (1971). *Some preliminary interpretations of lunar mass-wasting processes from Apollo 10 photography. Analysis of Apollo 10 photography and visual observations* (Vols. NASA-SP-232, pp. 14–20). Washington, D. C: NASA Spec. Publ.

Quantin, C., Allemand, P., & Delacourt, C. (2004). Morphology and geometry of valles marineris landslides. *Planetary Space Science*, *52*(11), 1011–1022. doi:10.1016/j.pss.2004.07.016

Rib, H.T., & Liang, T. (1978). Recognition and identification. In R.L. Schuster & R.J. Krizek (Eds.), *Landslide analysis and control: Transportation research board special report, 176* (pp. 34–80). Washington: National Academy of Sciences.

Robinson, M.S., Brylow, S.M., Tschimmel, M., Humm, D., Lawrence, S.J., Thomas, P.C., … Hiesinger, H. (2010). Lunar Reconnaissance Orbiter Camera (LROC) instrument overview. *Space Science Reviews*, *150*(1–4), 81–124. doi:10.1007/s11214-010-9634-2

Scaioni, M., Giommi, P., Brunetti, M.T., Carli, C., Cerroni, P., Cremonese, G., … Wu, Y. (2016). The 'Moon mapping' project to promote cooperation between students of Italy and China. *Archives of the Photogrammetry, Remote Sensing and Spatial Information Sciences*, *XLI-B6*, 71–78. doi:10.5194/isprs-archives-XLI-B6-71-2016

Sentil Kumar, P., Keerthi, P., Sentil Kumar, A., & Mustard, J. (2013). Gullies and landslides on the Moon: Evidence for dry-granular flows. *Journal of Geophysical Research, Planets*, *118*, 206–223. doi:10.1002/jgre.20043

Speight, J.G. (1977). Landform pattern description from aerial photographs. *Photogrammetry*, *32*, 161–182. doi:10.1016/0031-8663(77)90012-6

Van Zuidam, R.A. (1985). *Aerial photo-interpretation in terrain analysis and geomorphologic mapping. International Institute for Aerospace Survey and Earth Sciences (ITC)* (pp. 442). The Hague: Smits Publishers.

Vijayan, S., Vani, K., & Sanjeevi, S. (2013). Crater detection, classification and contextual information extraction in lunar images using a novel algorithm. *Icarus*, *226*, 798–815. doi:10.1016/j.icarus.2013.06.028

Waltham, D., Pickering, K.T., & Bray, V.J. (2008). Particulate gravity currents on Venus. *Journal of Geophysical Research, Planets*, *113*, E2. doi:10.1029/2007JE002913

Williams, D.A., O'Brien, D.P., Schenk, P.M., Denevi, B.W., Carsenty, U., Marchi, S., … Davison, T.M. (2013). Lobate and flow-like features on asteroid Vesta. *Planetary Space Science*. doi:10.1016/j.pss.2013.06.017

Xiao, Z., & Komatsu, G. (2013). Impact craters with ejecta flows and central pits on Mercury. *Planetary and Space Science*, *82-83*, 62–78. doi:10.1016/j.pss.2013.03.015

Xiao, Z., Zeng, Z., Ding, N., & Molaro, J. (2013). Mass wasting features on the Moon–How active is the lunar surface? *Earth and Planetary Science Letters*, *376*, 1–11. doi:10.1016/j.epsl.2013.06.015

Yordanov, V., Scaioni, M., Brunetti, M.T., Melis, M.T., Zinzi, A., & Giommi, P. (2016). Mapping landslides in lunar impact craters using Chebyshev polynomials and Dem's. *International Archives of the Photogrammetry, Remote Sensing and Spatial Information Sciences*, *XLI-B6*, 17–24. doi:10.5194/isprs-archives-XLI-B6-17-2016

Zinzi, A., Capria, M.T., Palomba, E., Giommi, P., & Antonelli, L.A. (2016). MATISSE: A novel tool to access, visualize and analyse data from planetary exploration missions. *Astronomy and Computing*, *15*, 16–28. doi:10.1016/j.ascom.2016.02.006

Automatic Extraction and Identification of Lunar Impact Craters Based on Optical Data and DEMs Acquired by the Chang'E Satellites

Zhizhong Kang, Zhongfei Luo, Teng Hu, and Paolo Gamba, *Fellow, IEEE*

***Abstract*—Craters form the basis for lunar geological stratigraphy and yield significant information on terrain evolution and the history of the solar system. Thus, the recognition of lunar impact craters is an important branch of modern planetary studies. To resolve issues associated with the insufficient and inaccurate extraction of quantitative information about lunar impact craters, this study proposes an algorithm for the automatic extraction and identification of impact craters that is based on CCD stereo camera images and associated digital elevation model (DEM) data that were acquired by the Chang'E satellites. The proposed procedure works by jointly characterizing a crater candidate by means of its 2-D and 3-D features. Specifically, the novel procedure discussed in this paper selects possible crater candidates based on the extraction of geometric features from optical images and improves the final selection using 3-D features that are extracted from the DEM. Additionally, this study addresses for the first time to accurately identify different types of impact craters based on the 2-D and 3-D characteristics of the crater bottoms as well as topographic transects across the craters. The proposed approach is tested on multiple data sets that were acquired by the Chang'E satellites and provides a very high level of accuracy in both the detection and identification phases.**

***Index Terms*—Aspect, digital elevation model (DEM), impact crater, random sample consensus.**

I. Introduction

THE MOON is the closest celestial body to the Earth and has long been a focus of the scientific community. At the beginning of the Twenty-first century, leading countries and organizations in the aerospace industry initiated a new round of lunar exploration projects with the goal of returning to the moon [1]. The coverage area and data resolution of China's "Chang'E-1" and "Chang'E-2" satellites have been improved [2], and these satellites have provided reliable data for studies of the spatial differences and distributions of linear and circular structures that are associated with impact craters [3]–[7]. The "Chang'E-1" and "Chang'E-2" satellites have played a prominent role in these studies because they provide relatively fine-resolution multispectral and LIDAR data [2].

Manuscript received November 15, 2014; revised August 27, 2015; accepted September 16, 2015. Date of publication October 15, 2015; date of current version January 08, 2016.

Z. Kang, Z. Luo, and T. Hu are with the School of Land Science and Technology, China University of Geosciences, Beijing 100083, China (e-mail: zzkang@cugb.edu.cn; zfluo@cugb.edu.cn; huteng@cugb.edu.cn).

P. Gamba is with Telecommunications and Remote Sensing Laboratory, University of Pavia, Pavia 27100, Italy (e-mail: paolo.gamba@unipv.it).

Color versions of one or more of the figures in this paper are available online at http://ieeexplore.ieee.org.

Digital Object Identifier 10.1109/JSTARS.2015.2481407

Lunar exploration data have been used for a variety of purposes. Montopoli *et al.* [3], [4] performed numerical simulations to investigate the capability of a microwave radiometric sounder (MiWaRS) of the European student moon orbiter (ESMO) mission to determine the characteristics of the Moon's regolith subsurface and detect the presence of rocks and ice under the near-surface layer. Hu *et al.* [5] proposed a detailed method to compute the brightness temperature (TB) over a lunar crater, while Hu *et al.* [6] performed a crossover analysis and adjustment of Chang'E-1 laser altimeter data. Additionally, Namiki *et al.* [7] studied the far-side gravitational field of the moon using Selenological and Engineering Explorer (SELENE) data.

The complex topography and geomorphology of the moon's surface have been studied by determining the distribution and characteristics of linear and circular structures [8]–[12]. Impact craters are the most typical geomorphological unit and the most basic geomorphological features of the moon, and their morphological characteristics and spatial distribution have been examined in recent studies. Xie *et al.* [13] proposed a method for detecting craters that is based on infrequently used morphological characteristics. Leroy *et al.* [14] developed a generalized Hough transform (GHT)-based ellipse detection method for identifying asteroid impact craters. Cheng *et al.* [15] used the Conic Fitting method to automatically identify asteroid impact craters in the framework of optical navigation by spacecraft and were able to successfully identify 90% of the asteroid impact craters and reduce the misclassification rate to less than 5%. By exploiting fuzzy edge detectors and the Hough/Radon transform, Salamuniccar and Loncaric [16] proposed a crater detection algorithm to search for impact craters that are not in existing catalogues using digital topographic data. Magee *et al.* [17] proposed a cross-correlation-based template matching method and demonstrated it using test images. Burl *et al.* [18] conducted experiments with data from a lunar mare region that were acquired by the Clementine spacecraft using a continuous scalable template matching method.

The focus of all of these studies was on detecting craters as opposed to categorizing them, and no joint exploitation of 2-D and 3-D data was considered. Therefore, a novel algorithm that is aimed at the simultaneous automatic extraction and identification of impact craters using optical images from the Chang'E stereo CCD camera and a corresponding digital elevation model (DEM) is still necessary. The approach that is proposed in this work selects possible crater candidates based on geometric features that are extracted from optical images and improves the final selection using 3-D features from the DEM. Additionally, other 3-D features, including the slope and bottom of the crater and a topographic transect across each crater, are extracted and combined to identify the crater type, which is important for geological and geomorphological studies of the lunar surface.

The overall structure of the approach includes the following processing steps, which are further described and discussed in following sections.

1) A robust edge extraction operator and bilateral filtering are employed to extract the edges of impact craters from optical images. False edge points are removed by looking for geometrical consistency between the gradient direction of a candidate edge point and the light direction.
2) A RANdom SAmples Consensus (RANSAC) technique is then applied to extract the best fitting circular shape from the extracted edge points. The ratio between the number of edge points inside the impact crater and the number of theoretical edge points is used as a constraint for the RANSAC process to remove false hypotheses.
3) DEM data are analyzed to remove crater candidates that do not exhibit continuous 3-D features on the crater walls. A novel use of the variance of difference of aspects (DOA) is proposed.
4) The final extraction and identification of the selected craters is performed based on other 3-D features, such as abrupt changes of the normal vectors, point-cloud ratios of the walls and bottom, the spatial distribution of the 3-D points at the crater bottom, and the 3-D characteristics of the crater transects.

II. Preliminary Extraction of Crater Candidates From CCD Camera Images

The preliminary extraction of crater candidates is performed using images that were acquired by the CCD camera onboard the Chang'E-1/2 satellites. Because of the sun illumination, craters exhibit characteristic patterns in optical images [19] and have distinctive edge features, such as nearly round edges; the illuminated areas of impact craters are relatively bright, while the nonilluminated areas are relatively dark. The first step in this procedure is a denoising pretreatment (described in the next section). The edges of potential impact craters are then extracted. The third step is the removal of most of the nonedge points based on the gradients of the edges, and the edge points are then fitted using the RANSAC method.

A. Noise Removal and Edge Extraction

Noise patterns may exhibit similar patterns to those of real edges, and the effectiveness of the extraction of impact craters is determined by the accurate extraction of edges. To remove the effects of noise, the input data sets are denoised using a bilateral filter, which is a nonlinear, self-adaptive filter that considers both spatial information and gray similarity; it also discards

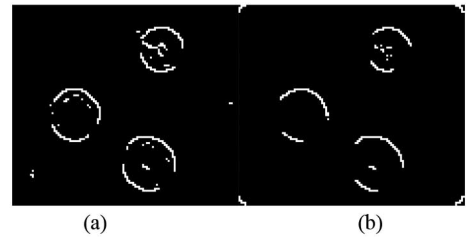

Fig. 1. Effect of noise filtering on edge extraction. (a) Results from an unfiltered image. (b) Results after noise removal.

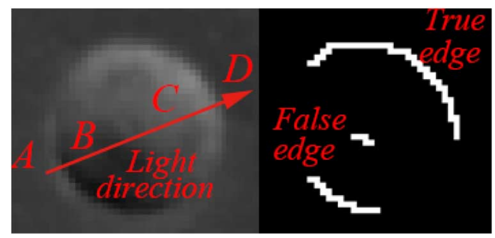

Fig. 2. Edge extraction results for a typical impact crater.

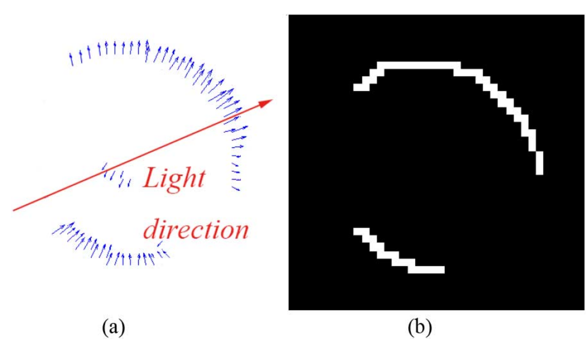

Fig. 3. Removal of nonedge points from a potential impact crater image. (a) Gradient direction of the impact crater. (b) Resulting image after the nonedge points are removed.

noise while retaining edge information [20]. Thus, bilateral filters are effective for edge extraction. Fig. 1 shows an example that uses the Robert edge extraction operator.

Edge extraction methods include the Robert, Sobel, Prewitt, and Canny operators. After noise removal and the fitting technique described below are applied, the results of these techniques are not significantly different, although the Robert operator requires the least computational work.

B. Removal of Nonedge Points

Even after the denoising procedure, a few false edges may still be extracted due to illumination effects. For example, in Fig. 2, the edges between regions A and B and between regions C and D are true edges of the crater, whereas the edges between regions B and C are false edges. False edges can be identified and removed by exploiting the direction of the light, which is computed based on the camera acquisition time and the view angle with respect to the sun's apparent position. The gray value of a true edge decreases in the direction of the light, whereas the gray value of a false edge may increase.

Specifically, if the false edges are caused by the contrast between the shadow and the illuminated regions inside the crater, the gradient of this edge will be oriented in the opposite direction to the light direction (Fig. 3). Accordingly, the absolute value of the angle between the gradient and the light direction will be greater than 90° (the value of the angle ranges from $-180°$ to $180°$). In contrast, the gradient direction for true edges is expected to be the same as that of the light direction, which in turn causes the absolute value of the angle between the two to be less than 90°. This condition is expressed in (1)

$$\nabla f \cdot n > 0 \tag{1}$$

where n represents the light direction vector, and ∇f is the gradient on the edge that is detected at $(x,\ y)$. The product in (1) is a scalar product. If the gradient direction of an edge point forms an angle that is less than 90° from the light direction, (1) is satisfied. Otherwise, the edge point is considered to be a false edge.

C. RANSAC-Based Edge Fitting

To complete the first phase of the crater candidate selection, we can exploit the fact that impact craters are nearly round; therefore, impact craters can be extracted using circle fitting. Instead of using a standard least squares method, this study uses the RANSAC approach [21] because it can be applied to fit multiple crater candidates simultaneously. The RANSAC algorithm is also more efficient because it does not use all of the edge points for the fitting. Instead, the RANSAC algorithm uses initial data that satisfy as few fitting conditions as possible and uses a consensus to expand the data set; in addition, the RANSAC algorithm fits data by searching for models.

The process of fitting impact craters using the RANSAC algorithm involves several steps.

1) First, three points are randomly selected from the edge points because three points are sufficient to make a first guess for the circle (2)

$$x^2 + y^2 + ax + by + c = 0 \tag{2}$$

where $a = -2A, b = -2B, c = A^2 + B^2 - R^2,\ (A, B)$ are the coordinates of the center of the circle, and R is the radius (units: meters).

2) The difference between the radius of the fitted circle and the distance between the extracted ith edge point and the center (d_i) is then computed as follows:

$$\Delta d_i = |d_i - R| \tag{3}$$

3) Finally, all of the points for which $\Delta d < \Delta d_{th}$, where Δd_{th} is a selected threshold value, are labeled as edge points inside the crater. The number (N) of points that satisfies $\Delta d < \Delta d_{th}$ can be used as a criterion to evaluate the hypothesis model in the original RANSAC framework. However, in the case that the data points contain multiple models, it is likely that the model that has the most inliers is a false model [Fig. 4(b)]. In the image, the number of edge points should be approximately equal to the length of the edge (in pixels). Fig. 4(b) shows that if the circle hypothesis is false, there is a low expectation that the ratio of the number of edge points inside the impact crater to the number of theoretical edge points (the perimeter L of the fitted circle) is equal to 1. This ratio is computed using (4) and can be employed as the criterion for hypothesis testing in the following processing steps. Fig. 4(c) shows that this procedure eventually selects only the correct circles

$$p = N/2\pi R \times 100\%. \tag{4}$$

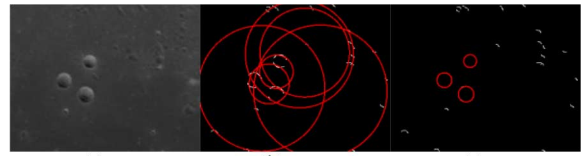

(a) (b) (c)

Fig. 4. Fitting procedure for impact crater edges. (a) Candidate craters. (b) Fitting procedure using the number of points that pass the verification procedure as a criterion. (c) Fitting procedure using the ratio of the number of the edge points inside the impact crater to the number of theoretical edge points as a criterion.

a) The hypothesis testing process is repeated until the number of sampling iterations reaches a predefined threshold, which is called T

$$T = \frac{(\log(1-p))}{\log(1-(1-\varepsilon)^n)} \tag{5}$$

where p is the confidence probability, and ε is the outlier rate, which is computed as the number of outliers in the data divided by the number of data points.

b) The circle model with the largest value of the ratio p is selected as the best model, and all inlier points that are consistent with this model are used to compute the optimal model parameters through least-squares adjustment.

c) The edge points that are inside the current impact crater are removed from the initial edge points. The procedure then restarts from the first step to fit another crater.

III. Removal of Incorrectly Extracted Impact Craters Based on the Continuity of Aspects of the Crater Walls

The extraction of impact craters from CCD camera images is primarily based on the image features of the crater. However, other structures on the moon's surface, such as valleys and faults, may result in similar 2-D geometric features. Therefore, incorrect impact crater extractions may occur when the craters are extracted solely based on images. Impact craters are ring-shaped, and each crater wall has a 360° rotational symmetry. Incorrect extraction results can be removed based on whether or not the distribution of the aspects of the impact crater wall points is continuous. First, the DEM data that correspond to a potential impact crater are extracted, and the range of the crater wall is determined. The continuity of the aspects of the crater wall points is then analyzed, and impact craters with unusual shapes are removed.

A. Determination of the Ranges of Crater Walls and Calculation of Aspects

The slope reflects the degree of inclination of a terrain. The relatively steep slopes on the inside of an impact crater range have inclinations from approximately 25° to 50°, and the gentle slopes on the outside of the craters range from approximately 3° to 8° [22]. The slope of the crater wall is steepest from the outside edge to the inside. Moreover, the cross section of a crater wall is usually symmetrical. The slopes of the impact craters can be computed using the DEM data, and the point-cloud data within the range of each crater wall are obtained by limiting the threshold values of the slope (the default range is set between 25° and 50°).

The slopes and aspects are then computed [23]. The slope (S) and aspect (A) of a point on the surface are functions of the rates of change of the elevation of the terrain surface function $Z = f(x, y)$ (unit: meters) in the east–west and south–north directions

$$\begin{cases} S = \arctan\sqrt{f_x^2 + f_y^2} \\ A = 270^\circ - \arctan\frac{f_y}{f_x} + 90^\circ\frac{f_x}{|f_x|} \end{cases} \tag{6}$$

where f_x represents the rate of change of the elevation in the east–west direction, and f_y represents the rate of change of the elevation in the south–north direction. The slope is computed using the second-order difference in the horizontal and vertical directions. Only points with slopes in the range 25°–50° are extracted.

B. Analysis of the Continuity of the Aspects of the Crater Walls

Fig. 5(a) and (b) shows an impact crater and a simulated nonimpact structure, respectively. Most impact craters are ring-shaped, so the values of the aspects of the crater wall points are continuously distributed within the range 0°–360°. The red line in Fig. 5(c) shows a continuous distribution of the aspect values of the crater wall points, although the numbers of points with similar aspect values clearly varies. The blue line in Fig. 5(c) shows that a nonimpact crater lacks wall points with aspect values from 20° to 150°. However, it is difficult to evaluate the continuity of the distribution of aspect values that is illustrated in Fig. 5(c).

To address this issue, the aspects of the crater wall points are sorted within the range 0°–360°, and the differences between the adjacent values of the sorted aspects (DOAs) are computed. Statistical calculations are then performed on the DOA values. Fig. 5(d) shows that the DOA distribution of an impact crater is concentrated approximately 0°, while the DOA distribution of the nonimpact structure has a peak at 146°, which makes it clearly recognizable.

To statistically characterize the DOA distribution, its standard deviation σ is computed. The DOA σ values for the impact and nonimpact crater walls in Fig. 5 are equal to 0.20 and 37.67, respectively, which illustrates the use of the DOA variance as a criterion to discriminate between the two crater types.

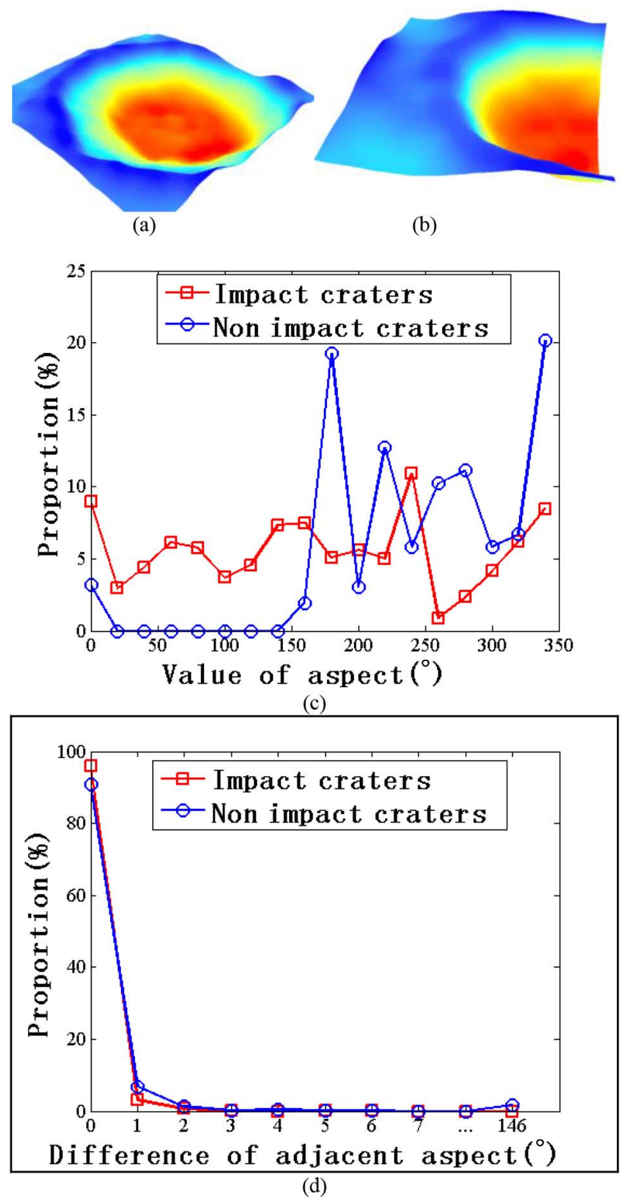

Fig. 5. Significant differences in the aspects of adjacent points in impact craters and nonimpact craters. (a) Impact crater. (b) Nonimpact crater. (c) Histogram of the distributions of the aspects of an impact crater and a nonimpact crater. (d) Histogram of the DOA of an impact crater and a nonimpact crater.

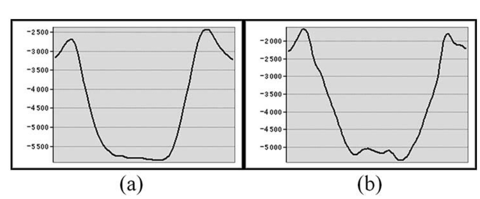

Fig. 6. Topographic transects across complex craters. (a) Transect across a flat-bottomed type complex impact crater. (b) Transect across a central uplift type complex impact crater.

TABLE I
CLASSIFICATION OF IMPACT CRATERS

Types	Characteristics	Crater examples
Simple bowl-shaped craters	A simple bowl-shaped crater has a bowl-shaped structure with a diameter that is generally less than or equal to 20 km. Simple bowl-shaped craters are generally formed in regions with thick lunar soil and have smooth inner walls and stable slopes. A simple bowl-shaped crater has a relatively small bottom area and a relatively large depth-diameter ratio.	
Complex impact craters (central uplift type)	The difference between the structure of a central uplift complex impact crater and the structure of a simple crater starts approximately 7.5 km from the center. Central uplift craters generally have diameters greater than 35 km. A central uplift crater has a relatively large bottom area and contains an uplifted region in the center of the crater, which is slightly lower than the crater wall.	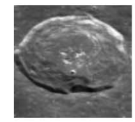
Complex impact craters (flat-bottomed type)	The difference between the structure of a flat-bottomed type complex impact crater and the structure of a simple crater starts approximately 7.5 km from its center. A flat-bottomed crater has a relatively large bottom area.	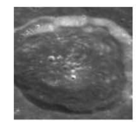
Monocyclic or polycyclic impact craters	A polycyclic impact crater has multiple well-developed ring structures. Collapse phenomena are clearly discernible on the walls of polycyclic impact craters, which have complicated and variable structures. Polycyclic impact craters generally have diameters of 175-450 km but can be larger.	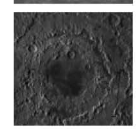

IV. CALCULATION OF THE PARAMETERS OF IMPACT CRATERS AND IDENTIFICATION OF TYPES OF IMPACT CRATERS

A. *Calculation of Parameters*

In contrast to image data, DEM data can be used to illustrate the 3-D topographic structure of an impact crater; thus, DEM data are suitable for studies of the extraction of quantitative information about impact craters as well as studies of the identification of impact craters. The normal vectors of the edge points of an impact crater change abruptly compared with those of the wall points, so the edge points can be extracted by calculating the rates of change of the normal vectors. Impact craters have round edges, and the edge points were fitted using the least squares method to calculate the basic parameters of the impact crater.

1) Calculation of the Normal Vectors of Points: When the value of N (the number of neighboring points) and a point p_i are given, the approximate tangent plane of point p_i can be obtained through its neighboring point sets q_j $(1 \leq j \leq N)$. The covariance matrix $\mathbf{c}$ was computed using the neighboring points (7). The normal vector is the unitized eigenvector that corresponds to the least eigenvalue of the covariance matrix c, which was determined by the principal component analysis (PCA) algorithm [24]

$$c = \sum\nolimits_{j=1}^{N} (x_j - x_i)^T (x_j - x_i) \tag{7}$$

where $\mathbf{x}_i$ represents the coordinates of the point p_i, and $\mathbf{x}_j$ denotes the coordinates of the neighboring point of p_i.

2) Extraction and Fitting of Edge Points Based on Abrupt Changes of the Normal Vectors: The rate of change of a normal vector (k) can be expressed as

$$\begin{cases} k = \sqrt{d_x^2 + d_y^2} \\ d_x = \arccos(c_6 \cdot c_4) \\ d_y = \arccos(c_8 \cdot c_2) \end{cases} \tag{8}$$

where d_x represents the rate of change of the normal vector in the east–west direction, d_y represents the rate of change of the normal vector in the south–north direction, and c represents the unit normal vector, with c_6 and c_4 representing the neighboring points in the west–east direction and c_8 and c_2 representing the neighboring points in the north–south direction. The key to calculating k is in the calculation of d_x and d_y; similar to calculating the slopes, d_x and d_y were also solved within a local range.

The distribution of angles between the normal vectors of the crater wall points and the horizontal plane was concentrated, and the angles between the normal vectors of the edge points and that of the horizontal plane are mostly concentrated approximately 90°. The difference between 90° and the mean angle between the point-cloud normal vector of the crater wall and the surface can be used as the threshold value of the rate of change of the normal vector. The rate of change of the normal vector of an edge point should satisfy the following condition

$$k \leq |\pi/2 - \theta_0| \tag{9}$$

where θ_0 is the threshold value that represents the difference between 90° and the mean angle between the point-cloud normal vector of the crater wall and the surface. The edge points are extracted and fitted using the least squares method. The circle equation is shown in (2). After solving for a, b, and c, the parameters of the circle can also be solved. We solve the

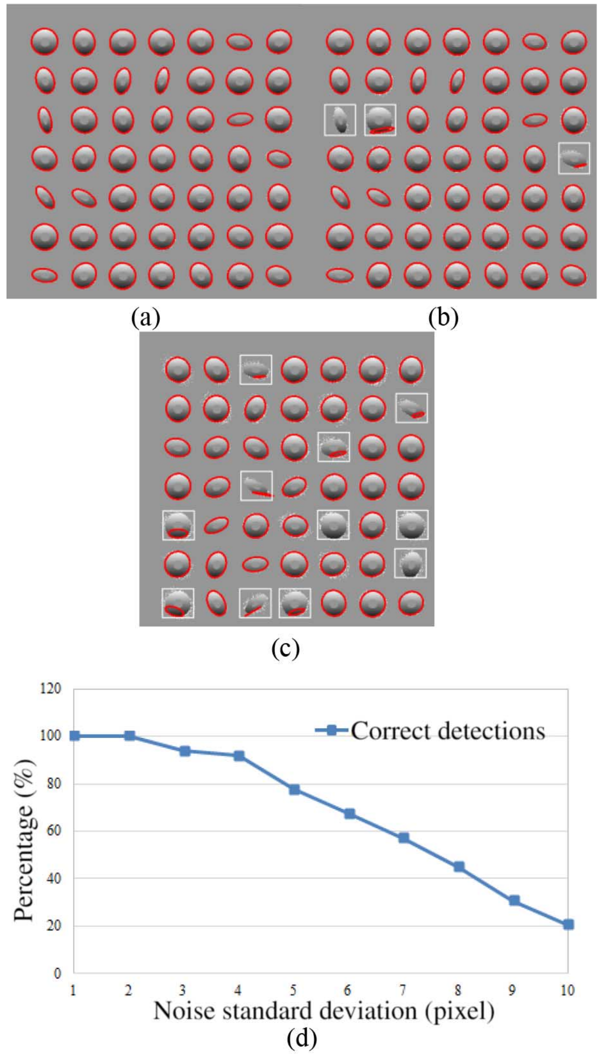

Fig. 7. Extraction of impact craters from simulated images with different noise standard deviation. (a) 2 pixels. (b) 3 pixels. (c) 6 pixels. (d) Histogram of correct detections with increasing noise standard deviation.

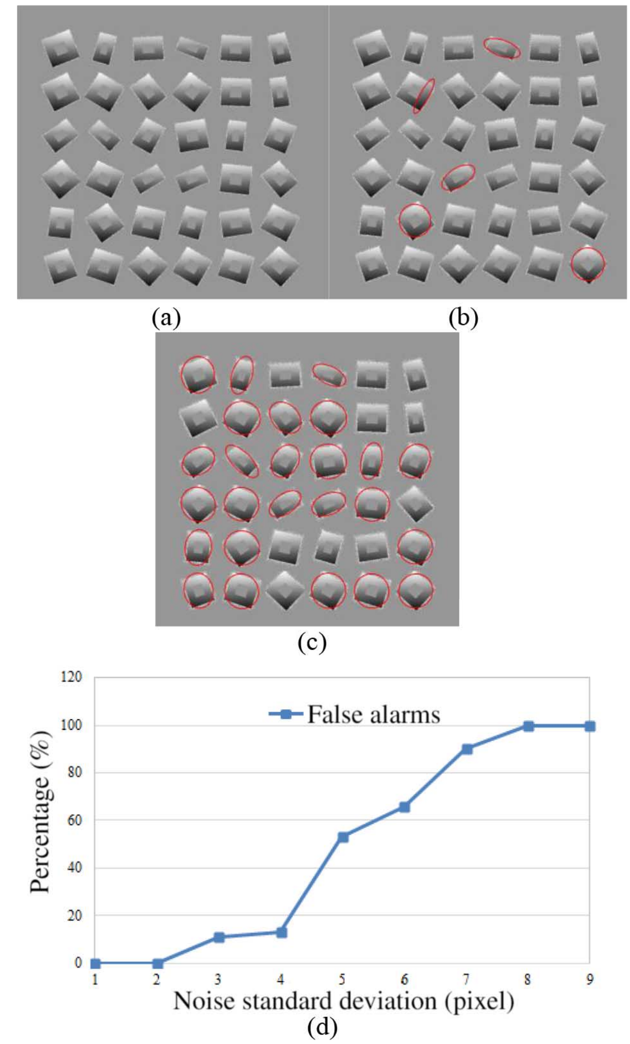

Fig. 8. False alarms of noncraters from simulated images with different noise standard deviation. (a) 2 pixels. (b) 3 pixels. (c) 6 pixels. (d) Histogram of false alarms with increasing noise standard deviation.

following equation:

$$\begin{bmatrix} a \\ b \\ c \end{bmatrix} = \left(\begin{bmatrix} x_1 & y_1 & 1 \\ \vdots & \vdots & \vdots \\ x_n & y_n & 1 \end{bmatrix}^T \begin{bmatrix} x_1 & y_1 & 1 \\ \vdots & \vdots & \vdots \\ x_n & y_n & 1 \end{bmatrix} \right)^{-1} \begin{bmatrix} x_1 & y_1 & 1 \\ \vdots & \vdots & \vdots \\ x_n & y_n & 1 \end{bmatrix}^T \begin{bmatrix} -x_1^2 - y_1^2 \\ \vdots \\ -x_n^2 - y_n^2 \end{bmatrix} \quad (10)$$

where $(x,\ y)$ represents the coordinates of the edge point X, Y.

B. Identification of the Types of Impact Craters Based on Their Section Lines

Impact craters are generally classified into three major types: simple bowl-shaped impact craters, complex impact craters (including central uplift craters, and flat-bottomed complex impact craters) and monocyclic or polycyclic impact craters (Table I). Crater types can be identified based on the areas of the crater bottoms as well as several features of topographic transect across the crater. Because monocyclic or polycyclic impact basins have extremely complicated structures, this study classified impact craters into "simple" and "complex" types (including central uplift and flat-bottomed complex impact crater types).

The ratio of the area of the bottom of a complex impact crater to its total area is larger than that of a simple impact crater; the area of the bottom of a complex impact crater accounts for more than 20% of its total area, whereas the area of the bottom of a simple impact crater is less than 20% of its total area. To compute the areas of an impact crater and its bottom, we generate a triangulated irregular network (TIN) for each point segment and sum the areas of the triangles.

The two types of complex impact craters (flat-bottomed and central uplift) can be identified based on features of their topographic transects (Fig. 6). A transect across a flat-bottomed impact crater has two peaks that are generally located at the two ends, whereas a transect across a central uplift impact crater generally has at least three peaks. The type of complex impact crater can be determined based on the number and locations of the peaks on its transect.

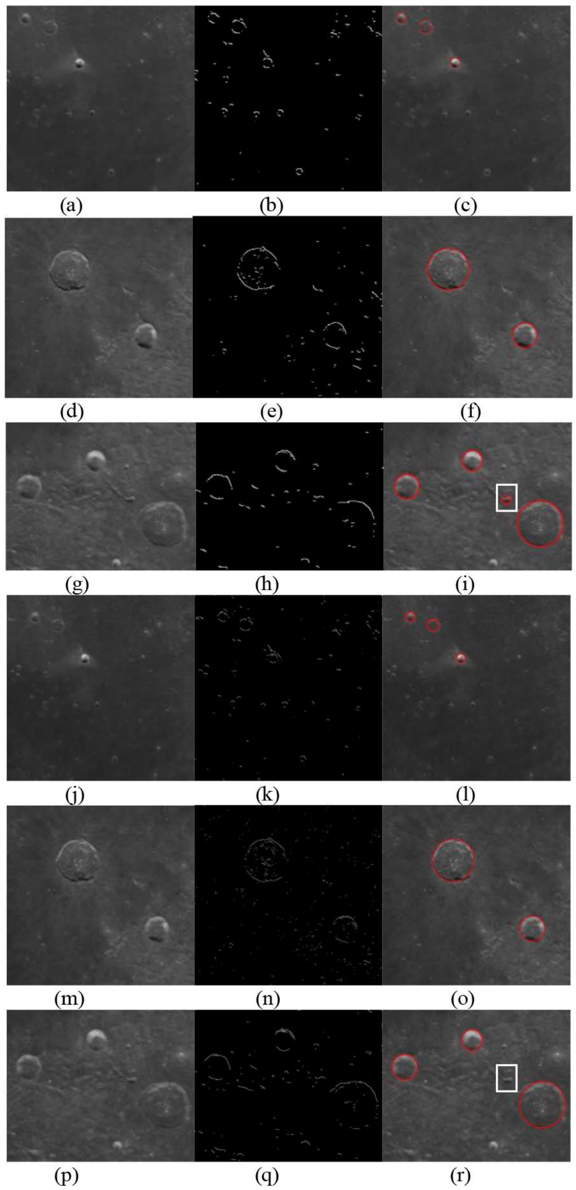

Fig. 9. Extraction of impact craters from six real optical images (see the text). (a) Experimental image 1. (b) Edge extraction of image 1. (c) Extraction results of image 1. (d) Experimental image 2. (e) Edge extraction of image 2. (f) Extraction result of image 2. (g) Experimental image 3. (h) Edge extraction of image 3. (i) Extraction result of image 3. (j) Experimental image 4. (k) Edge extraction of image 4. (l) Extraction result of image 4. (m) Experimental image 5. (n) Edge extraction of image 5. (o) Extraction result of image 5. (p) Experimental image 6. (q) Edge extraction of image 6. (r) Extraction result of image 6.

V. Experimental Results

The proposed approach was tested on both synthetic and real data sets. The real data set comprises six images and DEM data obtained from the Chinese lunar exploration project acquired by the Chang'E-1 and Chang'E-2 satellites. The images were acquired by a three-line array CCD stereo camera in a push-broom fashion. The orbit height of Chang'E-1 was 200-km above the lunar surface, so the swath width was 60 km, and the spatial resolution was 120 m. The orbit height of Chang'E-2 was 100-km above the lunar surface; accordingly,

TABLE II
Crater Extraction Results

Image sources	Chang'E-1			Chang'E-2		
Optical data set no.	1	2	3	4	5	6
Manual extraction	3	2	3	3	2	3
Automatic extraction	3	2	4	3	2	3
False extraction	0	0	1	0	0	0

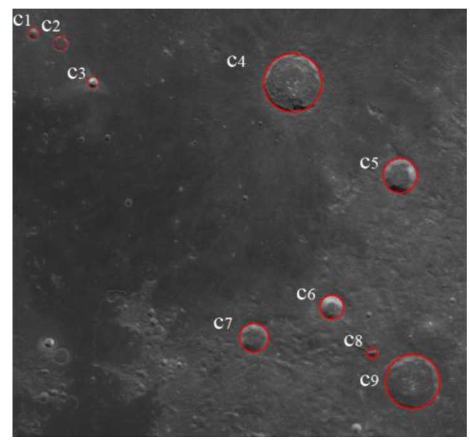

Fig. 10. Extraction of craters from a Chang'E-1 optical image.

the swath width was 43 km, and the spatial resolution was 7 m. The DEM was generated automatically from the images that were acquired by the image array of the forward view, backward view, and nadir view of the Chang'E-1 CCD stereo camera using the three-line array photogrammetric method. The DEM has horizontal and vertical accuracies of 192 and 120 m, respectively, and a spatial resolution of 500 m (website: http://moon.bao.ac.cn/ceweb/datasrv/dmsce1.jsp).

To investigate the dependence of the proposed algorithm on the DEM resolution, DEM data with lower spatial resolutions (i.e., 1000 and 1500 m) were downsampled from the 500-m resolution data. Moreover, 1800 elliptical impact craters [partially illustrated in Fig. 7(a–c)] were simulated with random eccentricities (0–1 in steps of 0.1), orientations (0°–180° in steps of 1°), and sizes (radii from 20 to 25 pixels) to verify the proposed image-based extraction method for impact craters. One thousand noncraters [rectangle; partially illustrated in Fig. 8(a)–(c)] were also simulated with orientations (0°– 180° in steps of 1°), and sizes (radii from 20 to 25 pixels). Noise with different variances (0–10 pixels) was also added to the edge points of the simulated impact craters and noncraters.

A. *Results of the Extraction of Simulated Impact Craters*

The percentage of correct detections and false alarms for the simulated craters and noncraters was statistically analyzed as a function of the noise standard deviation Fig. 7(a), (b), (c) shows the extraction of the simulated craters with noise standard deviation of 2, 3, and 6 pixels, respectively. The correct detections

TABLE III
STATISTICAL DOAs OF CRATERS EXTRACTED FROM THE CHANG'E-1 DATA SET SHOWN IN FIG. 10

Crater ID	Standard deviation σ (°)			Crater? (Yes/no)
	500 m	1000 m	1500 m	
c1	2.20	5.20	8.78	Yes
c2	11.08	11.74	11.80	No
c3	2.41	4.01	7.47	Yes
c4	0.21	0.52	0.74	Yes
c5	0.64	1.44	2.34	Yes
c6	1.07	2.78	4.96	Yes
c7	0.71	1.92	2.94	Yes
c8	20.83	20.51	16.52	No
c9	0.51	0.70	1.20	Yes

TABLE IV
PARAMETERS AND TYPES OF CRATERS EXTRACTED FROM THE DATA SET SHOWN IN FIG. 10 (500-M RESOLUTION DEM)

Impact crater images (c1-c9 except c2 and c8)	Coordinates of the centers (m)	Radii (m)	Point cloud ratios of the crater bottoms (%)	Transects	Types
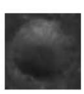	(−96 607, 151 948)	4227	1.45	—	Simple impact crater
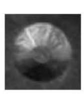	(−55 471, 117 937)	3524	1.48	—	Simple impact crater
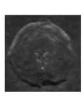	(81 850, 117 524)	21 353	51.20		Complex crater (central uplift type)
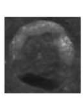	(155 705, 54 015)	11 697	57.06		Complex crater (flat-bottomed type)
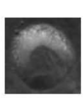	(108 342, −36 875)	8199	6.81	—	Simple impact crater
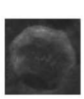	(54 699, −57 566)	10 048	26.27	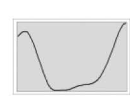	Complex crater (flat-bottomed type)
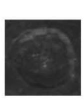	(163 900, −88 601)	17 361	78.51	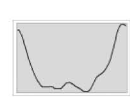	Complex crater (central uplift)

were determined in terms of the differences between the simulated and computed parameters of elliptical impact craters, i.e., the major axis, minor axis, center, and orientation. The corresponding thresholds were kept fixed to 3 pixels for all differences/distances, and 10° for the orientation difference. As expected, the percentage of correct detections decreases as the noise standard deviation increases [Fig. 7(d)]. Assuming 80% as the minimum value for a successful extraction, the graph shows that the maximum noise standard deviation manageable by the proposed approach is 5 pixels.

The RANSAC framework was implemented to fit elliptical impact craters from the edge points of simulated noncraters.

TABLE V
PARAMETERS AND TYPES OF EXPERIMENTAL CRATERS (1000-M RESOLUTION DEM)

Impact crater images (c1-c9 except c2 and c8)	Coordinates of the centers (m)	Radii (m)	Point cloud ratios of the crater bottoms (%)	Transects	Types
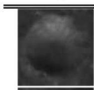	—	—	—	—	—
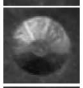	—	—	—	—	—
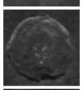	(82 752, 117 712)	20 305	50.40		Complex crater (central uplift type)
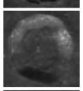	(155 695, 54 729)	10 650	47.46		Complex crater (flat-bottomed type)
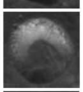	(108 233, −36 534)	7597	4.02	—	Simple impact crater
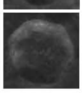	(53 640, −56 951)	8615	25.80	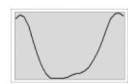	Complex crater (flat-bottomed type)
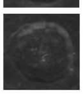	(161 987, −88 503)	17 861	66.12		Complex crater (central uplift)

The hypothesis models passed the verification process proposed in Section II-C were identified as false alarms. The percentage of false alarms increases with the increase of noise standard deviation [Fig. 8(d)]. Assuming 20% as the maximum value for false alarms, the graph shows that the maximum standard deviation is 4 pixels. Figs. 7(a) and 8(a) also show that when the noise standard deviation was set as a reasonable value, i.e., 2 pixels, the percentages of correct detections and false alarms are, respectively, 100% and 0%, which demonstrates that the eccentricity and orientation have negligible impacts on the detection.

B. Results of the Extraction of Impact Craters from Chang'E Optical Images

Finally, impact craters were automatically extracted from the six optical images described above. Three images were acquired by the Chang'E-1 satellite [Fig. 9(a), (d), (g)], and three were acquired by the Chang'E-2 satellite [Fig. 9(j), (m), (p)] in the same areas as the images that were acquired by the Chang'E-1 satellite. These six images covered areas between 32 °W and 59 °W latitude and 41 °N and 55 °S longitude. Each of the six images underwent filtering, edge extraction, and fitting using the RANSAC method. Because the resolution of the DEM data was lower than that of the images, the size of successfully extracted and identified craters is dependent on the resolution of the DEM data. The spatial resolution of the DEM data that were employed was 500 m; thus, only impact craters with radii of more than 4 km were extracted. Fig. 9 shows the results of extracting the impact craters from the images.

Table II shows the extraction results of the experimental images. "Manual extraction" refers to impact craters that were obtained by visual identification, "automatic extraction" refers to impact craters that were obtained using the algorithm, and "false-extraction" refers to nonimpact craters that were extracted by the algorithm. The results show that all of automatically extracted craters in the Chang'E-2 images are consistent with those from the manual extraction. However, in the Chang'E-1 images, the automatically extracted crater that is highlighted by the white rectangle in Fig. 9(i) is inconsistent with the manual extraction results. The difference between the performance of the proposed algorithm on the Chang'E-1 images (120 m resolution) and the Chang'E-2 images (7 m resolution) indicates that a higher image resolution can improve the robustness of the extraction of impact craters.

C. Removal of Incorrectly Extracted Impact Craters

To better explain the effects of jointly using 2-D and 3-D data, Fig. 10 considers the nine impact craters that were extracted from a Chang'E-1 data set. The craters are numbered from left to right and from top to bottom (c1–c9).

To exploit 3-D data, the point-cloud data of the impact craters are extracted from the corresponding DEM data at different resolutions (i.e., 500, 1000, and 1500 m). We then extract points on the impact crater walls with slope angles between 25° and 50°. The aspects of the crater wall points are then sorted, and the differences between the adjacent values of the sorted aspects are calculated. As presented in Section III-B, the standard deviation σ of the DOA of each crater is computed (Table III). The results show that the standard deviations of the DOAs of craters c2 and c8 that were computed using the 500-m resolution DEM data were significantly larger than those of the other craters, so the two craters are identified as incorrectly extracted craters. Table III also indicates that the standard deviation σ increases as the DEM resolution decreases. As a result, the standard deviation of the DOA of crater c2 that was computed using the 1500-m resolution DEM data becomes less abnormal, which in turn shows that a lower DEM resolution may degrade the robustness of the identification of incorrectly extracted craters.

TABLE VI
PARAMETERS AND TYPES OF EXPERIMENTAL CRATERS (1500-M RESOLUTION DEM)

Impact crater images (c1-c9 except c2 and c8)	Coordinates of the centers (m)	Radii (m)	Point cloud ratios of the crater bottoms (%)	Transects	Types
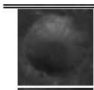	—	—	—	—	—
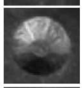	—	—	—	—	—
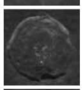	(82 462, 119 282)	20 835	51.20	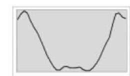	Complex crater (central uplift type)
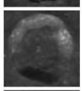	(155 488, 54 988)	11 183	50.41	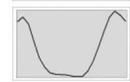	Complex crater (flat-bottomed type)
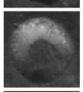	(108 038, −36 040)	6985	7.02	—	Simple impact crater
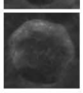	(54 223, −57 153)	8862	26.70		Complex crater (flat-bottomed type)
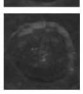	(163 443, −88 692)	15 032	70.22		Complex crater (central uplift)

Compared with the results presented in Section V-B, impact crater c8 is identified as an incorrectly extracted impact crater, which is consistent with the manual identification. However, the identification of impact crater c2 as a false crater is inconsistent with the manual image identification results. A detailed analysis of the distribution of the DOAs that were computed using the corresponding DEM data shows that impact crater c2 is a false impact crater and that the visual identification of this crater was erroneous. These results highlight the usefulness of DEM data for impact crater identification.

D. Calculation of the Parameters of Impact Craters and Identification of the Type of Impact Crater

To classify the impact craters, the DEM data of the seven identified impact craters are used to extract the rates of change of the normal vectors and the crater edge points. Finally, the ratios of the impact crater bottoms with respect to all of the points within the radius of the crater can be computed. If an impact crater is classified as a "complex" type, the morphological characteristics of its topographic transect are used to determine whether it is a flat-bottomed impact crater or a central uplift impact crater.

Tables IV, V and VI show the results for different DEM resolutions. Because of their small sizes, the parameters of craters c1 and c3 were not calculated for the coarse DEMs. The results show that the impact crater types that were identified using the 500-m resolution DEM are consistent with those that were identified using the 1000-m resolution and 1500-m resolution DEMs. As a result, impact craters c3, c5, c9, and c10 are classified as complex craters. Because crater c9 has two relatively clear peaks in its transect and contains a significantly uplifted region at the bottom, it is further classified as a central uplift impact crater.

VI. CONCLUSION

This study introduces an automatic algorithm that uses optical data sets and associated DEM data to improve the detection of lunar impact craters and provides the first automatic classification of lunar impact craters. Data sets that were acquired by the Chang'E-1 and Chang'E-2 satellites were used to validate the algorithms.

The experimental results show that the joint use of 2-D and 3-D data is resolution dependent; the results from the Chang'E-2 images were better than the results from the Chang'E-1 images. The results also indicate that the proposed standard variance of the DOA is an excellent 3-D quantitative index that can be used to extract impact craters.

The main limitation of this study is that it primarily identifies "simple" and "complex" impact craters. Future research will thus focus on performing the extraction and identification of monocyclic or polycyclic basins and other geological structures. Moreover, because the amplitude of the brightness temperature that is observed by a passive radiometer depends on the slope angle [10], we plan to use this additional information to further improve the extraction and identification of lunar craters.

REFERENCES

[1] Z. Ouyang and C. Li, "The progress and the development strategy of deep space exploration in our country," *Chin. Aerosp.*, no. 12, pp. 28–32, 2002.

[2] C. Li *et al.*, "The image data processing of Chang'E-1 and the image mapping to the Moon," *Chin. Sci. D*, no. 3, pp. 294–306, 2010.

[3] M. Montopoli, A. Di Carlofelice, P. Tognolatti, and F. S. Marzano, "Remote sensing of the Moon's sub-surface with multi-frequency microwave radiometers: A numerical study," *Radio Sci.*, vol. 46, p. RS1012, 2011.

[4] M. Montopoli, A. Di Carlofelice, M. Cicchinelli, P. Tognolatti, and F. S. Marzano, "Lunar microwave brightness temperature: Model interpretation and inversion of spaceborne multi-frequency observations by a neural network approach," *IEEE Trans. Geosci. Remote Sens.*, vol. 49, no. 9, pp. 3350–3358, Sep. 2011.

[5] G. Hu *et al.*, "Brightness temperature calculation of lunar crater: Interpretation of topographic effect on microwave data from Chang'E," *IEEE Trans. Geosci. Remote Sens.*, vol. 52, no. 8, pp. 4499–4510, Aug. 2014, doi:10.1109/TGRS.2013.2282342.

[6] W. Hu *et al.*, "Crossover analysis and adjustment for Chang'E-1 laser altimeter data," *Acta Geod. Cartographica Sin.*, vol. 42, no. 2, pp. 218–224, 2013.

[7] N. Namiki *et al.*, "Far side gravity field of the moon from four-way Doppler measurements of SELENE (Kaguya)," *Science*, vol. 323, no. 5916, pp. 900–905, 2009.

[8] S. Chen *et al.*, "The mapping to geological analysis by lunar satellite remote sensing in rainbow ray area," *Chin. Sci. Phys. Mech. Astron.*, vol. 40, no. 11, pp. 1370–1379, 2010.

[9] N. L. Chabot, G. V. Hoppa, and R. G. Strom, "Analysis of lunar lineaments: Far side and polar mapping," *Icarus*, vol. 147, no. 1, pp. 301–308, 2000.

[10] T. Morota and M. Furumoto, "Asymmetrical distribution of rayed craters on the Moon," *Earth Planet. Sci. Lett.*, vol. 206, no. 3, pp. 315–323, 2003.

[11] E. R. Urbach and T. F. Stepinski, "Automatic detection of sub-km craters in high resolution planetary images," *Planet. Space Sci.*, vol. 57, no. 7, pp. 880–887, 2009.

[12] B. Hawke *et al.*, "The origin of lunar crater rays," *Icarus*, vol. 170, no. 1, pp. 1–16, 2004.

[13] Y. Xie *et al.*, "Crater detection using the morphological characteristics of Chang'E-1 digital elevation models," *IEEE Geosci. Remote Sens. Lett.*, vol. 10, no. 4, pp. 885–889, Jul. 2013.

[14] B. Leroy *et al.*, "Crater detection for autonomous landing on asteroids," *Image Vis. Comput.*, vol. 19, no. 11, pp. 787–792, 2001.

[15] Y. Cheng *et al.*, "Optical landmark detection for spacecraft navigation," *Adv. Astronaut. Sci.*, vol. 114, pp. 1785–1803, 2003.

[16] G. Salamuniccar and S. Loncaric, "Method for crater detection from Martian digital topography data using gradient value/orientation, morphometry, vote analysis, slip tuning, and calibration," *IEEE Trans. Geosci. Remote Sens.*, vol. 48, no. 5, pp. 2317–2329, May 2010.

[17] M. Magee *et al.*, "Automated identification of Martian craters using image processing," in *Proc. Lunar Planet. Inst. Sci. Conf. Abstr.*, 2003, vol. 34, pp. 17–21.

[18] M. C. Burl *et al.*, "Automated detection of craters and other geological features," in *Proc. 6th Int. Symp. Artif. Intell. Robot. Autom. Space*, 2001, pp. 1–8.

[19] L. Jin *et al.*, "Characteristics of lunar craters on the first image of Chang'E-1 satellite," *J. Jilin Univ.*, vol. 39, no. 5, pp. 942–946, 2009.

[20] C. Tomasi and R. Manduchi, "Bilateral filtering for gray and color images," in *Proc. IEEE 6th Int. Conf. Comput. Vis.*, 1998, pp. 839–846.

[21] M. A. Fischler and R. C. Bolles, "Random sample consensus: A paradigm for model fitting with applications to image analysis and automated cartography," *Commun. ACM*, vol. 24, no. 6, pp. 381–395, 1981.

[22] K. Li *et al.*, "Research on dating of the mare basalts based on the automatic identification of impact craters in the northern region of mare imbrium on the Moon (LQ-4)," *Earth Sci. Front.*, vol. 19, no. 6, pp. 47–59, 2012.

[23] L. W. Martz *et al.*, "An outlet breaching algorithm for the treatment of closed depressions in a raster DEM," *Comput. Geosci.*, vol. 25, no. 7, pp. 835–844, 1999.

[24] C. Lange and K. Polthier, "Anisotropic smoothing of point sets," *Comput. Aided Geom. Des.*, vol. 22, no 7, pp. 680–692, 2005.

Zhizhong Kang received the Ph.D. degree in photogrammetry and remote sensing from Wuhan University, China, in 2004.

From 2006 to 2008, he worked as a Postdoctoral Researcher with Delft University of Technology, Delft, The Netherlands. Currently, he is an Associate Professor and the Head with the Department of Remote Sensing and Geo-Information Engineering, China University of Geosciences, Beijing, China. He has authored more than 60 referred journal and conference publications. His research interests include digital photogrammetry and computer vision including vehicle-based image sequence processing, processing of laser scanning data, and lunar structure recognition and extraction.

Dr. Kang has served as Regional Coordinator for Asia of ISPRS WG V/3 and Member of Committee on Photogrammetry and Remote Sensing, Chinese Society for Geodesy Photogrammetry and Cartography. He was the recipient of Natural Science Foundation of China (NSFC) Grants in 2009, 2012, and 2015, and also the recipient of 2015 ERDAS Award for Best Scientific Paper in Remote Sensing by ASPRS, for the paper "Z. Kang, F. Jia, L. Zhang, A robust image matching method based on optimized BaySAC, *Photogrammetric Engineering & Remote Sensing*, vol. 80, no. 11, pp. 1041–1052, 2014."

Zhongfei Luo was born in Guangyuan, Sichuan Province, China, in 1992. He received the B.S. degree in surveying and mapping engineering from the China University of Geosciences, Beijing, China, in 2013. Currently, he is pursuing the M.S. degree in photogrammetry and remote sensing at the same university.

Since 2013, he has been engaged in the research of structure extraction from the moon. His research interests include the remote sensing image processing, the segmentation of point cloud data, image matching, and 3-D reconstruction.

Teng Hu received the Ph.D. degree in cartography and geographical information engineering from Wuhan University, Wuhan, China, in 2013.

Currently, he is a Lecturer of Remote Sensing and Geo-Information Engineering, China University of Geosciences, Beijing, China. His research interests include digital photogrammetry and computer vision including processing of UAV data, stereo matching, and lunar structure recognition and extraction.

Paolo Gamba (SM'00–F'13) received the Laurea degree in electronic engineering "*cum laude*" from the University of Pavia, Pavia, Italy, in 1989, and the Ph.D. degree in electronic engineering from the same university, in 1993.

He is an Associate Professor of Telecommunications with the University of Pavia, where he also leads the Telecommunications and Remote Sensing Laboratory. He has authored more than 110 papers in international peer-review journals and presented more than 250 research works in workshops and conferences.

Dr. Gamba has served as Editor-in-Chief of the IEEE GEOSCIENCE AND REMOTE SENSING LETTERS, from 2009 to 2013, and from October 2005 to May 2009, he has served as a Chair of the Data Fusion Committee of the IEEE Geoscience and Remote Sensing Society. Currently, he is the Chair of the Chapters' Committee of the same society. Since 2001, he has been the Organizer and Technical Chair of the biennial GRSS/ISPRS Joint Workshops on "Remote Sensing and Data Fusion over Urban Areas." He also served as Technical Cochair of the 2010 IEEE Geoscience and Remote Sensing Symposium, Honolulu, Hawaii, July 2010, and Technical Cochair of the 2015 IEEE Geoscience and Remote Sensing Symposium, Milan, Italy. He has been the Guest Editor of special issues of the IEEE TRANSACTIONS ON GEOSCIENCE AND REMOTE SENSING, the IEEE JOURNAL OF SELECTED TOPICS IN REMOTE SENSING APPLICATIONS, *ISPRS Journal of Photogrammetry and Remote Sensing*, *International Journal of Information Fusion*, and *Pattern Recognition Letters* on the topics of urban remote sensing, remote sensing for disaster management, pattern recognition in remote sensing applications. He has been invited to give keynote lectures and tutorials in several occasions about urban remote sensing, data fusion, and EO data and risk management.

COMPARATIVE STUDY OF LUNAR ROUGHNESS FROM MULTI - SOURCE DATA

Y. Lou, Z. Kang

School of Land Science and Technology, China University of Geosciences(Beijing), 29 Xueyuan Road, Haidian District, Beijing 100083, China - aileenlou@163.com

KEY WORDS: Lunar, roughness, Root-mean-square Height, Morphological Surface Roughness, DEM, DOM

ABSTRACT:

The lunar terrain can show its collision and volcanic history. The lunar surface roughness can give a deep indication of the effects of lunar surface magma, sedimentation and uplift. This paper aims to get different information from the roughness through different data sources. Besides introducing the classical Root-mean-square height method and Morphological Surface Roughness (MSR) algorithm, this paper takes the area of the Jurassic mountain uplift in the Sinus Iridum and the Plato Crater area as experimental areas. And then make the comparison and contrast of the lunar roughness derived from LRO's DEM and CE-2 DOM. The experimental results show that the roughness obtained by the traditional roughness calculation method reflect the ups and downs of the topography, while the results obtained by morphological surface roughness algorithm show the smoothness of the lunar surface. So, we can first use the surface fluctuation situation derived from RMSH to select the landing area range which ensures the lands are gentle. Then the morphological results determine whether the landing area is suitable for the detector walking and observing. The results obtained at two different scales provide a more complete evaluation system for selecting the landing site of the lunar probe.

1. INTRODUCTION

Because of long time in the lunar geologic age, the moon is relatively cold, rigid and complete. And the surface has not been affected by plate movement, atmosphere, water or life, so the moon keeps the geological record for nearly 4 billion years (Jolliff B L,2006). The surface roughness is the ruggedness in the meaning of topography. In a certain research scope, it refers to a mathematical expression of the surface fluctuation condition at an analysis scale. Meantime it can reflect the rolling extent of surface. The roughness records the geologic activities such as erosion, sedimentation, accumulation and filling of the planets. And it is one of the important parameters to evaluate the safety of ground engineering. At the same time, it can also provide an important reference for finding a soft landing field of the surveyed spacecraft in the appropriate terrain (Shepard M K,2001). As a result of the sun weathered, the migration of moon shell by the internal stress, and ups and downs on the surface of the moon by the external impact, the trances generated on the lunar surface is the roughness. So it is possible to analyse the evolution history, the internal stress and the external impact of the lunar according to the roughness.

For the calculation of the lunar surface roughness, Michael K. Shepard proposes Root-mean-square height, Root-mean-square deviation, Root-mean-square slope, Autocorrelation length, Median and absolute slope and some other methods (Shepard M K,2001). Many domestic and foreign scholars also use the Hurst index as a measurement of the lunar roughness (Orosei, R et al,2003). These above methods are suitable for data with terrain elevation values. For grayscale binary images, in recent years Cao, et al. proposes a morphological algorithm to calculate the lunar roughness (W. Cao et al,2014). The roughness of three specific lunar surface highlands has been studied, and the result shows the roughness plays an important role in studying the material composition of the lunar surface and the geological age of different stratigraphic units (Yokota Y et al.2008). The roughness of Mare Imbrium proves that there is a correlation between the lunar roughness and the lithology of the geological units (Yan Yanzi et al, 2014). The surface roughness of each parameter in the horizontal section of Sinus Iridum has been calculated, and the geomorphological features of the area are interpreted (Xi Xiaoxun et al, 2012). Few people use multi-source data to compare and analyse the old and new methods to searching new information.

In this paper, we selected the tail of Montes Jura in the eastern of Sinus Iridum and the Crater Plato as the study areas. Based on the Digital Elevation Model of LRO and the Digital Orthophoto Map of Chang'e II, the roughness is calculated respectively by Root-mean-square height and Morphological Surface Roughness algorithm. Then we compare the two different results to obtain the characteristics and application scope of the two roughness algorithms. It can be more conducive to select the appropriate landing point for the lunar probe in the future.

2. DATA AND METHOD

2.1 Research area

In this paper, Sinus Iridum and Crater Plato the two large craters, which are created by "Heavy Bombardment" in Mare Imbrium, are selected as the experimental areas. The whole area is filled with mare basalt after the heavy impact.

Sinus Iridum is an important bay in the northwest of Mare Imbrium with a central latitude and longitude of N44 °6 ', W 31°30 ', a diameter of 259 km and a bottom area of 47750.927 km^2. The northwest of Sinus Iridum is surrounded by the Montes Jura and is adjacent to the craters of crater Bianchini and crater Maupertuis (Chen Shenbo, et al,2010). And it is the landing point for CE-3 satellite. This paper focuses on the tail of the southeast of Montes Jura which is covered by various topography, such as plains, mountains and impact craters. This area is mainly covered by ridges. And some sporadic small ejecta are also scattered. So the various geometric roughness features can be comprehensive analysed.

Crater Plato is a large pit located between the north of Mare Imbrium and Mare Frigoris, and its west is Montes Jura and Sinus Iridum (John W M G, 1972). The center position is about N51 ° 6 ', W9 ° 5'. (USGS, 2008). The crater is an irregularly polygonal, with a diameter of about 106 km and an average crater depth of

1.8 km. It is now widely believed that the Crater Plato is generated after Mare Imbrium event, and the crater age is about 3.84Ga. The bottom of crater is full of basal.

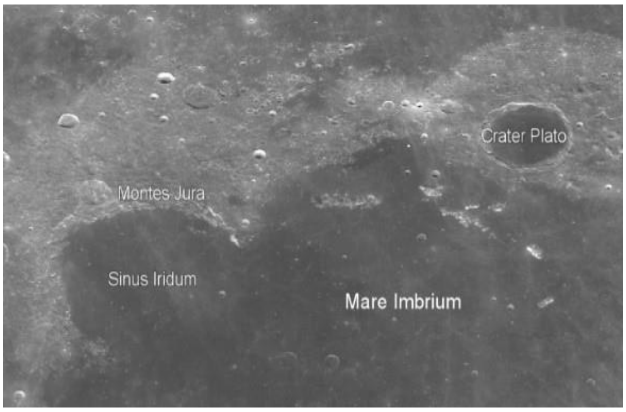

Figure 1. DOM of the experimental area

2.2 Roughness calculation Based on DEM

2.2.1 Data

The data used in this study is DEM whose accuracy is 30 m from LRO (Lunar Reconnaissance Orbiter). LRO is the first mission of the National Aeronautical and Space Pioneer Robot Program, which was implemented on June 18, 2009. LOLA is the laser altimeter of the six scientific instruments（Smith, D.et al,2010a; Smith, D.et al,2010b）. LOLA has 5 beams, with a nominal accuracy of 10 cm. It can be used to characterize the micro-geomorphic features on the lunar surface and select the future landing point for robots and human beings (Rosenburg et al, 2011). Using the global elevation data obtained by the sensor, lunar surface DEM is produced. The three-dimensional rendering images of the experimental area DEM as shown below.

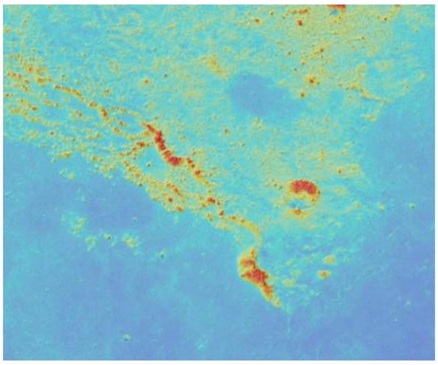

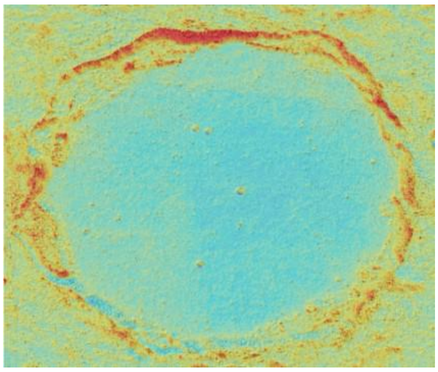

Figure 2. DEM Height rendering images of the tail of Montes Jura southeast (up) and Crater Plato (down)

2.2.2 Root-mean-square height

Shepard et al. have proposed several parameters for quantifying the planet's surface roughness. These parameters are usually defined on the basis of elevation data. The relatively commonly used and simple ones are the Root-mean-square height and Root-mean-square deviation. The Root-mean-square height shows the extent of the surface height deviating from the average height, which is expressed in the vertical direction. While the Root-mean-square deviation shows the change in the horizontal height which uses the structural function. The meaning of the two method is more or less the same, so this paper selects the Root-mean-square height for roughness calculation.

In general, a best fit linear function is subtracted from the DEM data. Through simplifying, a series of height values with the zero average are gotten. Expressed as

$$\xi = \left[\frac{1}{n-1}\sum_{i=1}^{n}(z(x_i)-\bar{z})^2\right]^{1/2} \tag{1}$$

where n is the number of sample points
$z(x_i)$ is the height of the point x_i in the lunar surface
$\bar{z}$ is the average of all elevation

In this paper, the raster image is read line by line to sample. And the 3*3 window is used to calculate the whole DEM data. The average value of all the pixels in the window is calculated. Then the formula (1) is used to calculate the Root-mean-square height value of the central pixel to replace its original value.

2.2.3 Results

The roughness based on the two experimental DEM regions is calculated by the Root-mean-square height, and the results are shown in Fig.3. It can be seen that the result derived from the traditional method expresses the extent of the terrain ups and downs. The lunar roughness shows the dichotomy characteristic. That is, the lunar mare roughness is low, while roughness of the highland is high. The higher values of roughness are mainly distributed at the edge of the craters, which own the changeable terrain. While the lower roughness is mainly distributed in plains, because the terrain is gentle and the terrestrial changes are small.

The roughness both in the ridges and the fissures is high in the Montes Jura region. The mountain area is not all covered by the high roughness, there are also some gentle areas that own low roughness among the mountains. The roughness of Crater Plato indicates that there is a clear boundary between the bottom area and the edge. And the boundary between the ejecta and the edge is also clear. The bottom, the wall, the edge and the ejecta can be clearly distinguished by using the roughness image. And it can be seen that some sporadic small impact craters exist at the bottom with a large rough value.

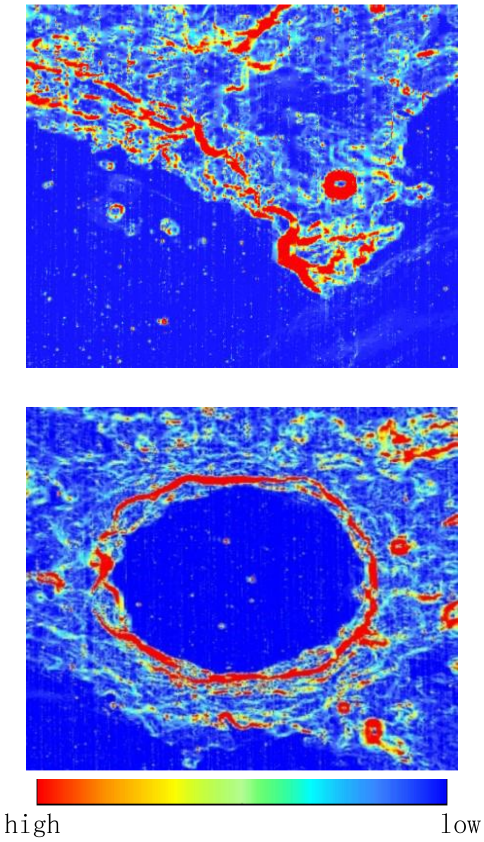

Figure 3. RMSH results images of the tail of Montes Jura southeast (up) and Crater Plato (down)

2.3 Roughness calculation Based on DOM

2.3.1 Data

CE-2 satellite successfully launched on October 1, 2010. Besides six goals had been successful completed, a number of important scientific data had gotten until April 1, 2011. CE-2 loads 5 categories of scientific detection equipment: CCD stereo camera, laser altimeter, γ / X-ray spectrometer, microwave detectors and space environment detector. During the half year flighting around the moon, the CCD stereo camera takes photos of the global surface to obtain the lunar digital orthophoto map with a spatial resolution of 7 m (Ye J et al. 2013). The CE-2 DOM of the two experimental areas are shown as Figure 4.

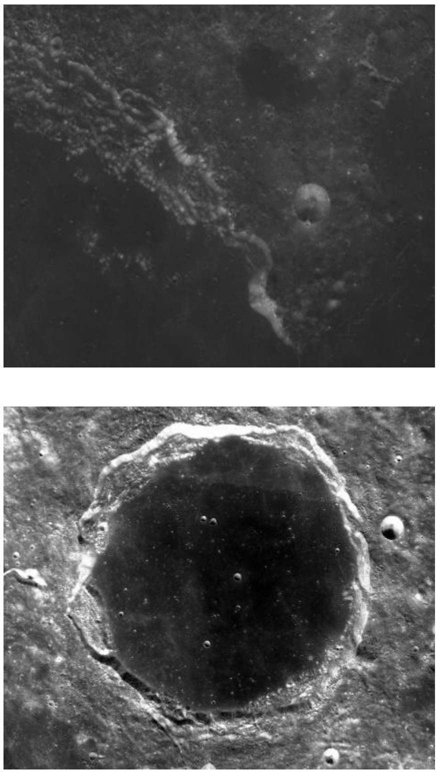

Figure 4. CE-2 DOM of the tail of Montes Jura southeast (up) and Crater Plato (down)

2.3.2 Morphological Surface Roughness

In this paper, we use the Morphological Surface Roughness proposed by W. Cao to deal with the DOM of CE-2. Unlike traditional roughness calculations based on ground elevation values, the algorithm utilizes grey-scale images. The surface roughness of the grey-scale images is defined as the difference between Morphological Closing operator and Morphological Opening operator. And it is usually constructed by the highest and lowest points of the structuring element's (SE) shape (P. Soille, 2013; W.Gonzalez and RE Woods, 2013). As an important theory of geological applications, Solide puts forward two common morphological operators: morphological opening and morphological closing (P. Soille, 2013). MO operator removes the redundant structures created by erosion. The MO function γ is defined as follows:

$$[\gamma_B(f)](x) = \delta_B[\varepsilon_B(f)] \tag{2}$$

MC solves the problem of dilation by implementing erosion in the dilated surface.MC function $\emptyset$ is defined as

$$[\emptyset_B(f)](x) = \varepsilon_B[\delta_B(f)] \tag{3}$$

Where
$$[\varepsilon_B(f)](x) = \min_{b \in B} f(x+b) \tag{4}$$

$$[\delta_B(f)](x) = \max_{b \in B} f(x+b) \tag{5}$$

Using the two operations two types of roughness forms can be produced. MO operation extracts the convex area while MC represents roughness characteristics by the concave distribution. The difference between the two surfaces is defined as the terrain surface roughness, the formula is as follows:

$$R_{MSR} = \emptyset_B(f) - \gamma_B(f) \tag{6}$$

2.3.3 Results

The roughness results obtained by using the MSR algorithm are shown as figure 5. We can know that the roughness obtained by MSR is described on a smaller scale, which is not related much to the overall fluctuation of the area. It is a description of the roughness in a small range. Except a crater shows high roughness, the roughness value of Montes Jura other regions is low. This area is in a steady condition. In spite of that, the roughness difference between mountains and plains can also be clearly distinguished. However, the roughness at the bottom of the crater with light fluctuation is high, and the ejecta around the crater has the high roughness. There are also some unusual low roughness points in the region, the following part will describe the reason in detail.

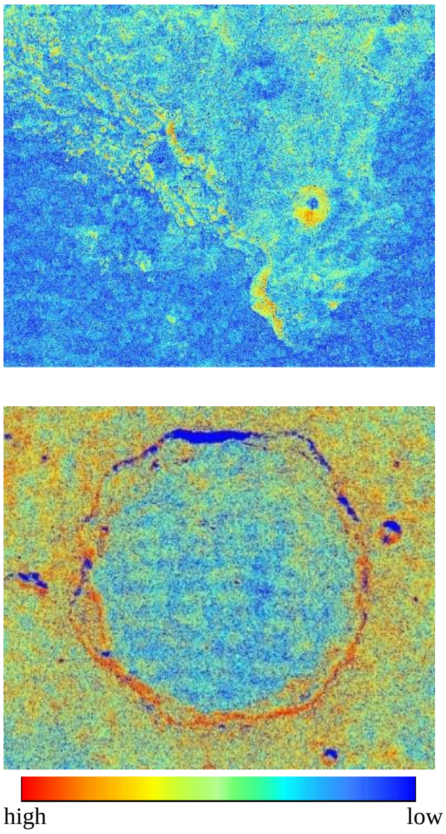

Figure 5. Results by using MSR of the tail of Montes Jura southeast (up) and Crater Plato (down)

3. RESULTS AND DISCUSSION

3.1 Montes Jura

The distribution of Montes Jura and every ridge can be clearly observed on the RMSH image. The roughness values of the mountain area are high, especially in the areas which the elevation of ridge is jumped. However, it is not obvious found on the MSR image. Compared with the lunar mare, the roughness of the mountain area is high, but the extent of roughness is not a lot. Because the morphological algorithm eventually shows the smoothness of the surface. As long as the lithology of the region is the same one, the surface physical properties tend to be consistent, so the range of the roughness change is small. In addition, the roughness of lunar mare is low by using RMSH, while on the MSR image there are some high roughness areas existing on the surface because of the unsmooth basalt. The correlation between the lunar roughness and the lithology of the geological unit reflects the influence of the geological effect on the formation and evolution of the lunar landscape.

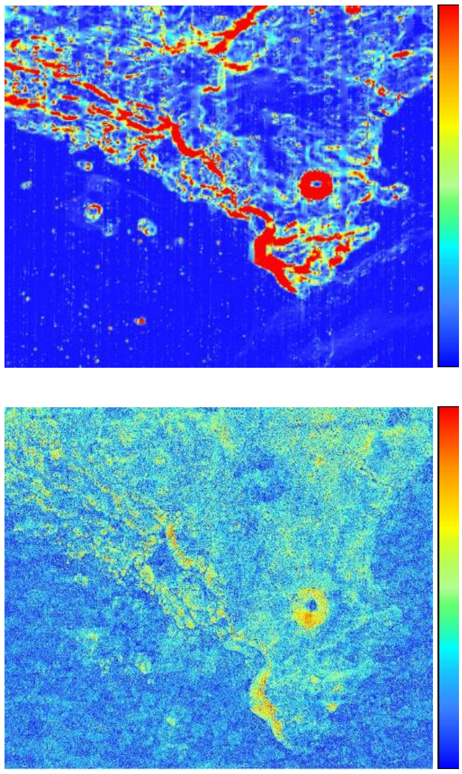

Figure 6. Results by using RMSH (up) and MSR (down) of the tail of Montes Jura southeast

3.2 Crater Plato

The distribution of the crater ejecta can be seen apparently in the traditional RMSH image. The bottom, the wall, the edge and the ejecta four parts of the crater can be clearly distinguished. But the ejecta appearance cannot be seen distinctly in MSR image. Because the ejecta material is in cluttered distribution, the overall roughness of the ejecta area is high. The terrain should be gentle at the bottom of the crater, but some high roughness also exists at the bottom of the plain. That indicates that terrain of the crater bottom is not rugged, but the rock surface is rough. Compared with the results obtained by the RMSH, an anomalous region is found in the northern part of the crater on the MSR result. The area is at the edge of the crater, and the roughness value should be similar to the other area edges, but the roughness obtained from the image is extremely low. So that is presumably related to the lithology of the rock at the edge.

The lunar surface minerals possess their own unique diagnostic characteristic absorption bands. By using these bands directly or combining them, the minerals can be identified (Lucey et al, 1995). making use of the spectral data of SELENE, the band

https://doi.org/10.5194/isprs-archives-XLII-3-W1-99-2017

ratioing is used to reflect the characteristic spectra of the various rocks according to the reflectivity of different rocks (Fischer E M et al, 1996). After several tests, high reflectance of olivine is found at the edge of the crater. Olivine has the glass luster, and its surface is relatively smooth so that the reflectance is high. For this reason, the area is bright on the DOM image. And the roughness based on images using MRS will show the low value on the surface.

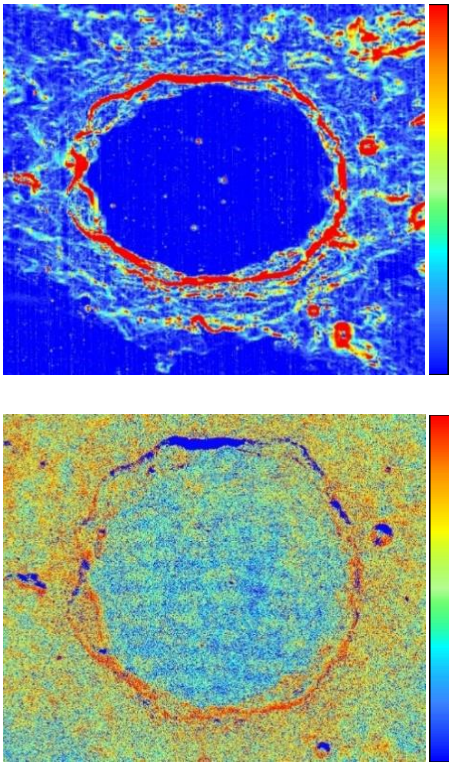

Figure 7. Results by using RMSH (up) and MSR (down) of Crater Plato

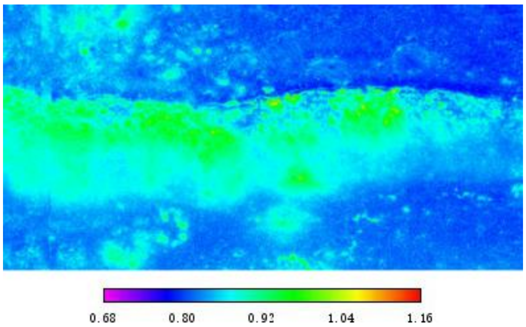

Figure 8. Reflectance spectra of northern cape of Crater Plato edge

4. CONCLUSIONS

Data used in this paper including DEM of LRO, CE-2 DOM and the MI data of SELENE. And these data are processed by RMSH, MSR and Band Ratioing respectively. From the results, it is found that the fluctuation largely determines the value of RMSH roughness while lightly effects on the roughness gotten form MSR. The value of the morphological roughness reflects the smooth and rough of the area surface, which is influenced by the lithology of the land largely. Compared with RMSH method, MSR uses a smaller scale. Since MSR calculation is based on the grey-scale image, the illumination becomes one important influencing factor. The reflectivity of different lunar substances is various, so we can gain more information from the MSR results reflected by the illumination.

Based on the above conclusions, we can use the roughness to select the probe's suitable landing points. According to the surface fluctuation situation derived from RMSH, the landing area range can be settled. This can ensure that the lunar probe lands are in a gentle area. And then use the morphological results of the surface smoothness to determine whether the roughness of the landing area is suitable for the detector walking and observing. The combination of the two results provides a new way for selecting future planetary probe landing points.

REFERENCES

Cheng S, Meng Z, Cui T, et al., 2010. Remote Sensing Geological Analysis of Lunar Satellite in Sinus Iridum[J]. Scientia Sinica Phys, Mech & Astron, 40(11), pp.1370-1379.

Fischer E M, Pieters C M., 1996. Composition and exposure age of the Apollo 16 Cayley and Descartes regions from Clementine data: Normalizing the optical effects of space weathering. Journal of Geophysical Research, 101(E1), pp.2225-2234.

John W M G, David Schleicher, 1972. Geologic atlas of the moon, Plato quadrangle. Department of the interior United States Geological Survey, I-701 LAC-12.

Jolliff B L, Gaddis L R, Ryder G, et al., 2006. New Views of the Moon : Reviews in Mineralogy and Geochemistry. Washington: Mineralogical Society of America.

Lucey, P.G., G.J. Taylor, and F Malaret, 1995. Abundance and distribution of iron on the Moon. Science, 268, pp.1150-1153.

Orosei R, Bianchi R, Coradini A, et al., 2003. Self - affine behavior of Martian topography at kilometer scale from Mars Orbiter Laser Altimeter data. Journal of Geophysical Research Atmospheres, 108(4).

P.Soille, 2013. Morphological image analysis: principles and applications. Springer Science & Business Media.

Rosenburg, M.A., Aharonson, O., Head, J.W., Kreslavsky, M.A., Mazarico, E., Neumann, G.A., Smith, D.E., Torrence, M.H., Zuber, M.T., 2011. Global surface slopes and roughness of the Moon from the lunar orbiter laser altimeter. Journal of Geophysical Research, 116, E02001

Shepard M K, Campbell B A, Bulmer M H, et al., 2001. The roughness of natural terrain: A planetary and remote sensing perspective. Journal of Geophysical Research, 106(E12), pp.32777–32795.

Smith, D.E, Zuber, M., Jackson, G., Cavanaugh, J, et al., 2010a. The Lunar Orbiter Laser Altimeter investigation on the Lunar Reconnaissance Orbiter mission. Space Science Reviews. 150, pp.209–241.

Smith, D.E., Zuber, M.T., Neumann, G.A., Lemoine, et al., 2010b. Initial observations from the Lunar Orbiter Laser Altimeter (LOLA). Geophysical Research Letters, 37(18) , pp.109-118.

USGS. 2008. 1:1 Million-Scale Maps of the Moon. United States Geological Survey, LAC11-LAC12.

W. Cao, Z. Cai, and Z. Tang, 2014. Lunar surface roughness based on multiscale morphological method. Planetary and Space Science, 108, pp. 13–2.

W. Gonzalez and R. E. Woods, 2013. Digital image processing using matlab (second edition). Journal of Applied Sciences, 8, pp. 956–965.

Xi Xiaoxu, Wu Zhiyuan, et al., 2012. The Interpretation of the Land Form of Sinus Iridum on the Moon Based on the Roughness. Remote Sensing for Land & Resources, 24(1), pp.95-99.

Yan Y, Tang G, Xiong L, et al., 2014. Lunar surface roughness of Mare Imbrium based on DEMs. Geographical Research, 33(8), pp.1442-1456.

Ye J, Huang J, Zhang T, et al., 2013. The Achievements of CE-2 Satellite Technology and the Prospect of China 's Deep Space Exploration. Science China Technological Sciences, (5), pp.467-477.

Yokota Y, Haruyama J, Honda C, et al., 2008. Lunar topography: Statistical analysis of roughness on a kilometer scale. Advances in Space Research, 42(2), pp.259–266.

ACCURATE REGISTRATION OF THE CHANG'E-1 IIM DATA BASED ON LRO LROC-WAC MOSICA DATA

Z. Yang , Z. Kang *

[a] Department of Remote Sensing and Geo-Information Engineering, School of Land Science and Technology, China University of Geosciences, Xueyuan Road, Beijing, 100083 CN - (2012160015, zzkang)@ cugb.edu.cn

Commission III, ICWG III/II

KEY WORDS: Chang'E-1, IIM, LROC-WAC, Accurate Registration, Homography Matrix

ABSTRACT:

In the detection of the moon, the visible and near-infrared reflectance data of the lunar material are important information sources for lunar chemical substances and mineral inversion. The Interferometer Imaging Spectrometer (IIM) aboard the Chang'E-1 lunar orbiter is the first multispectral imaging spectrometer for Chinese lunar missions. In this paper, we use the mosaic image of global moon acquired by the Wide-angle Camera (WAC) of the Lunar Reconnaissance Orbiter Camera (LROC) to realize the accurate registration of Chang'E-1 IIM hyperspectral images. Due to the lack of GCPs, the emphasis of this work is to find a huge number of homologous points. The method proposed in this paper is to obtain several homologous points by manually matching, and then we utilize those points to calculate the initial homography matrix of LROC-WAC image and IIM image. This matrix is used to predict the area on IIM image where homologous points may be located, and the locations of the homologous points are determined by the orientation correlation in frequency domain. Finally we save the parts of homologous points which satisfied the conversion relationship of initial homography matrix to calculate homography matrix again. We use this iterative way to obtain a more accurate location of the homologous points. In this process, we take into account that the geometric deformations of different regions on IIM image are quite different. Therefore, we added image threshold segmentation based on the initial homography matrix in the experiment, and completed the above work of finding the homologous points on the segmented images. The final realization of registration accuracy of IIM images are in 1-2 pixels (RMSE). This provides a reliable data assurance for the subsequent study of using IIM images to inverse the lunar elements.

1. INTRODUCTION

For the past few decades, image registration has been widely used in many applications including image mosaic (Tsai et al., 2010), deformation detection (Radke et al., 2005), image fusion (Zhang et al., 2011),cartography (Moigne et al., 2012),etc. The purpose of image registration is to obtain two image spatial transform relationships corresponding to the same region, to achieve image to another image transformation. The image registration from different data sources is conducive to data fusion, and then extracts more useful information.

The Wide-angle Camera (WAC) of the Lunar Reconnaissance Orbiter Camera (LROC), almost every month to achieve global moon image coverage (Denevi et al., 2010) , hereinafter referred to as LROC. The Interference Imaging Spectrometer (IIM) is one of the eight payloads of Chang'E-1, responsible for obtaining mineralogical and lunar mineral chemistry information (Ouyang et al., 2010). The reflectance spectral characteristics of lunar surface materials is an important information source for detecting the material properties of the lunar surface and the quantitative inversion of the mineral elements(Lucey, 2006; Zou et al., 2004).The accurate registration of IIM images can provide data for the inversion of global lunar geology mineral elements.

Image registration methods proposed in literatures consist of the following four step like components: feature detection, feature matching, transform model estimation, image resampling and transformation.(Falco et al., 2008). Each of the mentioned registration steps plays an important role in the registration process. However, among them one of the important steps is the feature matching step(Hossein-Nejad and Nasri, 2016). Feature matching directly affects the results of image registration. At present, the methods of feature matching mainly includes: cross-correlation(Guizar, 2008; Wolberg and Zokai, 2000), FFT-based cross-correlation (Chen et al., 1995; Foroosh et al., 2002; Gilbert, 2002; Reddy and Chatterji, 1996a; Reddy and Chatterji, 1996b),least squares technique (He et al., 2007; Zhao et al., 2016),image matching based on SIFT(Hossein-Nejad and Nasri, 2016; Yi et al., 2008). The least squares method is suitable for cases where the error points are less. SIFT-based feature matching produces more error points, and Wei, Wang et al. proposed the use of RANSAC to eliminate error points(Wei et al., 2008). However, through this way, IIM images have few correct points remain. It is feasible to manually select the homologous points for registration, but a lot of homologous points will cost a huge time and effort. Therefore, the difficulty of IIM and LROC images registration is to find a large number of accurate homologous points on the condition of saving manpower

In this paper, we selected a certain number of homologous points as control points, and try to ensure that these points are evenly distributed on the image. We segmented the IIM and LROC images, and calculated the homography matrix based on the control points from segmented IIM and LROC image blocks. And then, by using the homography matrix, we can predict the position of homologous points. The identity of the homologous

* Corresponding author

points is by orientation correlation in frequency domain(Fitch et al., 2002).After image matching, we utilized RANSAC(Wei et al., 2008) to remove the error points. And the method of weighted least squares is used to update the homography matrix; the final positions of the homologous points are output after several iterations. IIM image data of three orbits (2841, 2842, and 2843) are tested by this method. The accuracy estimation of the registration results is based on more than 200 checking points of each orbits obtained manually. These checking points are not participating in the experiments, which can be used for assessment of the whole image registration results. The RMSE of checking points from different IIM orbits image registration results are in 1-2 pixels.

This paper is divided into four sections. The experimental principle used in this paper is in the second section. The results of the experiment and analysis are in the third section. The conclusion and future work is at the end of this paper.

2. RESEARCH DATA AND METHOD

2.1 Research Data

The IIM images cover about 78% of the lunar region, distributed between 70 ° S and 70 ° N. IIM uses push-sweep imaging, single-orbit imaging width of 25.6km, imaging height of 200km, space resolution of 200m. The IIM images have 32 bands in the range between 480 and 960 nm(Ouyang et al., 2010) . The experimental data used in this paper are 2C level of radiation data which calibrated by the laboratory. As the data of the 1-5, 32 bands SNR are relatively lower, so the experiments exclude these bands(Mingliang et al., 2015; Wu et al., 2012).

The baseline data used in this paper is the mosaic data of the global lunar monochromatic (645nm) image of the Lunar Reconnaissance Orbiter Camera (LROC) Wide Angle Camera (WAC). In order to realize the accurate registration of IIM data, the original IIM images are converted to the moon equirectangular system with LROC image, and the LROC image is resampled to have the same resolution of 200 m/pixel as the IIM images. We also use low-pass filter processing IIM images to smooth image noise. The 25, 20, 11 bands of 26 bands on IIM images are used for RGB color synthesis, which have a better quality. Taking into account the illumination change between IIM images and LROC image is too large. We performed histogram matching of IIM images based on LROC image. Finally, we create the gray-scale image of the IIM images to complete subsequent image matching.

Image registration requires homologous points, the use of traditional cross-correlation method or SIFT method cannot extract a lots of homologous points on the IIM image with high accuracy.Therefore, some homologous points are added as control points in the experiment firstly. These control points can be used to calculate the initial homography matrix, and predict the homologous point's position.

2.2 Proposed Accurate Registration Method

In this paper, the process of accurate registration is divided into four parts: image segmentation, image matching by orientation correlation(Fitch et al., 2002), fitting the homologous points with quadratic polynomial model (Wong and Fieguth, 2009), image resampling by nearest neighbor resampling and transformation. The main contents of this paper are the image segmentation, image matching and eliminate the mismatch points. Therefore, in the following description, we mainly explain these parts.

2.2.1 Image Segmentation: IIM images cover large area in the south-north latitude, which requires more homologous points in order to achieve accurate registration of IIM images. Furthermore, the position offsets between the IIM images and the LROC image from different region are different. The whole IIM image cannot be corrected by the simple rotation translation. In this paper, the original IIM and LROC images are divided and calculated the homography matrix(Wang and Liu, 2006) corresponding to the segmented images. Since the homography matrix can define the interrelationship between the two images, any point on an image can find the corresponding point on another image, and the corresponding point is unique(Ueshiba and Tomita, 2003). Using the homography matrix to achieve it's predicted of the homologous point. Each image block after image segmentation corresponds to a homography matrix. In this way, it is possible to improve the accuracy of the predicted homologous point's position. It is easier to find the correct coordinates of the homologous point by image matching around the position, and to obtain more accurate homologous points.

The entire image segmentation process can be divided into two steps: image segmentation, image combination. The final realization of the images is unevenly divided. The realization of the method: The IIM and LROC images are divided into small image blocks, and the manually selected control points are also divided into the corresponding image blocks, and then calculate the homography matrix of the current IIM image block and the LROC image block. The current image block is recorded as 1, which indicates the image block has been judged. The equation for the homography matrix is as follows:

$$\begin{bmatrix} x' \\ y' \\ 1 \end{bmatrix} = \begin{bmatrix} a1 & a2 & a3 \\ a4 & a5 & a6 \\ a7 & a8 & 1 \end{bmatrix} \cdot \begin{bmatrix} x \\ y \\ 1 \end{bmatrix} \tag{1}$$

Where x' and y' correspond to the vertical and horizontal coordinates of the pixel point on the IIM image blocks, respectively $[x' \quad y' \quad 1]^T$ is the representation of the homogeneous coordinates of the point. The x and y correspond to the horizontal and vertical coordinates of the LROC image pixel point respectively, and the homogeneous coordinates are expressed as$[x \quad y \quad 1]^T$. The a1 to a8 correspond to the eight independent pending parameters of the homography matrix, and the image can be corrected at 8 degrees of freedom. So solve the homography matrix at least 4 pairs of homologous points. We use the control point coordinates (greater than 4) of the current images block on LROC to obtain the homography matrix by least squares(Bin et al., 2011). And then create four neighborhood directions of the current image block; four neighborhood directions diagram is as follows:

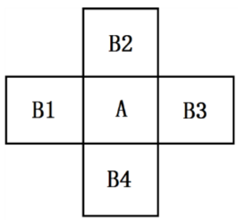

Figure 1 Four neighborhood direction diagram

Traverses the four neighbourhoods direction of the current image block, if the image block of the current traversal direction exists and is not marked as 1,and it is judged whether or not the image block can be merged with the current image block A. At the same time, mark the image block of the current traversal direction as 1. The control point coordinates of the current traversing direction LROC image block (e.g., B1) are substituted into the homography matrix, and we can obtained a calculated coordinates k_i of IIM images block. The actual value k_i' has already obtained by manually selected. Thus we can use the offset between the calculated value and actual value. We calculate the mean value of those offsets. The calculation equation is as follows, where num indicates the number of control points corresponding to the current image block. If the mean f_k is less than a certain threshold, it is assumed that the homography matrix can also be applied to the image blocks of the current traversal direction and the current traversal direction can be combined.

$$\mathrm{f}_k = \frac{\sum_{i=1}^{num} \|H \cdot k_i - k_i'\|^2}{num} \tag{2}$$

Here we set the threshold f_k of 3. After that the homography matrix of the combined image was calculated by least squares method. At the same time if the calculated value is greater than the threshold in this step, the image block of current traversal direction will not be combined, and determine the next direction of the current image block.

In this process, there may be cases where the number of control points of the image block is less than 4, this time the current image block is merged directly with its traversing direction image block until the number of control points of the combined image block can be used to calculate the homography matrix, and then the image blocks were judged whether can be combined. When the image segmentation is completed, the image blocks of LROC image and IIM images are output along with their corresponding control point coordinates. Subsequent matches are done on those split images.

2.2.2 Image Matching: The illumination of IIM and LROC images vary greatly, after the histogram matching, this difference still exists, reflected in the image is the grayscale difference between homologous points. The traditional image matching methods are mainly based on the grayscale, the grayscale difference between homologous points will lead to a large number of image points match failure or mis-match. Therefore, in this paper ,we use orientation correlation(Fitch et al., 2002). This method is robust to changes in light.

Using the control points' coordinates on the segmented image blocks, the homography matrix (Equation 1) is calculated by least squares. The coordinates of pixels on the LROC image blocks are substituted into the homography matrix to obtain corresponding predictions of IIM images, and the coordinates of the homologous points can be obtained by using orientation correlation.

Firstly, the IIM and LROC orientation images were constructed: Traversing the pixel points $f(x,y)$ on the LROC image blocks, creating search window centered on $f(x,y)$ .and a search window with same size centered on the predicted point $g(x,y)$ on the IIM image blocks, and the orientation image is created as follows:

$$f_d(x,y) = sgn\left(\frac{\partial f(x,y)}{\partial x} + i\frac{\partial f(x,y)}{\partial y}\right) \tag{3}$$

$$\mathrm{sgn(x)} = \begin{cases} 0, & \text{if } |\mathrm{x}| < 0 \\ \dfrac{x}{|x|}, & \text{otherwise} \end{cases}$$

$$\frac{\partial f(x,y)}{\partial x} = f(x+1,y) - f(x,y)$$

$$\frac{\partial f(x,y)}{\partial y} = f(x,y+1) - f(x,y)$$

Where $f(x,y)$ represents the gradient of the original image at the coordinates x and y, and f_d (x, y) corresponds to the image pixel value after the orientation image is created. The sgn(x) represents a signal function. The orientation image of the search window on the IIM image is also created according to equation 3, and the value of its pixel on orientation image is denoted as $g_d(x,y)$ .Orientation images are matched using correlation (Gilbert, 2002).Correlation is computed quickly with Fast Fourier Transforms(FFTs).The $F_D(k,l)$ is denoted by $f_d(x,y)$ after fast Fourier transform, and $G_D(k,l)$ corresponds to the value of $g_d(x,y)$ after fast Fourier transform. IFFT () is the inverse transform function of fast Fourier, and $G_D{}^*(k,l)$ is conjugate to the complex value of $G_D(k,l)$. The correlation coefficients matrix obtained by the image correlation is calculated as follows:

$$\mathrm{IFFT}(F_D(k,l) \cdot G_D{}^*(k,l)) \tag{4}$$

By obtaining the maximum value of the correlation coefficients' matrix, we can get the offset of the homologous point position relative to the center pixel of the IIM search window, and then we can get the coordinate of homologous point.

2.2.3 Error Points Removal: The homologous points obtained by orientation correlation may be exist error points. The method used in this paper to remove the error points is RANSAC(Hartley and Zisserman, 2003). If the image matching can obtain N pairs of the homologous points, the matching point pair P_i andP_i' respectively correspond to the points obtained by the LROC image and the points obtained by the orientation correlation on IIM images. The homography matrix H is estimated according to the optimal value of the cost function J, as shown in function 5.

$$\mathrm{J} = \sum_{i=1}^{N} (\|H \cdot P_i - \mathrm{P}_i'\|^2 + \|H^{-1} \cdot \mathrm{P}_i' - P_i\|) \tag{5}$$

After the RANSAC estimate, we can obtain the homography matrix H which minimizes the above cost function J. According to the equation 6, we determine whether P_i is the internal point or the outer point according to the European distance (Equation 6). If P_i is the internal point, and then preserve the points pair P_i andP_i'.The number of internal points is M and the number of external points is N-M.

$$\begin{gathered} \text{distance}=\|H \cdot P_i - \mathrm{P}_i'\|^2 + \|H^{-1} \cdot \mathrm{P}_i' - P_i\|^2 \\ \mathrm{f(x)} = \begin{cases} \text{distance} < \mathrm{t}^2, & \text{internal point} \\ \text{distance} \geq t^2, & \text{outer point} \end{cases} \end{gathered} \tag{6}$$

Where t is the value after test, set to 0.8, i = 1... N. The homography matrix H obtained by RANSAC only describes four pairs of the homologous points, and its accuracy is difficult to be guaranteed. In addition to the estimation of the homography matrix, the control points we selected should also be included. However, taking into account the control points relative to the homologous points obtained from image matching should have higher accuracy, so we use weighted least

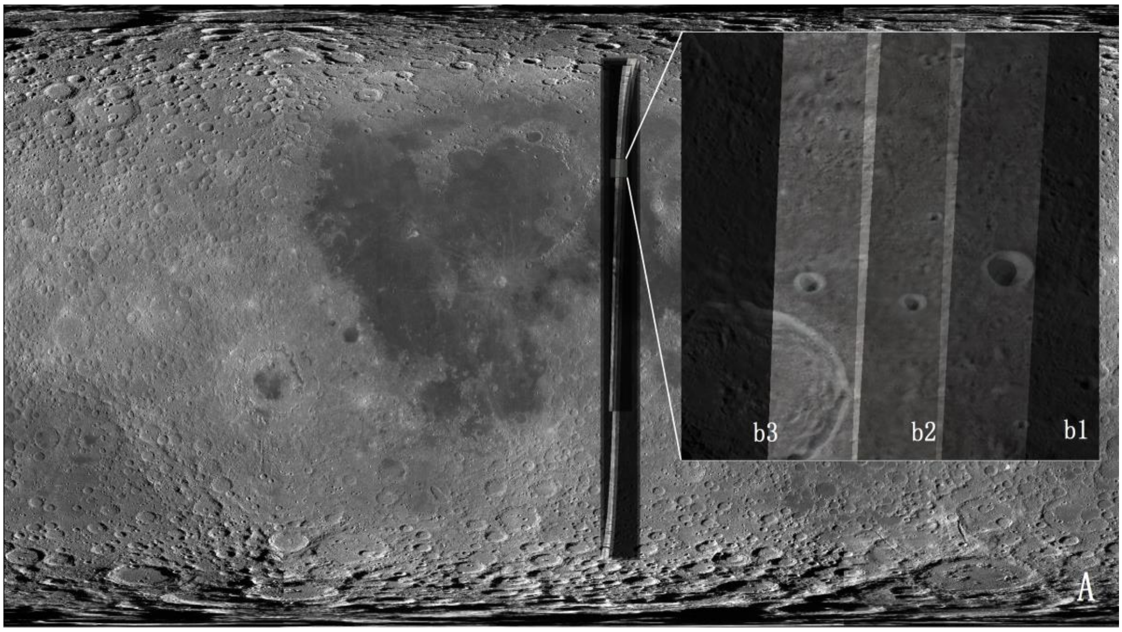

Figure 2. LROC image (A) and three orbiter images of IIM: image 2841(b1), image 2842 (b2), image 2843 (b3)

squares method to calculate the homogeneity matrix by the homologous points preserved from RANSAC and the control points.

The homography matrix is used to replace the initial homography matrix to predict the position of the homologous points, and the image matching and error point removal are repeated. At the same time, the manually selected control points on the LROC image block are substituted into the homography matrix to obtain the predicted values on the IIM image block, and calculate the mean offset between all predicted points and their actual values (Equation 2). Iterating this process and found that the mean offset is smaller. When the mean offset tends to be stable, the number of iterations is output and the iterations is stopped .The final positions of the homologous points are output.

3. EXPERIMENTAL RESULT AND ANALYSIS

3.1 Experimental Data

The study data are shown in Figure.2: Fig.A is the LROC image of the global lunar, and b1, b2, b3 represent the IIM image of orbit 2841, 2842, 2843 which be registered in the experiments. The data of the orbit 2843 has a large difference with the data of the orbit 2841, 2842 in the coverage of the north and south latitudes (coverage smaller), so the data is considered separately in the subsequent image segmentation.

3.2 Result of Accurate Registration

The contents of the experiment include the image segmentation, the image matching, and the removal of the mismatch points. Through the above experiments we can obtain a large number of homologous points from IIM images of orbits 2841, 2842, 2843, respectively. The quadratic polynomial of LROC image and IIM image is fitted with these homologous points, and the polynomial is used to realize the accurate registration of IIM image data by image nearest neighbor resampling.

In this paper, the accurate registration flow chart is as follows, in which part of the dashed box is the main experimental contents of this paper:

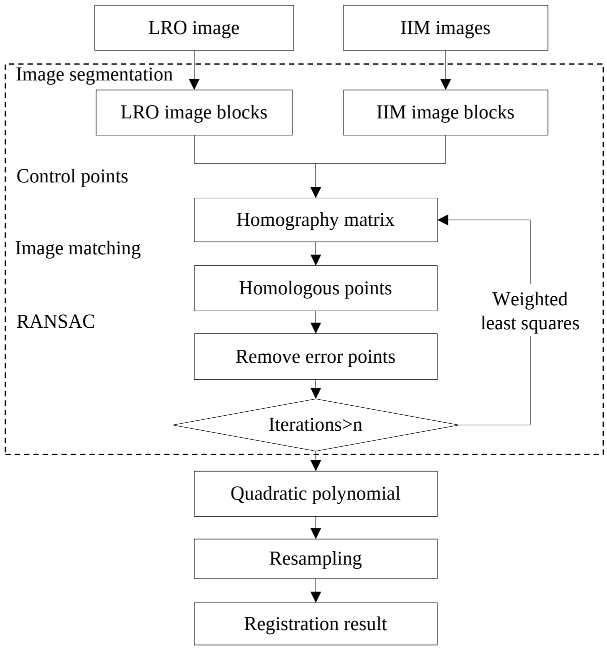

Figure 3. The accurate registration flow chart

3.2.1 Image Segmentation: Image segmentation can be divided into image segmentation and image combination. Different sizes of image blocks can be obtained after the image segmention. We should try to ensure that the small image block before combining should contain at least four manually selected control points, so as to be used to calculate the homography matrix to determine the combine threshold (Equation 2). This point we have already mentioned in the section 2.2.1. In addition, IIM images on both sides (Fig.6 b1, b2, b3) have no data, in the experiment the corresponding range of IIM images and LROC image should not be added into the image segmentation. Finally, different size of image blocks both on LROC image and IIM images were obtained(Orbit 2841，2842，2843).

The following table shows the number of control points manually selected on the three orbits of IIM in this paper, the number of cutting times in the image x and y directions, and the number of image blocks corresponding to each orbital images acquired after image segmentation. It can be seen from the table that the number of cutting images is related to the number of manually selected control points. As the IIM orbital image 2843 is not complete, it has a different number of split. Its number of pixels in the x, y direction is less than orbital images of 2841, 2842.

Orbits	Control points	Cutting number (x direction)	Cutting number (y direction)	Image blocks
2841	156	12	10	7
	108	12	9	6
	80	12	7	5
	60	12	5	6
2842	156	12	10	6
	108	12	9	6
	80	12	7	5
	60	12	5	5
2843	107	7	6	7
	85	7	5	5
	66	7	4	4
	53	7	4	4

Table 1. IIM images of each orbital data segmentation

3.2.2 Orientation Correlation and Error Points Removal: After image segmentation we get the image blocks of the IIM images for each orbit. In the image matching process, each orbit image of the IIM to traverse all the image blocks on them, to complete the image matching and get homologous points of whole orbit. So the image matching is actually completed on the different size of image blocks. In the image matching, we calculate the initial homography matrix (Equation 1) based on the coordinates of the control points corresponding to the image blocks. Since only the control points are calculated, the weights of all control points is set to 1.And then traverse the points on the LROC image block and substitute them into the homography matrix to obtain the predicted value of the coordinates of the homologous points on IIM image block. Create a search window with a size of 29*29 centered on the predicted coordinate and create a window of the same size centered on the point on the LROC image block to complete the orientation correlation (2.2.2). The match is completed in the frequency domain, the matching time of the method is short and the image matching can be done in a few minutes. We use RANSAC to remove the mismatch points (2.2.3) of the image, and use the remained “internal points” combining with manual selected control points to update the homography matrix by weighted least squares method.

Due to the high precision of the manually selected control points, and the number of control points is relatively small; we give the control points weighted value of 1 after several tests. However, the method proposed in this paper to obtain a large number of the homologous points as the weight of 0.1. The updated homography matrix can be used to calculate the predicted coordinates of the homologous points and to complete the image matching. All the image blocks after four iterations the mean offset of manually selected control points between predict value and actual value tend to be stable (Equation 2), and finally output the homologous points.

Each orbit of the image data we have carried out four groups of experiments to test a different number of manually selected control points through the method proposed in this paper to get a huge number of homologous points. The final number of homologous points and the matching time as follows:

Orbits	Homologous points	Matching time（s）
2841	1135	182
	1124	178
	1778	162
	1907	151
2842	1416	188
	1869	169
	1354	178
	788	138
2843	1423	180
	1077	171
	1335	161
	828	131

Table 2. The number of homologous points and matching time

3.3 Results Analysis

In this paper, we use a number of homologous points added manually on the image to evaluate the registration results of our proposed method. Those homologous points can be viewed as checking points. Checking points selection method: creating grid in the LROC and IIM original image (Fig.4 a), manually select the checking points on the image added grid. The purpose of this step is to ensure that the checking points are evenly distributed on the image. These points are not included in the experiments in this paper and can be used as an assessment of the entire IIM image registration result. After the experiments in the text we can automatically get a large number of the homologous points, those points were used to fit the quadratic polynomial model to achieve the registration of the IIM images added checking points (Fig.4 b) The ideal result of the registration is that the IIM images after registration can be completely coincident with the LROC image, and the positions of the checking points are coincident (Fig.4 c).

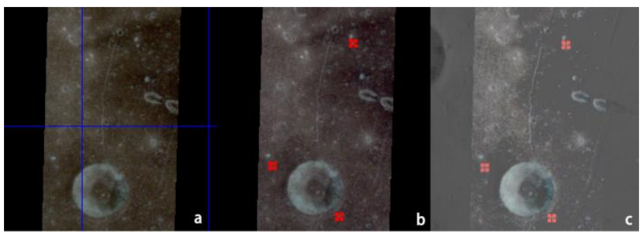

Figure 4 Checking points selection diagram

If the checking point’s location of IIM registration image and LROC image exist deviation .This can be considered as the error of registration results. Based on this criterion, we evaluated the registration results using the offsets between the checking points on the corrected IIM image and the checking point coordinates of the corresponding position on the LROC image, where the orbit 2841 selected 366 checking points, orbit 2842 selected 363 checking points, orbit 2843 selected 284 checking points.

The following table shows the root mean square error (RMSE) of the checking points’ offset, the number of homologous points obtained from the above experiments and the number of manually selected control points. From this table we can draw the conclusion that the method proposed in this paper can extract a huge number of homologous points, and the RMSE of all experiments are within two pixels, of which the bold displays are the best results of three orbital image registrations.

Orbits	RMSE/Number of homologous points/Number of control points			
	Experiment1	Experiment2	Experiment3	Experiment4
2841	1.440/1907/60	1.423/1778/80	**1.323/1149/108**	1.378/1135/156
2842	1.488/788/60	**1.424/1449/80**	1.500/1869/108	1.575/1416/156
2843	1.553/828/53	1.509/1335/66	1.474/1077/85	**1.385/1423/107**

Table 3.The RMSE of check points' offset on three orbit IIM images after registration

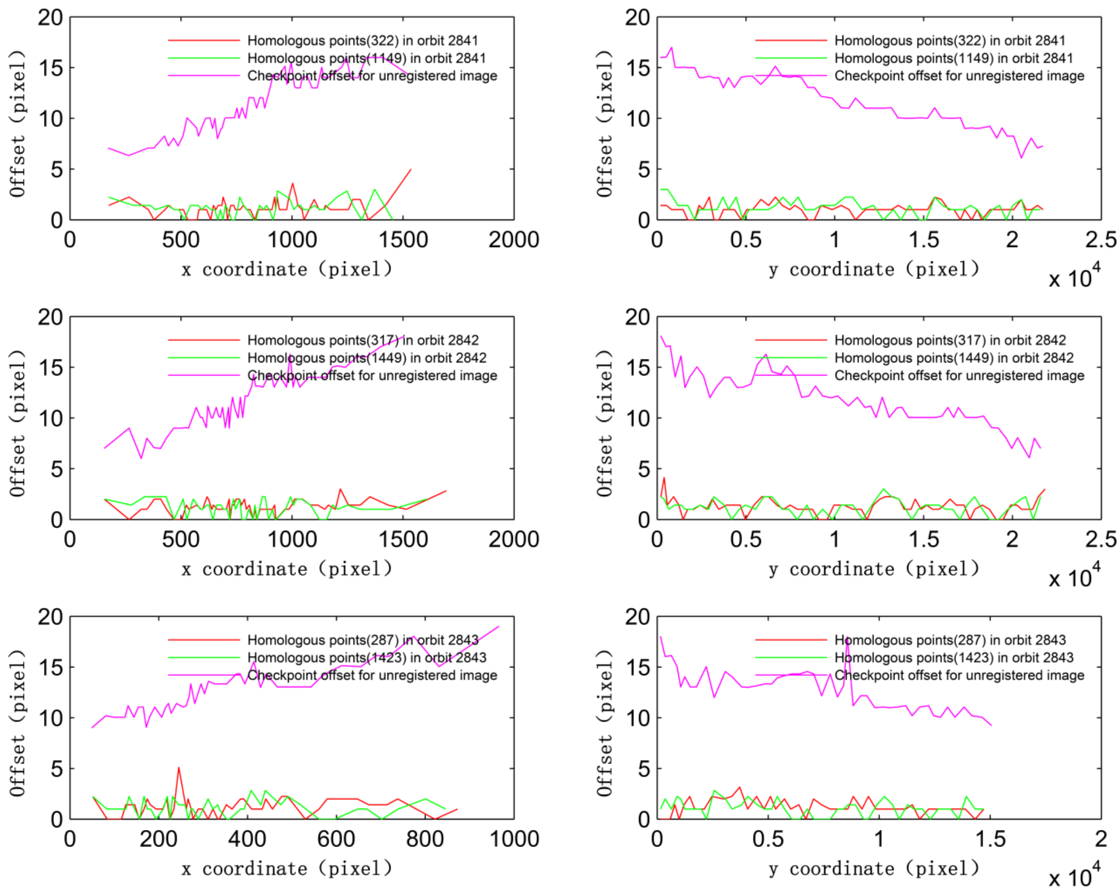

Figure 5.The offsets of three orbit IIM images are displayed in x direction and y direction

Fig.5 shows the checking points' offsets from each orbit of the IIM image displayed in the x-direction and y-direction of the image. The pink line corresponds to the checking points' offsets between the origin IIM images and LRO image, the green line corresponds to the checking points' offsets by method proposed in this paper, while the red line corresponds to the checking points' offsets of manually selected homologous points. It can be seen the method proposed in this paper can realize the accurate registration of IIM images .Compared the checking points' offsets of registration method by manually selected homologous points and registration method proposed in this paper, it can be seen that the maximum offsets of the registration method by manually selected homologous points is reduced through the registration method proposed in this paper. Where the 2841 orbital offset in x direction is reduced from five pixels to three pixels, the maximum offset of the orbit 2842 in the x direction is also reduced from three pixels to two pixels, and the maximum value of the offset in y direction of orbit 2842

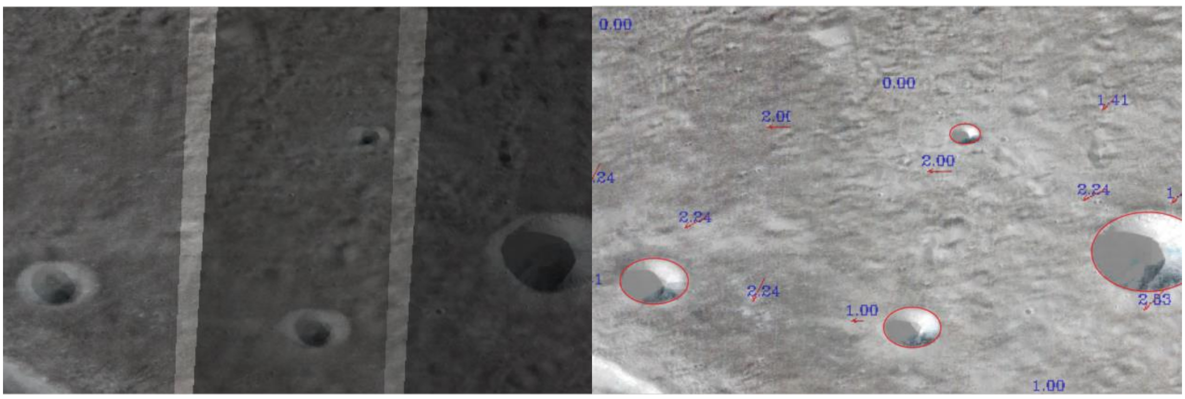

Figure 6.The results of comparison before and after registration

is reduced from four pixels to two pixels, the maximum offset in the orbit 2843 x direction is reduced from five pixels to two pixels. The offsets of all points are within 3 pixels.

The positions of the larger checking point's offsets before image registration are mainly concentrated on the upper panel and the right panel of the image. The difference between the entire IIM images offsets can reach more than a dozen pixels. After image registration, the checking points' offsets of the IIM and LRO images no longer reflect this trend. The checking points' offsets between the registration images and LRO image are all reduced to a smaller value.

Finally, we marked the checking point's offsets in size and direction on the mosaic image of three orbital images. Fig.6 in the left picture shows results that the original three orbits of the IIM images superimposed on the LROC image, Fig.6 on the right is the mosaic of the IIM registration images superimposed on the LROC image, and the arrow indicates the direction of the offset. We circled the lunar craters in red. There existed a large deviation between the IIM images and the LROC image before the IIM images are registered, and the positions of lunar craters coincide after registration. The sizes of these offsets marked on the map are basically within 2 pixels.

4. CONCLUSIONS AND FUTURE WORKS

IIM images have a large coverage in the north-south latitude. Therefore, the registration method in this paper focuses on how to obtain a huge number of accurate homologous points to achieve accurate registration. In this paper, the image segmentation method is used to divide the image into image blocks of different sizes, and the manually selected control points on the image blocks were used to calculate the homography matrix. By using the homography matrix can predict the homolography points' position, and then based on the orientation correlation to obtain the homologous point coordinates to achieve image registration. The experiment results show that the proposed method in this paper can obtain a huge number of accurate coordinates of the homologous points. The RMSE of checking points of best registration results on three orbital IIM images are all within 1.5 pixels. The method propose in this paper can achieve the accurate registration of the image. Subsequent studies will focus on how to further reduce the manual selection of control points to obtain more accurate results.

REFERENCES

Bin, W.U., Zhu, H.Y., Xiao, X.T., Xue, T., 2011. Extraction of plane target image features based on homography matrix in visual measurement. *Journal of Optoelectronics Laser* 22, 1211-1215.

Chen, Q., Defrise, M., Deconinck, F., 1995. Symmetric Phase-Only Matched Filtering of Fourier-Mellin Transforms for Image Registration and Recognition. *Pattern Analysis & Machine Intelligence IEEE Transactions on* 16, 1156-1168.

Denevi, B.W., Robinson, M.S., Sato, H., Hapke, B.W., Eliason, E.M., Hiesinger, H., Jolliff, B.L., Malin, M.C., Mcewin, A.S., Ravine, M.A., 2010. Lunar Reconnaissance Orbiter Wide Angle Camera Observations of the Moon, *European Planetary Science Congress 2010*, p. 333".

Falco, I.D., Cioppa, A.D., Maisto, D., Tarantino, E., 2008. Differential Evolution as a viable tool for satellite image registration. *Applied Soft Computing* 8, 1453-1462.

Fitch, A.J., Kadyrov, A., Christmas, W.J., Kittler, J., 2002. Orientation Correlation, *British Machine Vision Conference 2002, BMVC 2002, Cardiff, Uk, 2-5 September*, pp. 133--142.

Foroosh, H., Zerubia, J.B., Berthod, M., 2002. Extension of phase correlation to subpixel registration. *IEEE Transactions on Image Processing A Publication of the IEEE Signal Processing Society* 11, 188-200.

Gilbert, R., 2002. Evaluation of FFT Based Cross-Correlation Algorithms for Ppaper Image Velocimetry. *University of Waterloo*.

Guizar, M., 2008. Efficient subpixel image registration by cross-correlation. *Optics Letters* 33, 156.

Hartley, R., Zisserman, A., 2003. Multiple View Geometry in Computer Vision. *Cambridge University Press*.

He, Y., Yap, K.H., Chen, L., Chau, L.P., 2007. A Nonlinear Least Square Technique for Simultaneous Image Registration and Super-Resolution. *IEEE Transactions on Image Processing* 16, 2830-2841.

Hossein-Nejad, Z., Nasri, M., 2016. An adaptive image registration method based on SIFT features and RANSAC transform ☆. *Computers & Electrical Engineering*.

Lucey, P.G., 2006. Understanding the Lunar Surface and Space-Moon Interactions. *Reviews in Mineralogy & Geochemistry* 60, 83-219.

Mingliang, M.A., Wang, C., Shi, R., Gao, W., 2015. The Research and Assessment of Topographic Registration and Correction of Chang'E-1 IIM Data Based on LRO LOLA DEM Data. *Journal of Geo-Information Science*.

Ouyang, Z.Y., Chunlai, L.I., Zou, Y.L., Zhang, H.B., Chang, L., Liu, J.Z., Liu, J.J., Wei, Z., Yan, S.U., Wen, W.B., 2010. Primary scientific results of Chang'E-1 lunar mission. *Science China Earth Sciences* 53, 1565-1581.

Radke, R.J., Andra, S., Al-Kofahi, O., Roysam, B., 2005. Image change detection algorithms: a systematic survey. *IEEE Transactions on Image Processing A Publication of the IEEE Signal Processing Society* 14, 294.

Reddy, B.S., Chatterji, B.N., 1996a. An FFT-based technique for translation, rotation, and scale-invariant image registration. *IEEE Transactions on Image Processing A Publication of the IEEE Signal Processing Society* 5, 1266-1271.

Tsai, C.L., Li, C.Y., Yang, G., Lin, K.S., 2010. The edge-driven dual-bootstrap iterative closest point algorithm for registration of multimodal fluorescein angiogram sequence. *IEEE Transactions on Medical Imaging* 29, 636-649.

Ueshiba, T., Tomita, F., 2003. Plane-based calibration algorithm for multi-camera systems via factorization of homography matrices, *IEEE International Conference on Computer Vision*, 2003. Proceedings, pp. 966-973 vol.962.

Wang, J., Liu, Y., 2006. Characteristic Line of Planar Homography Matrix and Its Applications in Camera Calibration, *International Conference on Pattern Recognition*, pp. 147-150.

Wei, W., Hong, J., Tang, Y., 2008. Image Matching for Geomorphic Measurement Based on SIFT and RANSAC Methods, *International Conference on Computer Science and Software Engineering*, pp. 317-320.

Wolberg, G., Zokai, S., 2000. Image registration for perspective deformation recovery, *Aerosense*, p. 12.

Wong, A., Fieguth, P., 2009. Fast phase-based registration of multimodal image data. *Signal Processing* 89, 724-737.

Wu, Y., Zhang, X., Yan, B., Gan, F., Tang, Z., Xu, A., Zheng, Y., Zou, Y., 2012. Global absorption center map of the mafic minerals on the Moon as viewed by CE-1 IIM data. *Science China* 55, 561-562.

Yi, Z., Zhiguo, C., Yang, X., 2008. Multi-spectral remote image registration based on SIFT. *Electronics Letters* 44, 107-108.

Zhang, Q., Wang, L., Li, H., Ma, Z., 2011. Similarity-based multimodality image fusion with shiftable complex directional pyramid. *Pattern Recognition Letters* 32, 1544-1553.

Zhao, W., Tian, Z., Yang, L., Yan, W., Wen, J., 2016. Image registration using a kernel partial least squares based mismatches removal method. *AEU - International Journal of Electronics and Communications* 70, 427-435.

Zou, Y.L., Liu, J.Z., Liu, J.J., Xu, T., 2004. Reflectance Spectral Characteristics of Lunar Surface Materials. *Research in Astronomy and Astrophysics* 4, 97-104.

AUTOMATIC DETECTION AND RECOGNITION OF CRATERS BASED ON THE SPECTRAL FEATURES OF LUNAR ROCKS AND MINERALS

L. Ye [a], X. Xu [a], D. Luan [a], W. Jiang [a], Z. Kang [a] *

[a] Surveying and Mapping Engineering, School of Land Science and Technology, China University of Geosciences (Beijing), Xueyuan Road, Haidian District, Beijing, 100083 CN – ljyebj@163.com

KEY WORDS: Spectral Characterististics, MI , Band Ratio Method, Impact Crater Classification

ABSTRACT:

Crater-detection approaches can be divided into four categories: manual recognition, shape-profile fitting algorithms, machine-learning methods and geological information-based analysis using terrain and spectral data. The mainstream method is Shape-profile fitting algorithms. Many scholars throughout the world use the illumination gradient information to fit standard circles by least square method. Although this method has achieved good results, it is difficult to identify the craters with poor "visibility", complex structure and composition. Moreover, the accuracy of recognition is difficult to be improved due to the multiple solutions and noise interference. Aiming at the problem, we propose a method for the automatic extraction of impact craters based on spectral characteristics of the moon rocks and minerals: 1) Under the condition of sunlight, the impact craters are extracted from MI by condition matching and the positions as well as diameters of the craters are obtained. 2) Regolith is spilled while lunar is impacted and one of the elements of lunar regolith is iron. Therefore, incorrectly extracted impact craters can be removed by judging whether the crater contains "non iron" element. 3) Craters which are extracted correctly, are divided into two types: simple type and complex type according to their diameters. 4) Get the information of titanium and match the titanium distribution of the complex craters with normal distribution curve, then calculate the goodness of fit and set the threshold. The complex craters can be divided into two types: normal distribution curve type of titanium and non normal distribution curve type of titanium. We validated our proposed method with MI acquired by SELENE. Experimental results demonstrate that the proposed method has good performance in the test area.

1. INTRODUCTION

The Moon is the nearest celestial body to the Earth and catches lots of attention for a long time(Ouyang, 2005). The surface of lunar is covered with a variety of big and small circular structures including craters, lunar rays and arched structures associated with craters, which are significant features of the lunar surface (Ouyang, 2005). The formation process of impact craters, morphological characteristics and spatial distribution provide clues and methods of the study about the lunar evolution in different aspects for people (Huang, 2009). The researches on lunar craters have a significant influence on the process of human understanding and exploration of the moon.

At present, the researches on impact craters in the world mainly attach importance to how to extract impact craters in CCD images or DEM data by using related algorithms. Few scholars have carried out further research on the extracted craters. Based on the illumination gradient information, Junhua Feng et al use the Chang'e-1 CCD images to fit the edge ellipses by the least square method (Feng, 2010). Zongyu Yue et al studied on the identification of impact craters using the visible / near-ultraviolet band images obtained from Clementine (Yue, 2008). Based on cross-correlation, M Magee et al proposed a method of template matching, which is calculated by the standardized cross-correlation method and found that the method is suitable for small, relatively simple craters (Magee, 2003). Y Sawabe et al added UV-VIS band multispectral data to the study about the automatic identification and classification of craters from Clenmentine and Apollo lunar highlands and lunar mare. In the experiment, they found that the FeO2 content in the crater was lower than that in the surrounding area (Sawabe, 2005). Based on the Hough transformation, K Homma introduces the thought of parallel computing, experimenting with SELENE image data, increasing the computational speed greatly without affecting the recognition accuracy (K Homma, 1997). Jr Kim et al eliminated more than 85% error extracted carters by using the Eigenspace construction algorithm based on artificial neural networks proposed by Turk and Pentland (Kim, 2005). Tomasz F Stepinski, Erik R Urbach et al used the decision tree algorithm for the candidate impact craters, which is based on setting decision conditions to determine whether they belong to impact craters. (Stapinski,2009; Urbach,2009).

Taking into account the accuracy of the data constraints, impact craters have a high error extraction rate. Few scholars try to remove error craters and automatically classify them. Accordingly, we propose an algorithm to determine the correctness of the extracted craters and realize the automatic classification based on the spectral characteristics of the lunar rock and minerals in this paper.

2. EXTRACT CRATERS FROM MI

Under the conditions of sunlight, Zhongfei Luo used CCD data whose spectral channel is 500-700nm (Chen, 2009) to extract the craters by an automatic detection algorithm based on feature matching (Luo, 2014). The thinking of extraction includes threshold segmentation, region growing, adding conditions of image characters, extracting the edge of craters and fitting into standard circles. The extraction is based on four image characters. Figure 1 is the flow diagram of extracting algorithm.

* Corresponding author. This is useful to know for communication with the appropriate person in cases with more than one author.

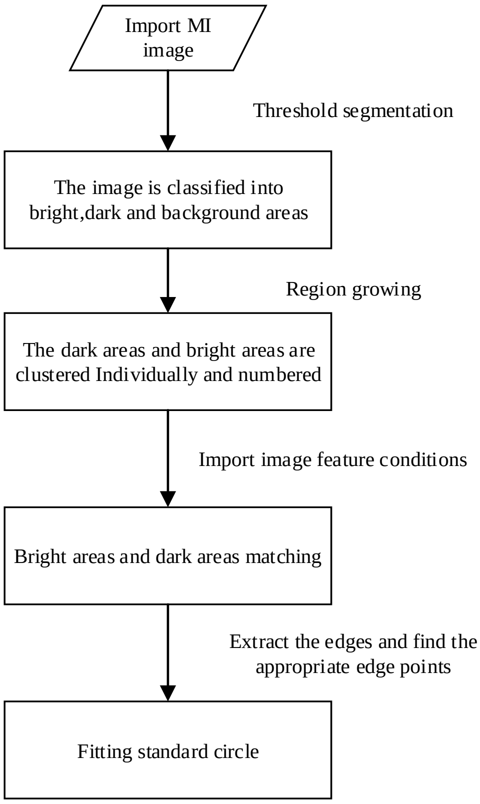

Figure 1. Automatic crater detection algorithm based on feature matching

MI data contains 9 bands and the Spectral channel is 415-1550nm. Because craters in MI images still match the four image characters: ①The edges of craters are close to circle. ②The line which connects the center of the highlight and the shadow is nearly parallel to the direction of sun light. ③The ratio between the area of the craters and distance between the center of light and the shadow fluctuates in a certain range. ④The gray value variation of the light and the shadow is small (Jin, 2009), we can use the algorithm proposed by Luo to extract the craters. We use the matching features, as follows to extract craters.

$$\left.\begin{array}{ll} \theta < 20^{\circ} & \\ s = (S_a + S_b)\ /\pi r^2 & s > 0.3 \\ p = min\ (S_a / S_b , S_b / S_a) & p < 3.9 \end{array}\right\} \quad (1)$$

where θ = the angle between direction of sun light and line connecting the center of the highlight and the shadow.
S = the ratio between number of pixels in the light and shadow and area of a circle whose radius equals the distance between the center of light and shadow.
S_a = the number of pixels in the shadow.
S_b = the number of pixels in the light.
r = the distance between the center of light and shadow.
p = the minimum value of the ratio between the number of pixels in the shadow and the light.

Figure 2 is the effect picture of extracting craters in a sample of MI images.

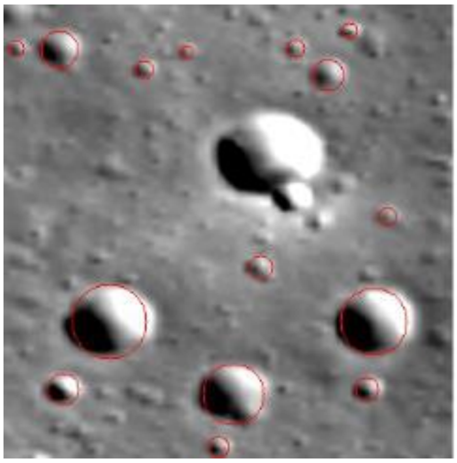

Figure 2. Effect picture of extraction algorithm based on feature matching (N39°-40°, E323°-324°, the center wavelength is 1548nm, the spatial resolution is 62m)

3. ERROR ELIMINATION

The structure and material composition of the impact craters is complicated, and the lighting conditions vary from region to region. It leads to that provided that merely in the sunlight, the extractions of the impact craters on CCD images which based on condition matching have error extractions. In this paper, by determining whether the standard circles contain "non iron" element, we make error eliminations for the craters which have been extracted by the extraction algorithm based on feature matching. Due to the special environment of the lunar, lunar regolith has unique mineral composition and completely different from the earth, and there is a great quantity of nanoscale elemental iron in the lunar regolith particles even cemented glass because of a lot of space weathering (Taylor LA., 2005). The mineral absorption characteristics of the moon are mainly influenced by ferrous iron and titanium from the crystal structure aspect (Wang Zhenchao, 2011). In the study of data from Clenmentine and Apollo lunar highlands and lunar mare, Y Sawabe et al found that the concentration of FeO2 in the crater was much lower than in the surrounding area (Sawabe, 2005).

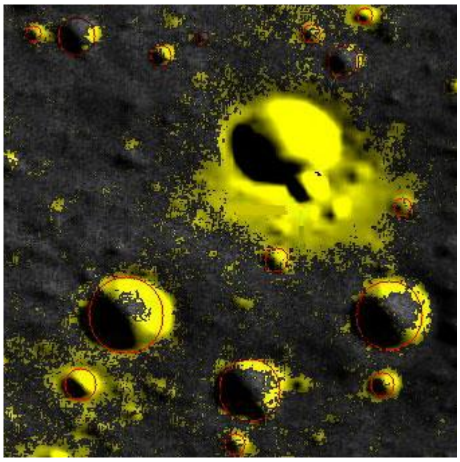

Figure 3. Effect picture of error elimination (N39°-40°, E323°-324°, the center wavelength is 1548nm, the spatial resolution is 62m, the yellow area in the picture is defined as regions rich in "non iron" element, and the gray area are regions rich in iron)

Lunar regolith contains a large amount of iron. It can be inferred that when a meteorite strikes the moon, the lunar regolith was spilled, the iron content in the craters less compared to the outside. The iron information can be extracted using the central wavelength of 1250nm/750nm (Yu, 2009). We make iron extraction ratio less than a certain threshold defined as "non iron" element. If the extracted standard circle contains the "non iron" element, it can be considered that the standard circle is extracted correctly, otherwise it is wrong. Figure 3 is the effect picture of error elimination.

4. CRATER CLASSIFICATION

In this paper, we divided the correct craters into the simple and complex type, and the complex type can be divided into normal distribution curve type of titanium and non normal distribution curve type of titanium.

4.1. Divide Craters into Simple and Complex Type

The air of the moon is very thin and it almost can be considered a vacuum. Its surface crystalline rock, molten glass etc directly exposed to the universe, suffered from the solar wind, cosmic rays and meteorites radiation and impact. The surface of the depth of about tens of nanometers formed because of weathering influences (Wang, 2011). The impact strength and weathering effect of large-diameter impact craters are generally stronger relative to small-diameter craters, and their morphological and material composition is more complex. The diameter of simple crater is generally less than 4km (Zhao, 2011).

Table 1 is for the sample area of the four craters whose diameters are about 4km. It can be seen that the profile line and the distribution of titanium content in the craters are quite different. Therefore, we use 4km as the threshold, the diameter of crater less than 4km is divided into simple impact crater, more than 4km is divided into complex crater.

4.2. The Classification of Complex Craters

Mare basalt can be divided into three types based on the content of titanium, namely high titanium basalt, low titanium basalt, and high-alumina low-titanium basalt (Cloutis, 1991). As shown in Table 2, the shape of the more regular crater such as flat, no uplift, etc., the titanium content distribution curve in line with or similar to the normal distribution. Irregular shape of the impact of the crater, such as containing the central peak and uplift, etc., the titanium content distribution curve in the fitting of the normal curve effect is much worse. We can determine the result of fitting by calculating the adjusted R-square of fit. The formula is as equation (2).

$$adjusted\ R\text{ - }square = 1 - SSE(n\text{-}1)/SST(v) \tag{2}$$

Where $SSE = \sum_{i=1}^{n} w_i(y_i - \hat{y}_i)^2$
$SST = \sum_{i=1}^{n} w_i(y_i - \bar{y})^2$

The information of the titanium element is extracted by the band ratio with the center wavelength of 415nm/750nm (Yu, 2009). The non normal distribution curve type of titanium craters should match following formula:

$$adjusted\ R\text{ - }square = 1 - SSE(n\text{-}1)/SST(v) <= 0.9 \tag{3}$$

Otherwise the craters are classified as normal distribution curve type of titanium.

position	shape	normal curve fitting	profile
N42°-41°, E335°-336°	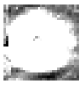	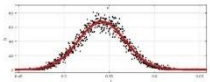 adjusted R-square: 0.9661	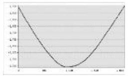
N48°-49°, E327°-328°		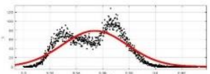 adjusted R-square: 0.7830	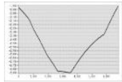

Table 2. A comparison of regular and irregular craters

5. EXPERIMENT AND ANALYSIS

The method described in this paper based on the data of multi band images (MI) obtained by SELENE. The total number of bands is nine. Wavelengths of five bands located in visible light spectrum are 415nm, 750nm, 900nm, 950nm, 1000nm. Those images have 20m spatial resolution. Another four bands whose spatial resolution is 62m belong to near-infrared and their wavelengths are 1000nm, 1050nm, 1250nm, 1548nm. We use DEM from LOLA of LRO, whose spatial resolution is 30m, comparing with results of our method to judge the accuracy of our classification. The tested area located in a mid-latitude area from 39°N-50°N, 25°W-38°W in Sinus Iridum.

number	position	shape	diameter	normal curve fitting	adjusted R-square	profile
1	N41°-40°, E334°-335°		4.0km	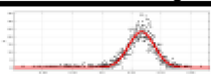	0.9200	
2	N41°-40°, E335°-336°		4.4km	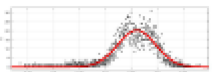	0.8662	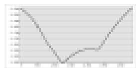
3	N42°-41° ,E335°-336°		4.5km	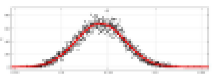	0.9661	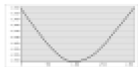
4	N43°-42° ,E329°-330°		4.2km	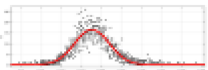	0.8744	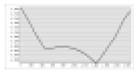

Table 1. A comparison of 4 impact craters whose diameters are about 4km.

5.1. Result of Extraction in MI

Carry out threshold segmentation, region growing, adding conditions of image characters, extracting the edge of craters and fitting into standard circles to the MI image of N39°-40°, E323°-324°. Figure 4 shows the result of extraction.

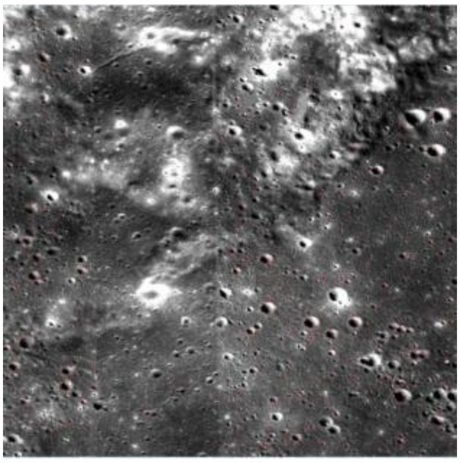

Figure 4. The result of extraction. The strip in the picture was obtained under different sunlight condition. As a result, some craters were not extracted in this paper. We just discuss wrong extraction. We do not take non extracted into consideration.

5.2. Elimination of Wrong Extracted Craters

We deal with the above image by using band ratio 1250nm/750nm to get the information of iron. After processing, the max and min of DN value in this image are 2.522866 and 0.997822 separately. Then, set the area whose DN value between 0.997822 and 1.35 as "non iron" area. The testing result was in Figure 5. Craters in red circles are extracted by the algorithm based on feature matching. In the red squares are craters right for artificial recognition but wrong for "non iron" algorithm. Pink squares show craters wrong for artificial recognition, right for "non iron" algorithm. Green squares are right for both artificial recognition and "non iron" algorithm. Other craters signed only by red circles are wrong for both artificial recognition and "non iron" algorithm.

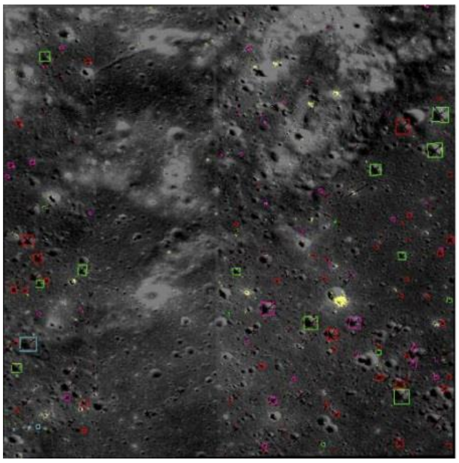

Figure 5. Extracting and "non iron" algorithm result

By judging whether the extracted standard circle contains "non iron" region or not, the correctness of the impact crater could be judged. Table 3 is the confusion matrix of 505 extracted craters.

Artificial Recognition / "Non iron" Algorithm	right	wrong
right	20	36
wrong	65	384

Table 3. Confusion matrix of wrong extracted craters

Accuracy of algorithm based on feature matching:
(20+65) /505=16.8%
Accuracy of "non iron" algorithm:
(20+384) /505=80.0%

As is shown above, in mid-latitude area the accuracy of algorithm based on feature matching is low. What is more, after adding "non iron" algorithm, the accuracy significantly improved.

5.3. Identify the Types of Craters

There are no craters whose diameters are greater than 4km in N39°-40°, E323°-324°, so all the craters in this area belong to simple type. Gather statistics of craters whose diameters are greater than 4km in N40°-50°, E322°-335°. Carry out band ratio 415nm/750nm to these images, to get the information of titanium (Yu, 2009). Match the distribution of titanium with normal distribution curve and calculate the adjusted R-square. In the following table 4, craters 1, 3, 5, 7, 8, 9, 10, 11, 13 have adjusted R-square less than 0.9, they are non normal distribution curve type of titanium, others are normal distribution curve type of titanium.

5.4. Discussion

Currently, the research on impact craters in the world mainly stays at the extraction level, and the accuracy of the extraction is limited due to the limitation of the data accuracy and the multiplicity of Solutions. What's more, few scholars study further inspection and classification after extracting the craters. Aiming at this problem, this paper presents a crater inspection and classification algorithm based on the spectral characteristics of lunar rocks and minerals.

In the process of experiment, we found that the distribution of iron in the crater is less, while iron is rich in lunar regolith . Therefore, speculated that this phenomenon is due to the impact on surface, soil is splashing out. Based on the statistics of 15 craters with diameter greater than or equal to 4km in the experimental area, it is found that the diameter of the crater approximately 4km shows great difference. Hence, in this article, threshold as the 4km in diameter, craters whose diameters are less than 4km are divided into simple type, the others are divided into complex type. Some craters whose wall or bottom has uplifted part, and the distribution of titanium content have a large proportion near the uplifted part, as shown in Figure 6.

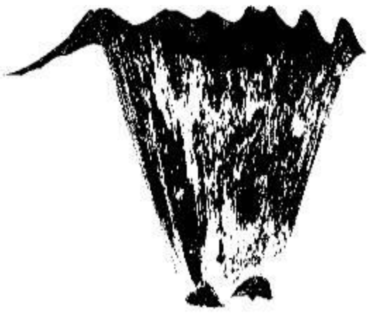

Figure 6. Effect picture of titanium content in impact crater, the white area is relatively high content of titanium parts, N43° - 44°, E333° - 334°

Speculates that is because the craters breaking the surface material, release of pressure results to the spring back and the deeper underground materials exposed. Speculates that the

https://doi.org/10.5194/isprs-archives-XLII-3-W1-199-2017

mechanism is shown in Figure 7.


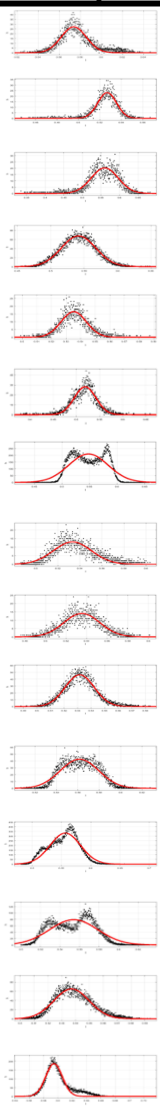
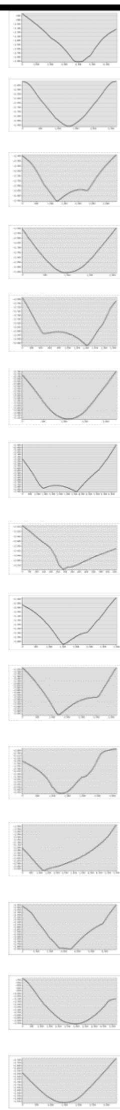

number	position	shape	diameter	Type	normal curve fitting	adjusted R-square	profile
1	N41°-40° E323°-324°		7.6KM	Non normal		0.8949	
2	N41°-40° E334°-335°		4KM	Normal		0.92	
3	N41°-40° E335°-336°		4.4KM	Non normal		0.8662	
4	N42°-41° E335°-336°		4.5KM	Normal		0.9661	
5	N43°-42° E329°-330°		4.2KM	Non normal		0.8744	
6	N44°-43° E326°-327°		5.2KM	Normal		0.9142	
7	N44°-43° E333°-334°		14KM	Non normal		0.7835	
8	N44°-43° E335°-336°		4KM	Non normal		0.7927	
9	N46°-45° E325°-326°		5.2KM	Non normal		0.8298	
10	N47°-46° E327°-328°		7KM	Normal		0.8463	
11	N48°-47° E323°-324°		7.4KM	Non normal		0.8959	
12	N49°-48° E326°-327°		15KM	Normal		0.9292	
13	N49°-48° E327°-328°		12KM	Non normal		0.783	
14	N49°-48° E328°-329°		8KM	Normal		0.9393	
15	N50°-49° E334°-335°		10KM	Normal		0.9455	

Table 4. Statistical table of impact craters whose diameters are greater than 4km

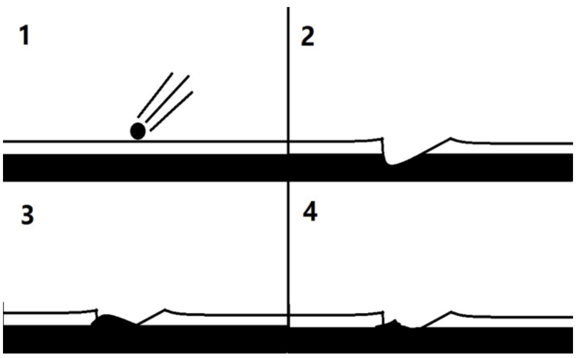

Figure 7. Schematic diagram of the different forming mechanism of the uplift part and the non-uplift part of the titanium content. The white and black parts in the figure are different strata, and their titanium content is different.

It is believed that with the improvement of data accuracy and the optimization of research methods, the relative relationship between the material composition and its morphological structure will be deeper understood and investigated.

6. CONCLUSIONS

Based on the spectral characteristics of the lunar rocks and minerals, the error removal and the classification of impact craters are carried out in this paper, and the following conclusions are obtained:

1. By determining whether the standard circle contains "non iron" element to determine whether the extraction of the craters is correct, we raised the crater correct extraction rate from 16.8% to 80.0% in the mid-latitude test area.

2. We calculated 15 craters whose diameters are greater than 4km in the test area. The titanium content distribution of each complex crater was compared with normal curve. After the threshold was set by adjusted R-square, we

divided the complex craters into the normal/non normal distribution curve type of titanium, in order to achieve the purpose of classification of complex craters.

3. A classification of complex types based on the distribution of titanium content is proposed.

Due to the limited number of impact craters in the test area and the complexity of the morphological structure and material composition of the impact crater itself, the method we proposed has large room for improvement. We will study the relative relationship between the morphological structure and the material composition in the next stage and try to use the method of deep learning in which a large number of craters will be trained to improve the accuracy of the algorithm and be fully automated.

REFERENCE:

Chen, W., 2009. The identification of special targets based on special features of Chang'e-1 CCD data. *Remote Sensing for Land & Resources,* (4), pp. 40-44.

Feng, J., 2010. Autonomous crater detection and matching on planetary surface. *Acta Aeronautica et Astronautica Sinica,* 31(9), pp. 1858-1863.

Homma, K., 1997. Massively parallel processing for crater recognition. Lunar and Planetary Science XXVIII, pp. 589.

Jin, L., 2009. Characteristics of lunar craters on the first image of Chang'e-1 satellite. *Journal of Jilin University (Earth Science Edition),* 39(5), pp. 942-946.

Kim, J., 2005. Automated crater detection, a new tool for mars cartography and chronology. *Photogrammetric Engineering & Remote Sensing,* 71(10), pp. 1205-1217.

Luo, Z., 2014. The automatic extraction and recognition of lunar impact craters fusing CCD images and DEM data of Chang'e-1. *Acta Geodaetica et Gartographica Sinica,* 43(9), pp. 924-930.

Magee, M., 2003. Automated identification of Martian craters using image processing. Lunar and Planetary Science XXXIV, pp. 2-3.

Sawabe, Y., 2005. Automatic crater detection algorithm for the lunar surface using multiple approaches. Journal of Remote Sensing Society of Japan, 25(2), pp. 157-168.

Stepinski, T., 2009. Machine cataloging of impact craters on mars. *Icarus,* 203(1), pp. 77-87.

Turk, M., 1991. Eigenfaces for recognition. *Journal of Cognitive Neuroscience,* 3(1), pp. 71-86.

Urbach, E., 2009. Automatic detection of Sub-Km craters in high resolution planetary images. *Planetary & Space Science,* 57(7), pp. 880-887.

Wang, J., 2015. A global inventory of lunar craters: identification, classification, and distribution. *Progress in Geography,* 34(3), pp. 330-339.

Wang, Z., 2011. Analysis of spectral charateristics of Lunar soil and quantitative inversion of minerals information. China University of Geosciences (Beijing).

Yu, Y., 2009. The inversion of vegetation structural parameters using dual-baseline polarimetric SAR interferometry. *Remote Sensing for Land & Resources,* (4), pp. 45-52.

Yue, Z., 2008. Automatic identification by object-oriented classification method. *Chinese Science Bulletin,* 53(22), pp. 2809-2813.

Coarse-to-Fine Extraction of Small-Scale Lunar Impact Craters From the CCD Images of the Chang'E Lunar Orbiters

Zhizhong Kang, Xingkun Wang, Teng Hu, and Juntao Yang

***Abstract*— Lunar impact craters form the basis for lunar geological stratigraphy, and small-scale craters further enrich the basic statistical data for the estimation of local geological ages. Thus, the extraction of lunar impact craters is an important branch of modern planetary studies. However, few studies have reported on the extraction of small-scale craters. Therefore, this paper proposes a coarse-to-fine resolution method to automatically extract small-scale impact craters from charge-coupled device (CCD) images using histogram of oriented gradient (HOG) features and a support vector machine (SVM) classifier. First, large-scale craters are extracted as samples from the Chang'E-1 images with spatial resolutions of 120 m. The SVM classifier is then employed to establish the criteria for classifying craters and noncraters from the HOG features of the extracted samples. The criteria are then used to extract small-scale craters from higher resolution Chang'E-2 CCD images with spatial resolutions of 1.4, 7, and 50 m. The sample database is updated with the newly extracted small-scale craters for the purpose of the progressive optimization of the extraction. The proposed method is tested on both simulated images and multiple resolutions of real CCD images acquired by the Chang'E orbiters and provides high accuracy results in the extraction of the small-scale impact craters, the smallest of which is 20 m.**

***Index Terms*— Chang'E satellites, charge-coupled device (CCD) images, histogram of oriented gradient (HOG) feature, small-scale impact craters, support vector machine (SVM) classifier.**

I. Introduction

IN RECENT years, the leading countries and organizations in the aerospace industry have initiated a new round of lunar exploration projects, such as NASA's Lunar Reconnaissance Orbiter and Lunar Crater Observation and Sensing Satellite, China's Chang'E-1 and Chang'E-2 orbiters [1], and Japan's SELenological and Engineering Explorer, with the goal of returning to the moon [2]. These satellites have provided reliable data for the planetary researches, such as studies of the spatial differences and distributions of the linear and circular structures associated with impact craters [3]–[7].

The complex topography and geomorphology of the moon's surface have been studied by determining the distributions and characteristics of linear and circular structures [8]–[12]. Impact craters are among the most noticeable geomorphological unit on the planetary surface. Their morphological characteristics and spatial distributions have been researched in recent studies, which yields significant information primarily regarding studies of relative and absolute surface chronologies, erosional processes, hydrological evolution, and climate history [13]. To date, a large number of crater detection algorithms have been proposed. The morphological fitting-based methods, such as circular Hough transform [14]–[16] and generalized Hough transform-based ellipse detection method [17], were exploited to automatically identify impact craters from the planetary images. Xie *et al.* [18] proposed a method for detecting craters that is based on infrequently used morphological characteristics, such as centers and rims of simple craters, and the slopes and derivatives of complex ones, to complete current crater catalogs. Cheng *et al.* [19] used the conic fitting method to automatically identify asteroid impact craters in the framework of optical navigation by spacecraft, which can provide the detection rate with over 90% and the false alarm rate with less than 5%. Salamunićcar and S. Lončarić [20] proposed a crater detection algorithm based on fuzzy edge extraction operator and the Hough/Radon transform to identify impact craters from digital topographic data, which can update the existing crater catalogs. Ding *et al.* [21] selected crater candidates using multiresolution feature point extraction and then obtained craters using region growing, edge extraction, and ellipse fitting based on the statistical method. Kang *et al.* [22] proposed a method to extract possible crater candidates based on their geometric features using charge-coupled device (CCD) images from the Chang'E-1 satellites and improved the final selection by using 3-D features extracted from digital elevation model. These unsupervised methods have the advantage of being fully autonomous without human annotation. Nevertheless, as the previous studies [22]–[24] introduced, the morphological fitting-based methods are generally suitable for extracting large craters.

With the increasing availability of the high-resolution imagery or topography data, many researchers were also devoted to detecting and cataloging small-scale impact craters,

Manuscript received August 30, 2017; revised February 2, 2018 and June 7, 2018; accepted June 15, 2018. This work was supported in part by the Natural Science Foundation of China under Grant 41471360 and in part by the National Key Research and Development Program of China under Grant 2016YFE0104400. *(Corresponding author: Zhizhong Kang.)*

The authors are with the School of Land Science and Technology, China University of Geosciences, Beijing 100083, China (e-mail: zzkang@cugb.edu.cn; 1145441876@qq.com; huteng@cugb.edu.cn; jtyang66@126.com).

Color versions of one or more of the figures in this paper are available online at http://ieeexplore.ieee.org.

Digital Object Identifier 10.1109/TGRS.2018.2852717

which can extend the database of the geological tectonics of the moon to better estimate the geological ages of various moonscapes, on planetary surface. Bandeira *et al.* [25] automatically recognized Martian impact craters with radii larger than 5 pixels based on a probability volume created by template matching on images of planetary surface. Grumpe and Wöhler [26] synthetically generated templates based on Lunar Orbiter Laser Altimeter track data and knowledge about the reflectance behavior of the surface as well as the known illumination and viewing geometry for automatic detection of small craters (<10 km diameter). Following the idea of generating crater templates developed by Grumpe and Wöhler [26], Salih *et al.* [27] developed a template-based crater detection method for a mosaic of wide-angle camera images of the Lunar Reconnaissance Orbiter Camera under known illumination condition to obtain the crater size-frequency distribution, which is then utilized for estimating the absolute model age of the surface. However, template matching-based method requires a known illumination direction of examined area, and its recognition accuracy is greatly affected by the templates and the detection sensitivity threshold.

In addition to the template matching-based methods, scholars also introduced machine learning into the automatic identification of small craters and constructed the model classifier to detect them. Stepinski *et al.* [28] considered round and symmetric topographic depressions using the Mars Orbiter Laser Altimeter 128 pixels/degree digital elevation model of Mars as crater candidates, which were assigned either crater or noncrater labels using decision trees. Urbach and Stepinski [12] developed a fully automatic detection of sub-kilometer craters in large panchromatic images centered on the Nanedi Valles on Mars. To date, many crater detection methods have been inspired by face or pedestrian detection which used gray-scale texture and shape features, such as local binary pattern (LBP) [29], Haar-like [30], and histogram of oriented gradient (HOG) [31], and learned a supervised method for identification, which can enhance the classification accuracy. Xin *et al.* [24] first extracted dark-area regions as crater candidates in a full high-resolution imaging science experiment image and then detected small crater inside a candidate site using Adaboost classifier which combined LBP and Haar-like. Liu *et al.* [32] considered the impact crater as a closed basin structure and detected impact crater region using watershed algorithm from lunar digital elevation model. Di *et al.* [33] developed a boosting method that combined LBP, Haar-like, and scaled Haar-like, for crater detection from topographic data. Bandeira *et al.* [34] proposed a crater detection method for identifying sub-kilometer craters in high-resolution panchromatic images. In their framework, they first found crater candidates using shape features, and then used texture features, namely, Haar-like, in combination with boosting-based method to identify these candidates into craters and noncraters. Martins *et al.* [35] automatically recognized impact craters from Mars surface images captured by the Mars Orbiter Camera onboard Mars Global Surveyor probe with Haar-like features combined with a boosting algorithm. Wang *et al.* [36] proposed a new sparse boosting method, into which an improved sparse kernel density estimator was integrated, for automatically detecting sub-kilometer craters using texture features extracted from a large and high-resolution image of Martian surface. Jin and Zhang [37] automatically detected small craters from the images acquired by high-resolution stereo camera (HRSC) onboard Mars Express based on the modified boosting method, which was learned by constructing a dual-threshold weak classifier and adjusting the criterion of updating weights in the training process. For these conventional passive learning methods, in which the training samples are generally chosen randomly without interaction with the classifier, their recognition performances are primarily determined by the quality and quantity of training samples.

In order to improve the classifier performance or reduce the number of samples that the classifiers require, some strategies, such as feature dimension reduction [13], [38], active learning or semisupervised learning [39], and transfer learning [40], were also adopted in crater detection. Cohen and Ding [13] improved the classification performance of a Bayesian classifier by reducing the number of texture features via genetic search method to detect impact craters larger than 200 m in nadir panchromatic image acquired by HRSC aboard Mars Express spacecraft. Liu *et al.* [38] used Bernoulli trials for removing irrelevant texture features to detect small craters that were between 200 and 5000 m in diameters. Liu *et al.* [39] built an adaptive learning system that combined active learning with semisupervised learning to automatically recognize sub-kilometer craters using Haar-like features extracted from high-resolution panchromatic planetary images. Ding *et al.* [40] developed an automatic detection framework for sub-kilometer craters. In their framework, image texture features were extracted, in combination with boosting method to classify crater candidates into craters and noncraters. For the regions where surface morphology differs from what is characterized by the training data, transfer learning was integrated with boosting method to improve the detection performance. These strategies have led to the significant progresses for impact crater detection. However, the following challenges remain for automatically detecting the small-scale craters: impact craters, especially small-scale craters, generate various degrees of degeneration [40], which results in lack of the robust and highly descriptive features of impact craters. Moreover, the morphology among the small-scale craters is significantly different, which causes the difficulty of choosing the training samples.

Consequently, this paper presents a novel coarse-to-fine approach to extract small-scale craters using large-scale craters as samples, from which the extraction criteria are determined using the features of HOG of the samples. The contributions of the proposed method comprise the following.

1) HOG features are used to measure the similarity among impact craters, which is insensitive to the illumination change.
2) A coarse-to-fine extraction strategy is developed. We first establish a coarse sample library, consisting of the large-scale craters extracted by Kang *et al.* [22], to learn an initial support vector machine (SVM) classifier.

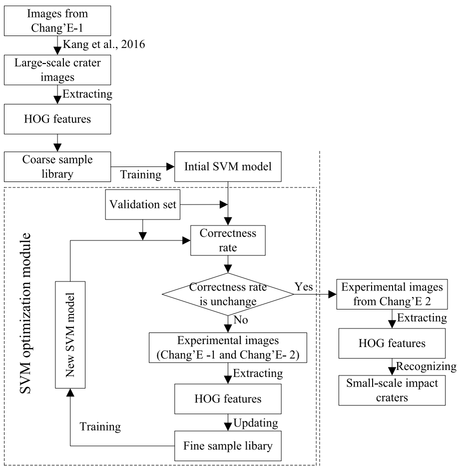

Fig. 1. Workflow of our proposed method.

(a) (b)

Fig. 2. Comparison between (a) large-scale crater in Chang'E-1 image and (b) small-scale crater in Chang'E-2 image.

(a) (b)

Fig. 3. Effect of noise filtering on edge extraction. (a) Results from an unfiltered image. (b) Results after noise removal.

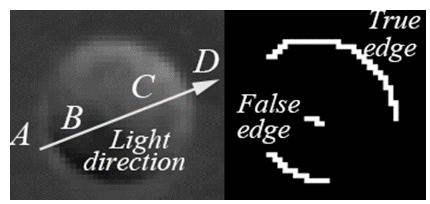

Fig. 4. Edge extraction results for a typical impact crater.

Considering the fact that planetary surfaces are not homogeneous [40], new crater samples are iteratively added to the existing training set, which is exploited to optimize the SVM classifier.

We describe the algorithm of the coarse-to-fine extraction of the small-scale lunar impact craters in Section II. Section III discusses the test results, after which we offer conclusions and suggestions for further research in Section IV.

II. Coarse-to-Fine Extraction of Small-Scale Lunar Impact Craters

Unlike most objects subjected to automated recognition in images, impact craters, especially small-scale impact craters, usually are abundant [39] and lunar surfaces are heterogeneous, where nonuniform surface morphology frequently exists [40]. Since impact craters of different sizes may have similar characteristic patterns, i.e., nearly round edge, this paper proposes a novel coarse-to-fine strategy to extract small-scale craters using a machine learning method, which employs the HOG features of large-sized craters as training samples.

Fig. 1 shows the workflow of our proposed method. First, large-scale craters are extracted from the Chang'E-1 images with spatial resolutions of 120 m using the method proposed by Kang *et al.* [22], and HOG features of the extracted large-scale craters and noncraters are calculated to establish a coarse sample library. Then, we adopt the SVM classifier as a base classifier to find the criteria for distinguishing craters from noncraters since SVM performs well in determining the classifications with limited samples [41]–[43]. In the step of learning, the small-scale craters are identified from the high-resolution Chang'E-2 images using the learned SVM classifier and the SVM classifier performance is progressively optimized by the fine sample library that is updated using the HOG features of the extracted small-scale craters. Finally, these criteria are used to extract small-scale craters from the higher resolution Chang'E-2 CCD images with spatial resolutions of 1.4, 7, and 50 m. Key algorithms of our proposed method are given in more detail in the following.

A. Establishment of Training Sample Database

As shown in Fig. 2, the large craters in the Chang'E-1 images look similar to the smaller ones in the Chang'E-2 images. Therefore, the extraction of training samples is performed using the method proposed by Kang *et al.* [22] on the images acquired by the CCD camera onboard the Chang'E-1 orbiters.

To remove the effects of noise, the input data sets are denoised using a bilateral filter, which is a nonlinear, self-adaptive filter that considers both spatial information and gray similarities; it also discards noise while retaining the edge information [44]. Afterward, the Robert operator is used for edge extraction because it requires less computational work than other operators, such as the Sobel, Prewitt, and Canny operators. However, a few false edges may still be extracted due to illumination effects, as shown in Fig. 3(b).

False edges are identified and removed by exploiting the direction of the light, which is computed based on the camera acquisition time and the viewing angle with respect to the sun's apparent position provided by the configuration file of each image. The process is implemented using the fact that the gray value of a true edge decreases in the direction of the light, whereas the gray value of a false edge may increase (Fig. 4). Specifically, if the false edges are caused by the contrast between the shadow and the illuminated regions inside the crater, the gradient of this edge will be oriented in the opposite direction to the light direction. Accordingly, the absolute value of the angle between the gradient and the light direction will

This article has been accepted for inclusion in a future issue of this journal. Content is final as presented, with the exception of pagination.

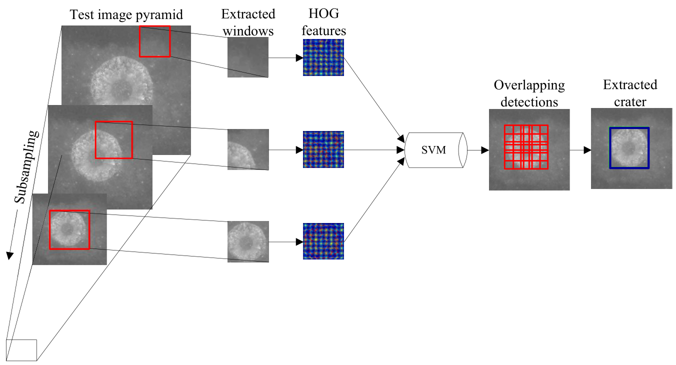

Fig. 5. Example of detecting crater regions.

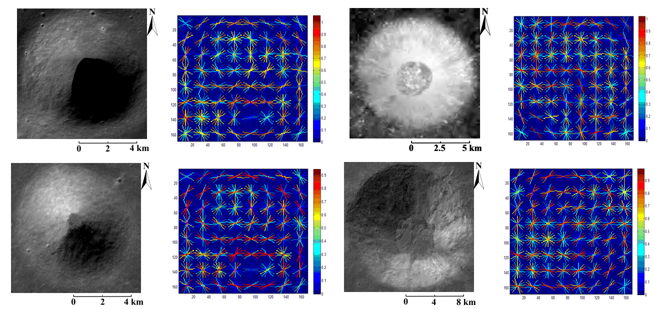

Fig. 6. Craters in the images with different illuminations.

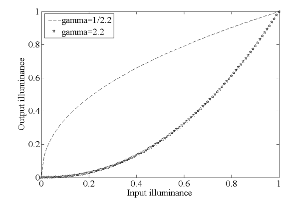

Fig. 7. Relationship between illuminance and gamma index.

be greater than 90°. (The value of the angle ranges from −180° to 180°). In contrast, the gradient direction of a true edge is expected to be the same as that of the light direction, which in turn causes the absolute value of the angle between the two to be less than 90°. This condition is expressed as follows:

$$\nabla f \cdot n > 0 \tag{1}$$

where n represents the light direction vector, and ∇f is the gradient on the edge that is detected at (x, y). The product in (1) is a scalar product. If the gradient direction of an edge point forms an angle that is less than 90° from the light direction, (1) is satisfied. Otherwise, the edge point is considered to be a false edge. Then, impact craters are extracted using the RANSAC-based circle fitting approach, which exploits the fact that impact craters are nearly round. Both craters correctly extracted craters as positive samples and noncraters as negative samples are added to the training sample database.

B. Detecting Crater Regions

In the step of SVM-based recognition, following face or pedestrian detection, we scan the whole test images using a sliding window [45] and each extracted sliding window is classified as impact crater or nonimpact crater (as shown in Fig. 5). To detect impact craters of different sizes, we resize the test image iteratively and fix the size of sliding window. During iteration, the test image is decreased to 0.9 times the size of the previous one. The iteration is terminated till the size of maximum crater in the test image is decreased less than the size of sliding window. Due to the sliding window in crater detection, a crater may be detected multiple times by different sizes of sliding windows. Thus, we use the nonmaximum suppression method based on the mean-shift algorithm [46] to check the position of the detected impact crater regions and delete the repeated ones.

C. Criteria for Classifying Craters and Noncraters

The illumination of craters in CCD images of different satellites may vary from each other, and the crater shapes can differ to some extent. As a feature descriptor which is invariant to changes in illumination, shadows, and geometric and photometric transformations, HOG features are used to classify craters and noncraters. Fig. 6 shows that the gray values of the crater are only distributed in the dark areas owing to illumination or shadows, which results in the loss of the image information. Therefore, before the extraction of a HOG feature, gamma correction [47] is implemented on the image to reduce the influences of illumination and shadows.

1) Gamma Correction: Gamma correction is a nonlinear operation applied to the gray values of an input image, which is defined by the following power-law expression:

$$V_{\text{out}} = A V_{\text{in}}^{\gamma} \tag{2}$$

where the nonnegative real input value V_{in} is raised to the power γ and multiplied by the constant A, to get the output value V_{out}. In the common case of $A = 1$, the inputs and outputs are typically in the range of 0–1 [48].

When the gamma index is less than 1, the image intensity and the image contrast of a low gray value will be enhanced (Fig. 7).

Fig. 8 illustrates that after the gamma correction, the distribution of the intensities of the crater image becomes even so that the crater in the image becomes easily recognizable [Fig. 8(c) and (d)].

2) Generation of HOG: Dalal and Triggs [31] proposed HOG features in 2005, which was first used in the field of pedestrian detection. The basic idea of HOG features is that the local appearance of an object can be well described by the distribution of the gradient intensities and edge directions. To extract HOG features, the image is divided into small regions (i.e., cells) and a HOG is generated for each cell as its feature descriptor. Local illumination and the contrast between the foreground and background may vary, which leads to a large variation of gradient intensities. Therefore, adjacent cells are merged into a block, where gradient intensities are normalized to form the feature descriptor of the block for the purpose of reducing the influence of illumination. The feature descriptors of all the blocks are sequentially joined

This article has been accepted for inclusion in a future issue of this journal. Content is final as presented, with the exception of pagination.

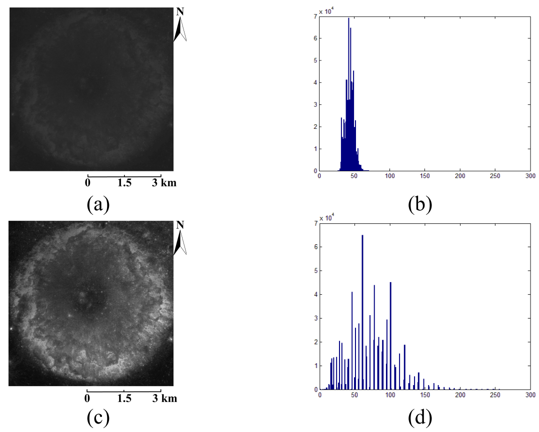

Fig. 8. Results of gamma correction (gamma = 1/2.2). (a) Crater image before correction. (b) Histogram of intensities before correction. (c) Crater image after correction. (d) Histogram of intensities after correction.

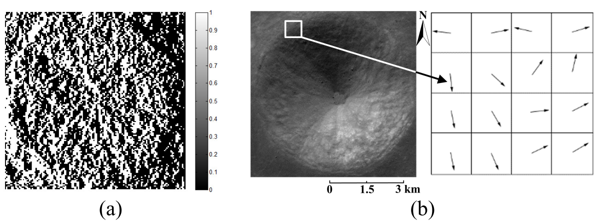

Fig. 9. Gradient intensity and gradient direction of a crater. (a) Gradient intensity. (b) Gradient direction.

to form the HOG feature of the image. Since a HOG feature is generated from local cells, and the distortions of geometry and illumination can only be present in larger areas, these features are invariant to changes in illumination and geometric and photometric transformations. Moreover, a HOG feature is able to describe the shape of an object to be detected, so it is quite suitable for the extraction of lunar craters which are similar to the shape of a circle. The detailed process is as follows:

1) First, the horizontal and vertical gradients of each pixel (i, j) are computed, from which the gradient intensity and gradient direction of the pixels (Fig. 9) are calculated using the following equation:

$$\begin{cases} G_i = f(i+1, j) - f(i-1, j) \\ G_j = f(i, j+1) - f(i, j-1) \\ G(i, j) = \sqrt{G_i(i, j)^2 + G_j(i, j)^2} \\ \alpha(i, j) = \tan^{-1}\left(\dfrac{G_j(i, j)}{G_i(i, j)}\right) \end{cases} \quad (3)$$

where $f(i, j)$ is the gray value of the pixel (i, j), $G_i(i, j)$ is the horizontal gradient, $G_j(i, j)$ is the vertical gradient, $G(i, j)$ is the gradient intensity, and $\alpha(i, j)$ is the gradient direction.

2) The image is evenly divided into cells (4×4 pixels). Fig. 10(a) shows that from the starting point at the top left corner, every 2×2 adjacent cells are merged into a block. The range of the gradient direction (0°–360°) is divided into nine bins [Fig. 10(b)]. A histogram is then generated for the nine bins to count how many gradient direction values of the pixels in a cell fall into each bin. Fig. 11 illustrates the histograms of the four cells in a block. Table I shows the bin number relative to the directions. If a gradient direction value falls into one of the nine bins shown in Fig. 11, its gradient intensity is added to the corresponding bin in the histogram.

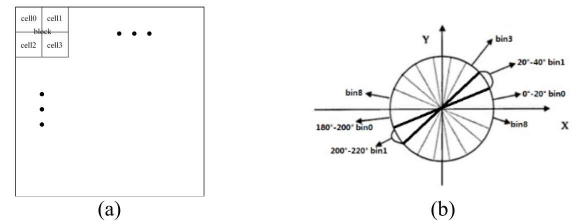

Fig. 10. Process of generating a HOG. (a) Evenly divided cells. (b) Division of the range of the gradient direction (0°–360°).

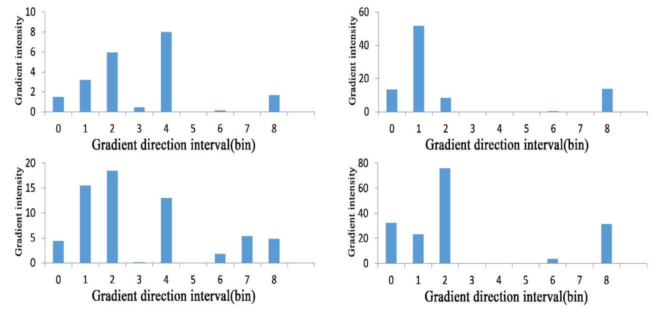

Fig. 11. HOGs of the four cells in a block.

TABLE I

BIN NUMBERS RELATIVE TO THE DIRECTIONS

Bin number	0	1
Angle range	[0°,20°)∪[180°,200°)	[20°,40°)∪[200°,220°)
Bin number	2	3
Angle range	[40°,60°)∪[220°,240°)	[60°,80°)∪[240°,260°)
Bin number	4	5
Angle range	[80°,100°)∪[260°,280°)	[100°,120°)∪[280°,300°)
Bin number	6	7
Angle range	[120°,140°)∪[300°,320°)	[140°,160°)∪[320°,340°)
Bin number	8	
Angle range	[160°,180°)∪[340°,360°)	

Due to the correlation between adjacent cells in the image and adjacent bins of the gradient directions, if the histogram of a cell is generated by only considering that cell, many of the gradient directions in the cell may be concentrated in one bin, which is not really the case. To tackle this problem, trilinear interpolation is employed to generate the histogram of a cell.

In Fig. 12, as far as a pixel (i, j) is concerned, it locates at cell 0 and its gradient direction falls into bin 3 in the histogram. The distances between pixel (i, j) and the centers of the four adjacent cells (i_1, j_1), (i_2, j_1), (i_1, j_2), and (i_2, j_2), as well as the differences between the gradient directions of pixel (i, j) and the central directions of its neighboring bins 2 and 3, are regarded as the weights with which (4) is

This article has been accepted for inclusion in a future issue of this journal. Content is final as presented, with the exception of pagination.

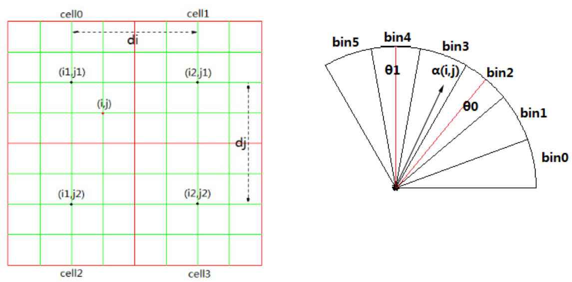

Fig. 12. Illustration of trilinear interpolation.

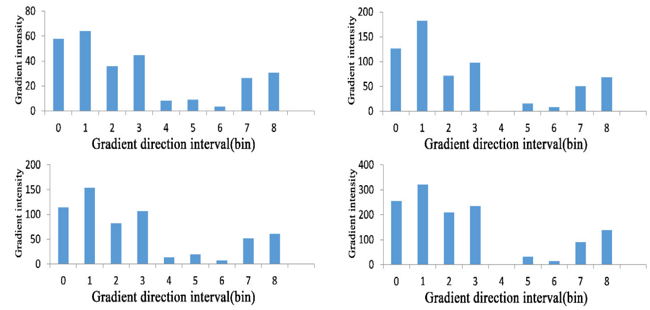

Fig. 13. Histograms of gradient directions of the four adjacent cells generated by using trilinear interpolation.

used to add the gradient intensity of pixel (i, j) to those of its neighboring bin 2 and bin 3 in the histogram of cell0, cell1, cell2, and cell3

$$
\begin{aligned}
&h(i_1, j_1, \mathrm{bin2}) \leftarrow h(i_1, j_1, \mathrm{bin2})\\
&\quad + G(i, j)\left(1 - \frac{i - i_1}{d_i}\right)\left(1 - \frac{j - j_1}{d_j}\right)\left(1 - \frac{\alpha(i, j) - \theta_0}{d_\theta}\right)\\
&h(i_1, j_1, \mathrm{bin3}) \leftarrow h(i_1, j_1, \mathrm{bin3})\\
&\quad + G(i, j)\left(1 - \frac{i - i_1}{d_i}\right)\left(1 - \frac{j - j_1}{d_j}\right)\left(1 - \frac{\alpha(i, j) - \theta_1}{d_\theta}\right)\\
&h(i_2, j_1, \mathrm{bin2}) \leftarrow h(i_2, j_1, \mathrm{bin2})\\
&\quad + G(i, j)\left(1 - \frac{i - i_2}{d_i}\right)\left(1 - \frac{j - j_1}{d_j}\right)\left(1 - \frac{\alpha(i, j) - \theta_0}{d_\theta}\right)\\
&h(i_2, j_1, \mathrm{bin3}) \leftarrow h(i_2, j_1, \mathrm{bin3})\\
&\quad + G(i, j)\left(1 - \frac{i - i_2}{d_i}\right)\left(1 - \frac{j - j_1}{d_j}\right)\left(1 - \frac{\alpha(i, j) - \theta_1}{d_\theta}\right)\\
&h(i_1, j_2, \mathrm{bin2}) \leftarrow h(i_1, j_2, \mathrm{bin2})\\
&\quad + G(i, j)\left(1 - \frac{i - i_1}{d_i}\right)\left(1 - \frac{j - j_2}{d_j}\right)\left(1 - \frac{\alpha(i, j) - \theta_0}{d_\theta}\right)\\
&h(i_1, j_2, \mathrm{bin3}) \leftarrow h(i_1, j_2, \mathrm{bin3})\\
&\quad + G(i, j)\left(1 - \frac{i - i_1}{d_i}\right)\left(1 - \frac{j - j_2}{d_j}\right)\left(1 - \frac{\alpha(i, j) - \theta_1}{d_\theta}\right)\\
&h(i_2, j_2, \mathrm{bin2}) \leftarrow h(i_2, j_2, \mathrm{bin2})\\
&\quad + G(i, j)\left(1 - \frac{i - i_2}{d_i}\right)\left(1 - \frac{j - j_2}{d_j}\right)\left(1 - \frac{\alpha(i, j) - \theta_0}{d_\theta}\right)\\
&h(i_2, j_2, \mathrm{bin3}) \leftarrow h(i_2, j_2, \mathrm{bin3})\\
&\quad + G(i, j)\left(1 - \frac{i - i_2}{d_i}\right)\left(1 - \frac{j - j_2}{d_j}\right)\left(1 - \frac{\alpha(i, j) - \theta_1}{d_\theta}\right)
\end{aligned}
\tag{4}
$$

where $h(i_1, j_1, \theta) \ldots h(i_2, j_2, \theta)$ denotes the statistics of the gradients of bin 2 and bin 3 in the histogram of cell 0, cell 1, cell 2 and cell 3; $G(i, j)$ and $\alpha(i, j)$, respectively, indicate the gradient intensity and direction of pixel (i, j); d_i and d_j are the horizontal and vertical differences between the central pixels of adjacent cells; and d_θ represents the angular difference between the central directions of two neighboring bins. The size of a cell is set as 4×4 pixels, while the width of a bin is 40°, so $d_i = d_j = 4$ pixels, $d_\theta = 40°$.

As presented above, the weighted gradient intensity of each pixel is added to those of its neighboring bins in the histogram of the four cells adjacent to the pixel of interest, which finally produces the histogram of the gradient directions for each cell (Fig. 13).

When the whole image is divided into cells for computation, an aliasing effect will be present if only the correlations between the pixels in a cell are considered instead of the pixels between adjacent cells. As a result, the gradient directions of pixels may be concentrated in a certain bin, which fails to represent the true distribution of those gradient directions of an image (Fig. 13). Fig. 13 shows that an evener histogram of gradient directions can be generated, because the algorithm of trilinear interpolation well considers the correlations between pixels in adjacent cells. To generate the histogram of gradient directions or the descriptor of a block, the histograms of the cells in a block are sequentially connected into the histogram of the gradient directions or the descriptor of the block. Due to the variation of the local illumination and the contrast between the foreground and background, the gradient intensity varies greatly within a cell or a block. Therefore, the L2-norm (5) was used to normalize the connected histograms

$$
v' = \frac{v}{\sqrt{\|v\|_2^2 + e^2}} \tag{5}
$$

where v is the descriptor before normalization, and v' is that one after normalization. $\|v\|_2^2$ is the 2-norm of v, and e is a small constant to keep the denominator as nonzero.

Fig. 14 illustrates the normalized block histogram of the gradient directions of the four different craters and two non-craters. In the normalized histogram, the gradient intensity of a bin increases, with the color varying from blue to red. From Fig. 14, we can tell that the histograms of the same block (highlighted in red squares) in the four crater image patches are similar to each other (e.g., the same bin reaches the highest gradient direction value), while the histograms of the same block in the two noncrater image patches are obviously different.

The descriptors of all the blocks are finally connected into a HOG feature (Fig. 15). As shown in Fig. 15, although the sizes of the crater images of Fig. 15(a)–(c) are different, their HOG features look similar, e.g., the edge of the crater presents in a near circular shape, while the HOG feature of the noncrater is irregular. This fact shows the potential of the proposed coarse-to-fine strategy for extracting small-sized craters using HOG features.

D. Crater Extraction Using SVM Classifier

After the generation of a HOG feature, we need to decide a classifier for crater extraction. In the field of machine learning,

This article has been accepted for inclusion in a future issue of this journal. Content is final as presented, with the exception of pagination.

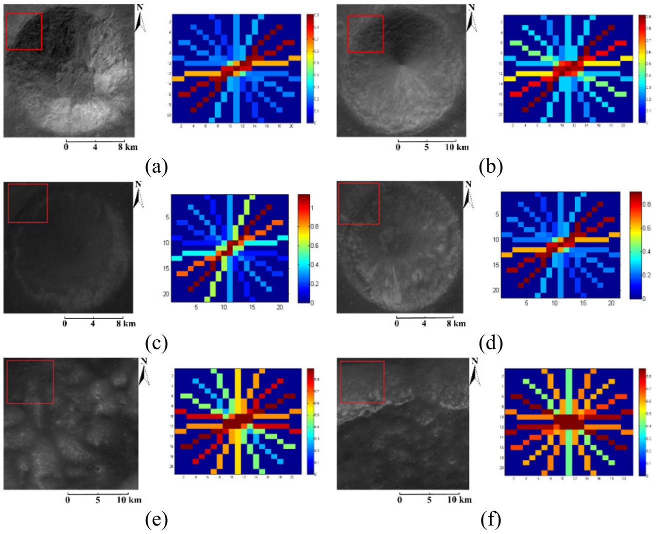

Fig. 14. Normalized block histograms of gradient directions of craters and noncraters. (a) Crater 1. (b) Crater 2. (c) Crater 3. (d) Crater 4. (e) Noncrater 1. (f) Noncrater 2.

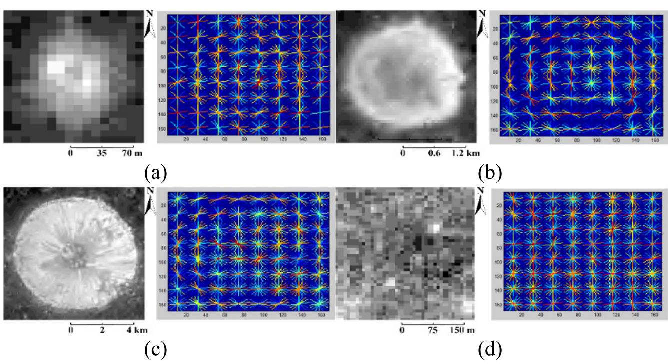

Fig. 15. HOG features of impact craters with different sizes. (a) Impact crater with 125 m diameter and its HOG feature. (b) Impact crater with 2000 m diameter and its HOG feature. (c) Impact crater with 8000 m diameter and its HOG feature. (d) Noncrater and its HOG feature.

SVM [44] displays a unique advantage when the training samples are limited and the dimensions of the features are large. Since the number of lunar impact craters is limited and a HOG feature is a high-dimensional feature, we employed SVM as the classifier to extract impact craters.

We can regard the process of crater extraction as a binary classification. The SVM classifier [44] is a binary classifier, which key idea is to map the nonlinearly separable feature space into a higher dimensional space by using kernel function, such as radial basis function (RBF) [49], and then construct the optimal hyperplane that should be as far away from the samples of both classes as possible, which is based on structural risk minimization. Suppose the sample set $T = \{(\boldsymbol{x}_1, y_1), (\boldsymbol{x}_2, y_2), \ldots, (\boldsymbol{x}_\mathrm{n}, y_\mathrm{n})\}$, where $\boldsymbol{x}_i$ denotes the HOG feature descriptor of a sample, y_i indicates the label of a sample, which is set to 1 for the crater and 0 for the noncrater, and n is the number of samples.

The SVM classification task can be converted into a mathematical function. The following equation represents a separating hyperplane:

$$f(\boldsymbol{x}) = \boldsymbol{\omega}^\mathrm{T}\boldsymbol{x} + b \tag{6}$$

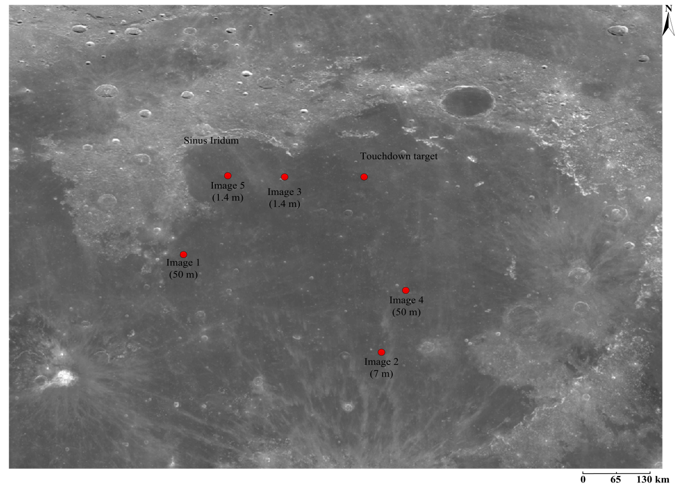

Fig. 16. Distribution of experimental CCD images with different resolutions.

where $(\boldsymbol{\omega}, b)$ is the eigenvector and eigenvalue calculated by SVM based on the samples; x is the HOG feature of an object; if the $\mathrm{sgn}(f(x)) = +1$, the object is a crater; and if the $\mathrm{sgn}(f(x)) = -1$, the object is a noncrater. The following equation is used to solve the optimal hyperplane:

$$\min \frac{1}{2}\|\boldsymbol{\omega}\|^2 \quad \text{s.t.,} \quad y_i(w^\mathrm{T}x_i + b) \geq 1, \quad i = 1, \ldots, n \tag{7}$$

where $\|\boldsymbol{\omega}\|$ denotes the norm of the eigenvector that is the length of the eigenvector; the shortest interval between sample points is regarded as 1; thus, we can have $y_i(\boldsymbol{w}^\mathrm{T}x_i + b) \geq 1$, $i = 1, \ldots, n$. For the details, please refer to [50].

E. Update of Sample Library

As proposed in Section II-A, the large-sized craters which are extracted from the Chang'E-1 images are employed as the initial samples. When identifying small-sized craters, inevitably, there are false or missing extractions. Therefore, we keep updating the sample library with extracted small-sized craters as positive samples and noncraters as negative samples, which can progressively optimize the recognition performance of SVM.

III. Experimental Results

The proposed approach was tested on both simulated images and real CCD images with different resolutions which were acquired by Chang'E orbiters and downloaded from the Science and Application Center for Moon and Deep Space Exploration of China (website: http://moon.bao.ac.cn). Fig. 16 shows the regions covered by the experimental images, which are near the landing site of Chang'E-3 (19.51° W, 44.12° N). The images were acquired using a three-line array CCD stereo camera in a push broom fashion. The orbital height of Chang'E-1 was 200 km above the lunar surface, so the swath width was 60 km, and the spatial resolution was 120 m. The orbital height of Chang'E-2 was 100 km above the lunar surface; accordingly, the swath width was 43 km, and the spatial resolution was 7 m. When passing by Sinus Iridum, the orbiter lowered its orbit to 15 km above the lunar surface;

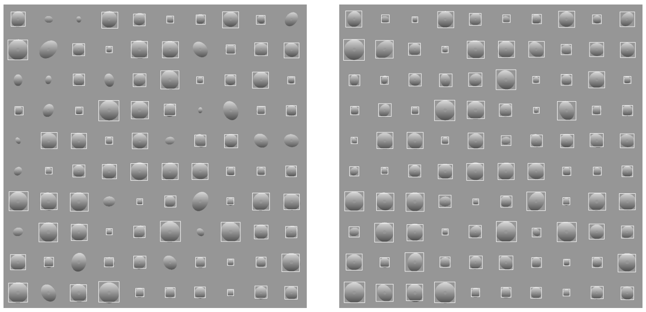

(a) (b)

Fig. 17. Coarse-to-fine extraction of simulated impact craters with different scales and different eccentricities. (a) Detection results using initial SVM classifier. (b) Detection results using optimized SVM classifier.

the spatial resolution of the CCD images acquired was accordingly increased to 1.4 m. The spatial resolution of the lunar ortho-images generated from the CCD images was 50 m.

A. Extraction of Simulated Impact Craters

To verify the effectiveness of the coarse-to-fine strategy, a simulated experiment in this paper was conducted. The simulated crater detections were determined in terms of the differences between the simulated and computed parameters of elliptical impact craters, i.e., the major axis, minor axis, center, and orientation. The simulated and computed parameters of elliptical impact craters were set randomly, where the range of orientation was $[0°, 180°)$, the range of eccentricity was $[0, 0.7]$, or the range of roundness was $[0.51, 1]$, the minimum number of pixel of major axis was 20, and the maximum number of pixel of major axis was 80. In the simulated experiment, we first used a coarse simulated crater library, which only consisted of standard circular craters, to learn an SVM classifier. As shown in Fig. 17(a), the standard circular craters and the elliptical craters with small eccentricity could be correctly detected. However, some synthetic elliptical craters with large eccentricity failed to be detected since the HOG features of these craters differed from that of standard circular craters. Then, we used the extracted elliptical craters with small eccentricity to progressively update the simulated crater library for optimizing the SVM classifier. As shown in Fig. 17(b), the synthetic craters with large eccentricity could be correctly recognized by the optimized SVM classifier.

B. Extraction of Coarse Samples From Chang'E-1 CCD Images

As presented in Section II-A, the extraction of coarse samples was performed using the method proposed by Kang *et al.* [22] (Fig. 18). We extracted 200 correct craters from the Chang'E-1 CCD images as the positive samples [Fig. 19(a)] and selected 168 noncraters as the negative samples [Fig. 19(b)]. Table II lists the statistics of the sizes of the positive samples. The diameters of the correct craters are mostly larger than 5000 m.

C. Extraction of the Craters From the Chang'E-2 CCD Images Based on Coarse Samples

Experiments were implemented using the Chang'E-2 CCD images with different resolutions based on the coarse

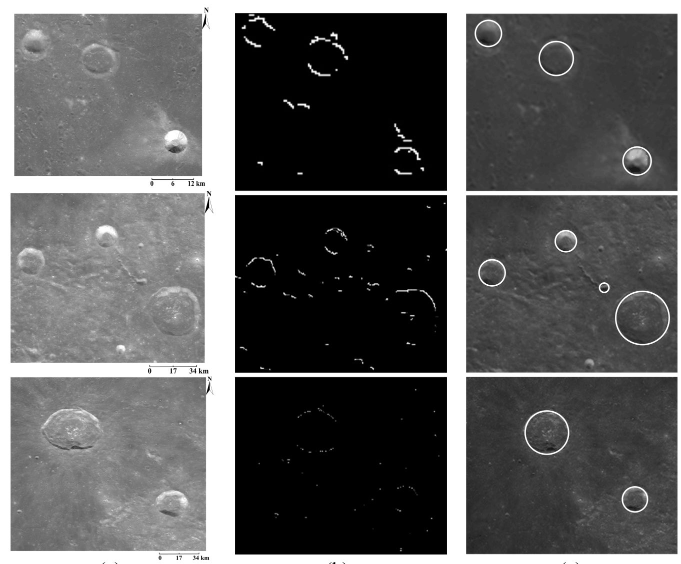

(a) (b) (c)

Fig. 18. Results of the extraction of initial samples. (a) Chang'E-1 CCD images. (b) Edge extraction after image denoising. (c) RANSAC-based edge fitting.

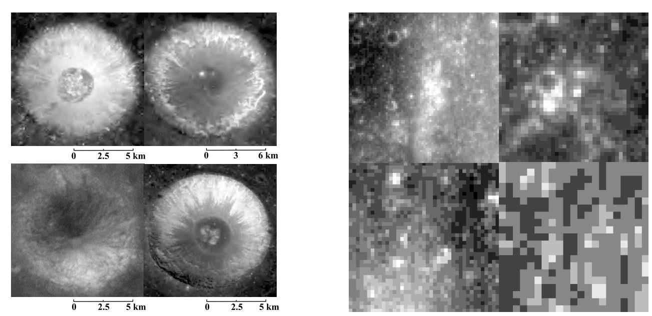

(a) (b)

Fig. 19. Coarse samples extracted from Chang'E-1 CCD images (partial). (a) Positive samples. (b) Negative samples.

TABLE II
STATISTICS OF THE SIZES OF THE POSITIVE SAMPLES

Diameter of craters (m)	Number
<5000	35
5000-10000	82
10000-20000	59
>20000	24

samples extracted from the Chang'E-1 images. In our experiment, the optimal values of the relaxation variable ξ and the parameter of the RBF σ as $\xi = 2.5$ and $\sigma = 0.0455$. Figs. 20–22 show the extraction results of the different resolution CCD images.

Tables III and IV show the statistics of the results from the three different resolution CCD images. The results acquired by using visual interpretation were considered to be ground truths. Although the HOG features of the craters in the Chang'E-1 and Chang'E-2 images may look similar, we can still find many dissimilar cases due to the clear illumination variations between the Chang'E-1 and Chang'E-2 images (Fig. 23). As a result, the average extraction rate is only 25% when only using the samples acquired from the Chang'E-1 images.

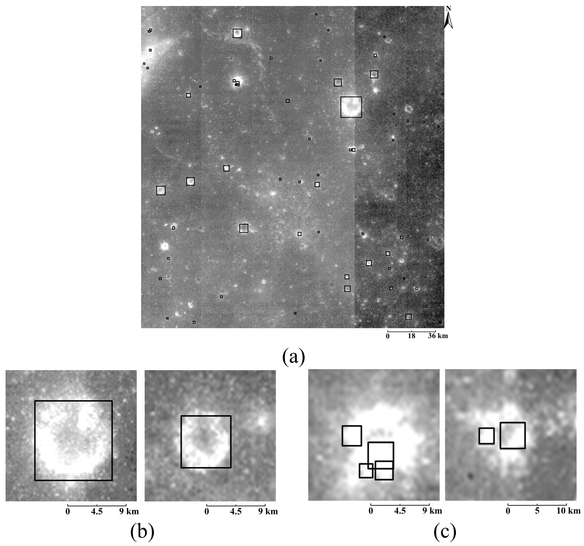

Fig. 20. Results of 50-m-resolution CCD images (Image 1). (a) Overview. (b) Correct impact craters. (c) Falsely extracted craters.

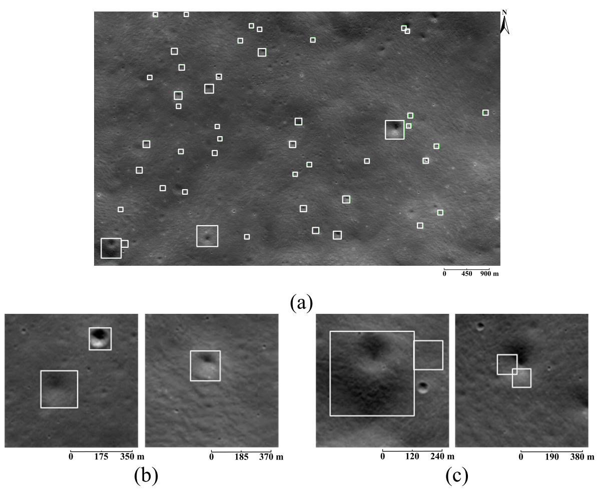

Fig. 21. Results of 7-m-resolution CCD images (Image 2). (a) Overview. (b) Correct impact craters. (c) Falsely extracted craters.

TABLE III

RESULTS OF THE EXTRACTION OF CRATERS FROM THE CHANG'E-2 CCD IMAGES BASED ON INITIAL SAMPLES

	Image(A)	Image(B)	Image(C)
Image size(pixel × pixel)	3034 × 3234	1481 × 981	1553 × 1468
Visual interpretation	242	186	276
Proposed method	65	54	88
False extraction	10	13	8
Missed extraction	187	145	196
Extraction rate (%)	22.72	22.04	28.99

D. Results of the Extraction of Craters in the Chang'E-2 CCD Images Based on Chang'E-2 Samples

To improve the extraction, we updated the sample database with the impact craters extracted from the Chang'E-2 CCD images based on some initial samples. A set of 240 impact craters under different illuminations were selected as positive samples, and 120 noncraters were selected as negative samples (Fig. 24).

To test the generalization ability of the sample set containing the craters with different resolutions, i.e., to select an optimal sample set which can perform well on different resolution images, we divided the samples into two categories, i.e., a training sample set and a test sample set. A training sample set comprising 200 positive samples and 100 negative samples

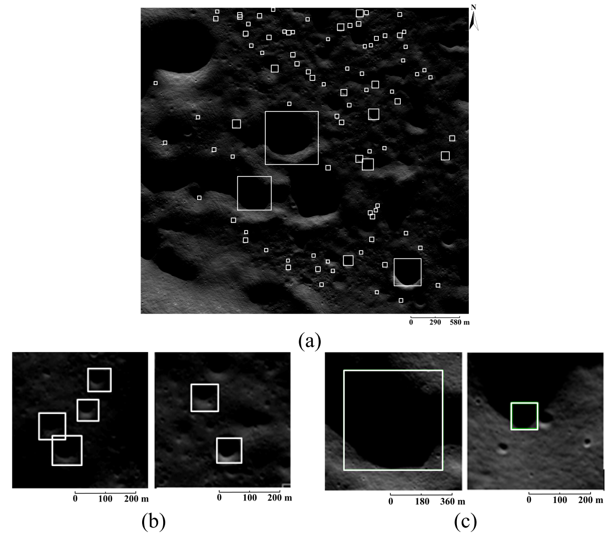

Fig. 22. Results of 1.4-m-resolution CCD images (Image 3). (a) Overview. (b) Correct impact craters. (c) Falsely extracted craters.

TABLE IV

SIZES OF THE IMPACT CRATERS EXTRACTED FROM THE CHANG'E-2 CCD IMAGES BASED ON INITIAL SAMPLES

Image(A)		Image(B)		Image(C)	
Diameter of craters(m)	Quantity	Diameter of craters(m)	Quantity	Diameter of craters(m)	Quantity
<1500	22	<300	27	<100	62
1500-3000	23	300-600	12	100-200	15
>3000	10	>600	2	>200	3

TABLE V

TEST RESULT OF THE OPTIMAL SET OF SAMPLES

Test sample set	Number of the set	Number of error detection	Rate of error detection
Positive samples	40	1	2.5
Negative samples	40	2	5

TABLE VI

TEST RESULTS OF DIFFERENT KERNEL FUNCTIONS

Kernel functions	Number of error detection	Rate of error detection (%)
Linear kernel function	19	23.75
Polynomial kernel function	12	15
RBF kernel function	3	3.75

This article has been accepted for inclusion in a future issue of this journal. Content is final as presented, with the exception of pagination.

TABLE VII
TEST RESULT OF DIFFERENT PARAMETERS

Parameters	Number of error detection	Rate of error detection (%)
$\xi = 0.25, \sigma = 0.0037$	11	13.75
$\xi = 0.5, \sigma = 0.0037$	3	3.75
$\xi = 2.5, \sigma = 0.0037$	26	32.5
$\xi = 0.5, \sigma = 0.0020$	9	11.25
$\xi = 0.5, \sigma = 0.0050$	8	10.00

TABLE VIII
RESULT OF DIFFERENT QUANTITIES OF SAMPLES

Quantities of samples	Number of extraction	Rate of extraction (%)
80	23	9.5
550	207	85.5
900	108	44.63
1450	107	44.22

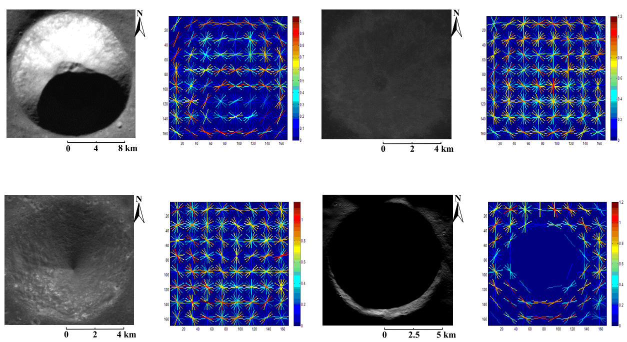

Fig. 23. HOG features of impact craters under different illuminations.

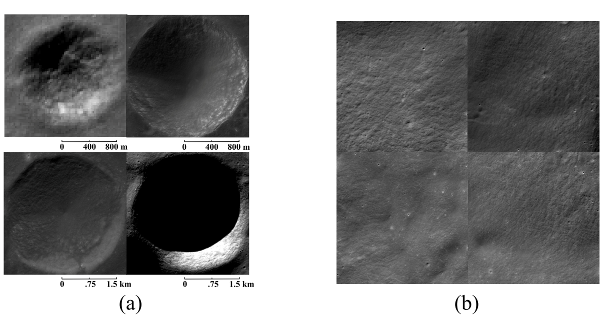

Fig. 24. Samples acquired from Chang'E-2 images. (a) Positive samples. (b) Negative samples.

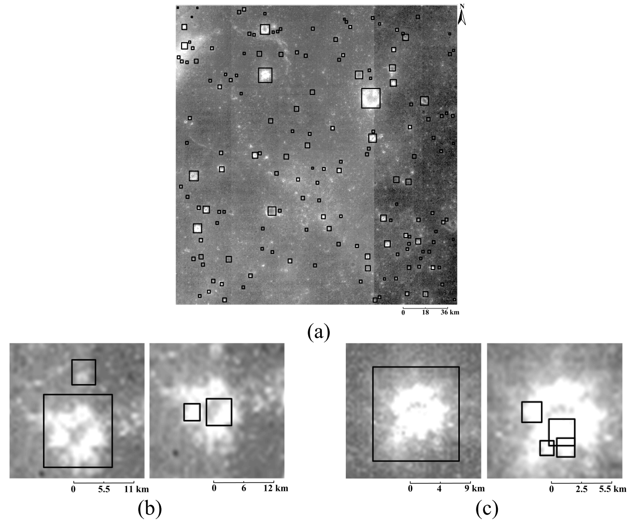

Fig. 25. Optimized extraction results of 50-m-resolution CCD images (Image I). (a) Overview. (b) and (c) Comparison between the results before or after the optimization: the above images show the results based on Chang'E-2 samples, while the images below illustrate the results based on initial Chang'E-1 samples.

TABLE IX
RESULTS OF THE EXTRACTION OF CRATERS FROM THE CHANG'E-2 CCD IMAGES AFTER THE UPDATE OF THE SAMPLE SET

	Image 1	Image 2	Image 3
Image size(pixel $\times$ pixel)	3040×3234	1481×981	2793×2841
Visual interpretation	242	186	276
Proposed method	216	161	242
False extraction	9	6	10
Missed extraction	35	31	44
Extraction rate (%)	85.53	83.2	84.05

TABLE X
SIZES OF THE IMPACT CRATERS EXTRACTED FROM THE CHANG'E-2 CCD IMAGES AFTER THE UPDATE OF THE SAMPLE SET

Image 1		Image 2		Image 3	
Diameter of craters(m)	Quantities	Diameter of craters(m)	Quantities	Diameter of craters(m)	Quantities
800-1500	160	100-250	81	20-45	101
1500-2000	35	250-350	59	45-90	90
>2000	12	>350	15	90-230	32
				>230	9

was randomly selected, and the other samples were included in a test sample set. The SVM classifier was trained by using a training sample set and verified by using a test sample set. The above process was iterated to find an optimal sample set for the crater extraction from Chang'E-2 images (Table V). During the process, different kernel functions were also tested. Table VI shows that the RBF kernel function had the best performance. Table VII indicates that the optimal values of the relaxation variable ξ and the parameter of the RBF were $\xi = 0.5, \sigma = 0.0337$.

Since machine learning is a continuous learning progress, we need to expand the sample set to increase the rate of extraction. However, if SVM is employed as a classifier, too many samples are not able to achieve a high rate of extraction. Table VIII shows that the rate of extraction was remarkably improved (9.5%–85.5%) when the number of samples increased from 80 to 550, while the extraction rate clearly decreased (44.63%) when the number of samples increased to 900 and stayed stable afterward.

Both Figs. 25–27 and Tables IX and X illustrate that the optimization ensures a high extraction rate (84% in average) by updating the sample set with extracted craters from the Chang'E-2 images. Moreover, the proposed method is able to extract craters as small as 20 m in diameter.

TABLE XI
RESULTS OF THE EXTRACTION OF CRATERS USING BOTH THE PROPOSED METHOD AND THE BOOSTING-BASED METHOD

Test scenes	Methods	Visual interpretation	True extraction	False extraction	Missed extraction	Extraction rate (%)
Image 4	The proposed method	391	335	49	56	85.6
	Boosting-based method		327	87	64	83.7
Image 5	The proposed method	411	328	59	82	79.8
	Boosting-based method		321	88	90	78.1

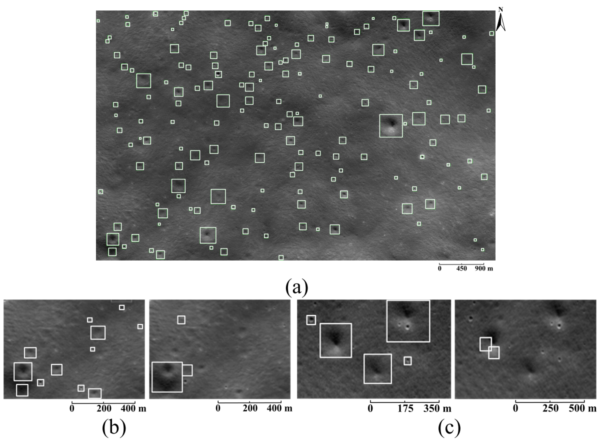

Fig. 26. Optimized extraction results of 7-m-resolution CCD images (Image 2). (a) Overview. (b) and (c) Comparison between the results before or after the optimization: the above images show the results based on Chang'E-2 samples, while the images below illustrate the results based on initial Chang'E-1 samples.

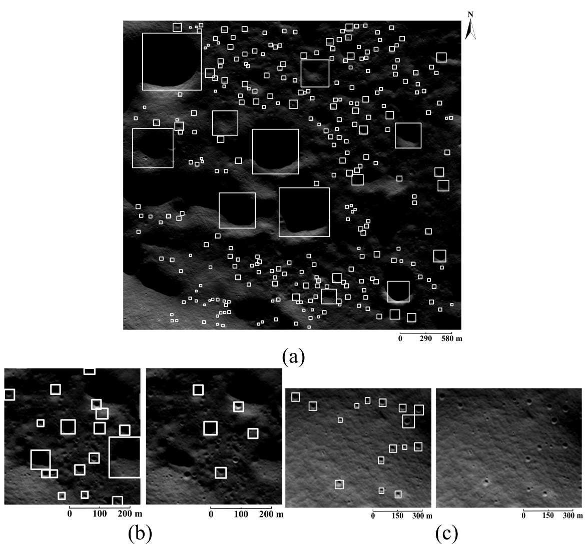

Fig. 27. Optimized extraction results of 1.4-m-resolution CCD images (Image 3). (a) Overview. (b) and (c) Comparison between the results before or after the optimization: the above images show the results based on Chang'E-2 samples, while the images below illustrate the results based on initial Chang'E-1 samples.

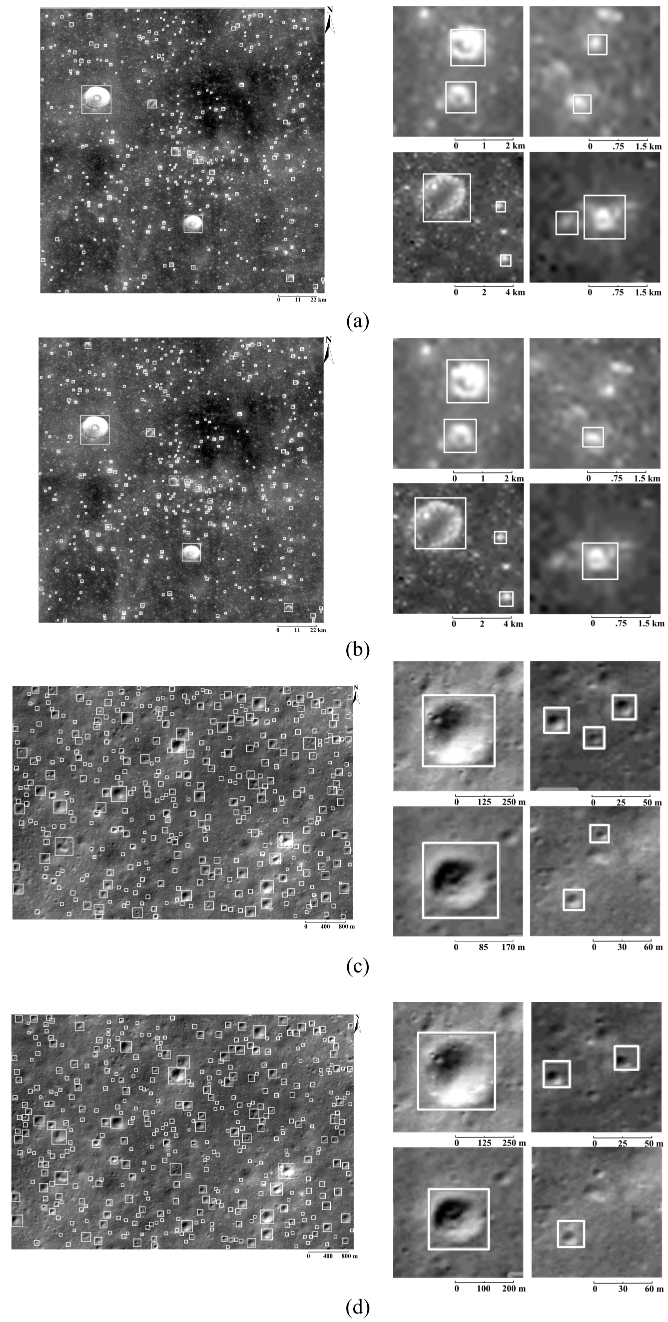

Fig. 28. Comparison between the proposed method and the boosting-based method. (a) Proposed method (Image 4). (b) Boosting-based method (Image 4). (c) Proposed method (Image 5). (d) Boosting-based method (Image 5).

E. Compared With Other Existing Method

To further verify the effectiveness and robustness of the proposed method in this paper, the frequently-used boosting-based method [24], [34], [35], [40] was compared to the proposed method using both image 4 and image 5. The boosting-based method extracted Haar-like features and LBP features and then learned an Adaboost classifier to distinguish craters from noncraters. Table XI lists the performance in extraction rate of the proposed method and the

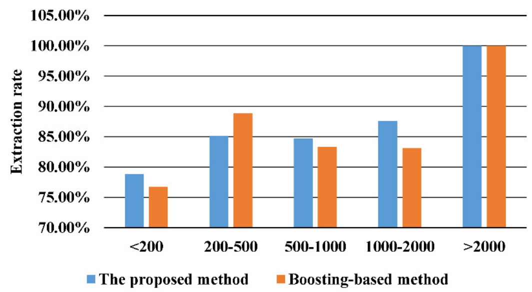

Fig. 29. Comparison of extraction rate on different size ranges between the proposed method and the boosting-based method.

boosting-based method. The proposed method in this paper is superior to the boosting-based method in terms of extraction rates with differences of 1.9% and 1.7%, respectively. Fig. 28 presents a comparison of the recognition results between the proposed method and the boosting-based method. Fig. 29 shows the comparison of extraction rate on different size ranges between the proposed method and the boosting-based method. As shown in Fig. 29, both the proposed method and the boosting-based method show a good recognition performance for extracting impact craters larger than 2000 m, whereas the proposed method shows higher extraction rates than the boosting-based method for impact craters with diameter of the range between 1000 and 2000 m, the range between 200 and 500 m, and less than 200 m, with the differences of 4.49%, 1.36%, and 2.07%, respectively.

IV. Conclusion

In this paper, a coarse-to-fine method was proposed to extract small-scale impact craters from the Chang'E satellites CCD images using HOG features and SVM classifiers. The SVM classifier was first trained by using the crater samples extracted from the Chang'E-1 images with the resolutions of 120 m to identify the craters and noncraters in terms of their HOG features. The sample set was then updated using the small-sized craters, which were acquired by employing an SVM classifier from the high-resolution Chang'E-2 images. The final extraction results with the high extraction rate were achieved after the optimization of the coarse-to-fine updating of the sample set. The proposed approach was tested on CCD images with different resolutions (from 120 to 1.4 m), which were acquired by the Chang'E satellites and covered the regions near the landing site of Chang'E-3 (19.51° W, 44.12° N). The experimental results show that the proposed approach can achieve a high extraction rate (83.6% on average) and is capable of extracting impact craters as small as 20 m from the images with multiple resolutions and under different illumination conditions, which verifies the high robustness and applicability of the presented coarse-to-fine extraction strategy. Moreover, the proposed method outperforms the boosting-based method for extracting impact craters with diameters of different size ranges.

This paper mainly focuses on impact craters with circular shapes; nevertheless, some geographical features such as small volcanic constructs or valleys have similar image characteristics as craters. The Compton–Belkovich volcanic complex, for example, contains features that are superficially similar to impact craters, but are in fact thought to be caldera structures. Therefore, future research will, thus, perform the extraction of irregularly shaped and complexly shaped craters and other geological structures. Moreover, because the amplitude of the brightness temperature that is observed by a passive radiometer depends on the slope angle, we plan to use this additional information to further improve the extraction and identification of lunar craters.

References

[1] C. Li *et al.*, "The global image of the Moon obtained by the Chang'E-1: Data processing and lunar cartography," *Sci. China Earth Sci.*, vol. 53, no. 8, pp. 1091–1102, 2010.

[2] Z. Ouyang and C. Li, "progress and the development strategy of deep space exploration in our country," *Chin. Aerosp.*, vol. 12, pp. 28–32, 2002.

[3] G. Hu *et al.*, "Brightness temperature calculation of lunar crater: Interpretation of topographic effect on microwave data from Chang'E," *IEEE Trans. Geosci. Remote Sens.*, vol. 52, no. 8, pp. 4499–4510, Aug. 2014.

[4] M. Montopoli, A. Di Carlofelice, M. Cicchinelli, P. Tognolatti, and F. S. Marzano, "Lunar microwave brightness temperature: Model interpretation and inversion of spaceborne multifrequency observations by a neural network approach," *IEEE Trans. Geosci. Remote Sens.*, vol. 49, no. 9, pp. 3350–3358, Sep. 2011.

[5] M. Montopoli, A. Di Carlofelice, P. Tognolatti, and F. S. Marzano, "Remote sensing of the Moon's subsurface with multifrequency microwave radiometers: A numerical study," *Radio Sci.*, vol. 46, no. 1, pp. 1–13, Feb. 2011.

[6] N. Namiki *et al.*, "Farside gravity field of the moon from four-way Doppler measurements of SELENE (Kaguya)," *Science*, vol. 323, no. 5916, pp. 900–905, 2009.

[7] H. U. Wenmin, K. C. Di, and Z. Yue, "Crossover analysis and adjustment for Chang'E-1 laser altimeter data," *Acta Geodaetica Cartograph. Sinica*, vol. 42, no. 2, pp. 218–224, 2013.

[8] N. L. Chabot, G. V. Hoppa, and R. G. Strom, "Analysis of lunar lineaments: Far side and polar mapping," *Icarus*, vol. 147, no. 1, pp. 301–308, 2000.

[9] B. R. Hawke *et al.*, "The origin of lunar crater rays," *Icarus*, vol. 170, no. 1, pp. 1–16, 2004.

[10] T. Morota and M. Furumoto, "Asymmetrical distribution of rayed craters on the Moon," *Earth Planet. Sci. Lett.*, vol. 206, nos. 3–4, pp. 315–323, 2003.

[11] S. Chen *et al.*, "The mapping to geological analysis by lunar satellite remote sensing in rainbow ray area," *Chin. Sci., Phys. Mech. Astron.*, vol. 40, no. 11, pp. 1370–1379, 2010.

[12] E. R. Urbach and T. F. Stepinski, "Automatic detection of sub-km craters in high resolution planetary images," *Planet Space Sci.*, vol. 57, no. 7, pp. 880–887, 2009.

[13] J. P. Cohen and W. Ding, "Crater detection via genetic search methods to reduce image features," *Adv. Space Res.*, vol. 53, no. 12, pp. 1768–1782, 2014.

[14] L. Bruzzone, L. Lizzi, P. G. Marchetti, J. Earl, and M. Milnes, "Recognition and detection of impact craters from EO products," in *Proc. ESA-EUSC Theory Appl. Knowl.-Driven Image Inf. Mining Focus Earth Observ.*, 2004, pp. 1–8.

[15] J. R. Kim, J. P. Muller, S. van Gasselt, J. G. Morley, and G. Neukum, "Automated crater detection, a new tool for mars cartography and chronology," *Photogramm. Eng. Remote Sens.*, vol. 71, no. 10, pp. 1205–1217, 2005.

[16] M. Magee, C. R. Chapman, S. W. Dellenback, B. Enke, W. J. Merline, and M. P. Rigney, "Automated identification of martian craters using image processing," in *Proc. 34th Annu. Lunar Planet. Sci. Conf.*, League City, TX, USA, Mar. 2003.

[17] B. Leroy, G. Medioni, E. Johnson, and L. Matthies, "Crater detection for autonomous landing on asteroids," *Image Vis. Comput.*, vol. 19, no. 11, pp. 787–792, 2001.

[18] Y. Xie, G. Tang, S. Yan, and H. Lin, "Crater detection using the morphological characteristics of Chang'E-1 digital elevation models," *IEEE Geosci. Remote Sens. Lett.*, vol. 10, no. 4, pp. 885–889, Jul. 2013.

[19] Y. Cheng, A. E. Johnson, L. H. Matthies, and C. F. Olson, "Optical landmark detection for spacecraft navigation," in *Proc. AAS/AIAA Space Flight Mech. Meeting*, 2003, pp. 1–19.

[20] G. Salamunićcar and S. Lončarić, "Method for crater detection from martian digital topography data using gradient value/orientation, morphometry, vote analysis, slip tuning, and calibration," *IEEE Trans. Geosci. Remote Sens.*, vol. 48, no. 5, pp. 2317–2329, May 2010.

[21] M. Ding, Y.-F. Cao, and Q.-X. Wu, "Autonomous craters detection from planetary image," in *Proc. Int. Conf. Innov. Comput. Inf. Control*, 2008, p. 443.

[22] Z. Kang, Z. Luo, T. Hu, and P. Gamba, "Automatic extraction and identification of lunar impact craters based on optical data and DEMs acquired by the Chang'E satellites," *IEEE J. Sel. Topics Appl. Earth Observ. Remote Sens.*, vol. 8, no. 10, pp. 4751–4761, Oct. 2015.

[23] P. G. Wetzler, R. Honda, B. Enke, W. J. Merline, C. R. Chapman, and M. C. Burl, "Learning to detect small impact craters," in *Proc. 7th IEEE Workshops Appl. Comput. Vis. (WACV/MOTION)*, vol. 1, 2005, pp. 178–184.

[24] X. Xin, K. Di, Y. Wang, W. Wan, and Z. Yue, "Automated detection of new impact sites on martian surface from HiRISE images," *Adv. Space Res.*, vol. 60, no. 7, pp. 1557–1569, Oct. 2017.

[25] L. Bandeira, J. Saraiva, and P. Pina, "Impact crater recognition on mars based on a probability volume created by template matching," *IEEE Trans. Geosci. Remote Sens.*, vol. 45, no. 12, pp. 4008–4015, Dec. 2007.

[26] A. Grumpe and C. Wöhler, "Generative template-based approach to the automated detection of small craters," in *Proc. Eur. Planet. Sci. Congr.*, 2013, pp. 1–2.

[27] A. L. Salih, P. Schulte, A. Grumpe, C. Wöhler, and H. Hiesinger, "Automatic crater detection and age estimation for mare regions on the lunar surface," in *Proc. 25th Eur. Signal Process. Conf. (EUSIPCO)*, 2017, pp. 518–522.

[28] T. F. Stepinski, M. P. Mendenhall, and B. D. Bue, "Machine cataloging of impact craters on Mars," *Icarus*, vol. 203, no. 1, pp. 77–87, 2009.

[29] T. Ojala, M. Pietikäinen, and T. Mäenpää, "A generalized local binary pattern operator for multiresolution gray scale and rotation invariant texture classification," in *Proc. 2nd Int. Conf. Adv. Pattern Recognit.*, 2001, pp. 397–406.

[30] P. Viola and M. Jones, "Rapid object detection using a boosted cascade of simple features," in *Proc. CVPR*, vol. 1, 2001, p. 511.

[31] N. Dalal and B. Triggs, "Histograms of oriented gradients for human detection," in *Proc. IEEE Comput. Soc. Conf. CVPR*, Jun. 2005, pp. 886–893.

[32] D. Liu, M. Chen, K. Qian, M. Lei, and Y. Zhou, "Boundary detection of dispersal impact craters based on morphological characteristics using lunar digital elevation model," *IEEE J. Sel. Topics Appl. Earth Observ. Remote Sens.*, vol. 10, no. 12, pp. 5632–5646, Dec. 2017.

[33] K. Di, W. Li, Z. Yue, Y. Sun, and Y. Liu, "A machine learning approach to crater detection from topographic data," *Adv. Space Res.*, vol. 54, no. 11, pp. 2419–2429, 2014.

[34] L. Bandeira, W. Ding, and T. F. Stepinski, "Detection of sub-kilometer craters in high resolution planetary images using shape and texture features," *Adv. Space Res.*, vol. 49, no. 1, pp. 64–74, Jan. 2012.

[35] R. Martins, P. Pina, J. S. Marques, M. Silveira, and M. Silveira, "Crater detection by a boosting approach," *IEEE Geosci. Remote Sens. Lett.*, vol. 6, no. 1, pp. 127–131, Jan. 2009.

[36] Y. Wang, G. Yang, and L. Guo, "A novel sparse boosting method for crater detection in the high resolution planetary image," *Adv. Space Res.*, vol. 56, no. 5, pp. 982–991, Sep. 2015.

[37] S. Jin and T. Zhang, "Automatic detection of impact craters on Mars using a modified adaboosting method," *Planet. Space Sci.*, vol. 99, no. 1, pp. 112–117, 2014.

[38] S. Liu, W. Ding, J. P. Cohen, D. Simovici, and T. Stepinski, "Bernoulli trials based feature selection for crater detection," in *Proc. 19th ACM SIGSPATIAL Int. Conf. Adv. Geograph. Inf. Syst.*, 2011, pp. 461–464.

[39] S. Liu, W. Ding, F. Gao, and T. F. Stepinski, "Adaptive selective learning for automatic identification of sub-kilometer craters," *Neurocomputing*, vol. 92, no. 3, pp. 78–87, 2012.

[40] W. Ding *et al.*, "Subkilometer crater discovery with boosting and transfer learning," *ACM Trans. Intell. Syst. Technol.*, vol. 2, no. 4, pp. 1–22, Jul. 2011.

[41] Y. Cao, H. Wei, H. Zhao, and N. Li, "An effective approach for land-cover classification from airborne lidar fused with co-registered data," *Int. J. Remote Sens.*, vol. 33, no. 18, pp. 5927–5953, 2012.

[42] T. S. Furey, N. Cristianini, N. Duffy, D. W. Bednarski, M. Schummer, and D. Haussler, "Support vector machine classification and validation of cancer tissue samples using microarray expression data," *Bioinformatics*, vol. 16, no. 10, pp. 906–914, 2000.

[43] P. G. Wetzler, R. Honda, B. Enke, W. J. Merline, C. R. Chapman, and M. C. Burl, "Learning to detect small impact craters," in *Proc. 7th IEEE Workshops Appl. Comput. Vis.*, Jan. 2005, pp. 178–184.

[44] C. Cortes and V. Vapnik, "Support-vector networks," *Mach. Learn.*, vol. 20, no. 3, pp. 273–297, 1995.

[45] C. H. Lampert, M. B. Blaschko, and T. Hofmann, "Beyond sliding windows: Object localization by efficient subwindow search," in *Proc. IEEE Conf. Comput. Vis. Pattern Recognit.*, Jun. 2008, pp. 1–8.

[46] N. Dalal, "Finding people in images and videos," Inst. Nat. Polytechn. Grenoble, Grenoble, France, 2006.

[47] S.-C. Huang, F.-C. Cheng, and Y.-S. Chiu, "Efficient contrast enhancement using adaptive gamma correction with weighting distribution," *IEEE Trans. Image Process.*, vol. 22, no. 3, pp. 1032–1041, Mar. 2013.

[48] D. Kumar and A. G. Ramakrishnan, "Power-law transformation for enhanced recognition of born-digital word images," in *Proc. Int. Conf. Signal Process. Commun.*, 2012, pp. 1–5.

[49] S. Chen, C. F. N. Cowan, and P. M. Grant, "Orthogonal least squares learning algorithm for radial basis function networks," *IEEE Trans. Neural Netw.*, vol. 2, no. 2, pp. 302–309, Mar. 1991.

[50] N. Cristianini and J. Shawe-Taylor, *An Introduction to Support Vector Machines and Other Kernel-Based Learning Methods*. Cambridge, U.K.: Cambridge Univ. Press, 2000.

Zhizhong Kang received the Ph.D. degree in photogrammetry and remote sensing from Wuhan University, Wuhan, China, in 2004.

He was a Post-Doctoral Researcher with the Delft University of Technology, Delft, The Netherlands, from 2006 to 2008. He is currently a Full Professor and the Head of the Department of Remote Sensing and Geo-Information Engineering, China University of Geosciences, Beijing, China. He has authored more than 60 referred journal and conference publications. His research interests include digital photogrammetry, LiDAR data processing, indoor modeling and navigation, and planetary remote sensing.

Dr. Kang has served as the Chair of ISPRS WG IV/5: Indoor/Outdoor seamless modeling, LBS, mobility. He received the 2015 ERDAS Award for Best Scientific Paper in remote sensing by the American Society for Photogrammetry and Remote Sensing.

Xingkun Wang received the master's degree from the School of Land Science and Technology, China University of Geosciences, Beijing, China.

His research interests include computer vision and lunar structure recognition and analysis.

Teng Hu received the Ph.D. degree in cartography and geographical information engineering from Wuhan University, Wuhan, China, in 2013.

He is currently a Lecturer with the Department of Remote Sensing and Geo-Information Engineering, China University of Geosciences, Beijing, China. His research interests include digital photogrammetry and computer vision including processing of UAV data, stereo matching, and lunar structure recognition and extraction.

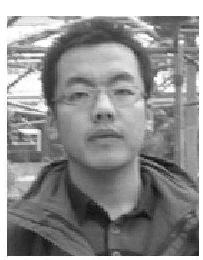

Juntao Yang received the master's degree in LiDAR technology from the China University of Geosciences, Beijing, China, in 2017, where he is currently pursuing the Ph.D. degree with the School of Land Science and Technology.

His research interests include LiDAR data processing, computer vision, and lunar structure recognition and analysis.